Universidade de Aveiro Departamento de Química

Universidade do Porto Faculdade de Engenharia
Departamento de Engenharia Química

Bondalti
2019

Químicos Industriais

Francisco José Almeida Loureiro

Desenvolvimento de materiais para reatores eletroquímicos cerâmicos de temperatura reduzida

Development of materials for reduced operation temperature ceramic electrochemical reactors

Universidade de Aveiro Departamento de Química

Universidade do Porto Faculdade de Engenharia
Departamento de Engenharia Química

Bondalti Químicos Industriais
2019

Francisco José Almeida Loureiro

Desenvolvimento de materiais para reatores eletroquímicos cerâmicos de temperatura reduzida

Development of materials for reduced operation temperature ceramic electrochemical reactors

Tese apresentada à Universidade de Aveiro para cumprimento dos requisitos necessários à obtenção do grau de Doutor em Engenharia da Refinação, Petroquímica e Química, realizada sob a orientação científica do Doutor Duncan Paul Fagg, Investigador Principal do Departamento de Mecânica da Universidade de Aveiro, do Doutor Adélio Miguel Magalhães Mendes, Professor Catedrático do Departamento de Química da Faculdade de Engenharia da Universidade do Porto, e do Doutor Alejandro França Gomes Ribeiro, Quadro Superior de Engenharia de Processos na Bondalti

Fundação para a Ciência e Tecnologia (FCT) e Bondalti. Bolsa de Investigação PD/BDE/114353/2016 e projeto POCI-01-0145-FEDER-032241, PTDC/CTM-CTM/32241/2017

o júri

presidente

Prof. Doutora Ana Isabel Couto Neto Da Silva Miranda
Professora Catedrática da Universidade de Aveiro

Doutor Glenn Christopher Mather
Investigador Principal da Universidad Autonoma de Madrid

Prof. Doutor João Carlos de Castro Abrantes
Professor Coordenador do Instituto Politécnico de Viana do Castelo

Prof. Doutor Christopher Michael Ashton Brett
Professor Catedrático da Universidade de Coimbra

Doutor Andrei Kavaleuski
Equiparado a Investigador Principal da Universidade de Aveiro

Doutor Duncan Paul Fagg (Orientador)
Equiparado a Investigador Principal da Universidade de Aveiro

agradecimentos

Aos meus orientadores, Duncan Fagg, Adélio Mendes e Alejandro Ribeiro pelo apoio incondicional, por acreditarem em mim e no meu trabalho e pela incansável paciência e disponibilidade.
A todos os meus colegas que passaram pelo NRD. Agradeço em especial à Vanessa Graça, ao Domingo Pérez-Coll, ao Sergey Mikhalev, à Laura Holz, ao Devaraj Ramasamy, à Isabel Antunes, ao Aliaksandr Shaula, à Zinaida Shakel, ao Pukazh Selvan pelo contante apoio, companheirismo e amizade.
A todos os colaboradores do departamento de Engenharia Mecânica pela ajuda e disponibilidade.
À direção da Bondalti, Diogo Mendes e Mário Jorge Pinho pelo acompanhamento e valorização do trabalho.
À minha família, pelo apoio incondicional e compreensão pela minha dedicação ao trabalho.
Aos meus amigos por acreditarem em mim.

palavras-chave

Cerato de bário dopado com ítria, condutividade protónica, pressão parcial de vapor de água, atmosfera nominalmente seca, reação química.

resumo

Os reatores eletroquímicos de membrana cerâmica protónica são tecnologias promissoras e eficientes para a produção de produtos químicos valiosos através da promoção eletroquímica de reações de hidrogenação/desidrogenação. Devido à sua elevada constante de equilíbrio para a hidratação, o cerato de bário dopado com ítria, $BaCe_{0,9}Y_{0,1}O_{3-\delta}$ (BCY10) apresenta uma das mais altas condutividades protónicas a baixas temperaturas, entre os óxidos cerâmicos condutores protónicos mais conhecidos (*p.e.*, ~ 10^{-3} S cm^{-1} a 400 °C em atmosferas humidificadas, p_{H2O} ~ 10^{-2} atm). Contudo, o BCY10 é comumente descartado para tais aplicações devido à sua fraca estabilidade química para a formação de hidróxido ou carbonato. Além disso, o uso de atmosferas humidificadas pode não ser viável para muitas sínteses químicas, devido a reações secundárias indesejáveis.

Este trabalho, portanto, centra-se nas propriedades de transporte eletroquímico do BCY10 em condições de humidade muito baixa (p_{H2O} < 10^{-4} atm e baixas temperaturas < 600 °C). As análises incluem o estudo da química de defeitos para esta composição em função das possíveis condições de trabalho, e a sua relação com as condutividades parciais das propriedades em *bulk*. O trabalho prossegue com a análise das condutividades específicas da fronteira de grão em termos das propriedades da dupla camada elétrica em função da temperatura e da atmosfera. As implicações de todas estas propriedades do BCY10 são então exemplificadas em dois exemplos de trabalho: *i*) o estudo de novos cátodos à base de $La_4Ni_3O_{10-\delta}$ para aplicações de cerâmicos protónicos, utilizando células simétricas de substratos BCY10, em que a resistência de polarização do eléctrodo deve ser corrigida devido à existência de curto-circuito no eletrólito, tendo em conta o número de transporte eletrónico do mesmo; *ii*) o estudo de uma célula completa feita de uma película fina de BCY10 em ambos os modos eletrolizador e pilha de combustível/bombagem iónica, em que cada um pode causar diferentes alterações nas resistências do eletrólito e dos elétrodos.

As condições utilizadas para o estudo do BCY10 são justificadas de forma compreensível em cada capítulo através de cálculos termodinâmicos, mostrando que é possível prevenir a decomposição da fase cerâmica em contato com atmosferas contendo hidrocarbonetos ou gases ácidos, *p.e.* CO_2 e H_2O. Além disso, destaca-se a relevância de tais condições no que diz respeito à possibilidade de aplicar este material em reações de síntese química industrialmente relevantes, mantendo hidratação e condutividade protónica elevadas. Este trabalho desbloqueia, assim, uma nova área de aplicação para os cerâmicos condutores protónicos a uma vasta gama de reações de hidrogenação/de-hidrogenação a baixas temperaturas e pressões parciais mínimas de vapor de água.

keywords

Yttrium-doped barium cerate, proton conductivity, water vapour partial pressure, nominally dry atmosphere, chemical reaction.

abstract

Electrochemical membrane reactors using proton-conducting ceramics are promising and efficient technologies for the production of valuable chemical products by the promotion of hydrogenation/dehydrogenation reactions. Due to a very high equilibrium constant for hydration, yttrium-doped barium cerate, $BaCe_{0.9}Y_{0.1}O_{3-\delta}$ (BCY10) presents one of the highest proton conductivities at low temperatures of the known proton-conducting ceramic oxides (*e.g.* ~ 10^{-3} S cm^{-1} at 400 °C under humidified atmospheres, p_{H2O} ~ 10^{-2} atm). Nonetheless, BCY10 is commonly discarded for such applications due to its poor chemical stability towards hydroxide or carbonate formation. Moreover, the use of humidified atmospheres may not be feasible for many chemical syntheses, due to undesired side reactions.

The current work, therefore, focus on the electrochemical transport properties of BCY10 in conditions of very low humidity (p_{H2O} < 10^{-4} atm and at low temperatures < 600 °C). The analyses include the study of the defect chemistry for this composition as a function of potential working conditions, and its relation to the partial conductivities of the bulk properties. Further work corresponds to the examination of the specific grain boundary conductivities in terms of space charge properties, as a function of temperature and atmosphere. The implications of all these properties of BCY10 are then exemplified in two working examples: *i*) the study of new $La_4Ni_3O_{10-\delta}$-based cathodes for proton ceramic applications, using symmetrical cells made of BCY10 substrates, where the polarisation resistance of the electrode must be corrected for significant electronic leakage by taking into account the electronic transport number of the electrolyte; *ii*) the study of a single-cell made of thin film BCY10 electrolyte under both electrolyser and fuel cell/ion pump modes, where these modes of operation are shown to cause variations in both electrolyte and electrode resistances.

The conditions used to study BCY10 are comprehensively justified in each chapter by thermodynamic calculations to be able to prevent the decomposition of the ceramic phase in contact with atmospheres containing hydrocarbons or acidic gases such as CO_2 and H_2O. Moreover, the relevance of such conditions is highlighted with respect to potential to apply this material to industrially relevant chemical synthesis reactions, while retaining hydration and high protonic conductivity. This work, thereby, unlocks a new application area for proton-conducting ceramics to a wide range of hydrogenation/de-hydrogenation reactions at low temperatures under minimum water vapour partial pressures.

Table of contents

List of figures

List of tables

List of abbreviations

NH_3 – ammonia

E_a – activation energy

a.c. – alternated current

O_{ad} – adsorbed oxygen atom

CO – carbon monoxide

CO_2 – carbon dioxide

CMR – ceramic membrane reactor

LNO+BCY10 – composite made of lanthanum nickelate and yttrium-doped barium cerate

DIL – dilatometry

d.c. – direct current

DFT – differential functional theory

DSC – differential scanning analysis

DFRT – distribution frequency relaxation times

χ_O – electronegativity of the oxide

χ_M – electronegativity of the metal cation

EIS – electrochemical impedance spectroscopy

EDS – energy dispersive X-ray spectroscopy

FE – faradaic efficiency

FBR – fluidized bed reactor

GC – gas chromatography

HER – hydrogen evolution reaction

H_2 – hydrogen (molecular)

H^+ – hydrogen (ionic)

IL – ionic liquid

Li^+ – lithium (ionic)

LNO – lanthanum nickelate ($La_4Ni_3O_{10-\delta}$)

MEA – membrane electrode assembly

MDA – methane dehydroaromatization

CH_4 – methane

MIEC – mixed ionic and electronic conductor

N_2 – nitrogen (molecular)

OCV – open circuit voltage

O_2 – oxygen (molecular)

O^{2-} – oxygen (ionic)

ABO_3 – perovskite structure

EngIQ – *Programa de Doutoramento em Engenharia da Refinação, Petroquímica e Química*

%RH – relative humidity

RT – room temperature

SEM – scanning electron microscopy

O_{ad}^- – surface adsorbed oxygen ion

TG – thermogravimetric analysis

H_2O – water

XRD – X-ray diffraction

BCY – yttrium-doped barium cerate ($BaCe_{1-x}Y_xO_{3-\delta}$)

BCY10 – $BaCe_{0.9}Y_{0.1}O_{3-\delta}$

BCZY – yttrium-doped barium cerate-zirconate ($BaCe_{1-x}Zr_xY_{0.1}O_{3-\delta}$)

BZY – yttrium-doped barium zirconate ($BaZr_{1-x}Y_xO_{3-\delta}$)

YSZ – yttrium-stabilized zirconia

List of symbols

E_a – activation energy

Ce_{Ce}^{x} – cerium ion sitting on a cerium lattice site, with neutral charge

Ce_{Ce}' – cerium ion sitting on a cerium lattice site, with negative charge

$R_{high,eon}$ – corrected high-frequency polarisation resistance

$R_{mid,eon}$ – corrected intermediate-frequency polarisation resistance

$R_{low,eon}$ – corrected low-frequency polarisation resistance

$R_{p,eon}$ – corrected total polarisation resistance

C – capacitance

C_{chem} – chemical capacitance

Q – constant phase element

$h^{\bullet}$ – electronic hole, with positive charge

ΔS – entropy variation

ΔH – enthalpy variation

K_O – equilibrium constant for oxidation

K_R – equilibrium constant for reduction

t_{eon} – electrolyte electronic transport number

R_{ion} – electrolyte ionic resistance

R_{eon} – electrolyte electronic resistance

R_{ohm} – electrolyte total resistance

E_f – Fermi energy

FLW – Finite length *Warburg*

ΔG^{o} – Gibbs energy variation

R – gas constant

t – *Goldschmidt* tolerance factor

p_{H2} – hydrogen partial pressure

R_{high} – high-frequency polarisation resistance

R_A – ionic radius of the perovskite A-site atom

R_O – ionic radius of the perovskite oxygen atom

R_B – ionic radius of the perovskite B-site atom

-Z'' – imaginary axis of the impedance plot

Z'' – imaginary axis of the impedance plot

R_{mid} – intermediate-frequency polarisation resistance

R_{low} – low-frequency polarisation resistance

E – Nernst potential

$V_O^{\bullet\bullet}$ – oxygen vacancy, with double positive charge

O_O^x – oxygen ion sitting on an oxygen lattice site, with neutral charge

$OH^{\bullet}$ – protonic defect, with positive charge

p_{O2} – oxygen partial pressure

E_0 – reversible potential

R – resistance / resistor

T – temperature

R_p – total polarisation resistance

RQ – resistor in parallel with a constant phase element

Z' – real axis of the impedance plot

p_{H2O} – water vapour partial pressure

Y_{Ce}' – yttrium ion sitting on a cerium lattice site, with negative charge

Greek symbols

ω – angular frequency

τ_0 – characteristic time constant

ϕ – constant phase element parameter

ρ – density

χ – electronegativity

σ – electrical conductivity

σ_0 – electrical conductivity pre-exponential factor

σ_{e^-} – electronic conductivity (electrons)

$\sigma_{h\bullet}$ – electronic conductivity (holes)

σ_{ion} – electrolyte ionic conductivity

σ_{eon} – electrolyte electronic conductivity

Ω – electrical resistance

σ_{O2-} – oxide-ion conductivity

δ – oxygen non-stoichiometry

σ_{H+} – protonic conductivity

Δ_{real} – residual differences between the real values of the impedance data and the fitting

Δ_{real} – residual differences between the imaginary values of the impedance data and the fitting

φ – space-charge barrier height potential

σ_T – total conductivity

τ – time constant

1. Introduction

Bondalti Chemicals S.A. is an industrial chemical company from Estarreja, Portugal, and a key player in Estarreja's chemical site complex. Operating in both organic and inorganic fields, Bondalti produces aniline needed for the production of the methylene diphenyl diisocyanate (MDI), as well as chlorine and sodium hydroxide. Other important products are sodium hypochlorite, hydrogen, hydrochloric acid, nitrobenzene, nitric acid, sulphanilic acid, cyclohexylamine and cyclohexanol.

The production in Estarreja is destined mainly for export. Bondalti is the leading seller of aniline in the European market and one of the main chlor-alkali producers in the Iberian Peninsula. The typical process of aniline production involves a set of three reaction steps and corresponds to the synthesis route industrially implemented in Bondalti. The main reactions of the process are the following, i) formation of nitric acid from the catalytic oxidation of ammonia, ii) reactions of benzene with a mixture of aqueous nitric acid and sulfuric acid to give nitrobenzene, and finally iii) catalytic reduction of the nitrobenzene with hydrogen to form aniline. The two main reactions of benzene nitration and reduction of the nitrobenzene usually produce large quantities of water. These reactions are also accompanied by other secondary reactions causing several unwanted organic by-products. Consequently, the obtained products are subject to a series of separation and purification stages, accordingly to the purity specifications of the formed aniline. This traditional process of producing aniline, therefore, involves high cost and risks, especially since the hydrogenation reaction takes place at elevated temperatures as required by the purification/refining stages.

Thus, the typical aniline production process has several drawbacks in that it involves high reaction and purification / refining times, high energy consumption and low atomic efficiency. Moreover, the overall process of aniline production involves the formation of a large number of by-products of negative environmental impact. In contrast, the alternative synthesis of aniline from a process involving only a direct amination reaction of benzene is much more attractive from an industrial point of view, as it would make a more direct use

of the raw materials and present a higher atomic efficiency. Moreover, the formation of harmful by-products would be reduced, thus meeting the global trends of sustainable development and green chemistry in the chemical industry [1].

The reaction of direct amination of benzene with ammonia to produce aniline is described by eqn (1.1). This reaction is limited by thermodynamic equilibrium and has a maximum conversion of only about 1% (300 °C and 300 bar) [2].

$$C_6H_{6(g)} + NH_{3(g)} \rightleftharpoons C_6H_5NH_{2(g)} + H_{2(g)} \quad (1.1)$$

The production of aniline through this reaction is, thus, only feasible if it is possible to shift the reaction balance to the production of aniline. The displacement of the reaction in the product direction can be accomplished by removing reaction products as they are formed. Since the direct amination reaction of benzene gives aniline and hydrogen, several investigators have, thus, proposed the removal of hydrogen using a membrane reactor permeable to this gas. The most common approach is to use palladium or palladium / silver membranes, as these membranes are extremely permeable to hydrogen at temperatures in excess of 300 °C. Nonetheless, to date, such selective hydrogen permeation still fail to present high conversions, above 20 % [3].

During the development of this thesis, Bondalti Chemicals S.A., in collaboration with the University of Aveiro and the Faculty of Engineering of University of Porto, has been developing the use of a membrane electrochemical reactor for the benzene amination reaction. This reactor has a configuration similar to a proton conduction solid oxide (H-SOFC) fuel cell and is intended for the active removal of the hydrogen formed in the reaction medium, by displacing the balance of the amination reaction towards the formation of the products. Since the reactor promotes the active removal of hydrogen from the reaction medium, it potentially allows a higher conversion of benzene to aniline [4].

The electrochemical reactor consists of a dense and proton conductive ceramic membrane, positioned between two porous electrodes: the anode and the cathode. The assembly formed by the anode, membrane and cathode is designated as a single-cell or MEA (Membrane Electrode Assembly). The anode consists of nickel and a ceramic protonic conductor, where the nickel has the function of both electronic conductor and catalyst to

the amination reaction, while the membrane or electrolyte allows the conduction of proton species, isolating the passage of electric current and the reagents and products of the reaction. Finally, the cathode formed by platinum-based materials catalyses the hydrogen reduction reaction. The intended working temperature range of this device is below 600 °C. Fig. 1.1 depicts the schematic representation of the electrochemical cell for the production of aniline.

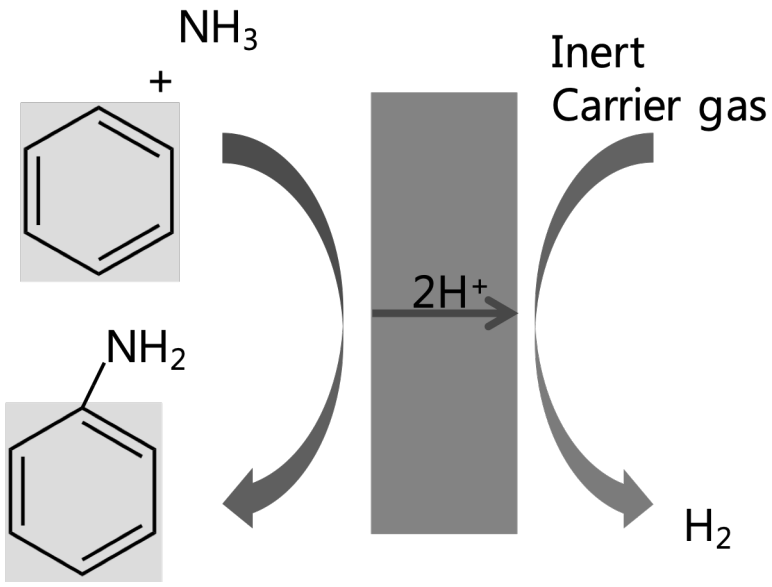

Fig. 1.1 – Schematic representation of the electrochemical cell for the production of aniline.

The work developed in the frame of *Programa de Doutoramento em Engenharia da Refinação, Petroquímica e Química* (EngIQ) focuses on the study of the intrinsic properties of the materials used by Bondalti in the fuel cell reactor. Specific aspects related to the direct amination of benzene are not disclosed here. Although the variables selected for the study limit themselves to the expected conditions of this electrochemical device for aniline production, the work offers extended impact for similar protonic devices that can be applied to a multitude of further chemical hydrogenation or dehydrogenation reactions under similar conditions. The current thesis was structured in order to satisfy the needs of Bondalti, by following these specific and necessary objectives:

a) Study of the electrochemical transport properties of the proton-conducting ceramic $BaCe_{0.9}Y_{0.1}O_{3-\delta}$ (BCY10) under very low water-vapour partial pressures in

both reducing and oxidising conditions with the aim of chemical production in the anode side at low to intermediate temperatures (below 600 °C);

b) Develop alternative cathode materials from the current solution used by the company (not disclosed here) to operate below 600 °C.

This thesis is organised by a compilation of articles in order to satisfy the agreement between the company and the academic institutions.

References

1 R. T. Baker and W. Tumas, *Science*, 1999, **284**, 1477–1479.

2 J. Becker and W. F. Hölderich, *Catal. Letters*, 1998, **54**, 125–128.

3 F. V Laar, E. Schwab, H. Voss, J-T, Anders, S. Crone, W. Mackenroth, WO/2007/025882, 2007.

4 A. Mendes, WO/2011/055343, 2011.

2. Literature review

2.1. Fuel cells

Fuel cells can use a diverse set of electrolytes and it is the nature of this component that normally defines the operation temperature (Fig. 2.1). In turn, it is the operating temperature that consequently defines the types of fuel that can be used and the kind of reforming that these fuels demand (internal or external) [1]. In the low temperature range, the most advanced technology, by a wide margin, is the proton exchange membrane fuel cell (PEMFC), leaving only fringe roles for the phosphoric acid fuel cell (PAFC) and the direct methanol fuel cell (DMFC). On the other hand, in the medium to high temperature range, the molten carbonate fuel cell (MCFC) and SOFC are mainly used, providing high power for stationary applications and potential integration with cogeneration systems (production of electricity and heat together) [2].

In this respect, solid oxide fuel cells (SOFCs) represent a capable technology to deliver sustainable and clean energy conversion in the future. These high-temperature targeted devices traditionally operate around 800 – 1000 °C, with high efficiency, zero emissions and silent function. The use of non-noble catalysts in the electrode materials and the possibility of co-generation are some of the advantages [3,4]. However, several key technical issues related to the high operating temperature have hindered the deployment of this transformative technology, to date, such as high systems costs and high-performance degradation rates, as well as slow start-up and shutdown cycles [5]. The elevated operation temperature also lead to severe degradation of cell components and demand expensive sealants and interconnection materials that increase the cost of the technology [3,4]. Over the past decade, considerable effort has, therefore, been focused in reducing the operating temperature of SOFCs down to the intermediate temperature range.

In this respect, proton-conducting oxides can open a new working window in the temperature range of 400 – 700 °C, as these electrolytes derive their ionic conductivity from the incorporation of protonic defects of high mobility [6].

Bridging the high and low temperature regimes, the more recent protonic ceramic fuel cell (PCFC) is, thus, a very promising technology because it offers the same flexibility of SOFC in terms of the type of fuels that can be used (e.g. hydrogen or hydrocarbons), is a completely solid state device, avoiding the problems associated with corrosive liquids, such as in MCFCs, and is able to be operated at intermediate temperatures where simpler thermal management and higher cell stabilities can be offered [7].

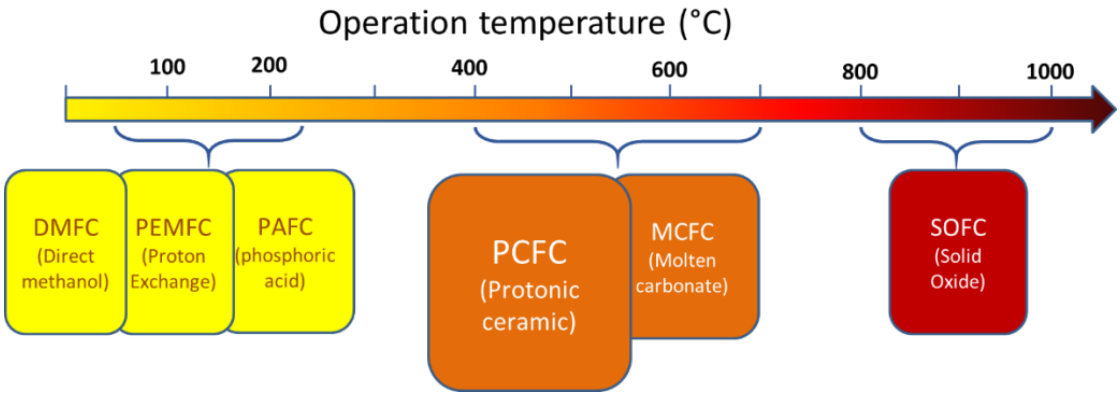

Fig. 2.1 – Status of the current fuel cell technologies and their targeted operation temperature range [8].

A PCFC is comprised of a proton conducting solid electrolyte, sandwiched between two porous electrodes (the anode and the cathode) [9]. The working principle is illustrated in Fig. 2.2. In PCFCs, the fuel (hydrogen or alternative hydrocarbons) is oxidised at anode side by creating protons and releasing electrons:

$$2H_{2(g)} \rightarrow 4H^{+} + 4e^{-} \qquad (2.1)$$

The protons formed at anode side migrate through the electrolyte towards cathode side where the formation of water takes place by reaction with oxygen:

$$4H^{+} + 4e^{-} + O_{2(g)} \rightarrow 2H_2O_{(g)} \qquad (2.2)$$

Conversely, in the case of oxide-ion conducting electrolytes, these mobile ions are formed at the cathode by oxygen reduction:

$$O_{2(g)} + 4e^{-} \rightarrow 2O^{2-} \qquad (2.3)$$

While on the other side, the anodic reaction will be:

$$2O^{2-} + 2H_{2(g)} \rightarrow 2H_2O_{(g)} + 4e^- \quad (2.4)$$

The global reactions, eqn (2.1) + (2.2) and eqn (2.3) + (2.4) and the corresponding cell *Nernstian* voltage ($V = -\Delta G/4F$), where the symbols have their usual meaning) are identical, however, the individual electrode reactions are distinct, as are the ionic transport mechanisms [10]. The difference in the chemical potential of gases at the electrodes is responsible for the movement of the ionic species, whereas, the electrochemical reactions occur mainly at electrode/electrolyte interface within a range of few micrometres into the electrodes from the electrolyte. This interfacial zone is termed as the functional layer while the remaining part of the electrode is primarily a current collector microstructure that should be porous to allow gas access to the functional layer [11].

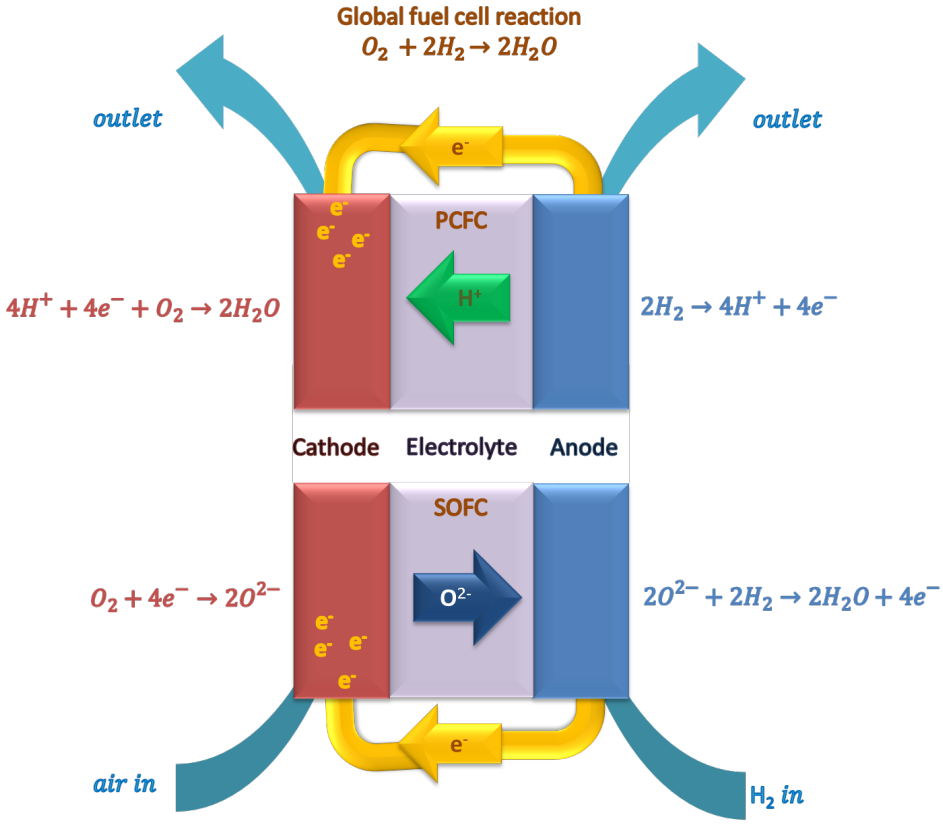

Fig. 2.2 – Schematics of a solid-state fuel cell in the case of oxide-ion conductor (SOFC) and proton conductor (PCFC) [8].

The electrolyte must be dense and gas tight to avoid the direct mixing of fuel and oxidant gases. In PCFCs, both the electrolyte and electrodes are based on stable ceramic-based materials. Electricity (and heat) are obtained under cell operating conditions as long as the

fuel and oxidant gases are provided to the cell [11,12]. An open circuit voltage (*OCV*) of ~ 1 V is attained when the cell is at unloaded state, defined by the Nernst potential [11], which is expressed as

$$E = E^0 - \frac{\mathrm{R}T}{2\mathrm{F}} \ln \left[\frac{p_{\mathrm{H2O}}}{p_{\mathrm{H2}} \cdot \sqrt{p_{\mathrm{O2}}}} \right] \quad (2.5)$$

where, E = Nernst potential, R = Universal gas constant, T = Temperature, F = Faraday constant, p_{H2}, hydrogen partial pressure, p_{H2O}, water-vapour partial pressure, p_{O2}, oxygen partial pressure. As the maximum voltage of a single cell is close to 1 V, several cells must be connected in series to form a so-called fuel cell "stack" to obtain higher voltages for practical application purposes [13]. A stack can be defined as a set of cells, where each cell is separated by an interconnector, whereas, the total fuel cell plant is designed based on the desired power output in stacks, connected either in series or parallel [11,13].

2.2. Separation Processes using Electrochemical Membrane Reactors

Separation processes are a crucial step in chemical and related industries, such as in the production of pharmaceutics, fertilizers, cosmetics, and foodstuffs, amongst others. The separation processes mainly occur in the purification step of the raw-materials, in the separation of reaction products and in the treatment of industrial effluents [14]. The most common processes include distillation, adsorption, and extraction. The majority of industrially important catalytic processes occur in a temperature range between 200 and 600 °C. For instance, the *Haber–Bosch* synthesis for ammonia (NH_3) production (450 – 550 °C) that involves the reaction of gaseous nitrogen and hydrogen over, typically, a Fe-based catalyst at high pressures (150 – 300 bar) [14,15]. Another example is the synthesis of methanol (200 – 300 °C), currently the second largest use of hydrogen, after that of ammonia synthesis [16]. Methanol is produced by the catalytic conversion of synthesis gas (a mixture of CO and H_2) by *Fischer–Tropsch* synthesis. The *Fischer–Tropsch* process is an important and flexible synthesis route that can be used to produce a wide variety of fuels and valuable hydrocarbons up to C_{5+} from synthesis gas [17,18]. Nonetheless, in all these process the desired chemical product must be separated from the overall product gas, In this respect, direct membrane-based processes have recently become an attractive alternative compared to the conventional separation processes in various chemical applications, especially due to their ability to induce electrochemical enhancements [19–22].

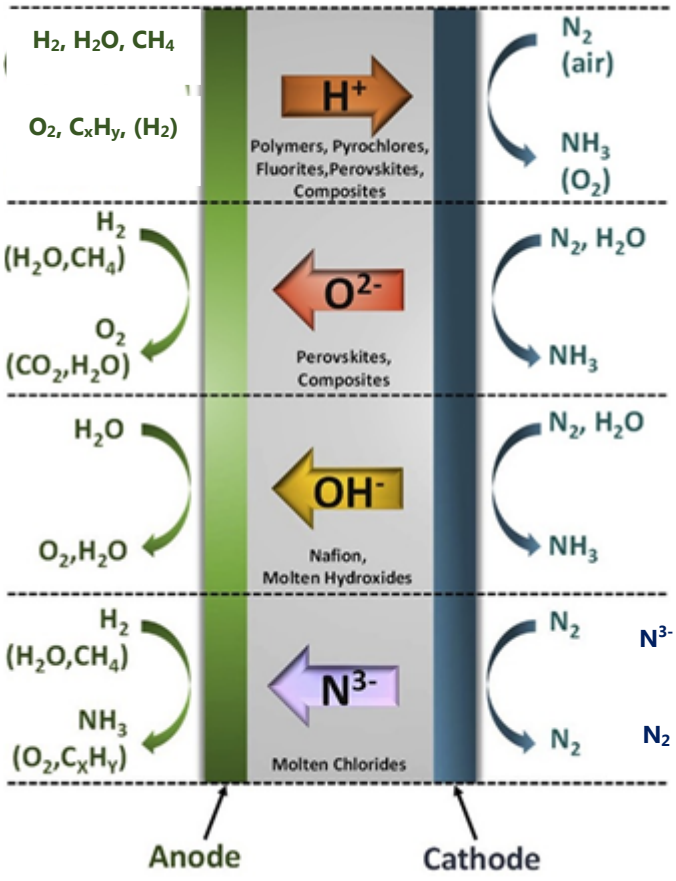

Fig. 2.3 – Schematic diagram of several electrochemical reactor configurations. Adapted from [19].

Electrochemical membrane reactors incorporate ion-conducting membranes that allow the selective permeation of single ionic species, *e.g.* H^+, O^{2-}, OH^-, N^{3-}, etc., whilst being impermeable to non-charged reaction species (Fig. 2.3). These reactors are, therefore, electrochemical cells, in which the oxidation and reduction reactions are carried out separately on catalyst/electrodes layers located on the opposite sides of the electrolyte. These devices are, thus, similar to fuel cells in the fact that they contain oxidation and reduction reactions at opposing electrodes. Nonetheless, these devices focus on producing increased yields of useful chemicals rather than electrical output [20,21]. The use of such kind of reactors presents several advantages such as: enhanced catalytic activity and selectivity, better process integration, reduced feedstock and easy reaction rate control [22]. Moreover, when these overall reactions are spontaneous, electrical energy can also be produced as a secondary product.

One interesting example is the one-step conversion of methane to C_2 compounds (*e.g.*, ethane and ethylene) that has become one of the most challenging problems in catalysis research. In the presence of a variety of catalysts, and in the temperature range from 600 to 900 °C, methane and oxygen react to produce C_2 hydrocarbons, with CO and CO_2 being the major carbon-containing by-products [23]. On this regard, Yentekakis *et al.* [24] obtained C_2 yields exceeding 85 % either by the electrochemical supply of O^{2-} on an (80 wt%) Ag – (19 wt%) Sm_2O_3 + (1 wt%) CaO anode or by using gaseous O_2 and a (80 wt%) Ag – (20 wt%) Sm_2O_3 catalyst (Fig. 2.4). These conversions were more than four times than those achieved with the best catalysts in the traditional configuration.

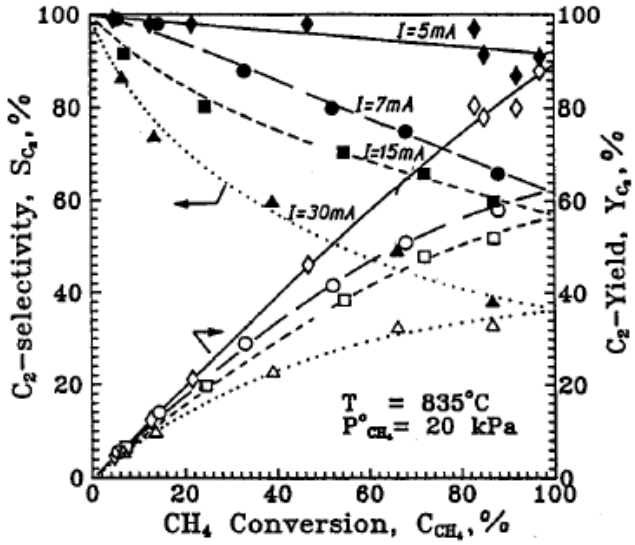

Fig. 2.4 – Effect of methane conversion and applied current on the C_2 hydrocarbon selectivity (filled symbols) and yield (open symbols). The cell reactor consisted of an Y_2O_3 (8 mol%)-stabilized ZrO_2 (YSZ) tube closed flat at one end with an appropriately machined water-cooled stainless-steel reactor cap attached to the other end, thus allowing for continuous gas feed and removal. The catalyst electrode was a porous Ag-Sm_2O_3 film coated on the inside walls of the YSZ tube. An Ag counter electrode was deposited on the outer walls of the YSZ tube [24].

Hibino *et al.* [25] studied the electrocatalytic conversion of methane to C_2 using a Li^+ solid electrolyte ($(Li_2O)_{0.17}(BaO)_{0.07}(TiO_2)_{0.76}$) and Au electrodes, and an alternating (*ac*) current. At open circuit voltage (*OCV*), the conversion of methane and the selectivity to C_2 hydrocarbons were 3 and 20 %, respectively. In contrast, at 3 V (*ac* current), the conversion of methane was twice than that obtained under *OCV* and the corresponding C_2 selectivity was enhanced in to 30 % (Fig. 2.5a). The noted improvement was explained to be due to promotion of the chemical reaction due to the pumping of Li^+ through the electrolyte

membrane, whereas, at *OCV* the reaction only occurs on the surfaces of the electrolyte and/or the two gold electrodes.

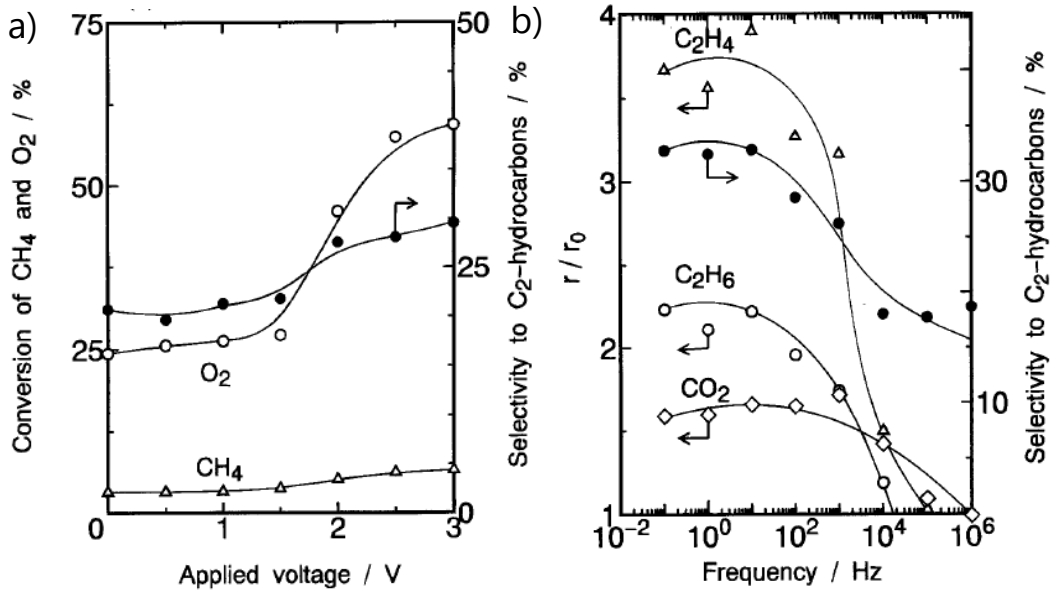

Fig. 2.5 – a) effect of the applied ac voltage on the conversion (open symbols) of methane and selectivity (filled symbols) to C_2 hydrocarbon; b) effect of frequency on formation rates of products (r/r_0) and selectivity to C_2 hydrocarbons (applied *a.c.* voltage: 3 V). The reaction temperature was 850 °C in a mixture of ~ 8.3 % methane and ~ 1.6 % oxygen in argon. A $Au|(Li_2O)_{0.17}(BaO)_{0.07}(TiO_2)_{0.76}|Au$ single-cell was used for this experiment [25].

A further analysis denoted that, as the frequency decreased from 100 kHz to 0.1 Hz (Fig. 2.5b), the selectivity became progressively larger, with peak performances obtained between 10 Hz and 1 Hz. Consequently, Li^+ ions started to migrate between the two gold electrodes and to improve the activity and selectivity of the electrode/electrolyte interface.

The discovery and development of high-temperature proton (H^+) conductors in the 1980s and the relatively moderate success with oxygen-ion (O^{2-}) cells directed several research groups into a totally different route based on methane dimerization via dehydrogenation rather than partial oxidation, as the undesirable oxygenates (CO, CO_2) could be avoided [23]. As an example of a proton conducting membrane, Morejudo *et al.* [26], reported a nonoxidative methane dehydroaromatization (MDA) using Mo/zeolite catalysts (Fig. 2.6). The authors compared this reaction to a standard fluidised bed reactor (FBR) with the integration of an electrochemical $BaZrO_3$-based membrane exhibiting both proton and oxide ion conductivity (ceramic membrane reactor – CMR). In the FBR, the aromatics yield

initially increased during the induction period, reaching a maximum of ~ 10 %, but rapidly fell as the reaction progressed. However, in the case of the electrochemical membrane reactor, the aromatics yield continued to increase beyond the induction period and attained a maximum of ~ 12 %, after which the catalyst activity started to decline (Fig. 2.6a). This enhancement was related to the catalyst stability. The high stability exhibited by the catalyst in the CMR arose from a decreased tendency to form coke, which became more evident for longer reaction times (Fig. 2.6b).

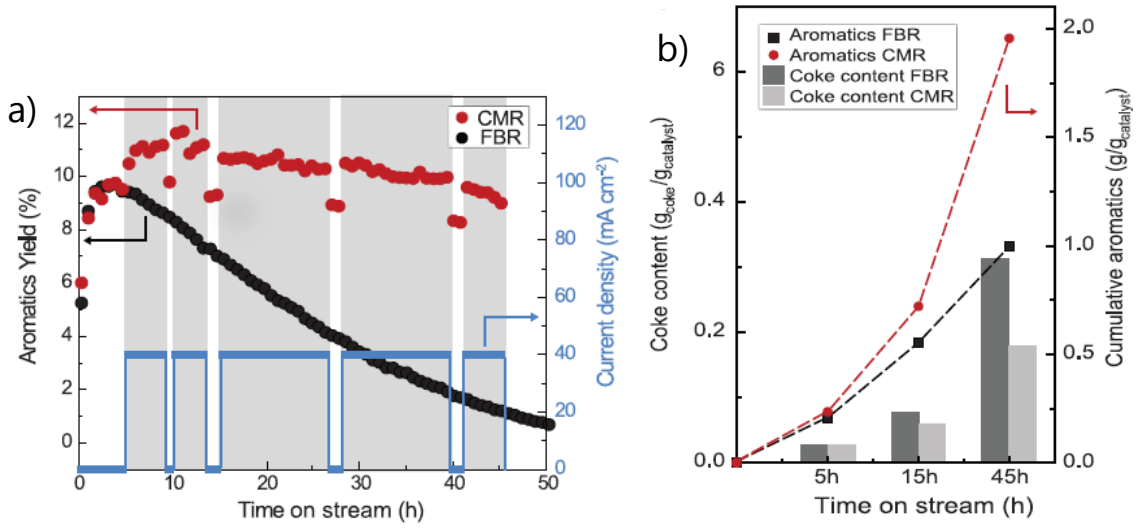

Fig. 2.6 – a) FBR and co-ionic CMR performance in MDA using a 6Mo/MCM-22 catalyst – aromatics yield versus time (gray-shaded areas indicate when hydrogen is extracted); b) coke deposition in 6Mo/MCM-22 and cumulative aromatics production in grams per gram of catalyst. Reaction conditions: 710 °C, 1500 mL g^{-1} $hour^{-1}$, 1 bar, and current density of 40 mA cm^{-2}. The tubular membrane consists of a dense $BaZr_{0.7}Ce_{0.2}Y_{0.1}O_{2.95}$ electrolyte film on a porous $BaZr_{0.7}Ce_{0.2}Y_{0.1}O_{2.95}$-Ni support, which also acted as a cathode. A Cu-based anode was applied on the electrolyte film facing the catalyst [26].

In another perspective, the growing concerns over the acceleration of global warming and climate changes due to the massive carbon dioxide emissions into the atmosphere arising from the production and consumption of fossil fuels have promoted interest in the production of synthetic hydrocarbon fuels. Xie *et al.* [27] reported the direct synthesis of methane from CO_2/H_2O in an oxygen-ion conducting solid state electrochemical cell $(La_{0.8}Sr_{0.2})_{0.95}MnO_{3-\delta}$-(anode)||YSZ-(electrolyte)||$La_{0.2}Sr_{0.8}TiO_{3.1}$-(cathode) by combining co-electrolysis of CO_2/H_2O and *in situ* Fischer-Tropsch-type synthesis (Fig. 2.7a) at 650 °C, where the current density reached ~ 85 mA cm^{-2} with an applied electrical voltage of 2 V (Fig. 2.7b). Methane was synthesised with a Faradaic yield of 2.8 % in the solid electrolyser,

while the main product was that of CO/H_2 with Faradaic yield of 74.2 %. The higher conversion of H_2O (25 %) than CO_2 (11.5 %), from a CO_2 excess mix, demonstrated that steam electrolysis is easier than CO_2 electrolysis in this device. In both processes, the conversion was limited by the performance of the catalyst used, emphasizing the need for catalyst development.

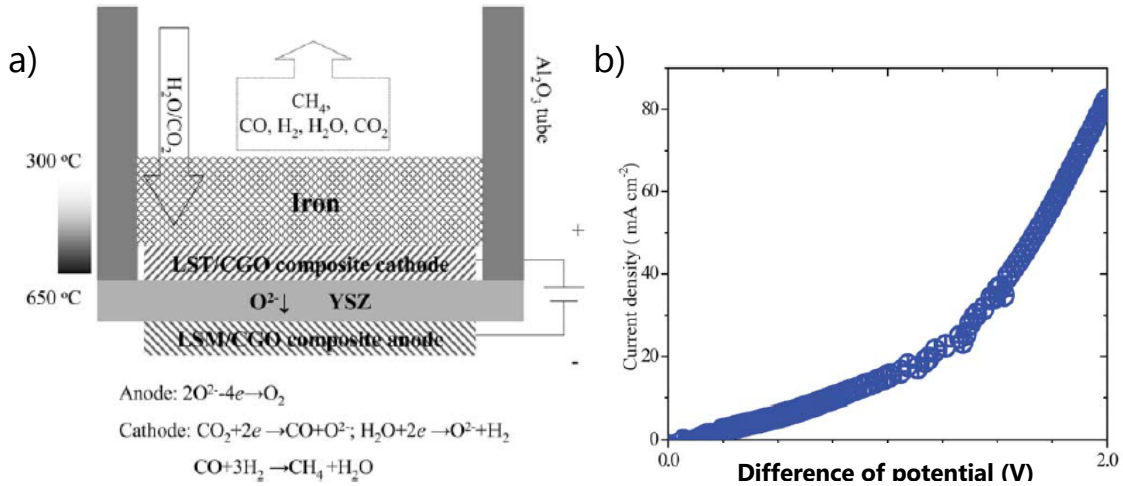

Fig. 2.7 – a) schematic of cell testing conditions and temperature region for porous iron catalyst; b) *j–V* of solid oxide electrolyser at 650 °C with anode exposed in static air and cathode in a mixture of CO_2/H_2O (2:1) [27].

This co-electrolysis of CO_2 and steam has generated special interest as it can provide a route to store the energy produced by intermittent sources of renewable energy (like wind and solar energy), while using stranded sources of CO_2 and waste heat (*e.g.*, from nuclear plants). Studies of this process using a proton conductor for an electrolyser are less frequent in the literature. As an example, Ruiz-Trejo & Irvine [28] used a protonic electrolyte based on $BaCe_{0.5}Zr_{0.3}Y_{0.16}Zn_{0.04}O_{2.88}$ with Pt electrodes (Fig. 2.8a). CO was successfully produced when CO_2 was fed on the cathode side. A higher CO conversion was reached with a high difference of potential (~ 9 V) across the cell. A Faradaic efficiency of ~ 9 % was estimated, with the losses being associated with the very high potential difference applied to drive significant current due to internal resistances. Cell performance was limited by elevated polarization resistances from the electrodes, due to the present lack of proper materials for proton conducting devices to operate at temperatures between 400 and 650 °C [28].

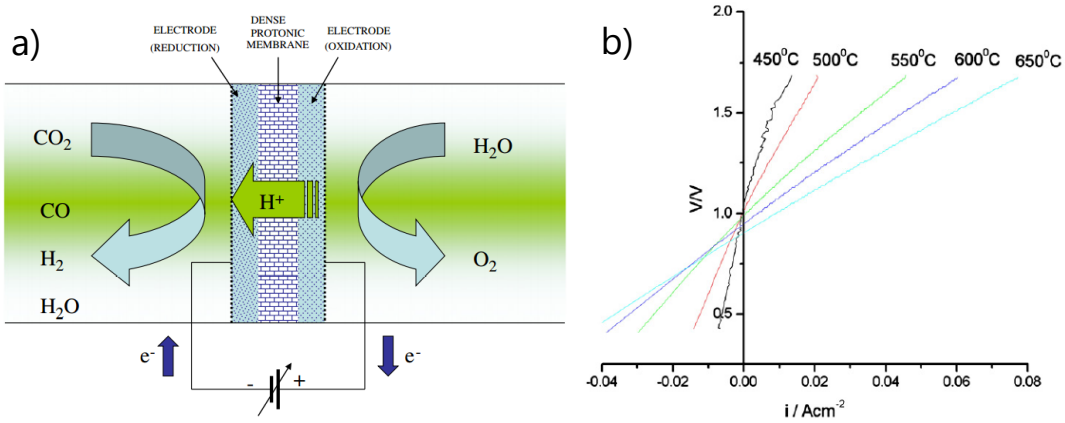

Fig. 2.8 – a) electrolysis cell with a proton conductor as the electrolyte; b) I-V curves of the Pt||$BaCe_{0.5}Zr_{0.3}Y_{0.16}Zn_{0.04}O_{2.88}$||Pt cell in fuel cell and electrolysis mode [28].

As a final example, ammonia is the second most produced chemical in the world, with high societal impact due to extensive application in agriculture and pharmacy. Nonetheless, its current production from natural gas accounts for approximately 5 % of global CH_4 consumption, with associated high levels of CO_2 emissions. In the work of Yun *et al.* [29], ammonia was electrochemically synthesized from N_2 and H_2O at 475 – 600 °C, using a $BaZr_{0.8}Y_{0.2}O_{3-\delta}$, proton conductor electrolyte (Fig. 2.9). Silver (Ag), platinum (Pt), and lanthanum strontium cobalt ferrite ($La_{0.6}Sr_{0.4}Co_{0.2}Fe_{0.8}O_{3-\delta}$ (LSCF6428)) were used as electrode electrocatalysts. Maximum ammonia formation rates of 4.9×10^{-11} mol cm^{-2} s^{-1} and 8.5×10^{-11} mol cm^{-2} s^{-1} were observed for the Ag and LSCF6428 electrocatalysts, respectively, under 0.8 V. However, the use of Pt electrocatalyst showed a negligible ammonia formation rate lower than 1×10^{-12} mol cm^{-2} s^{-1}, which was related to the high activity of Pt for the hydrogen evolution reaction rather than the ammonia formation reaction.

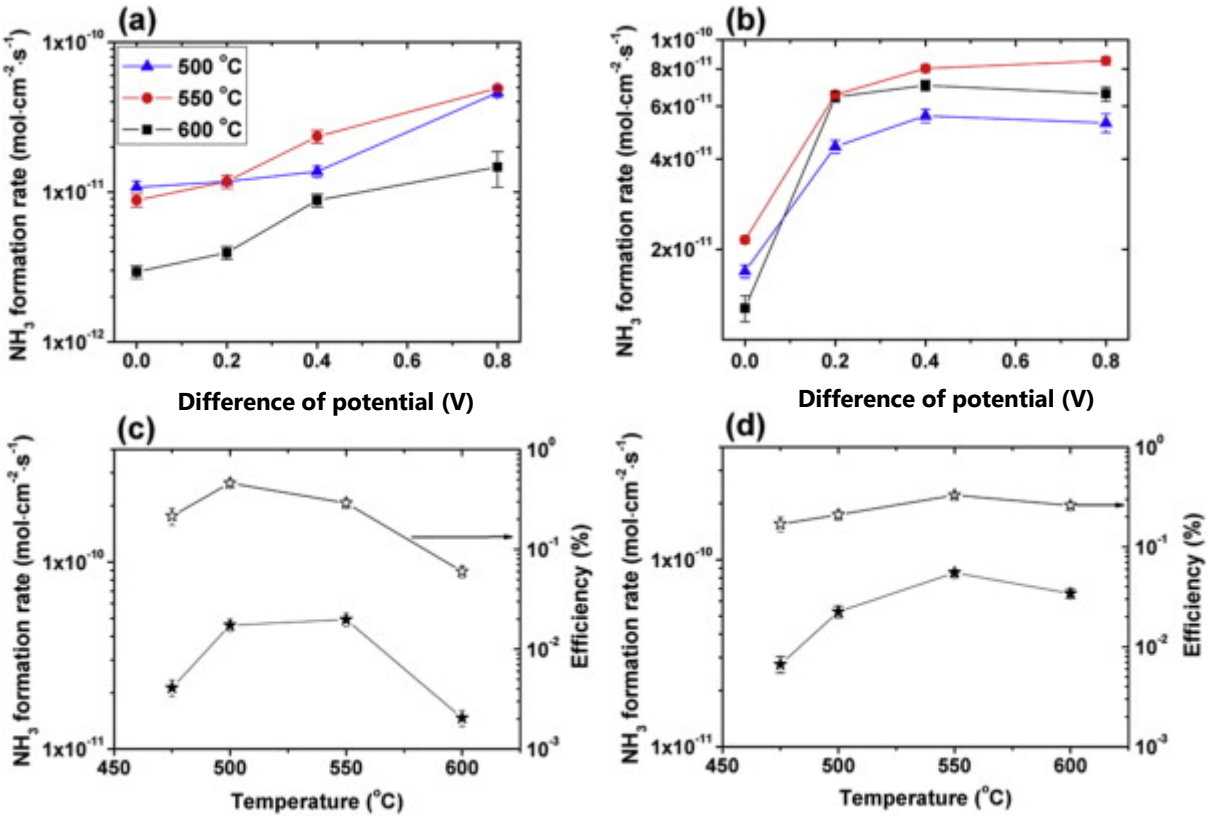

Fig. 2.9 – NH_3 formation rate as a function of temperature and applied voltage (a) Ag, (b) LSCF6428 and the maximum NH_3 formation rate and Faradaic efficiency with different temperatures at an applied difference of potential of 0.8 V (c) Ag, (d) LSCF. Measurements were made on single cells based on $BaZr_{0.8}Y_{0.2}O_{3-\delta}$ in a temperature range of 475 – 600 °C, at atmospheric pressure. Silver (Ag), platinum (Pt) or LSCF6428 were used for both anode and cathode electrocatalysts [29].

2.3. Ceramic proton-conducting electrolyte materials

The most widely studied protonic ceramics belong to the perovskite family of ABO_3 ceramic oxide structure (Fig. 2.10a). Typical proton conducting perovskites consist of a divalent alkaline earth element, such as Ba^{2+}, Sr^{2+} and Ca^{2+}, in the A-cation site, while a tetravalent rare-earth element, usually Ce^{4+} or Zr^{4+}, is present in the B-cation site. The stability and level of distortion of a perovskite lattice can be estimated by the *Goldschmidt* tolerance factor (*t*):

$$t = \frac{(R_A + R_O)}{\sqrt{2}(R_B + R_O)} \quad (2.6)$$

where R_A and R_B correspond to the ionic radius of the cations occupying the A and B site respectively, while R_O is the oxygen ionic radius. Stable perovskite structures can be obtained when *t* ranges between 0.75 – 1.0. Cubic symmetry has been observed for values in the range 0.95 – 1.04, while compounds having a tolerance factor in the range 0.75 – 0.90 typically have orthorhombic symmetry [30,31]. For this reason, the choice of dopants, namely their respective charges and sizes must be carefully considered as these factors can have a strong impact on perovskite stability and crystallographic structure [30,31].

The perovskite lattice can display nonstoichiometry with respect to all three sites (A, B and O), either individually (one site at a time) or in various combinations. B-site nonstoichiometry is, nonetheless, energetically unfavourable because of the important structural role of the B-site cations which form strong bonds with oxygen in a network consisting of BO_6 corner-sharing octahedra. Therefore, the vast majority of perovskite systems exhibit a fully occupied B-site, with few examples of B-site nonstoichiometric perovskites being known.

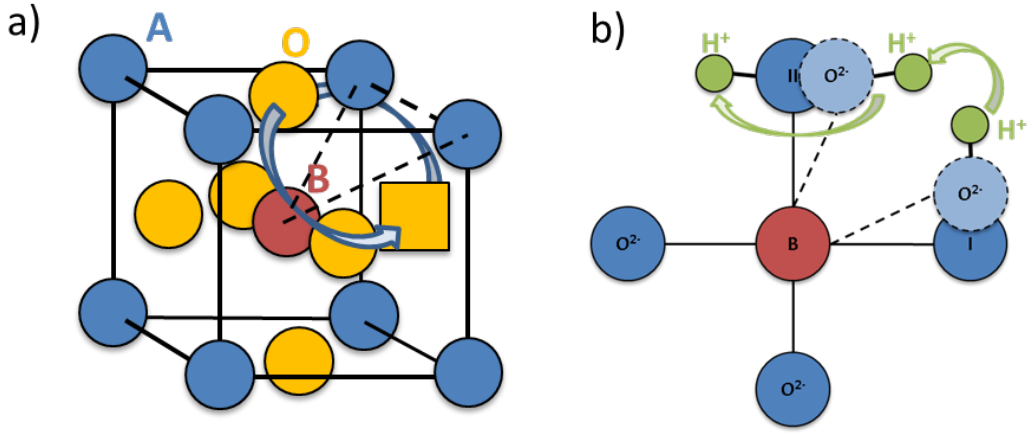

Fig. 2.10 – Schematic view of the types of conduction: a) oxygen ion vacancies in one ABO_3 perovskite involved in the ionic motion of one oxide ion (yellow); and b) a possible proton transfer mechanism from one oxygen ion to another in the same perovskite structure.

On the other hand, ionic conductivity is promoted when the B-site is partially substituted with suitable acceptor elements, such as Y^{3+}, In^{+3} or Gd^{3+} trivalent cations, leading to the formation of charge compensating oxygen vacancies ($V_O^{\bullet\bullet}$), according to *Kröger-Vink* notation:

$$(1-y)(Ce,Zr)O_2 + \left(\frac{y}{2}\right)M_2O_3 \Longrightarrow$$

$$\Longrightarrow (1-y)Ce,Zr_{Ce,Zr}^{x} + (y)\,M'_{Ce,Zr} + \left(2-\frac{y}{2}\right)O_O^x + \left(\frac{y}{2}\right)V_O^{\bullet\bullet} \qquad (2.7)$$

Proton conductivity can occur in such solid oxides due to the presence of oxide vacancies that are filled by the water vapour as protonic defects ($OH_O^{\bullet}$, Fig. 2.10b) as follows:

$$H_2O + V_O^{\bullet\bullet} + O_O^x \Leftrightarrow 2OH_O^{\bullet} \qquad (2.8)$$

Protonic conductors are complex in the fact that they are capable of offering mixed ionic conductivity (protonic and oxide-ion), as well as minor electronic conductivity, depending on the temperature and on the nature of the surrounding atmosphere. The origin of protonic conductivity is due to a high equilibrium constant for water absorption that allows these materials to offer high bulk protonic conductivity at intermediate temperatures in the presence of sufficiently humidified gases (typically, p_{H2O} = ~ 10^{-2} atm) [32–34].

In terms of total conductivity, the doped barium cerate, *e.g.* $BaCe_{1-x}M_xO_{3-\delta}$ (M = Y^{3+}, In^{3+}, Gd^{3+} etc.) shows the highest proton conductivity at intermediate temperatures [31,35–46]. Nonetheless, it has the tendency of reacting with acidic gases, *viz.* CO_2 and water vapour, which leads to the formation of insulating carbonate or hydroxide phases, respectively, on the surface of the material. This complication impedes the ability of this material to be used in highly humidified and carbon-based fuels, thus limiting its potential application range [31,35,39,47–51]. The typical degradation reactions in such atmospheres include:

$$BaCeO_{3(s)} + H_2O_{(g)} \rightarrow Ba(OH)_{2(s)} + CeO_{2(s)} \quad (2.9)$$

$$BaCeO_{3(s)} + CO_{2(g)} \rightarrow BaCO_{3(s)} + CeO_{2(s)} \quad (2.10)$$

$$BaCeO_{3(s)} + H_2S_{(g)} \rightarrow BaS_{(s)} + CeO_{2(s)} + H_2O_{(g)} \quad (2.11)$$

The chemical stability of doped barium cerates is well documented in the literature and huge efforts have been made to explore the reasons behind its chemical instability, using both conventional and non-conventional techniques [52–56]. For instance, Matsumoto *et al.* [53] studied the effect of dopant M in $BaCe_{0.9}M_{0.1}O_{3-\delta}$ (M = Y, Tm, Yb, Lu, In, or Sc) on the electrical conductivity in the temperature range of 400 – 900 °C and on the chemical stability with respect to CO_2 by thermogravimetry (TG). All compounds were found to interact with pure CO_2 at temperatures below 900 °C. Moreover, both the electrical conductivity (moistened H_2 or O_2, p_{H2O} = 1.9 x 10^{-2} atm) and the stability against carbonate formation, were suggested to be inversely affected by the electronegativity of the dopant element (Fig. 2.11), *i.e.* both the instability of the material and the conductivity increase with increasing ionic radius and increasing electronegativity (increasing basicity).

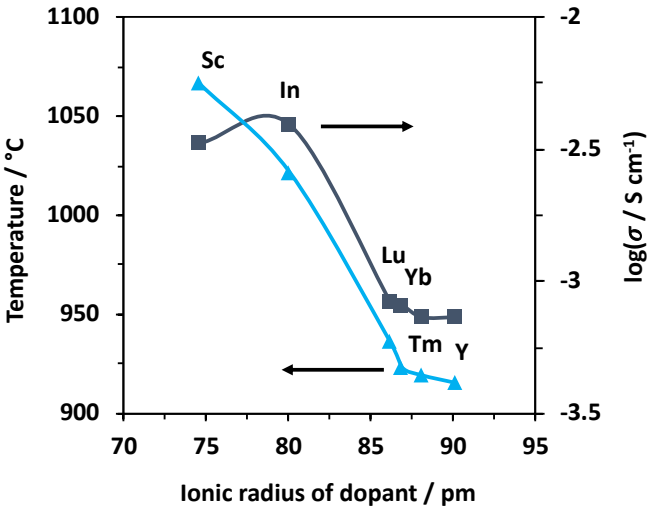

Fig. 2.11 – Carbonate formation temperature (blue) and the conductivity isotherm at 400 °C of $BaCe_{0.9}M_{0.1}O_{3-\delta}$ (M = Y, Tm, Yb, Lu, In or Sc) in moist H_2 as a function of the ionic radius of the dopant [53].

More recently, the work of Kim *et al.* [57], reported the presence of a nanometre-thick amorphous phase at the grain boundaries in proton-conducting $BaCeO_3$ polycrystals, that not only leads to a reduced proton mobility but also acts as a penetration path for H_2O and CO_2 gas molecules, facilitating chemical decomposition and collapsing of the microstructure (Fig. 2.12a). This effect could be minimized by controlling the composition to obtain Ba-deficient samples in which the intergranular amorphous layer could be reduced, leading to a mitigation of the reactivity with such molecules (Fig. 2.12b). Such presence of an amorphous layer on the interfaces between grains has also been documented in barium zirconate-based compositions [58,59].

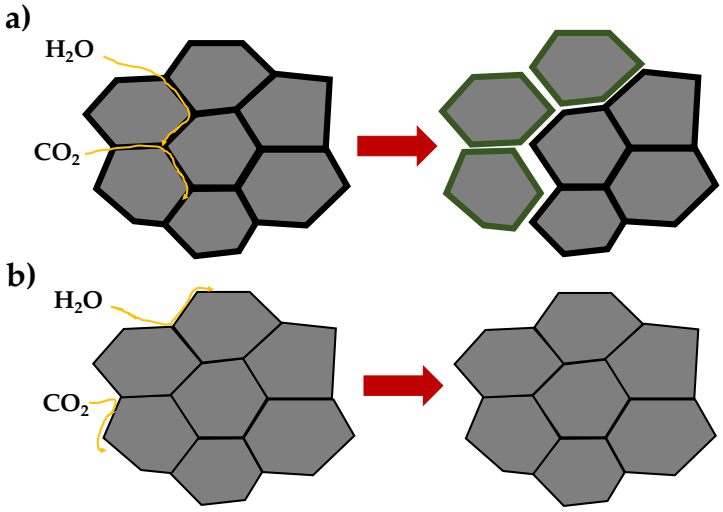

Fig. 2.12 – Schematic representation of microstructural changes upon reaction with water and carbon dioxide: a) Ba-stoichiometric compositions (thick amorphous intergranular phase); b) Ba-deficient compositions (thin amorphous intergranular phase).

Some further efforts to improve the stability of the barium cerate material, include the work of Handal *et al.* [60] who attempted the partial replacement of ceria with transition metals in samarium doped barium cerate, $BaCe_{0.9}Sm_{0.1}O_{3-\delta}$ (BCS10). Concentrations of 5 – 10 mol% of each of Fe and Co were introduced into the Ce-site of BCS. Thermogravimetric (TG) analysis showed high water uptake (~ 0.5 %) in the case of $BaCe_{0.85}Sm_{0.1}Co_{0.05}O_{3-\delta}$ (BCSC5), while $BaCe_{0.85}Sm_{0.1}Fe_{0.05}O_{3-\delta}$ (BCSF5) did not show a noteworthy uptake of water (Fig. 2.13a). TG also proved that the incorporation of Fe and Co in BCS had no positive effect on improving the chemical stability in CO_2 at elevated temperatures (Fig. 2.13b). Measurements were performed in air, 3 % H_2O/Ar, 5 % H_2/N_2, and 50 % CO_2/N_2 from room temperature until 1000 °C (heating/cooling).

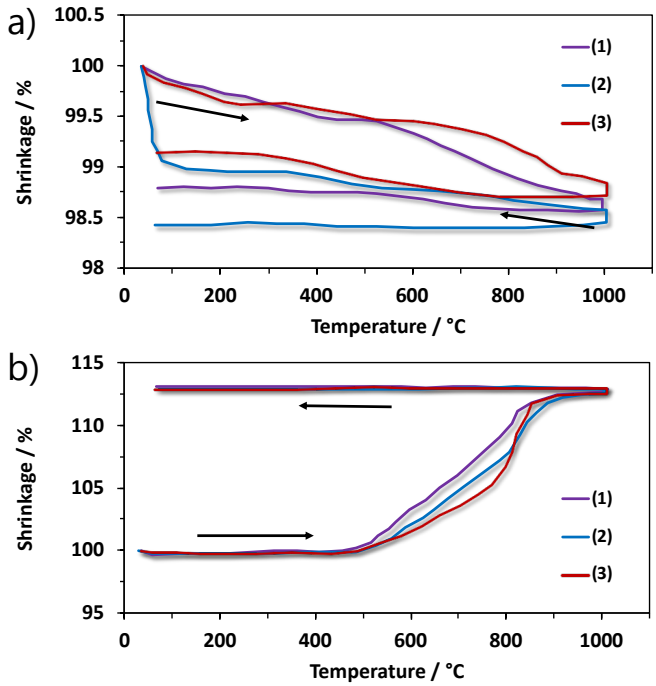

Fig. 2.13 – Thermogravimetric analysis (TG) of (1) $BaCe_{0.9}Sm_{0.1}O_{3-\delta}$ (BCS), (2) $BaCe_{0.85}Sm_{0.1}Fe_{0.05}O_{3-\delta}$ (BCSF5), and (3) $BaCe_{0.85}Sm_{0.1}Co_{0.05}O_{3-\delta}$ (BCSC5) samples sintered at 1200 °C for 8 h and measured under: a) 3 % H_2O/Ar and b) 50 % CO_2/N_2 at 10 °C min^{-1} [60].

In stark contrast to the cerate-based materials, the doped barium zirconate, $BaZr_{1-x}M_xO_{3-\delta}$ (M = Y^{3+}, In^{3+}, Gd^{3+}, etc.) material, not only offers much higher chemical stability under CO_2 and H_2O containing atmospheres but also shows superior bulk protonic conductivity [32,58,61–74]. Nonetheless, the doped barium zirconate material is very refractive by nature, with poor sinterability and grain growth and possesses very resistive grain boundaries. For these reasons, the material requires very high sintering temperatures (1600 – 1700 °C) and long annealing times (> 24 h), to achieve dense membranes with sufficient grain growth to minimise total grain boundary resistance [32,58,61–74]. Unfortunately, when high sintering temperatures are used, the real stoichiometry of the composition can be changed due to partial vaporisation of barium from the perovskite lattice, followed by potential segregation of Y_2O_3, both of which can reduce the proton conductivity [31,75–77].

All the above issues suggest that it is very difficult to process BZY as a dense electrolyte membrane. This is unfortunate, as a dense thin membrane is essential in fuel cells to prevent crossover of reactants across the membrane and the achievement of high open circuit potential (~ 1.1 V). Thus, to try and profit from the distinct advantages of the

zirconate and cerate systems, intermediate compositional ranges have been proposed to find a compromise between chemical stability, facile sintering and high electrical conductivity. This is the case of the well-known yttrium-doped barium cerate zirconate, $Ba(Ce,Zr)_{1-y}Y_yO_{3-\delta}$ (BCZY) solid-solutions [75,78–90]. In this family of solid solutions, the lattice symmetry increases with increasing Zr-content from orthorhombic to cubic and improvements in the stability of the system against carbonate formation are also noted. In contrast, when the Ce content is higher than that of Zr, grain growth and sinterability is improved [78,80–83,91].

Table 2.1 summarises the lattice parameters and the unit cell volume for the sintered pellets estimated from the XRD patterns formed by an acetate combustion process [78]. The lattice parameters of all the oxide compositions are in line with published data for other synthesis routes, highlighting the effectiveness of this method [80,81,83,91].

Table 2.1 – Lattice parameter and unit cell volume of $BaCe_{0.8-x}Zr_xY_{0.2}O_{3-\delta}$ materials synthesized by nitrate free acetate–H_2O_2 combustion method [78].

Nomenclature	***x*** **(Zr)**	**Lattice parameters (Å)**			**Space group**	**Unit cell volume ($Å^3$)**
		a	***b***	***c***		
BCY	0	8.921	6.182	6.184	*Pnma*	341.03
BCZY71	0.1	8.859	6.16	6.162	*Pnma*	336.3
BCZY44	0.4	4.32	4.32	4.32	*Pm-3m*	80.61
BCZY26	0.6	4.268	4.268	4.268	*Pm-3m*	77.74
BZY	0.8	4.222	4.222	4.222	*Pm-3m*	75.29

As an example of the BCZY system without the use of any sintering additive, Fig. 2.14 shows the pristine surface of BCZY ceramics prepared by acetate combustion and densified at 1500 °C. The micrographs show the low cerium-content, BCZY26, material to have poor densification. Nonetheless, the more cerium rich BCZY80, BCZY71 and BCZY44 pellets are shown to be fully dense. The corresponding relative densities and average grain sizes are shown in Table 2.2. The average grain size decreases substantially with introduction of Zr in the BCY lattice [82,83,92].

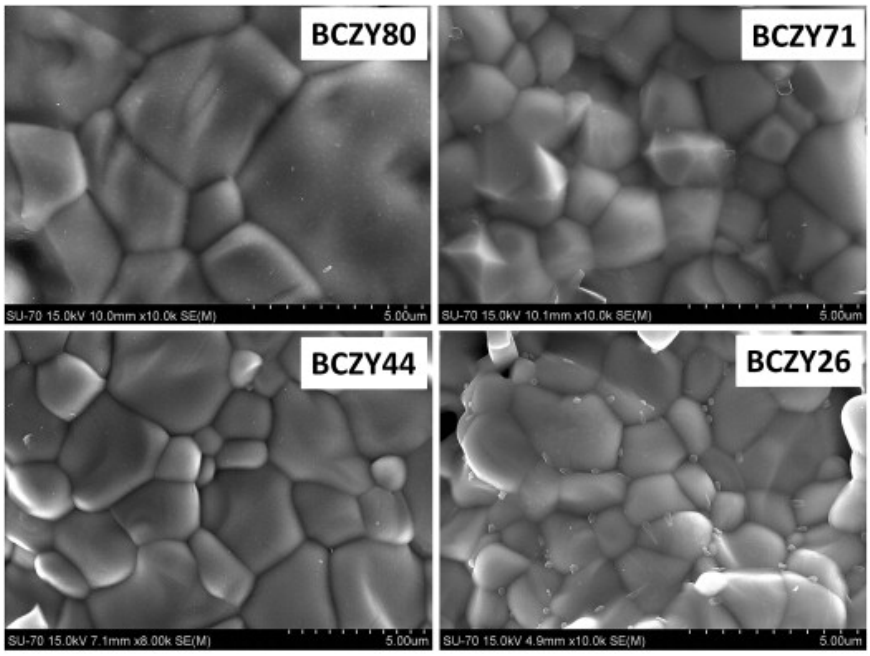

Fig. 2.14 – Scanning electron micrographs of surface of BCZY pellets sintered at 1500 °C for 8 h [78].

Table 2.2 – Grain size and relative density of $BaCe_{0.8-x}Zr_xY_{0.2}O_{3-\delta}$ materials synthesised by nitrate free acetate–H_2O_2 combustion method, isostatically pressed at 200 MPa and sintered at 1500 °C for 8 h [78].

***x* (Zr)**	**Relative density (%)**	**Grain size (μm)**
0	98.5	4.73 ± 1.65
0.1	98	1.94 ± 0.63
0.4	96	2.61 ± 0.82
0.6	92	1.75 ± 0.51
0.8	82	0.97 ± 0.18

Nasani *et al.* [78] studied the electrical properties (total, bulk and grain boundary) conductivities for BCZY71, BCZY44 and BCZY26 materials, Fig. 2.15 and Fig. 2.16.

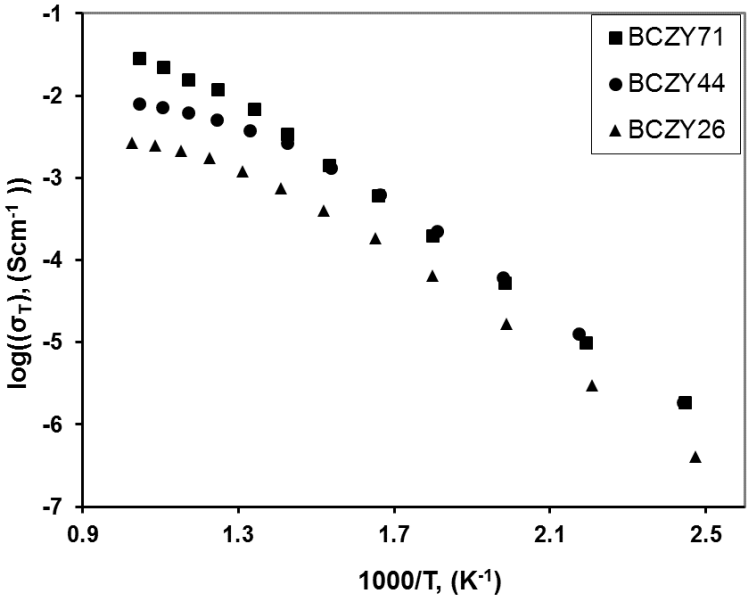

Fig. 2.15 – The temperature dependence of the total conductivity for $BaCe_{0.8-x}Zr_xY_{0.2}O_{3-\delta}$ (x = 0.1, 0.4 and 0.6) materials under a wet N_2 atmosphere, p_{H2O} = 0.026 atm [78].

All studied ceramics showed relative densities ≥ 92 % that of the theoretical after sintering the acetate combustion powders at 1500 °C for 5 hours [78]. Figure 2.15 shows that the total conductivity is notably higher for the BCZY71 and BCZY44 compositions with minor contents of Zr. The bulk behaviour is shown in Fig. 2.16a and shows a decrease with increasing Zr-content (more apparent with increasing temperature), in agreement with further literature data [82,93,94].

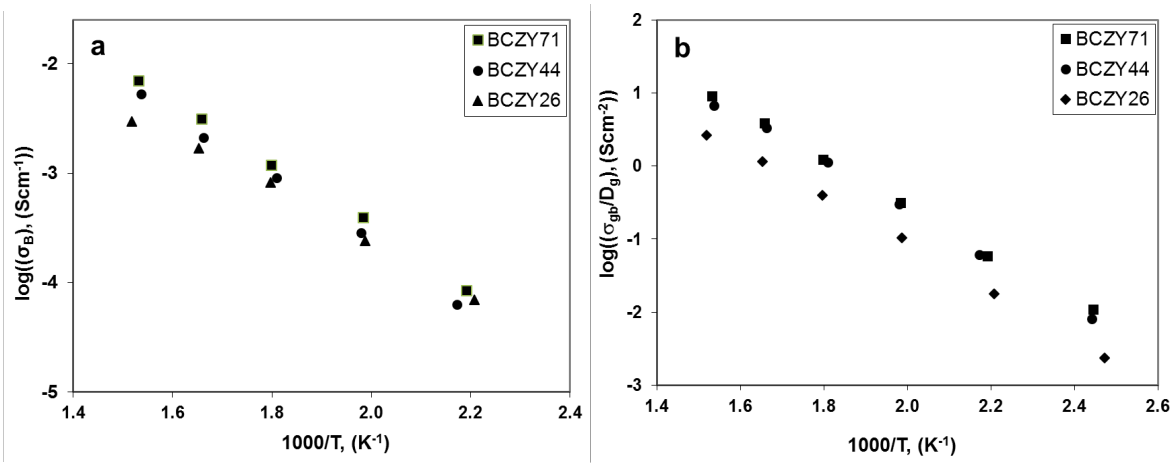

Fig. 2.16 – The temperature dependence of a) the bulk and b) the grain boundary conductivity for $BaCe_{0.8-x}Zr_xY_{0.2}O_{3-\delta}$ (x = 0.1, 0.4 and 0.6) materials under a wet N_2 atmosphere, p_{H2O} = 0.026 atm [78].

Concerning the grain boundary response, comparison of the intrinsic grain-boundary properties, can be made by assuming that the proportionality factor of the grain-boundary thickness (δ) remains constant in the brick-layer model [78]. By such assumption, the grain boundary conductivity can be normalized for microstructural variations by plotting $\sigma_{g.b}$* = $\sigma_{g.b.}/D$, (Fig. 2.16b), where D represents the mean grain size measured by SEM analysis [78].

Based on these results it was possible to state that the Ce-rich compositions, namely BCZY71 and BCZY44, have similar inherent grain boundary behaviour, while $\sigma_{g.b}$* is significantly lower for the Zr-rich composition BCZY26. Minor decreases in grain boundary conductivity with increasing Zr-content for cerium rich compositions have also been reported in the works of Yamazaki *et al.* [93] and Ricote *et al.* [92,94]. One can, thus, conclude that the significantly depleted total conductivity noted for the Zr-rich composition in Fig. 2.15 results from a combination of poor grain growth (Table 2.2), low intrinsic grain boundary conductivity and impaired bulk conductivity; factors that can be substantially improved by raising the Ce-content.

Notwithstanding the several advantages and disadvantages of each specific composition, $BaCe_{0.9}Y_{0.1}O_{3-\delta}$ (BCY10) is the electrolyte material adopted by Bondalti in the electrochemical cell for the direct amination reaction as this material offers the highest conductivity of the aforementioned perovskite phases at the lowest temperatures; temperatures that correspond to those of interest for the amination reaction. Hence, the focus given in this thesis will concentrate on this specific composition.

2.3.1. Electrical conductivity in oxides

The electrical conductivity in oxide materials depends on the concentration of the charge carriers, their charge and their mobility. The contribution of each species to the overall electrical conduction process is determined by combination of the defect concentration and the defect mobility, according to the following expression:

$$\sigma_{\mathrm{i}} = q_{\mathrm{i}}.\mu_{\mathrm{i}}.C_{\mathrm{i}} \qquad (2.12)$$

where q_i, C_i and μ_i represent the charge, the concentration and the mobility of the species i.

For solids with more than one charge carrier, the total conductivity corresponds to the sum of the partial contributions. These can be ionic or electronic in nature. In terms of ionic defects, both oxide-ion and protonic conductivities are typically found in these materials. For this reason, Fig. 2.17 shows the total conductivity as a function of temperature of several materials, for both oxygen-ion and protonic conductors. As can be seen in the figure, the oxygen-ion conductors typically show higher activation energies for conduction and demonstrate the higher conductivities at elevated temperatures, while, in contrast, the proton conductors classically show lower activation energies for conduction and maintain higher conductivities at lower temperatures.

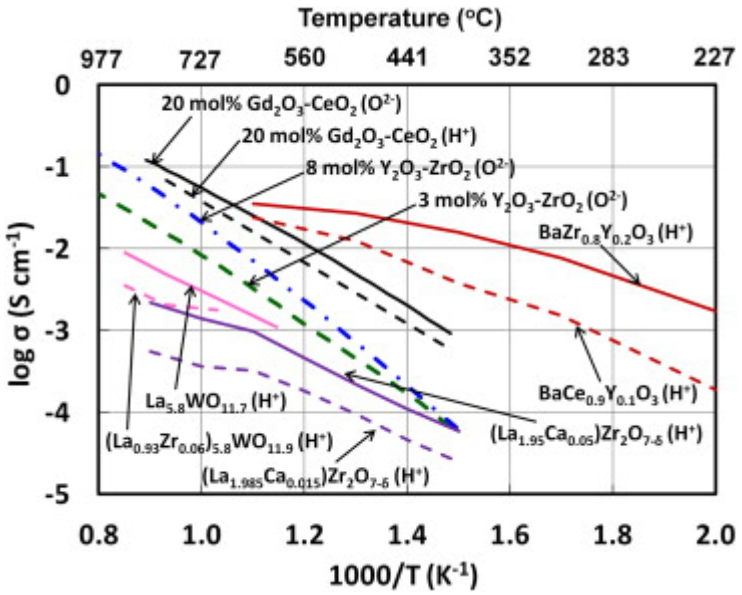

Fig. 2.17 – Proton (H^+) and oxygen ion (O^{2-}) conductivity of various ceramic electrolytes [95].

2.3.1.1. Oxygen defects

Generally, oxygen ionic conduction can occur in the perovskite structure when some of the oxygen sites are vacant (*i.e.*, when oxygen vacancies are present). As referred previously, the perovskite structure allows for oxygen deficient stoichiometry. In the case of BCY10 ceramics, the material consists of a ceramic oxide with ABO_3 perovskite structure that

contains large A^{2+} site cations, Ba^{2+}, and smaller B^{4+} site cations, Ce^{4+}, with partial substitution of the B-site by lower-oxidation-state cations, Y^{3+}, that are charge compensated by the formation of oxygen vacancies ($V_O^{\bullet\bullet}$), in *Kröger-Vink* notation [32]:

$$Ce_{Ce}^{x} + \frac{1}{2}O_O^x + \frac{1}{2}Y_2O_3 \Longrightarrow Y'_{Ce} + \frac{1}{2}V_O^{\bullet\bullet} + CeO_2 \quad (2.13)$$

The oxygen ionic transport mechanism is related to the movement of these oxygen vacancy defects in the crystallite. This movement is based on a diffusion process, thermally activated, which depends exponentially on the temperature (*Arrhenius* law):

$$\sigma = \frac{\sigma_0}{T} exp\left(\frac{-E_a}{RT}\right) \quad (2.14)$$

2.3.1.2. Protonic defects

In contrast, proton conductivity is due to hydration of the crystallographic structure by the presence of water vapour in the gas-atmosphere. The level of chemical diffusivity of protons in these materials can be related with the rate of proton hopping and the concentration of protonic charge carriers (thermodynamics of hydration). Water uptake in doped barium cerates and zirconates occurs as a result of filling oxygen vacancies generated from doping by the formation of hydroxyl groups, $OH_O^{\bullet}$:

$$H_2O + V_O^{\bullet\bullet} + O_O^x = 2OH_O^{\bullet} \quad (2.15)$$

with an equilibrium constant, K_w:

$$K_w = \frac{[OH_O^{\bullet}]^2}{[V_O^{\bullet\bullet}][O_O^x]p_{H2O}} \quad (2.16)$$

which in turn can further be expressed in terms of entropy, ΔS_w, and enthalpy, ΔH_w, of the water incorporation reaction:

$$K_w = \exp\left(\frac{\Delta S_w}{R}\right)\exp\left(-\frac{\Delta H_w}{RT}\right) \quad (2.17)$$

where T and R have usual meanings. Given eqn (2.13) and knowing that number of oxygen sites per formula unit of barium cerate is restricted to 3, implying the site restriction relationship:

$$2[V_O^{\bullet\bullet}] + [OH_O^{\bullet}] + [O_O^{x}] = 3 \quad (2.18)$$

With these relationships (eqn (2.16) – (2.18)), K_w can be reformulated as

$$K_w = \frac{4[OH_O^{\bullet}]^2}{p_{H2O}.(S-[OH_O^{\bullet}])(6-S-[OH_O^{\bullet}])} \quad (2.19)$$

and then the concentration of protonic defects is given by

$$[OH_O^{\bullet}] = \frac{3.K' - \sqrt{9K' - 6K'.S + K'.S^2 + 24S - 4S^2}}{K' - 4} \quad (2.20)$$

where $K' = K_w.p_{H2O}$ and $S = [M_B']$. Because the formation of protonic defects is accompanied by a significant weight increase, the concentration of protonic defects as a function of temperature and water partial pressure is generally measured by thermal gravimetric analysis (TG). Fig. 2.18 depicts the equilibrium constants for water absorption obtained for several proton-conducting ceramics.

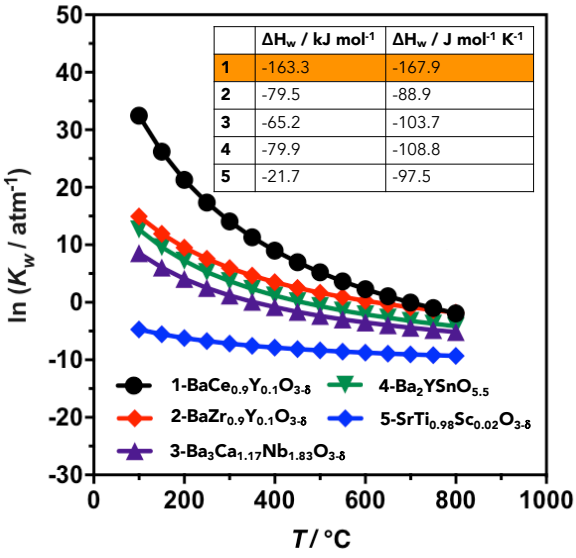

Fig. 2.18 – Equilibrium constant for water absorption in proton-conducting ceramics [96].

Table 2.3 compares the hydration enthalpies for barium doped cerates and zirconates. In these systems, the nature of the acceptor dopant and their concentration can be seen to greatly influence the extent of hydration. In general, the hydration entropy and enthalpy become more negative with increasing acceptor dopant content. Moreover, a much more negative hydration entropy and enthalpy are noted for the cerium-based perovskites in composition to that of the zirconates (Table 2.3).

Table 2.3 – Comparison of the hydration enthalpy and entropy values for different compositions.

Composition	ΔH_W / kJ mol^{-1}	ΔS_W / J mol^{-1} K^{-1}	Reference
$BaZr_{0.9}Y_{0.1}O_{3-\delta}$	-83.3	-91.2	[97]
$BaZr_{0.9}Y_{0.1}O_{3-\delta}$	-79.5	-88.9	[98]
$BaZr_{0.85}Y_{0.15}O_{3-\delta}$	-83.4	-92.1	[98]
$BaZr_{0.8}Y_{0.2}O_{3-\delta}$	-93.3	-103.2	[98]
$BaZr_{0.85}Yb_{0.15}O_{3-\delta}$	-62 ± 3	-56 ± 3	[99]
$BaCe_{0.6}Zr_{0.3}Y_{0.1}O_{3-\delta}$	-106	-104	[97]
$BaCe_{0.2}Zr_{0.7}Y_{0.1}O_{3-\delta}$	-93	-96	[97]
$BaCe_{0.9}Y_{0.1}O_{3-\delta}$	−138.0 ± 6.9	−142.2 ± 6.1	[100]
$BaCe_{0.9}Y_{0.1}O_{3-\delta}$	-122	-119	[101]
$BaCe_{0.9}Y_{0.1}O_{3-\delta}$	-163.3	-167.9	[32]
$BaCe_{0.9}Y_{0.1}O_{3-\delta}$	-123	-113	[97]
$BaCe_{0.9}Yb_{0.1}O_{3-\delta}$	-127	-126	[101]

2.3.1.3. Electronic defects

In ceria-based compositions, under very low oxygen partial pressures, typically changes in the oxygen non-stoichiometry ($\Delta\delta$) can occur at high temperatures, that can be related with the reduction of Ce^{4+} to Ce^{3+} in reducing conditions (Fig. 2.19) according to:

$$2Ce_{Ce}^{x} + O_{O}^{x} \Leftrightarrow V_{O}^{\bullet\bullet} + 2Ce_{Ce}' + \frac{1}{2}O_2 \quad (2.21)$$

with an equilibrium constant for reduction reaction described by:

$$K_R \approx \frac{[V_O^{\bullet\bullet}][Ce_{Ce}']^2 p_{O2}^{1/2}}{[O_O^x][Ce_{Ce}^x]^2} \quad (2.22)$$

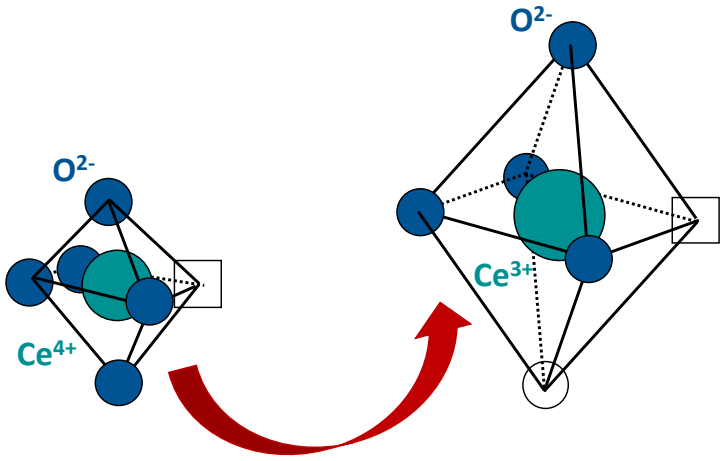

Fig. 2.19 – Schematic representation of the origin of electronic conductivity.

Fig. 2.20 depicts an example for stoichiometry loss of $Ce_{1-x}Gd_xO_{2-0.5x-\Delta\delta}$ obtained at 800 and at 1000 °C. We can observe that there are important stoichiometry changes with decreasing values of oxygen partial pressure, albeit being suppressed at lower temperatures, due to the decrease of equilibrium constant (eqn (2.22)). Unfortunately, no reports can be found in literature regarding the BCY10 composition, which makes it imperative in this thesis to determine the extent of oxygen stoichiometry changes in this composition as this phenomenon may have significant influence on the oxygen storage ability with impact on catalytic or electrocatalytic processes.

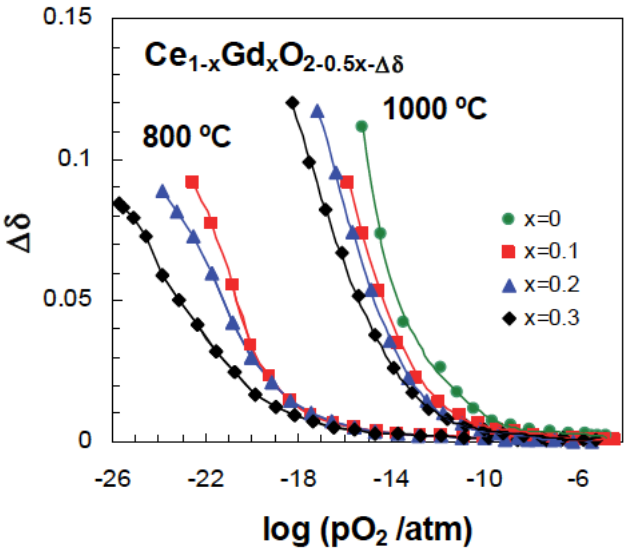

Fig. 2.20 – Typical example for Stoichiometry loss of $Ce_{1-x}Gd_xO_{2-0.5x-\Delta\delta}$ (x=0, 0.1, 0.2, 0.3) at 800 ºC and 1000 ºC as a function of the oxygen partial pressure [102].

Therefore, the subsequent existence of mixed valence ascribed to cerium reduction would be expected to introduce small-polaron electronic conduction (*i.e.* a localised, mobile electron, $\mathrm{Ce}'_{\mathrm{Ce}}$), in addition to the oxide-ion and protonic conduction. To estimate the equilibrium constant for cerium reduction, eqn (2.22) can be combined with the electroneutrality condition:

$$2[\mathrm{V}_{\mathrm{O}}^{\bullet\bullet}] + [\mathrm{OH}_{\mathrm{O}}^{\bullet}] \approx [\mathrm{Y}'_{\mathrm{Ce}}] + [\mathrm{Ce}'_{\mathrm{Ce}}] \tag{2.23}$$

and other mass and lattice position restrictions, on neglecting defect interactions and thus assuming nearly ideal behaviour, with the following relations between the concentrations of relevant species, stoichiometric changes ($\Delta\delta$), and fraction of trivalent additive (x):

$$[\mathrm{Ce}'_{\mathrm{Ce}}] = \frac{Z}{v_0}(2\Delta\delta) \tag{2.24}$$

$$[\mathrm{V}_{\mathrm{O}}^{\bullet\bullet}] = \frac{Z}{v_0}\left(\Delta\delta + \frac{x}{2}\right) \tag{2.25}$$

$$[\mathrm{Ce}_{\mathrm{Ce}}^{\mathrm{x}}] = \frac{Z}{v_0}(1 - x - 2\Delta\delta) \tag{2.26}$$

$$[\mathrm{O}_{\mathrm{O}}^{\mathrm{x}}] = \frac{Z}{v_0}\left(3 - \frac{x}{2} - \Delta\delta\right) \tag{2.27}$$

where Z is the number of atoms per unit cell and v_0, the unit cell volume. Substitution in eqn (2.22) one can obtain the values of equilibrium constant for reduction (K_{R}) from the entire range of values of $\Delta\delta$ versus p_{O2} at a given temperature T:

$$K_{\mathrm{R}}(T) = \frac{4\Delta\delta^2\left(\Delta\delta+\frac{x}{2}\right)p_{\mathrm{O2}}^{1/2}}{\left(3-\frac{x}{2}-\Delta\delta\right)(1-x-2\Delta\delta)^2} \tag{2.28}$$

Eqn (2.28) has been deduced without any assumption concerning the dependence of oxygen stoichiometry on the oxygen partial pressure and allows one to obtain the mass action constant as function of oxygen loss. On the other hand, the mass action constant relates to corresponding thermodynamic changes as:

$$\ln K_{\mathrm{R}} = \frac{\Delta S_{\mathrm{R}}}{\mathrm{R}} - \frac{\Delta H_{\mathrm{R}}}{\mathrm{R}T} \tag{2.29}$$

which allows the determination of the entropy (ΔS_{R}) and the enthalpy change (ΔH_{R}) of reduction [102]. As an example, Table 2.4 depicts literature value obtained for common ceria-

based oxygen ionic conducting compositions, highlighting typical values for the enthalpy changes where significant reduction occurs.

Table 2.4 – Enthalpy (ΔH_R) of reduction for different ceria-based based solid solutions materials.

Compound	ΔH_R / kJ mol^{-1}	Reference
$Ce_{0.9}Gd_{0.1}O_{2-x/2-\Delta\delta}$	410-420	[103]
	438	[104]
$Ce_{0.8}Gd_{0.2}O_{2-x/2-\Delta\delta}$	430	[103]
	385	[104]
$Ce_{0.9}Sm_{0.1}O_{2-x/2-\Delta\delta}$	400	[105]
$Ce_{0.8}Sm_{0.2}O_{2-x/2-\Delta\delta}$	385	[105]
	375	[106]

In addition to the electronic conductivity in reducing conditions, the perovskite proton conductor can also exhibit significant electronic conductivity in oxidising conditions (p-type), by the creation of electronic holes:

$$\frac{1}{2}O_2 + V_O^{\bullet\bullet} \leftrightarrow O_O^x + 2h^{\bullet} \quad (2.30)$$

with an equilibrium constant given by:

$$K_R \approx \frac{[V_O^{\bullet\bullet}][Ce'_{Ce}]^2 p_{O2}^{1/2}}{[O_O^x][Ce_{Ce}^x]^2} \quad (2.31)$$

Oishi *et al.* [101,107] determined the concentration of electronic holes (Fig. 2.21a) [107] and p-type transport numbers (Fig. 2.21b) [101] for BCY10 in wet conditions (p_{H2O} ~ 10^{-2} atm) between 600 – 900 °C. From Fig. 2.21b, we can observe the significant electronic transport in more oxidising conditions even at the lowest temperature of 600 °C, where the transport number is still above 0.2. Due to the competing nature of the hydration equation, eqn (2.15), and that of the formation of holes, eqn (2.30), we can envisage that in conditions of lower humidity the electronic contribution could rise to higher values.

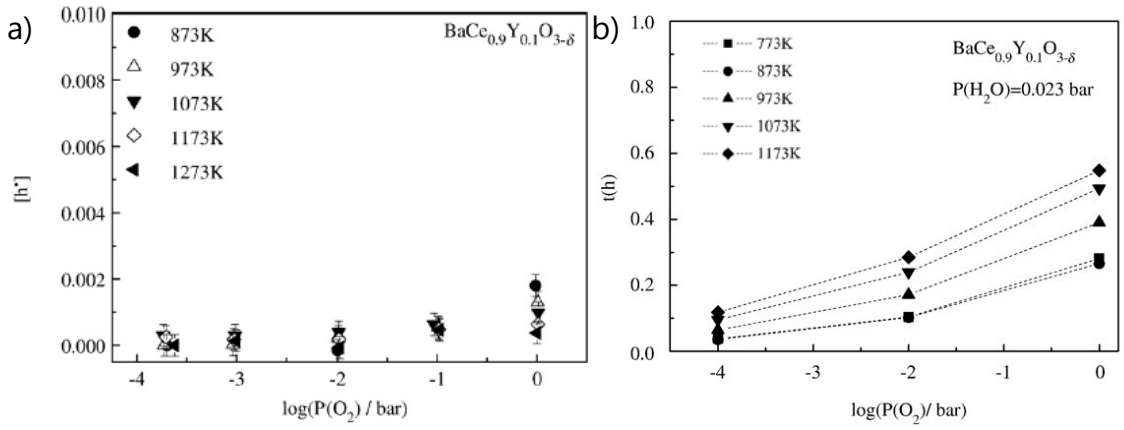

Fig. 2.21 – a) concentration of electronic holes as a function of p_{O2} in wet conditions [107]; b) transport number of electronic holes in BCY10 as a function of p_{O2} in wet conditions [101].

2.3.1.4. *Brouwer* diagrams

Brouwer diagrams are the standard representation of any alteration in the defect concentration as a function of the oxygen partial pressure. In this type of diagram, it is usual to distinguish several regions according to the conditions in the atmosphere. This systematic analysis can be very useful as a guide to study the material and its potential applications [108].

In the case of doped cerates, we should analyse the combined effects of non-stoichiometry, formation of native ionic defects, and the formation of protonic and electronic defects. Having found the set of reactions that best describes the defect chemistry of the material and the corresponding equilibrium constants, one then proceeds to the identification of possible regions where approximate electrical neutrality conditions can be assumed [108]. The trends for each of these regions can be summarised graphically as the example in Fig. 2.22. The exact representation of this figure requires the knowledge of the equilibrium constants (K_w, K_R and K_O), in order to calculate the concentration of each defect at a given temperature.

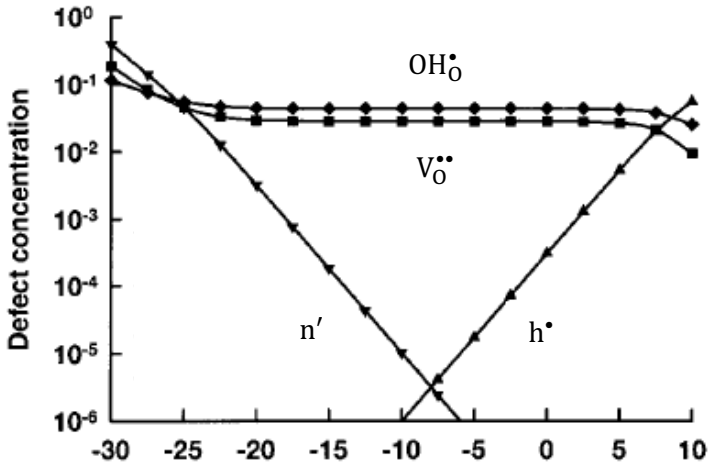

Fig. 2.22 – *Brouwer* diagram of defect concentrations in a perovskite proton conductor for the case $[M_B'] = 0.1$ and $p_{H2O} = 10^{-2}$ atm. Adapter from [109].

Since oxygen pressure and concentrations can vary from many orders of magnitude, it is convenient to use logarithmic scales. The slopes of this type of representations are still adequate to facilitate the identification of the expected dependence for each species (Table 2.5).

Table 2.5 – Summary of the equations describing the usual defects in yttrium-doped barium cerate.

Type	Equation	Equilibrium constant
Oxide-ion	$Ce_{Ce}^{x} + \frac{1}{2}O_O^x + \frac{1}{2}Y_2O_3 \Longrightarrow Y_{Ce}' + \frac{1}{2}V_O^{\bullet\bullet} + CeO_2$	-
Protonic	$H_2O + [V_O^{\bullet\bullet}] + [O_O^x] = 2OH_O^{\bullet}$	$K_w = \frac{[OH_O^{\bullet}]^2}{[V_O^{\bullet\bullet}][O_O^x]p_{H2O}}$ $[OH_O^{\bullet}] \propto p_{H2O}^{1/2}$
n-type	$2Ce_{Ce}^{x} + O_O^x \Leftrightarrow V_O^{\bullet\bullet} + 2Ce_{Ce}' + \frac{1}{2}O_2$	$K_R \approx \frac{[V_O^{\bullet\bullet}][Ce_{Ce}']^2 p_{O2}^{1/2}}{[O_O^x][Ce_{Ce}^x]^2}$ $[Ce_{Ce}'] \propto p_{O2}^{-1/4}$
p-type	$\frac{1}{2}O_2 + V_O^{\bullet\bullet} \leftrightarrow O_O^x + 2h^{\bullet}$	$K_O \approx \frac{[h^{\bullet}]^2}{[V_O^{\bullet\bullet}].p_{O2}^{1/2}}$ $[h^{\bullet}] \propto p_{O2}^{1/4}$
Electroneutrality	$[OH_O^{\bullet}] + 2[V_O^{\bullet\bullet}] + h^{\bullet} = [Y_{Ce}'] + [Ce_{Ce}'] + n'$	-

From the Table 2.5, we can understand that the concentration of the electronic charge carriers is shown to exhibit dependencies on both oxygen and water-vapour partial pressures. Due to the lack of enough experimental data of BCY10 in the literature regarding the equilibrium constants, and especially at low temperatures (*i.e.*, below 500 – 600 °C), it is imperative to analyse the electrochemical transport properties of this composition in the conditions of interest.

2.4. Electrode materials

The development of electrode materials for chemical production processes that utilise electrochemical protonic ceramic membranes has not received specific study to date. For this reason, this section reviews current knowledge of electrode materials that have been designed for proton ceramic fuel cells (PCFCs) to provide a baseline from which more dedicated chemical production electrodes can be developed.

In addition to the electrolyte material, a single-cell of proton ceramic fuel cell is also composed by the oxygen electrode (cathode) and the hydrogen electrode (anode). These electrode materials must offer tolerable chemical and structural stability during the cell operation at high temperatures, suitable conductivity (electronic or mixed electronic and ionic), proper percolation pathways of each conducting species, no inter-diffusion of elements between the various cell components, similar thermal expansion coefficients to the remaining cell components to avoid cracking during cell fabrication and operation, and sufficient porosity to allow the gas transport to and from the electrode reaction sites. Moreover, the component materials must be of low cost, easy fabrication and should not affect the sequential fabrication processing upon addition of further cell components. The typical ceramic electrode materials used for protonic ceramic fuel cells are described below.

2.4.1. Cathode

While high-performance, single-phase materials such as mixed ionic-electronic conducting oxides (e.g. (La,Sr)(Co,Fe)$O_{3-\delta}$ (LSCF) or (Ba,Sr)(Co,Fe)$O_{3-\delta}$ (BSCF)) have been identified for cathodes in oxide-ion conducting electrochemical devices, ideal cathode materials for protonic conducting analogues are yet to be finalised. This is perhaps not surprising, given the new nature of proton conducting electrical devices. However, the design of cathodes remains a critical challenge for the successful realisation of these devices to lower overall resistance losses.

The most widely studied cathode materials so far for solid oxide protonic applications have been rare earth doped nickelates (R_2NiO_4, R = Pr, Nd, rare earth elements) [110], $Ba(Pr_{1-x}Gd_x)O_{3-\delta}$, $PrBaCuFeO_{5+x}$ and the composite cathodes $La_{0.6}Sr_{0.4}Co_{0.2}Fe_{0.8}O_{3-\delta}$/$Ba(Zr_{0.1}Ce_{0.7}Y_{0.2})O_{2.9}$, $Sm_{0.5}Sr_{0.5}CoO_{2.25}$/$BaCe_{0.8}Sm_{0.2}O_{2.9}$, and $Ba_{0.5}Sr_{0.5}Co_{0.8}Fe_{0.2}O_{3-\delta}$/$BaCe_{0.8}Sm_{0.2}O_{2.9}$ [31,111]. Among all the homogeneous materials, the nickelate, Pr_2NiO_4, cathode has shown the lowest overpotential losses [110,112,113]. For the composite cathodes, more compositional flexibility is available and phases offering high electronic conductivity are generally mixed together with well-known proton conducting oxides from the zirconate and cerate perovskite families to increase the cell performance. The applicability of a cathode material for proton conducting cells is dependent not only on its electrochemical performance, but also its thermal expansion coefficient and chemical compatibility with electrolyte material. Platinum has also been used as cathode but is shown to degrade upon long time operation, to exhibit large overpotential losses and is also prohibitively expensive. Single phase mixed triple conducting (H^+, O^{2-}, e^-) cathode materials have also been developed recently, such as $NdBa_{0.5}Sr_{0.5}Co_{1.5}Fe_{0.5}O_{5+\delta}$ that possess a layered perovskite structure showing very promising cell performance that was stable for 500 h at 750 °C [114]. A further new triple mixed conducting cathode $BaCo_{0.4}Fe_{0.4}Zr_{0.1}Y_{0.1}O_{3-\delta}$ was designed recently by Duan *et al.* [115]. The cells made with this cathode have shown one of the best performances so far in PCFC history, *i.e.*, 455 mW cm^{-2} on H_2 and 142 mW cm^{-2} on CH_4 were achieved at 500 °C and the performance was shown to be maintained for 1400 hours without any degradation.

Fig. 2.23 shows a schematic representation of the possible mechanism of the oxygen reduction reaction and of the reaction at the cathode/electrolyte interface in protonic ceramic fuel cells. In the case of pure electronic conductors (Fig. 2.23a), *e.g.* Pt, the electroactive area is restricted to the triple phase boundary (TPB). Thus, the dissociated oxygen diffuses on the surface of the material to the TPB so that it can react with the protons to form and release gaseous water. Due to long transfer paths for oxygen ions, as they can only migrate on the surfaces, this type of cathode has the disadvantage of having a limited three phase boundary length and, hence, larger polarisation resistances.

In contrast, when using electron-oxygen ion mixed conductors as cathode materials (Fig. 2.23b), such as Pr_2NiO_4, the dissociated oxygen ions can partially diffuse through the bulk of the cathode to the TPB. In this situation, the transfer paths of oxygen species are enlarged, but still limited to specific TPBs. This type of material presents, nonetheless, usually lower polarisation resistances than those of pure electronic conductors (Fig. 2.23a).

When using electron-proton mixed conductors as a cathode (Fig. 2.23c), such as $BaCe_{0.5}Bi_{0.5}O_{3-\delta}$, the protons from the electrolyte can transfer through the bulk, and the reaction areas for protons and oxygen species are extended to the entire gas/cathode surface. This scenario provides even greater advantage over the previous cases.

Finally, a last case concerns the use of a composite configuration (Fig. 2.23d). Namely, using a cathode composed of an electronic-oxygen ion mixed conductors and proton conductors as cathode materials, such as $Sm_{0.5}Sr_{0.5}CoO_{3-\delta}$, SSC) and a proton conductor ($BaCe_{0.8}Sm_{0.2}O_{3-\delta}$, BCS), the TPB is enlarged into the bulk of cathode layers, which greatly promote the transfer and reaction of protons and oxygen species, resulting in very low polarisation resistances.

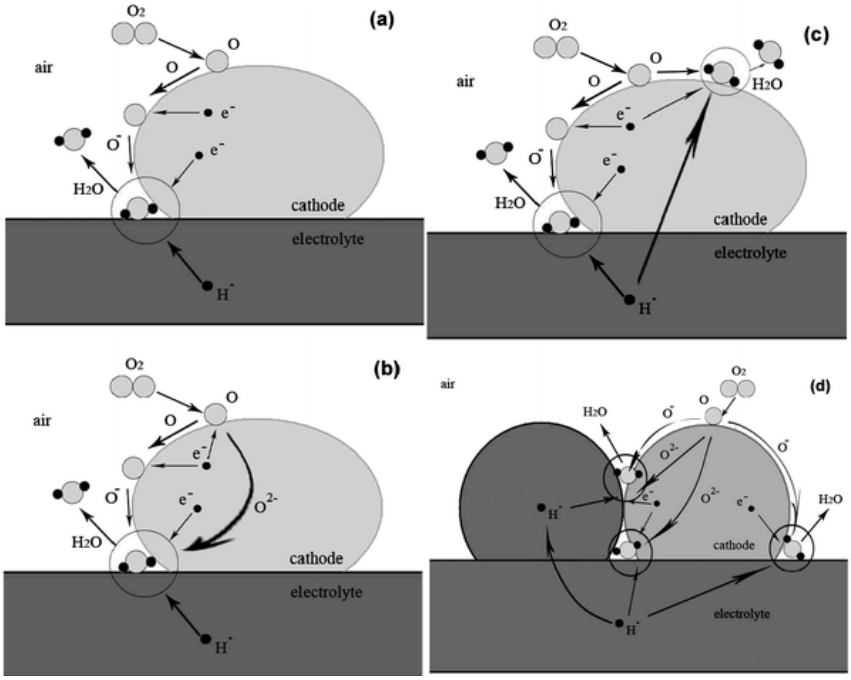

Fig. 2.23 – Schematic representation of possible cathode reaction mechanisms using proton-conducting electrolytes: a) electron conductor; b) electron-oxygen ion mixed conductor; c) electron-proton mixed conductor; and d) composites made of a proton conductor and an electronic-oxygen ion mixed conductor, as cathode materials [111].

One of the reasons for the large number of articles suggesting compositions of the perovskite structure for potential cathodes is related to the possibility to accommodation a wide variety of defects to modify their electrochemical behaviour in either reducing or oxidising environments. One good example concerns the high order nickelates, that is the layered *Ruddlesden-Popper* nickelate series (n=3), $Ln_{n+1}Ni_nO_{3n+1}$, which offer mixed oxide-ion and electronic conductivity (MIEC), where the electronic component is metallic in nature and increases with decreasing temperature [116]. At lower temperatures, *i.e.* ≤ 500 °C, as aimed in the current work, this behaviour offers large advantage over previously suggested electrodes from more common structural families that have been small polaronic in nature, *i.e.* with thermally activated electronic contributions in oxidising environments. The *Ruddlesden-Popper* structure is composed by alternate perovskite rock-salt layers, as depicted in Fig. 2.24.

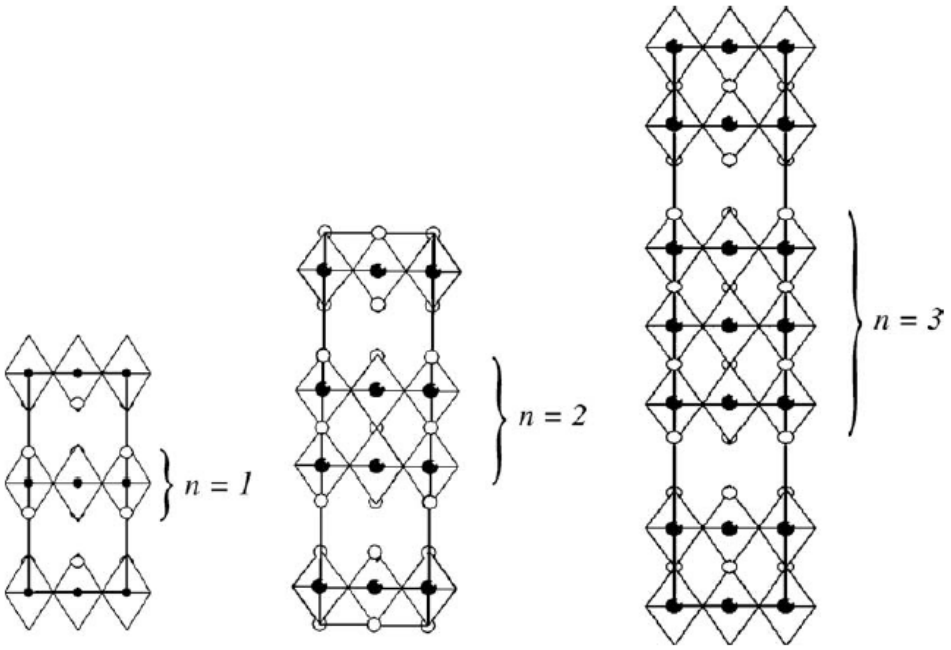

Fig. 2.24 –Illustration of the *Ruddlesden-Popper* phases, $La_{n+1}Ni_nO_{3n+1}$ (n = 1,2 e 3) [116].

This material allows an increase in conductivity with decreasing temperature for n = 3 (Fig. 2.25). The combination of this composition with a proton-conducting ceramic such as BCY/BCZY/BZY can thus be a potential alternative cathode material for use at low-temperature electrochemical reactors.

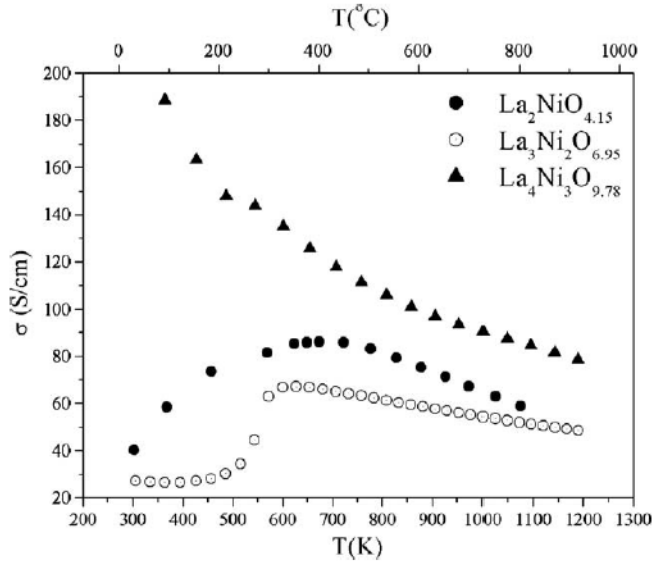

Fig. 2.25 – Electrical conductivity vs. temperature for $La_2NiO_{4.15}$, $La_3Ni_2O_{6.95}$ and $La_4Ni_3O_{9.78}$ from RT to 1173 K in air [116].

2.4.2. Anode

The anode is another main component of the fuel cell (also called as the fuel electrode) and its major role is to oxidise the fuel. The most commonly used anode in SOFCs is that of a composite cermet. A cermet anode consists of both metallic and ceramic (ionic conducting) phases (Fig. 2.26). The presence of the ceramic phase in this type of composite cermet prevents the coarsening of metallic particles at high temperatures, provides a closer match of thermal expansion coefficient (TEC) with the electrolyte, increases the three phase boundary length (TPBL) between the gas, the ionic and the electronic conducting phases, minimizes gas phase diffusion limitations and reduces polarisation losses. Several metallic composites (Ni, Cu, Pt, Ag, Co, Fe mixed with oxide ion conductors YSZ) have been employed as anodes in solid oxide fuel cells. Among these, nickel cermets have shown the most promising results due to their high catalytic activity towards for fuel (H_2, CH_4, etc.) oxidation. However, nickel cermets are susceptible to oxidation, carbon deposition and, sulphur poising which can reduce SOFC performance and longevity. More than a decade of research has been dedicated to optimise and explore the properties of nickel cermets in terms of phase analysis, microstructure, redox stability, cermet composition and, novel strategies to avoid the aforementioned problems

degradation issues in for oxide-ion conducting SOFCs. Linearly, researchers have adapted similar cermet strategies to proton conducting fuel cells by employing nickel cermets as anodes based on SOFC anode literature, but where the ceramic phase is now proton conducting. Hence, typical PCFC anodes have typically consisted of a metallic (mostly Ni or Cu) phase and protonic conducting ceramic oxides, such as those based on $Ba(Ce,Zr)(Y,Yb)O_{3-\delta}$. The anode must be designed to its specific function and, thus, must possess the following basic properties [117]: acceptable conductivity (electronic and ionic to function as an electrode, (> 10^2 S cm^{-1}), high chemical and structural stability, percolation pathways between metallic and ceramic phase, close thermal expansion coefficient to other cell components, adequate porosity for gas diffusion to allow unhindered gas transport to the reaction sites and good mechanical strength.

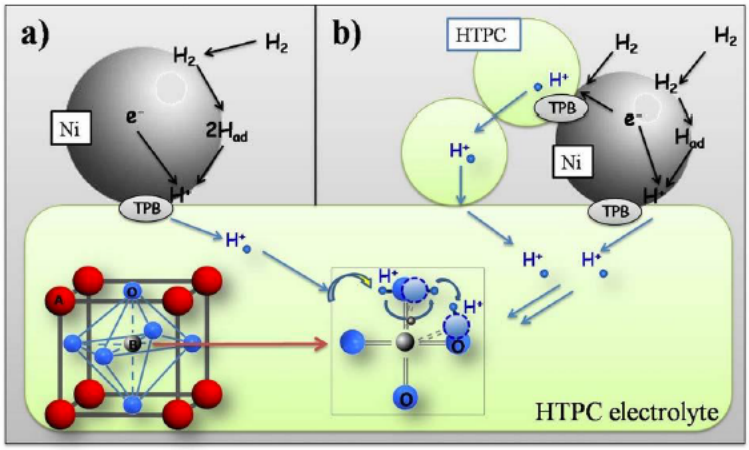

Fig. 2.26 – The mechanism of hydrogen oxidation at anode site: a) nickel and b) nickel cermet-containing proton conducting oxide [39].

A range of compositions have been studied [63] by changing the ratio of Ni to ceramic phase while their structure-property relationships are explained below in detail. With respect to the ceramic phase, anodes that contain $BaCeO_3$-based composites may be unsuitable for practical operation in hydrocarbon fuels, owing to the instability of $BaCeO_3$ in steam and CO_2 containing atmospheres [39,118]. On the contrary, acceptor doped $BaZrO_3$-based materials exhibit greater chemical stability in the aforementioned conditions and, thus, have been typically suggested to be more promising for use as anode cermet matrixes electrodes in these devices [39].

Another important characteristic of the anode is to provide electrical conductivity. The total electrical conductivity of PCFC anode *e.g.* Ni-BZY anode has a strong dependence on the Ni content in the composition (Fig. 2.27). The anode with 20 vol% Ni shows a typical Arrhenius behaviour in wet reducing atmosphere with an activation energy of ~ 0.58 eV, suggesting that mostly protons are involved in the total conductivity. On further increases of Ni volume to ≥ 30 %, a typical metallic behaviour is observed. A clear percolation threshold is achieved at above 40 vol%, as also suggested by Nasani *et al.* [63].

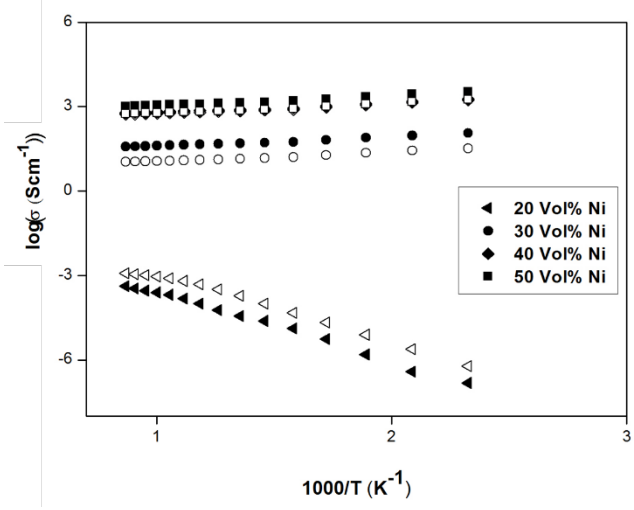

Fig. 2.27 – Arrhenius plots of Ni-BZY anodes under wet (open symbols) and dry (filled symbols) reducing atmospheres [63].

References

1 J. M. Andújar and F. Segura, *Renew. Sustain. Energy Rev.*, 2009, **13**, 2309–2322.

2 B. Zhu, X. Liu, Z. Zhu and R. Ljungberg, *Int. J. Hydrogen Energy*, 2008, **33**, 3385–3392.

3 O. Yamamoto, *Electrochim. Acta*, 2000, **45**, 2423–2435.

4 D. J. L. Brett, A. Atkinson, N. P. Brandon and S. J. Skinner, *Chem. Soc. Rev.*, 2008, **37**, 1568–1578.

5 E. D. Wachsman and K. T. Lee, *Science*, 2011, **334**, 935–939.

6 T. Schober, F. Krug and W. Schilling, *Solid State Ionics*, 1997, **97**, 369–373.

7 S. M. Haile, *Acta Mater.*, 2003, **51**, 5981–6000.

8 N. Nasani, F. Loureiro and D. P. Fagg, in *Functional Materials for Solid Oxide Fuel Cells: Processing, Microstructure and Performance*, Bentham Science Publishers, 2017, pp. 131–163.

9 N. Mahato, A. Banerjee, A. Gupta, S. Omar and K. Balani, *Prog. Mater. Sci.*, 2015, **72**, 141–337.

10 F. M. L. Figueiredo and F. M. B. Marques, *Wiley Interdiscip. Rev. Energy Environ.*, 2013, **2**, 52–72.

11 J. Larminie and A. Dicks, in *Fuel Cell Systems Explained*, Wiley Online Books, 2003, pp. 1-24.

12 F. de Bruijn, *Green Chem.*, 2005, **7**, 132–150.

13 S. C. Singhal and K. Kendall, in *High Temperature and Solid Oxide Fuel Cells: Fundamentals, Design and Applications*, eds. S. C. Singhal and K. B. T.-H. T. and S. O. F. C. Kendall, Elsevier Science, Amsterdam, 2003, pp. 1–22.

14 J. F. Richardson, *Gas Sep. Purif.*, 1990, **4**, 2–7.

15 M. Ouzounidou, A. Skodra, C. Kokkofitis and M. Stoukides, *Solid State Ionics*, 2007, **178**, 153–159.

16 R. P. W. J. Struis, S. Stucki and M. Wiedorn, *J. Memb. Sci.*, 1996, **113**, 93–100.

17 A. Ghareghashi, S. Ghader and H. Hashemipour, *J. Ind. Eng. Chem.*, 2013, **19**, 1811–1826.

18 M. R. Rahimpour, S. M. Jokar and Z. Jamshidnejad, *Chem. Eng. Res. Des.*, 2012, **90**, 383–396.

19 V. Kyriakou, I. Garagounis, E. Vasileiou, A. Vourros and M. Stoukides, *Catal. Today*, 2017, **286**, 2–13.

20 L. R. Struckmann, B. Munder, L. Chalakov and K. Sundmacher, in *Membrane Reactors: Distributing Reactants to Improve Selectivity and Yield*, Wiley-VCH Verlag GmbH & Co. KGaA., 2010, pp. 193–233.

21 C. Athanassiou, G. Pekridis, N. Kaklidis, K. Kalimeri, S. Vartzoka and G. Marnellos, *Int. J. Hydrogen Energy*, 2007, **32**, 38–54.

22 A. de Lucas-Consuegra, N. Gutiérrez-Guerra, J. L. Endrino, J. C. Serrano-Ruiz and J. L. Valverde, *J. Solid State Electrochem.*, 2015, **19**, 2991–2999.

23 M. Stoukides, *Catal. Rev.*, 2000, **42**, 1–70.

24 I. V Yentekakis, Y. Jiang, M. Makri and C. G. Vayenas, *Ionics (Kiel)*, 1995, **1**, 286–291.

25 T. Hibino, A. Masegi and H. Iwahara, *J. Electrochem. Soc.*, 1995, **142**, L72–L73.

26 S. H. Morejudo, R. Zanón, S. Escolástico, I. Yuste-Tirados, H. Malerød-Fjeld, P. K. Vestre, W. G. Coors, A. Martínez, T. Norby, J. M. Serra and C. Kjølseth, *Science*, 2016, **353**, 563–566.

27 K. Xie, Y. Zhang, G. Meng and J. T. S. Irvine, *Energy Environ. Sci.*, 2011, **4**, 2218–2222.

28 E. Ruiz-Trejo and J. T. S. Irvine, *Solid State Ionics*, 2012, **216**, 36–40.

29 D. S. Yun, J. H. Joo, J. H. Yu, H. C. Yoon, J.-N. Kim and C.-Y. Yoo, *J. Power Sources*, 2015, **284**, 245–251.

30 A. F. Sammells, R. L. Cook, J. H. White, J. J. Osborne and R. C. MacDuff, *Solid State*

Ionics, 1992, **52**, 111–123.

31 E. Fabbri, D. Pergolesi and E. Traversa, *Chem. Soc. Rev.*, 2010, **39**, 4355–4369.

32 K. D. Kreuer, *Annu. Rev. Mater. Res.*, 2003, **33**, 333–359.

33 K. D. Kreuer, *Solid State Ionics*, 1999, **125**, 285–302.

34 H. Iwahara, T. Mori and T. Hibino, *Solid State Ionics*, 1995, **79**, 177–182.

35 E. Fabbri, L. Bi, D. Pergolesi and E. Traversa, *Adv. Mater.*, 2012, **24**, 195–208.

36 A. V Bannykh and B. L. Kuzin, *Ionics (Kiel)*, 2003, **9**, 134–139.

37 B. L. Kuzin, S. M. Beresnev, A. V Bannykh and M. V Perfil'yev, *Russ. J. Electrochem.*, 2000, **36**, 424–430.

38 L.-G. Qiu, G.-L. Ma and D.-J. Wen, *Chinese J. Chem.*, 2005, **23**, 1641–1645.

39 E. Fabbri, D. Pergolesi and E. Traversa, *Sci. Technol. Adv. Mater.*, 2010, **11**, 44301.

40 A. N. Virkar and H. S. Maiti, *J. Power Sources*, 1985, **14**, 295–303.

41 W. Suksamai and I. S. Metcalfe, *Solid State Ionics*, 2007, **178**, 627–634.

42 D.-K. Lim, M.-B. Choi, K.-T. Lee, H.-S. Yoon, E. D. Wachsman and S.-J. Song, *Int. J. Hydrogen Energy*, 2011, **36**, 9367–9373.

43 N. V Sharova and V. P. Gorelov, *Russ. J. Electrochem.*, 2003, **39**, 461–466.

44 N. V Sharova, V. P. Gorelov and V. B. Balakireva, *Russ. J. Electrochem.*, 2005, **41**, 665–670.

45 M. W. and L. Qiu, *Chinese J. Chem. Phys.*, 2008, **21**, 286.

46 N. V Sharova and V. P. Gorelov, *Russ. J. Electrochem.*, 2004, **40**, 639–645.

47 W. G. Coors and D. W. Readey, *J. Am. Ceram. Soc.*, 2004, **85**, 2637–2640.

48 G. Ma, T. Shimura and H. Iwahara, *Solid State Ionics*, 1999, **120**, 51–60.

49 K. D. Kreuer, T. Dippel, Y. M. Baikov and J. Maier, *Solid State Ionics*, 1996, **86**–**88**, 613–620.

50 N. Bonanos, B. Ellis, K. S. Knight and M. N. Mahmood, *Solid State Ionics*, 1989, **35**, 179–188.

51 R. C. T. Slade and N. Singh, *Solid State Ionics*, 1993, **61**, 111–114.

52 A. Kruth and J. T. S. Irvine, *Solid State Ionics*, 2003, **162**–**163**, 83–91.

53 H. Matsumoto, Y. Kawasaki, N. Ito, M. Enoki and T. Ishihara, *Electrochem. Solid-State Lett.*, 2007, **10**, B77–B80.

54 A. K. Eriksson Andersson, S. M. Selbach, T. Grande and C. S. Knee, *Dalt. Trans.*, 2015, **44**, 10834–10846.

55 A. Lacz, *Ionics (Kiel)*, 2016, **22**, 1405–1414.

56 Y. Li, P.-C. Su, L. M. Wong and S. Wang, *J. Power Sources*, 2014, **268**, 804–809.

57 H.-S. Kim, H. Bin Bae, W. Jung and S.-Y. Chung, *Nano Lett.*, 2018, **18**, 1110–1117.

58 Z. Sun, E. Fabbri, L. Bi and E. Traversa, *Phys. Chem. Chem. Phys.*, 2011, **13**, 7692–7700.

59 J.-S. Park, J.-H. Lee, H.-W. Lee and B.-K. Kim, *Solid State Ionics*, 2010, **181**, 163–167.

60 H. T. Handal, A. Hassan, R. Leeson, S. M. Eloui, M. Fitzpatrick and V. Thangadurai, *Inorg. Chem.*, 2016, **55**, 729–744.

61 H. Donglin, H. Naoyuki and U. Tetsuya, *J. Am. Ceram. Soc.*, 2016, **99**, 3745–3753.

62 R. Muccillo, E. N. S. Muccillo, T. F. Andrade and O. R. Oliveira, *J. Therm. Anal. Calorim.*, 2017, **130**, 1791–1799.

63 N. Narendar, G. C. Mather, P. A. N. Dias and D. P. Fagg, *RSC Adv.*, 2013, **3**, 859–869.

64 H. S. Soares, X. Zhang, I. Antunes, J. R. Frade, G. C. Mather and D. P. Fagg, *J. Solid State Chem.*, 2012, **191**, 27–32.

65 T. Yang, F. J. A. F. J. A. Loureiro, R. P. Queirós, D. Pukazhselvan, I. Antunes, J. A. J. A. Saraiva, R. P. Queir, I. Antunes and J. A. J. A. Saraiva, *Int. J. Hydrogen Energy*, 2016, **41**, 1–10.

66 F. Bozza, K. Bator, W. W. Kubiak and T. Graule, *J. Eur. Ceram. Soc.*, 2016, **36**, 101–107.

67 H. Grant, M. Anthony, C. W. G. and R. Sandrine, *J. Am. Ceram. Soc.*, 2017, **101**, 1298–1309.

68 Z. Khani, M. Taillades-Jacquin, G. Taillades, M. Marrony, D. J. Jones and J. Rozière, *J. Solid State Chem.*, 2009, **182**, 790–798.

69 S. S. Baek, K. Y. Park, T. H. Lee, N. Lee, Y. Seo, S. J. Song and J. Y. Park, *Acta Mater.*, 2014, **66**, 273–283.

70 S. Ricote, N. Bonanos, A. Manerbino, N. P. Sullivan and W. G. Coors, *J. Mater. Chem. A*, 2014, **2**, 16107–16115.

71 S. Ziqi, F. Emiliana, B. Lei and T. Enrico, *J. Am. Ceram. Soc.*, 2011, **95**, 627–635.

72 H. Shimada, X. Li, A. Hagiwara and M. Ihara, *J. Electrochem. Soc.* , 2013, **160**, F597–F607.

73 A. Magrez and T. Schober, *Solid State Ionics*, 2004, **175**, 585–588.

74 J. Tong, D. Clark, L. Bernau, M. Sanders and R. O'Hayre, *J. Mater. Chem.*, 2010, **20**, 6333–6341.

75 S. M. Babiniec, S. Ricote and N. P. Sullivan, *Int. J. Hydrogen Energy*, 2015, **40**, 9278–9286.

76 T. S. W. and I. J. T. S., *Adv. Mater.*, 2006, **18**, 1581–1584.

77 N. Nasani, D. Ramasamy, I. Antunes, J. Perez and D. P. Fagg, *Electrochim. Acta*, 2015, **154**, 7–13.

78 N. Nasani, P. A. N. Dias, J. A. Saraiva and D. P. Fagg, *Int. J. Hydrogen Energy*, 2013, **38**, 8461–8470.

79 M. Liu, Y. Liu, L. Yang, M. Liu and Z. Tang, *J. Power Sources*, 2011, **196**, 9980–9984.

80 K. Katahira, Y. Kohchi, T. Shimura and H. Iwahara, *Solid State Ionics*, 2000, **138**, 91–98.

81 X. Ma, J. Dai, H. Zhang and D. E. Reisner, *Surf. Coatings Technol.*, 2005, **200**, 1252–1258.

82 P. Sawant, S. Varma, B. N. Wani and S. R. Bharadwaj, *Int. J. Hydrogen Energy*, 2012, **37**, 3848–3856.

83 E. Fabbri, A. D'Epifanio, E. Di Bartolomeo, S. Licoccia and E. Traversa, *Solid State Ionics*, 2008, **179**, 558–564.

84 J. Dailly, M. Ancelin and M. Marrony, *Solid State Ionics*, 2017, **306**, 69–75.

85 Y. Yoo and N. Lim, *J. Power Sources*, 2013, **229**, 48–57.

86 G. Taillades, P. Pers, V. Mao and M. Taillades, *Int. J. Hydrogen Energy*, 2016, **41**, 12330–12336.

87 L. Fan and P.-C. Su, *J. Power Sources*, 2016, **306**, 369–377.

88 Y. Okuyama, N. Ebihara, K. Okuyama and Y. Mizutani, *ECS Trans.*, 2015, **68**, 2545–2553.

89 Z. Khani, M. Taillades-Jacquin, G. Taillades, D. J. Jones, M. Marrony and J. Rozière, *Chem. Mater.*, 2010, **22**, 1119–1125.

90 L. Yang, S. Wang, K. Blinn, M. Liu, Z. Liu, Z. Cheng and M. Liu, *Science*, 2009, **326**, 126–129.

91 K. Takeuchi, C.-K. Loong, J. W. Richardson, J. Guan, S. E. Dorris and U. Balachandran, *Solid State Ionics*, 2000, **138**, 63–77.

92 S. Ricote, N. Bonanos, A. Manerbino and W. G. Coors, *Int. J. Hydrogen Energy*, 2012, **37**, 7954–7961.

93 Y. Yamazaki, R. Hernandez-Sanchez and S. M. Haile, *J. Mater. Chem.*, 2010, **20**, 8158–8166.

94 S. Ricote, N. Bonanos, M. C. Marco de Lucas and G. Caboche, *J. Power Sources*, 2009, **193**, 189–193.

95 S. Giddey, S. P. S. Badwal and A. Kulkarni, *Int. J. Hydrogen Energy*, 2013, **38**, 14576–14594.

96 K. D. Kreuer, *Annu. Rev. Mater. Res.*, 2003, **33**, 333–359.

97 S. Ricote, N. Bonanos and G. Caboche, *Solid State Ionics*, 2009, **180**, 990–997.

98 K. D. Kreuer, S. Adams, W. Münch, A. Fuchs, U. Klock and J. Maier, *Solid State Ionics*, 2001, **145**, 295–306.

99 J. S. Park, J. H. Lee, H. W. Lee and B. K. Kim, *Solid State Ionics*, 2012, **224**, 1–5.

100 D.-K. Lim, H.-N. Im, S.-J. Song and H.-I. Yoo, *Sci. Rep.*, 2017, **7**, 486.

101 M. Oishi, S. Akoshima, K. Yashiro, K. Sato, J. Mizusaki and T. Kawada, *Solid State Ionics*, 2009, **180**, 127–131.

102 D. Perez-Coll, P. Nunez and J. R. Frade, in *Advances in Ceramics - Synthesis and Characterization, Processing and Specific Applications*, ed. C. Sikalidis, InTech, Rijeka, 2011, pp 337-362.

103 D. Pérez-Coll, D. Marrero-López, J. C. Ruiz-Morales, P. Núñez, J. C. C. Abrantes and J. R. Frade, *J. Power Sources*, 2007, **173**, 291–297.

104 S. Wang, H. Inaba, H. Tagawa and T. Hashimoto, *J. Electrochem. Soc.*, 1997, **144**, 4076–4080.

105 T. Kobayashi, S. Wang, M. Dokiya, H. Tagawa and T. Hashimoto, *Solid State Ionics*, 1999, **126**, 349–357.

106 J. C. C. Abrantes, D. Pérez-Coll, P. Núñez and J. R. Frade, *Electrochim. Acta*, 2003, **48**, 2761–2766.

107 M. Oishi, S. Akoshima, K. Yashiro, K. Sato, J. Mizusaki and T. Kawada, *Solid State Ionics*, 2008, **179**, 2240–2247.

108 D. M. Smyth, *The Defect Chemistry of Metal Oxides*, Oxford University Press, 2000.

109 N. Bonanos and F. Willy Poulsen, *J. Mater. Chem.*, 1999, **9**, 431–434.

110 J. Dailly, S. Fourcade, A. Largeteau, F. Mauvy, J. C. Grenier and M. Marrony, *Electrochim. Acta*, 2010, **55**, 5847–5853.

111 R. Peng, T. Wu, W. Liu, X. Liu and G. Meng, *J. Mater. Chem.*, 2010, **20**, 6218–6225.

112 J. Dailly, M. Marrony, G. Taillades, M. Taillades-Jacquin, A. Grimaud, F. Mauvy, E. Louradour and J. Salmi, *J. Power Sources*, 2014, **255**, 302–307.

113 E. Quarez, Y. Oumellal and O. Joubert, *Fuel Cells*, 2013, **13**, 34–41.

114 J. Kim, S. Sengodan, G. Kwon, D. Ding, J. Shin, M. Liu and G. Kim, *ChemSusChem*, 2014, **7**, 2811–2815.

115 C. Duan, J. Tong, M. Shang, S. Nikodemski, M. Sanders, S. Ricote, A. Almansoori and R. O'Hayre, *Science*, 2015, **349**, 1321–1326.

116 G. Amow, I. J. Davidson and S. J. Skinner, *Solid State Ionics*, 2006, **177**, 1205–1210.

117 A. B. Stambouli and E. Traversa, *Renew. Sustain. Energy Rev.*, 2002, **6**, 433–455.

118 E. Fabbri, A. D'Epifanio, E. Di Bartolomeo, S. Licoccia and E. Traversa, *Solid State Ionics*, 2008, **179**, 558–564.

3. Methodology

In this chapter, we will address the fundamentals of the most important techniques used in this work as well as detailed explanation of the calculations employed in the following chapters.

3.1. X-ray diffraction (XRD)

The knowledge of the crystalline structure of a material is one of the most fundamental steps to understand its properties. XRD is one of the most powerful and widely used techniques for identification of crystalline phases and analysis of their unit cell dimensions [1]. In crystalline materials, the crystallographic information obtained by XRD is strictly related with the distance between crystalline planes, which can be measured through the diffraction phenomena. XRD makes use of the *Huygens–Fresnel* principle in that the wavelength of X-rays radiation is in the same order of magnitude as the distance between atoms placed in a periodic array, with inter-planar distance *d*, in a crystalline lattice (angstrom (Å)) [1].

When a crystalline material is irradiated by a monochromatic beam, each atom in the periodic array act as a scattering element, in which the electromagnetic waves are scattered in all directions by the scatters centres [1]. Waves scattered from different atoms can interact constructively at certain angles if the waves are in phase, giving rise to diffraction maxima [1]. In a solid material, the condition in which XRD occurs is schematically illustrated in Fig. 3.1.

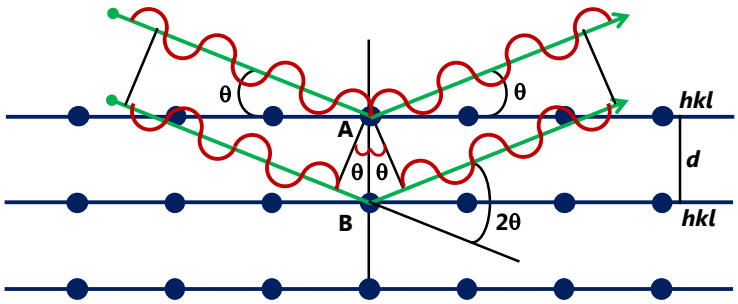

Fig. 3.1– Illustration diagram of the X-rays diffraction by a crystal (*Bragg* condition). Adapted from [1].

When an arbitrary group of parallel planes described by the *Miller* indexes (*hkl*) in a crystal, with an inter-planar distance *d*, is irradiated at an angle θ with a monochromatic beam of X-rays, the waves scattered by each crystalline plane (which have the same phase of the wave scattered by an arbitrary atom in these planes) will interfere constructively if the path difference between the incident and scattered waves in the two planes is a integer multiple of the wavelength [1]. Considering the two atoms A and B in Fig. 3.1, the path difference between the incident and scattered waves by these two atoms is equal to $2dsin(\theta)$, in which θ is the angle between the incident beam and the diffracting plane and d is the inter-planar distance. Therefore, the phenomenon of X-ray diffraction in a crystal occurs in the scattering directions that satisfy *Bragg*'s law, expressed by eqn (3.1) (where *n* is the diffraction order) and which is a consequence of the periodicity arrangement of the crystalline planes [1].

$$n\lambda = 2d\sin(\theta) \tag{3.1}$$

Since monochromatic X-ray radiation is used, only one first order diffraction maximum is produced by each set of parallel planes, detected at a specific angle between the incident and the diffracted waves, called the diffraction angle (2θ). Therefore, by scanning the diffraction angle, the diffractogram composed by the diffraction maxima associated to each crystalline plane in the crystal can be constructed. Since each material has a unique arrangement and number of atoms, its diffraction pattern is also unique [1]. Hence, X-ray diffraction is a valuable technique to identify the crystalline phases present in a sample, which could be a single crystal, polycrystalline powder or even thin films.

The identification of the crystalline phases using the diffractograms obtained by X-ray diffraction was performed by comparison with other diffractograms obtained for reference materials registered in the ICDD (International Centre for Diffraction Data) database. In this search for a match, information about the position of the diffraction maxima, peak intensity and intensity distribution as a function of diffraction angles was compared.

3.2. Scanning electron microscopy (SEM) and X-ray energy dispersive spectroscopy (EDS)

Scanning electron microscopy (SEM) is a high-resolution microscopic technique that can be used to retrieve information about the surface of materials with nanometric resolution and with large depth of field. The use of electrons allows for the use of a high number of different signals that are generated from the interaction between the materials and the electron beam (Fig. 3.2). Each one of these signals can give different type of information about the material under study, including chemical composition, surface topography, crystallography, atomic number distribution, electrical conductivity and others [2]. Using the appropriated detectors, the different signals can be acquired and analysed in the same equipment.

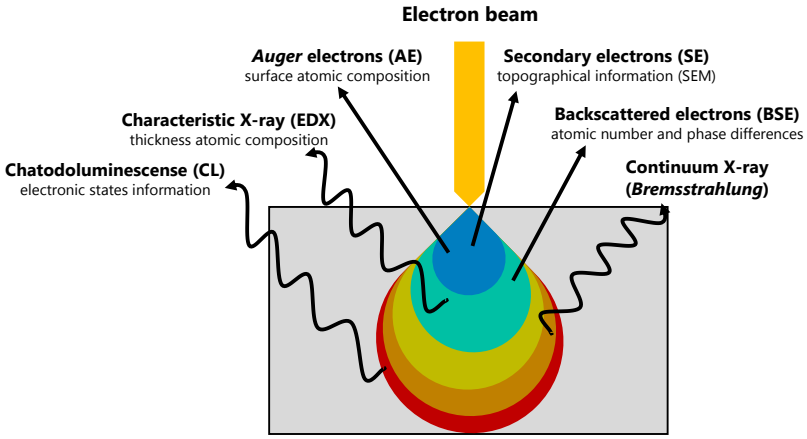

Fig. 3.2 – Various signals produced from the interaction between the electron beam and the sample.

The electron image can, therefore, be combined with other characterisation techniques in order to get information from a specific and localised region of the sample. As an example, energy dispersive X-ray spectroscopy (EDS) is often associated with electron microscopes, to identify specific chemical elements in the sample by the analysis of the emitted X-ray radiation [2]. This technique allows, not only to identify the chemical elements, but also to analyse the distribution of specific elements by mapping a specific region of the sample.

The monochromatic electrons are accelerated by the application of an acceleration voltage (kV) in the electron gun. A set of electromagnetic lenses are used to focus the electrons into a small, coherent beam and to direct the beam onto the surface of the sample.

The secondary electrons generated by the interaction of the electron beam and the materials, are used to imaging the surface of the samples [2]. Since the emission efficiency of the secondary electrons is very sensitive to the geometry and chemical characteristics of the surface as well as to the bulk chemical composition, the SEM can provide important information about surface topography and morphology of the samples. Typically, acceleration voltages in the range between 5 – 30 kV are used in the SEM and spatial resolutions in the order of 1 nm can be achieved [2].

The identification of the elements in the sample by EDS is based on the emission of X-rays from atoms excited by a higher energy X-ray (typically 10 – 30 keV). The region evaluated is located up to 10 µm below the sample surface, although the exact depth depends on the beam energy, on the density of the sample and on the material [2].

EDS is a technique that provides not only qualitative, but also semi-quantitative analysis with accuracies up to 99 % for flat polished samples and if standards are available. Usually, EDS devices are coupled to scanning or transmission electron microscopes in the form of a microanalyser that allows evaluating the chemical composition in a microscopic area [2].

3.3. Electrochemical impedance spectroscopy

The electrical characterisation of materials was performed by Electrochemical Impedance Spectroscopy (EIS). This technique imposes an *a.c.* sinusoidal field over a large frequency range. It has the benefit over *d.c.* measurements that the various phenomena can be separated, allowing to differentiate processes of the material due to their different times constants. Additionally, with continuous variation of applied potential on the sample, the electric field changes periodically its direction, avoiding polarisation phenomena that commonly occur by application of constant voltage on the ionic materials [3]. In *a.c.*

impedance spectroscopy measurements, one measures the complex impedance of a sample as a function of frequency. A single frequency voltage, $V(t)$, is applied across the sample:

$$V(t) = V_0.\sin(\omega t) \tag{3.2}$$

and the resultant current is measured, according to:

$$I(t) = I_0.\sin(\omega t + \phi) \tag{3.3}$$

where ω represents the angular frequency (2π x frequency), V_0 and I_0 the amplitude of signal and current, respectively; and ϕ, the phase shift (Fig. 3.2). By definition, impedance is defined by the opposition to the flow of charge in a system and is given by:

$$Z(\omega) = \frac{V(t)}{I(t)} \tag{3.4}$$

For a pure resistor, the voltage, V, and the resultant current, I, are in phase (ϕ = 0); while for in a pure capacitor I leads V by a phase angle of 90° (*i.e.*, f = 90°). In a real system, we can consider both capacity and resistive terms, due to the typical lags between voltage and current, by a phase angle less than 90°.

$$Z(\omega) = |\mathrm{Z}|.\cos(\phi) + \mathrm{j}.\sin(\phi) = Z' + j.Z'' \tag{3.5}$$

where the imaginary number, $j = \sqrt{-1} = \exp\left(j.\frac{\pi}{2}\right)$ indicates an anticlockwise rotation by $\frac{\pi}{2}$ relative to the real axis.

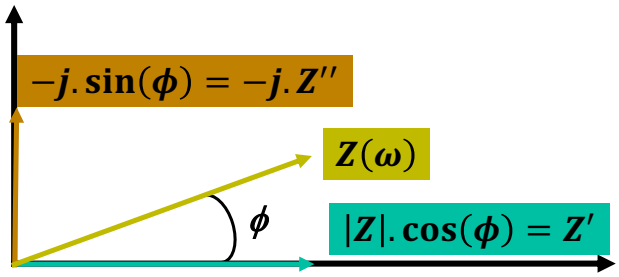

Fig. 3.3 – Phasor diagram of a generic electrical impedance.

Experimental impedance data are plotted by the Nyquist representation, which plots the imaginary component, *Z''*, against the real component, *Z'*, of the sample impedance, at different frequencies. Typically, the Nyquist representation of ceramic ionic conducting materials exhibit distinct arcs corresponding to different phenomena from the intragranular bulk and intergranular grain boundary transport on the electrolyte and to the electrode response. Due to their characteristic relaxation frequencies, the arc at high frequencies is normally attributed to conduction in grain interior (bulk), the intermediate frequency arc is attributed to the conduction in grain boundary, and that at low frequencies is attributed to the electrode response (Fig. 3.4). The analysis of the electrolyte and electrode responses can be represented by series combinations of a resistor (*R*) and a capacitor (*C*) elements in parallel, stated to be the equivalent circuit [3]. In ideal polycrystalline materials, the arcs correspondent to the bulk, grain boundary and electrode response can be conveniently modelled by three sub circuits in series, composed by parallel connection of a resistor and capacitor (*RC* element), Fig. 3.4.

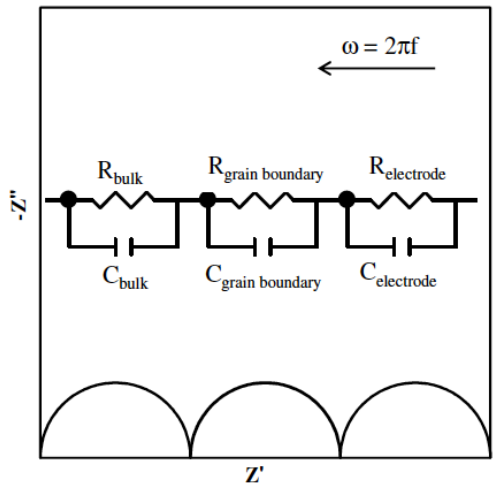

Fig. 3.4 – Schematic impedance plot in the Nyquist representation of an ideal crystalline material.

Nonetheless, many materials are found to give non-ideal responses. The semi-circles produced in the impedance plot are often depressed and have centres which are located below the real axis, which can be attributed to the relaxation processes with a distribution of relation times or other relaxation processes with different time constants, caused by for example inhomogeneous samples. In this situation, the simple combination of RC elements with a single time constant is insufficient to model this type of behaviour, and

the capacitor should be replaced by a Constant Phase Element (*Q*) in order to model conveniently the electrochemical processes. The CPE describes the behaviour of an element whose nature deviates from that of a pure resistor or capacitor and can be characterised from pseudo-capacitance, Y_0, and the parameter ϕ, related with depression of the semicircle obtained in a non-linear response [3], with the admittance given by:

$$Y_{\mathrm{Q}}(\omega) = Y_0(j\omega)^{\phi} \tag{3.6}$$

with a characteristic time constant given by:

$$\tau_0 = \sqrt[\phi]{R.Y_0} \tag{3.7}$$

3.4. Distribution frequency relaxation times (DFRT)

In SOFC research, EIS has plays a crucial role in characterising ionic transport properties in separate electrochemical cell components (*i.e.*, anode, electrolyte and cathode). The analysis of the impedance data is generally based on an equivalent circuit model (EQM) data analysis, which is limited on limited sets of direct electrical relations (*R*, *C*, *L*) and more complex transfer functions derived from the *Laplace* transform of (bounded) diffusion equations (*e.g.*, *Warburg* types, *Gerischer* and also empirical relations, such as the constant phase elements, *Q*) [4,5].

The impedance spectra in the *Argand* plane is obtained across a defined range of frequencies, thus, allowing to differentiate different electrochemical processes in both electrolyte (*i.e.*, bulk and grain boundary) and electrodes (*e.g.*, charge-transfer, diffusion, surface adsorption, gas-phase diffusion, etc.). Nonetheless, the traditional EQM method applied in porous electrodes with not well-defined microstructure (comprising a distribution of grain size, non-uniform porosity, as well as electrodes composed by more than one compound) may fail when different processes occur at very similar relaxation frequencies. In such case, the impedance data is composed by overlapped semicircles that need to be carefully analysed in order to obtain true physical information [4,5].

The definition of a distribution function of relaxation times (DFRT) has been found to be useful for analysing the measured impedance response. This DFRT, $R_{\mathrm{p}}.G(\tau)$, is found from the inversion of the following well-known equation [4,5]:

$$Z(\omega_i) = R_\infty + R_{\mathrm{pol}} \int_0^\infty \frac{\gamma(\tau)}{1+j\omega_i\tau} \mathrm{d}\tau = R_\infty + R_{\mathrm{p}} \int_{-\infty}^\infty \frac{G(\tau)}{1+j\omega_i\tau} \mathrm{dln}\tau \qquad (3.8)$$

with: $G(\tau) = \tau.\gamma(\tau)$ and: $\int_{-\infty}^\infty \frac{G(\tau)}{1+j\omega_i\tau} \mathrm{dln}\tau = 1$. R_∞ is the high-frequency cut-off resistance and R_{p} is the polarisation resistance.

The Fourier transform of the impedance data transforms the data from de dominion of frequency to that of time. Several routes were developed to the τ-domain: Fourier Transform (FT), Maximum Entropy [9,10] and *Tikhonov* Regularization (TR). Solving eqn (3.8) is described as being an "*ill-posed problem*", which means that different solutions can be obtained for $G(\tau)$. Among the different mathematical procedures, a common feature is that they all have a special parameter that must be adjusted to obtain an agreeable DFRT representation. The emphasis is, then, placed on reducing unwanted oscillations and obtaining a (mostly) positive distribution of $G(\tau)$ values. In this thesis, the DFRT analysis was executed using a Matlab programming code to the *Tikhonov* Regularization (TR) [4,5]. In addition, an exact representation can be calculated by:

$$R_{\mathrm{p}}.G(\tau)_{\mathrm{RQ}} = \frac{R}{2\pi}.\frac{\sin((1-\phi)\pi)}{\cosh\left(\phi\ln\left(\frac{\tau}{\tau_0}\right)\right)-\cos((1-\phi)\pi)} \qquad (3.9)$$

with: $\tau_0 = \omega_0^{-1} = \sqrt[\phi]{R.Y_0}$. The DFRT is then the sum of all separate contributions:

$$R_{\mathrm{p}}.G(\tau) = \sum_i R_{\mathrm{i}}.G(\tau)\,, R_{\mathrm{p}} = \sum_i R_{\mathrm{i}} \qquad (3.10)$$

Fig. 3.5a shows the impedance of the simulation, while the Fig. 3.5b presents the exact DFRT for this *R*(*RQ*)(*RQ*) circuit. The surface area under the peak represents the corresponding dc-resistance value of the related impedance expression [4,5].

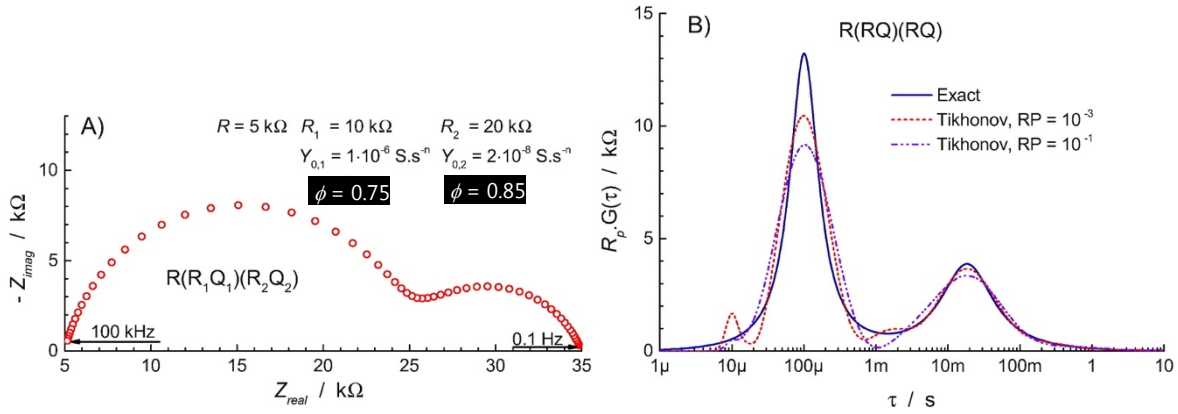

Fig. 3.5 – a) impedance simulation of the *R*(*RQ*)(*RQ*) model; b) exact DFRT with two TR simulations. *RP* = regularization parameter [4].

The width of the distribution function strongly depends on φ, as can be seen in Fig. 3.6. The insert shows the dependence of the full width at half maximum (FWHM, given in decades). When φ = 0.5, *i.e.* a diffusion type dispersion, the DFRT extends over a large range. For φ = 1 the Q becomes a capacitance. The DFRT of a (RC) is a δ-function, *i.e.* a vertical spike at $\tau_0 = RC$. The surface area of $R.G_{(RC)}(\tau)$ is not directly accessible from the graph, although mathematically it still equals *R*. In order to make the contribution of a (*RC*) better visible in the DFRT graph a *Gauss* function is applied as distribution function [5]:

$$R.G(\tau) \approx \frac{R}{W\sqrt{\pi}} e^{-\left(\frac{\ln\left(\frac{\tau_0}{\tau}\right)}{W}\right)^2} \qquad (3.11)$$

Where the parameter *W* determines the width and height of the curve.

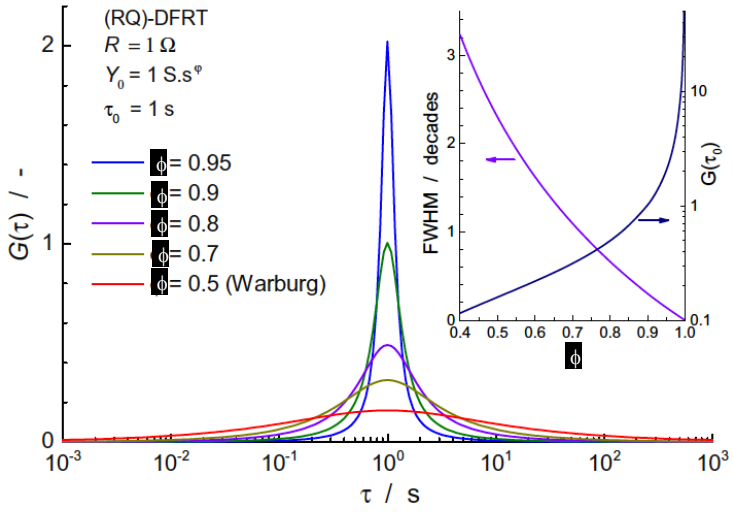

Fig. 3.6 – Distribution functions for a (*RQ*) *vs.* the frequency power, ϕ. The insert shows the relation between ϕ and the full width at half maximum (FWHM in decades) and the maximum $G(\tau_0)$ [5].

3.5. Determination of p_{O2} and p_{H2O} in nominally dry reducing conditions at low temperatures

The direct experimental determination of the oxygen partial pressure below ~ 600 °C is complicated due to the fact that typical oxygen sensors are made of YSZ, which becomes very resistive below this temperature. Hence, an experimental setup composed of two cell jigs was used to perform the experiments (Fig. 3.7). The sample was placed in a cell jig, which was subjected to the different gas feed composition and temperatures. The outlet of this cell was connected to a secondary cell jig fixed at 700 °C. Oxygen sensor values were collected from this second jig. Finally, the outlet of this cell was connected to a JUMO humidity meter, to collect the %*RH* (relative humidity).

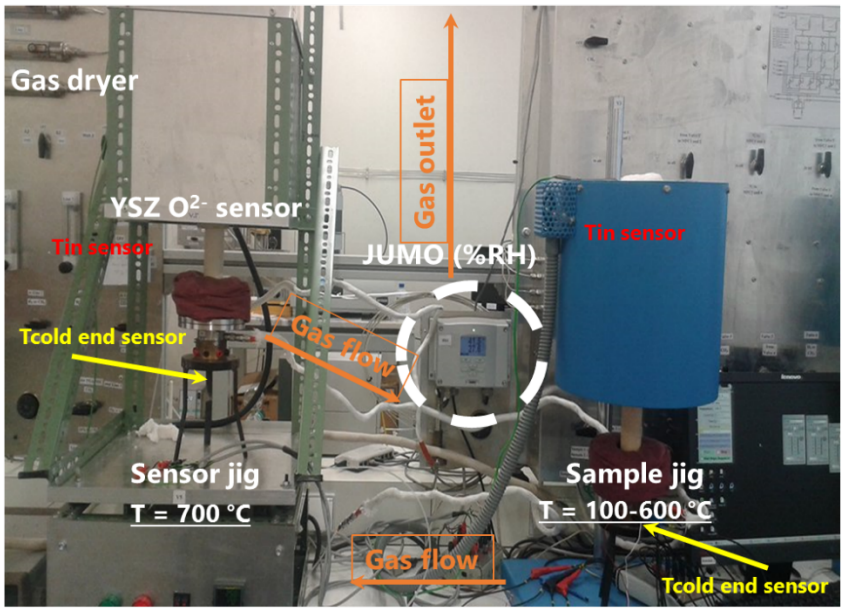

Fig. 3.7 – Experimental apparatus to measure the p_{O2} at low temperatures and in reducing conditions.

In reducing conditions, the following equilibrium was taken into account:

$$H_{2(g)} + \frac{1}{2}O_{2(g)} \leftrightarrow H_2O_{(g)} \tag{3.12}$$

with an equilibrium constant described by

$$K_{\text{eq.}} = \frac{p_{\text{H2O}}}{p_{\text{H2}} p_{\text{O2}}^{1/2}} \tag{3.13}$$

In this experimental configuration, we assume the following relation to be valid:

$$\frac{p'_{\text{H2O}}}{p'_{\text{H2}}} \approx \frac{p''_{\text{H2O}}}{p''_{\text{H2}}} \tag{3.14}$$

where prime (') and double prime ('') correspond to, respectively, the sample jig and sensor jig water and hydrogen partial pressures. Then, we begin by calculating the fractions of H_2O and H_2 in the feed stream:

$$x_{\text{H2O}} = p_{\text{H2O}} \times (Flux_{10\%\text{H2}-\text{N2}} + Flux_{\text{H2}}) \tag{3.15}$$

$$x_{\text{H2}} = (0.1 \times Flux_{10\%\text{H2}-\text{N2}}) + Flux_{\text{H2}} \tag{3.16}$$

where $Flux_{10\%\text{H2}-\text{N2}}$ and $Flux_{\text{H2}}$ are the flow of the feed gases in the mixture. The total fraction of feed gas is given by:

$$x_{\text{Total}} = Flux_{10\%\text{H2}-\text{N2}} + Flux_{\text{H2}} + x_{\text{H2O}} \tag{3.17}$$

From eqn (3.15) to (3.17), we then calculate the partial pressure of the hydrogenated species:

$$p'_{\text{H2+H2O}} = \frac{x_{\text{H2O}} + x_{\text{H2}}}{x_{\text{Total}}} \tag{3.18}$$

$$p'_{\text{H2+H2O}} = p'_{\text{H2O}} + p'_{\text{H2}} \tag{3.19}$$

Then, by combining eqn (3.14) with eqn (3.19) the hydrogen partial pressure in the sample jig can be obtained:

$$p'_{\text{H2}} = p'_{\text{H2+H2O}} \left(1 + \frac{p''_{\text{H2O}}}{p''_{\text{H2}}}\right)^{-1} \tag{3.20}$$

On assuming that $\frac{p'_{\text{H2O}}}{p'_{\text{H2}}} = \frac{p''_{\text{H2O}}}{p''_{\text{H2}}}$, we can calculate the $\frac{p''_{\text{H2O}}}{p''_{\text{H2}}}$ ratio from the sensor jig

$$\frac{p''_{\text{H2O}}}{p''_{\text{H2}}} = K_{\text{eq.}} \times (p''_{\text{O2}})^{1/2} \tag{3.21}$$

where the $K_{\text{eq.}}$ is the constant for water formation (eqn (3.14)) and the partial pressure of the sensor, double prime (''), is given by:

$$p''_{O2} = p_{O2,\text{ref.}} \times \exp\left(E''_{\text{sensor}} \times 4 \times \frac{F}{RT''}\right) \quad (3.22)$$

Finally, by combining eqn (3.14) with eqn (3.21), the value of the oxygen partial pressure, prime (′), from the sample jig is given by:

$$p'_{O2} = \left(\frac{p'_{H2O}}{p'_{H2}} K_w^{-1}\right)^2 \quad (3.23)$$

Fig. 3.8 depicts the dependence of p_{O2} on p_{H2}/p_{H2O}, in which we can observe a linear dependence, highlighting that in reducing conditions the values of p_{O2} are dependent on the equilibrium of H_2:H_2O content.

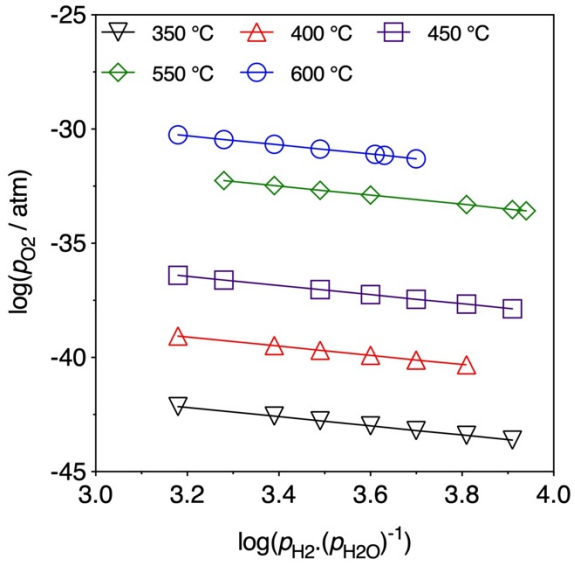

Fig. 3.8 – Dependence of p_{O2} on the ratio p_{H2}:p_{H2O} from the sample jig.

3.6. Coulombic titration

Data on oxygen stoichiometry for the perovskite composition $BaCe_{0.9}Y_{0.1}O_{3-\delta}$ were obtained by the coulometric titration technique. Coulometric titration was performed as a function of oxygen partial pressure (p_{O2}) in potentiostatic mode. This high-temperature titration experiment is a very sensitive technique to quantify changes in oxygen stoichiometry as a function of partial pressure and temperature [6]. The oxide sample is sealed in an electrochemical cell as illustrated in Fig. 3.9. The oxygen stoichiometry of the sample is tuned by the electrochemical pumping of oxygen into or out of the cell, using a solid electrolyte made of a pure oxygen-ion conductor (YSZ). The amount of oxygen pumped out or in the container is quantified by the difference of potential (*EMF*, V_0), which is measured by an additional electrolyte to act as an oxygen sensor [6]:

$$V_0 = \frac{RT}{4F} \ln \left[\frac{p_{O2}}{p_{O2}^{ref}} \right] \quad (3.24)$$

where R is the universal constant, T, absolute temperature, F, Faraday constant, and p_{O2} and p_{O2}^{ref} are the inside and outside oxygen partial pressures, respectively (p_{O2}^{ref} = 0.21 atm).

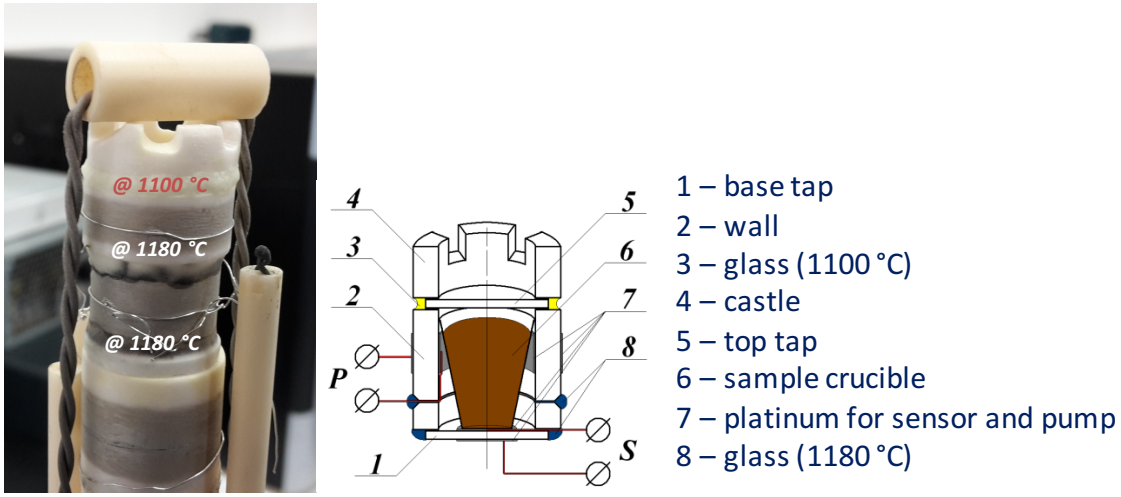

Fig. 3.9 – a) picture of the CT chamber; b) schematic details of the CT chamber.

Variations in oxygen content were measured with respect to a reference point of atmospheric oxygen pressure. The potentiostatic mode has the benefit that the unavoidable leakage current (I_{leak}) is given by the value to which the current decays after a

potentiostatic step [6]. The change in sample oxygen-nonstoichiometry ($\Delta\delta$) is given by the integration of the current (I) over time (t), through the yttria-stabilized zirconia (YSZ) solid electrolyte electrochemical cell (Fig. 3.10) [6]:

$$\Delta\delta = \frac{M}{m_{\text{sample}}} \int_{t=0}^{t=\infty} \frac{I(t) - I_{\text{leak}}}{2\text{F}} \, \text{d}t \tag{3.25}$$

where M is the molar mass, m_{sample}, the mass of the sample, and F, the Faraday constant. This includes correction of each powder titration measurement with an additional calibration (background) measurement of the empty setup if one attempts precise quantification of the amount of oxygen released. Measurements were performed using the experimental setup from Fig. 3.11.

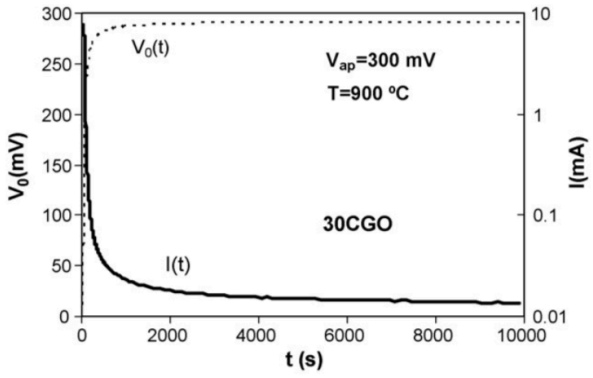

Fig. 3.10 – Time dependence of current (thick line) and voltage (dashed line) in the coulometric titration cell between two equilibrium states, after applying a generic voltage of 300 mV by the dc source [7].

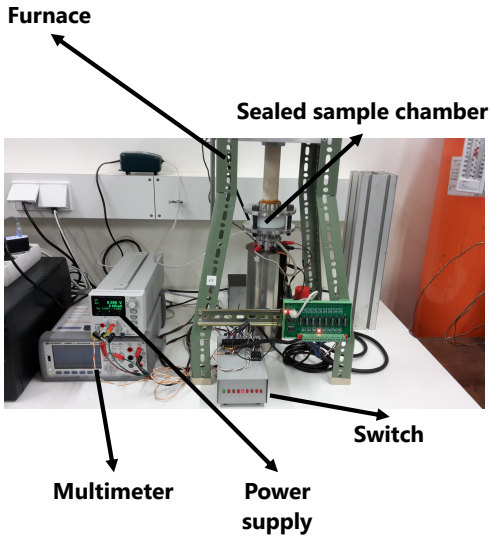

Fig. 3.11 – Experimental setup for the coulombic titration measurements.

The composition of the primary glass seal (softening temperature: 1180 °C), used in the sample container of Fig. 3.9a is 18 mol% MgO, 27 mol% BaO and 55 mol% SiO_2, followng previous work on glass seals for fuel cell applications, assuring good bonding between the cell elements as well as good properties of adherence and tightness [8]. The raw materials employed for melting the glasses were: silica sand, barium carbonate (Alfa Aesar), magnesium oxide (Panreac). The mixtures were melted at 1550 °C for 1 h and quenched in RT water. The obtained glass frit was milled in a mortar to obtain a fine powder, which was then mixed with a vehicle organic mixture (ethyl cellulose + terpineol, 2:1 wt%) to obtain the glass paste to seal the YSZ components. Additionally, for the upper part of the container, an addition of 15 wt% of Bi_2O_3 was used to achieve a lower softening temperature. Optimisation of the softening temperature of both glasses is listed in Table 3.1.

Table 3.1 – Optimisation of the high-temperature sealing glass softening temperature.

@ 1180 °C			**@ 1100 °C**		
Step no.	**T (°C)**	**Time (min)**	**Step no.**	**T(°C)**	**Time (min)**
1	1180	25	1	1115	25
-	-	-	2	1110	25
-	-	-	3	1105	25
-	-	-	4	1100	25

3.7. Thermodynamic calculations

Thermodynamic calculations for barium cerate stability against carbon dioxide and water vapour were performed using the following procedure to predict the spontaneity of the reactions:

$$\Delta G_{\mathrm{R}} = \Delta H_{\mathrm{R}} - T\Delta S_{\mathrm{R}} \tag{3.26}$$

$$\Delta H_{\mathrm{R}} = \Delta H_{\mathrm{R}}^{0} + \int_{298}^{T} \left[\sum_{\mathrm{p}} n_{\mathrm{p}} Cp_{\mathrm{p}} - \sum_{\mathrm{r}} n_{\mathrm{r}} Cp_{\mathrm{r}}\right] \mathrm{d}T \tag{3.27}$$

$$\Delta S_{\mathrm{R}} = \Delta S_{\mathrm{R}}^{0} + \int_{298}^{T} \left[\sum_{\mathrm{p}} \frac{n_{\mathrm{p}} Cp_{\mathrm{p}}}{T} - \sum_{\mathrm{r}} \frac{n_{\mathrm{r}} Cp_{\mathrm{r}}}{T}\right] \mathrm{d}T \tag{3.28}$$

Where C_{p} is the heat capacity, n_{p} and n_{r} are the stoichiometric coefficients of products and reactants, respectively, and $\Delta H_{\mathrm{R}}^{0}$ and $\Delta S_{\mathrm{R}}^{0}$ are the enthalpy and entropy change of chemical reactions, at standard conditions (298 K, 1 atm). In these equations, the temperature dependence of heat capacity (C_{p}) was described as a series of power of laws terms:

$$Cp = \mathrm{a} + \mathrm{b}T + \mathrm{c}T^{2} + \mathrm{d}T^{-2} \ldots \tag{3.29}$$

Where a, b, c and d are constants. The standard enthalpy ($\Delta H_{\mathrm{R}}^{0}$) and standard entropy ($\Delta S_{\mathrm{R}}^{0}$) of chemical reactions in reference state (298 K, 1 atm) were calculated from:

$$\Delta H_{\mathrm{R}}^{0} = \sum_{\mathrm{p}} n_{\mathrm{p}} \Delta H_{\mathrm{f,p}}^{0} - \sum_{\mathrm{r}} n_{\mathrm{r}} \Delta H_{\mathrm{f,r}}^{0} \tag{3.30}$$

$$\Delta S_{\mathrm{R}}^{0} = \sum_{\mathrm{p}} n_{\mathrm{p}} S_{\mathrm{f,p}}^{0} - \sum_{\mathrm{r}} n_{\mathrm{r}} S_{\mathrm{f,r}}^{0} \tag{3.31}$$

3.8. Defect chemistry model

Generally speaking, total electrical conductivity of proton conductors may be a sum of proton, oxygen ion, electron and hole contributions. Therefore, an electroneutrality law accounting all charged species involved in this condition can be expressed as follows:

$$[\mathrm{OH}_{\mathrm{O}}^{\bullet}] + 2[\mathrm{V}_{\mathrm{O}}^{\bullet\bullet}] + \mathrm{h}^{\bullet} = [\mathrm{Y}_{\mathrm{Ce}}'] + [\mathrm{Ce}_{\mathrm{Ce}}'] + \mathrm{n}' \tag{3.32}$$

Assuming no significant n- or p-type conductivity, extrinsic charge carriers of electronic nature can be excluded in the electroneutrality equation:

$$[\mathrm{OH_O^{\bullet}}] + 2[\mathrm{V_O^{\bullet\bullet}}] - [\mathrm{Y'_{Ce}}] - [\mathrm{Ce'_{Ce}}] = 0 \quad (3.33)$$

The mass action constants for water incorporation (eqn (2.16)) and for cerium reduction (eqn (2.22)) can be rearranged, respectively, as following:

$$[\mathrm{OH_O^{\bullet}}] \approx K_{\mathrm{w}}^{1/2} p_{\mathrm{H2O}}^{1/2} [\mathrm{V_O^{\bullet\bullet}}]^{1/2} \approx \mathrm{B}[\mathrm{V_O^{\bullet\bullet}}]^{1/2}, \text{ with } \mathrm{B} = K_{\mathrm{w}}^{1/2} p_{\mathrm{H2O}}^{1/2} \quad (3.34)$$

$$[\mathrm{Ce'_{Ce}}] \approx K_{\mathrm{R}}^{1/2} p_{\mathrm{O2}}^{-1/4} [\mathrm{V_O^{\bullet\bullet}}]^{-1/2} \approx \mathrm{A}[\mathrm{V_O^{\bullet\bullet}}]^{-1/2}, \text{ with } \mathrm{A} = K_{\mathrm{R}}^{1/2} p_{\mathrm{O2}}^{-1/4} \quad (3.35)$$

Combination of eqn (3.33) – (3.35) yields,

$$2[\mathrm{V_O^{\bullet\bullet}}] + \mathrm{B}[\mathrm{V_O^{\bullet\bullet}}]^{\frac{1}{2}} - \mathrm{A}[\mathrm{V_O^{\bullet\bullet}}]^{-\frac{1}{2}} - [\mathrm{Y'_{Ce}}] = 0 \quad (3.36)$$

Further simplification yields,

$$2[\mathrm{V_O^{\bullet\bullet}}]^{\frac{3}{2}} + \mathrm{B}[\mathrm{V_O^{\bullet\bullet}}] - \mathrm{A} - [\mathrm{Y'_{Ce}}][\mathrm{V_O^{\bullet\bullet}}]^{\frac{1}{2}} = 0 \quad (3.37)$$

Considering $[V_O^{\bullet\bullet}]^{\frac{1}{2}} = x^2$, a 3rd order polynomial is given

$$\mathrm{f(x)} = 2\mathrm{x}^3 + \mathrm{Bx}^2 - [\mathrm{Y'_{Ce}}]\mathrm{x} - \mathrm{A} = 0 \quad (3.38)$$

This equation was solved numerically:

$$x_{n+1} = x_n - \frac{\mathrm{f}(x_n)}{\mathrm{f}\prime(x_n)} \quad (3.39)$$

and the derivative is given by:

$$\mathrm{f}'(x) = 6x^2 + 2\mathrm{B}x - [\mathrm{Y'_{Ce}}] = 0 \quad (3.40)$$

References

1 R. Jenkins and R. L. Snyder, in *Introduction to X-ray Powder Diffractometry*, eds. R. Jenkins and R. L. Snyder, John Wiley & Sons, Ltd, 1996, pp. 1–22.

2 D. B. Williams and C. B. Carter, *Transmission Electron Microscopy: A Textbook for Materials Science*, Springer, 2009.

3 J. D. Livingston, *Electronic Properties of Engineering Materials*, Wiley, 1998.

4 B. A. Boukamp and A. Rolle, *Solid State Ionics*, 2017, **302**, 12–18.

5 B. A. Boukamp and A. Rolle, *Solid State Ionics*, 2018, **314**, 103–111.

6 D. Perez-Coll, P. Nunez and J. R. Frade, in *Advances in Ceramics - Synthesis and Characterization, Processing and Specific Applications*, ed. C. Sikalidis, InTech, Rijeka, 2011.

7 D. Pérez-Coll, D. Marrero-López, J. C. Ruiz-Morales, P. Núñez, J. C. C. Abrantes and J. R. Frade, *J. Power Sources*, 2007, **173**, 291–297.

8 M. J. Pascual, A. Guillet and A. Durán, *J. Power Sources*, 2007, **169**, 40–46.

4. Proton conductivity in yttrium-doped barium cerate in nominally dry reducing conditions for application in chemical synthesis

Abstract

Electrochemical membrane reactors using proton-conducting ceramics are promising and efficient technologies for the production of valuable chemical products by the promotion of hydrogenation/dehydrogenation reactions. Due to a very high equilibrium constant for hydration, yttrium-doped barium cerate, $BaCe_{0.9}Y_{0.1}O_{3-\delta}$ (BCY10) presents one of the highest proton conductivities at low temperatures of the known proton-conducting ceramic oxides (*e.g.* ~ 10^{-3} S cm^{-1} at 400 °C under humidified atmospheres, p_{H2O} ~ 10^{-2} atm). Nonetheless, BCY10 is commonly discarded for such applications due to its poor chemical stability towards hydroxide or carbonate formation. Moreover, the use of humidified atmospheres may not be feasible for many chemical syntheses, due to undesired side reactions. The current work, therefore, combines impedance spectroscopy, thermogravimetric analysis, coulometric titration and defect chemistry modelling to assess the limits for pure protonic conductivity in BCY10 in nominally dry atmospheres (p_{H2O} ~10^{-4} – 10^{-5} atm, at low temperatures < 600 °C); conditions where its stability and applicability to industrially relevant chemical synthesis reactions may be maintained, whilst still being hydrated. This work, thereby, unlocks a new application area for proton-conducting ceramics to a wide range of hydrogenation/de-hydrogenation reactions in the nominal absence of water.

4.1. Introduction

In addition to well-known potential applications, such as fuel cells, electrolysers, sensors and separation membranes, ceramic proton conductors have also been suggested for use in chemical synthesis, where hydrogenation or dehydrogenation reactions can be tailored electrochemically towards a desired chemical product [1]. Of the potential ceramic oxide proton conductors for this type of application, yttrium-doped barium cerate, $BaCe_{1-x}Y_xO_{3-\delta}$, (BCY) stands out as being one of the most interesting materials to use at lower temperatures, due to its superior proton conduction under these conditions (*e.g.* ~ 10^{-3} S cm^{-1} at 400 °C under humidified atmospheres, p_{H2O} ~ 10^{-2} atm) [2]. The material consists of a ceramic oxide with ABO_3 perovskite structure that contains large A^{2+} site cations, Ba^{2+}, and smaller B^{4+} site cations, Ce^{4+}, with partial substitution of the B-site by lower-oxidation-state cations, Y^{3+}, that are charge compensated by the formation of oxygen vacancies ($V_O^{\bullet\bullet}$), in *Kröger-Vink* notation [2]:

$$\mathrm{BaO} + (1-\mathrm{y})\mathrm{CeO_2} + \left(\frac{\mathrm{y}}{2}\right)\mathrm{Y_2O_3} \Longrightarrow \mathrm{Ba_{Ba}^x} + (1-\mathrm{y})\mathrm{Ce_{Ce}^x} + (\mathrm{y})\,\mathrm{Y_{Ce}'} + \\ + \left(3-\frac{\mathrm{y}}{2}\right)\mathrm{O_O^x} + \left(\frac{\mathrm{y}}{2}\right)\mathrm{V_O^{\bullet\bullet}} \qquad (4.1)$$

Proton conductivity arises due to the creation of protonic defects ($OH_O^{\bullet}$), upon filling of these oxygen vacancies in the presence of water vapor, as follows [3–6]:

$$\mathrm{H_2O} + \mathrm{V_O^{\bullet\bullet}} + \mathrm{O_O^x} \Leftrightarrow 2\mathrm{OH_O^{\bullet}} \qquad (4.2)$$

where the equilibrium constant of eqn (2), K_w, is approximately given by:

$$K_w \approx \frac{[\mathrm{OH_O^{\bullet}}]^2}{p_{\mathrm{H2O}}[\mathrm{V_O^{\bullet\bullet}}][\mathrm{O_O^x}]} \qquad (4.3)$$

Due to this requirement of humidification to induce proton conduction, the majority of previous conductivity studies on this material have concentrated, to date, on measurements performed in wetted atmospheres that are typically produced by bubbling incoming gases through liquid water at room temperature, yielding water vapor partial pressures, p_{H2O}, in the order of ~ 3 x 10^{-2} atm [7–11]. On the contrary, very little information is currently available on the limits of proton conductivity in this material at lower humidity levels, even though the very high equilibrium constant for hydration in doped barium cerate materials predicts

that they could be fully hydrated under much lower values of p_{H2O} [2]. This is an important point, as barium cerate-based materials, such as BCY, have typically been discarded for real world applications, due to their very poor chemical stability towards carbonate or hydroxide formation at low temperatures [12]. For example, Li *et al.* [13] studied the applicability of this material type for a micro-solid oxide fuel cell (μ-SOFC), based on a $BaCe_{0.9}Y_{0.1}O_{3-\delta}$ (BCY10) thin film electrolyte (300 nm) in the temperature range of 300 – 400 °C. The performance of the μ-SOFC was evaluated using air as oxidant gas and hydrogen as fuel gas, where neither of these inlet gases had been previously humidified. Despite this factor, the results showed continuous decrease in performance upon operation due to rapid decomposition of the BCY10 electrolyte into $BaCO_3$, $Ba(OH)_2$, and CeO_2, from reactions with CO_2 and H_2O, respectively, even at the low p_{CO2} level present in air (~ 4 x 10^{-4} atm) and under the water vapor partial pressure generated by the fuel cell reaction.

In contrast to this result, some successful applications of BCY can be found in the literature when this material had alternatively been applied for the goal of chemical production, for example, in ammonia synthesis [14–16], or the conversion of propane to propylene [17]. In both these applications, no notable chemical instability of BCY were reported; results that are likely to be due to the effective absence of carbon dioxide or significant moisture in these operations.

In this respect, the thermodynamics for the equilibrium of barium cerate with its decomposition products $Ba(OH)_2$ + CeO_2 in the presence of water vapor, Fig. 4.1a, suggests that for typical humidity levels of p_{H2O} ~ 3 x 10^{-2} atm no degradation should be theoretically predicted for temperatures above around 500 °C. Conversely, the corresponding thermodynamics for barium carbonate formation from reaction with CO_2 highlight much stricter requirements, where even very low partial pressures of CO_2 (*e.g.*, p_{CO2} > ~ 10^{-8} atm at 400 °C) could potentially cause barium cerate degradation, as depicted in Fig. 4.1a.

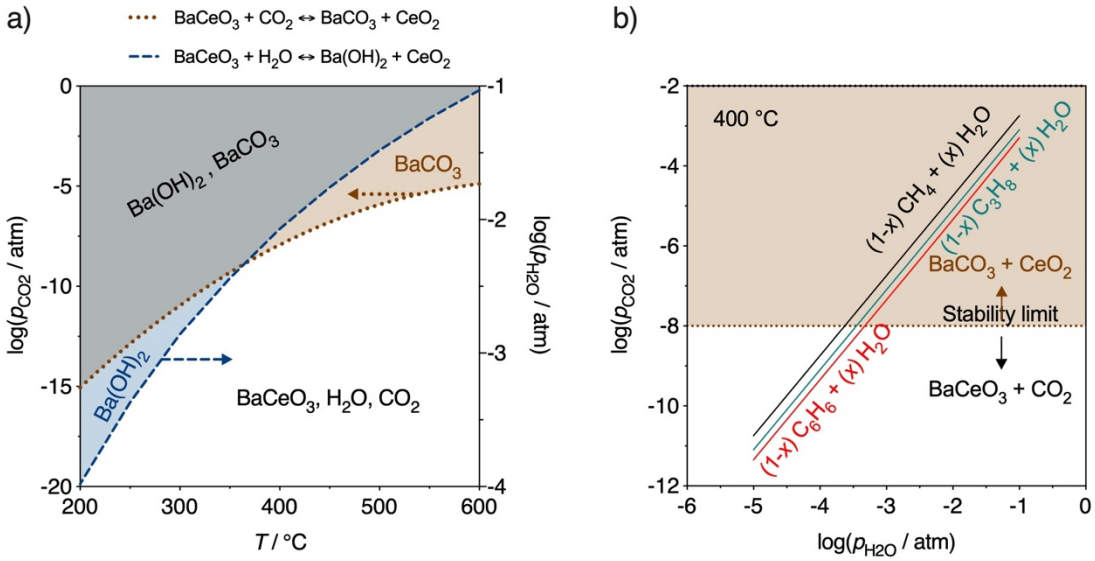

Fig. 4.1 – a) stability diagram calculated from the thermodynamic equilibrium for the formation of barium carbonate in terms of carbon dioxide partial pressure (p_{CO2}) and for the formation of barium hydroxide in terms of water partial pressure (p_{H2O}) and temperature; b) thermodynamic equilibrium for the formation of carbon dioxide from a hydrocarbon-based mixture and water at 400 °C. Calculations performed using *FactSage* software [18].

Hence, for prospective application of barium cerate-based materials in hydrogenation/dehydrogenation reactions that involve carbonaceous atmospheres, it is clear that it will be necessary to avoid potential equilibrium reactions with oxygen or water vapor that could otherwise undesirably lead to p_{CO2} levels that exceed these stability limits. At this juncture, it is also important to note that this requirement may imply working under conditions of extremely low humidity and low oxygen contents when using carbonaceous atmospheres. To try to put this into context, Fig. 4.1b assesses the maximum water vapor partial pressure that could be tolerated in different chemicals, as an example, to avoid generating levels of p_{CO2} that would lead to $BaCeO_3$ decomposition [18]. From Fig. 4.1b, one can predict that these values would range from ~ 10^{-3} < p_{H2O} < ~ 10^{-4} atm at 400 °C, depending on the example chemical reaction. In other words, much lower p_{H2O} values than the aforementioned limits typically required to prevent barium cerate degradation in non-carbonaceous atmospheres.

Another point to consider is that, the proton conducting ceramic must continue to offer sufficient proton conductivity under these conditions of very low humidity and temperature. In this respect, the superior conductivity of yttrium-doped barium cerate over the majority

of proton-conducting ceramics, coupled with its very high equilibrium constant for hydration, which can permit hydration at very low p_{H2O} values, are properties that may confer this material critical advantage [2]. Namely, the potential to use doped barium cerate-based materials in conditions of very low humidity at low temperature may unlock new application areas for proton-conducting ceramics to a wide range of hydrogenation/dehydrogenation reactions in the nominal absence of water ($p_{H2O} \leq 10^{-4}$ atm).

The current work, therefore, aims to assess the limits for pure protonic conductivity in BCY10 in nominally dry atmospheres (p_{H2O} ~10^{-4} – 10^{-5} atm, at T < 600 °C); conditions where its stability and applicability to industrially relevant chemical synthesis reactions may be maintained [1]. The determination of the partial conductivities in proton-conducting ceramics is most often conducted through the electromotive force (emf) method, where a membrane in a dual-atmosphere chamber is exposed to controlled hydrogen and water-vapor partial pressure gradients [19]. Nonetheless, this requirement complicates the direct determination of the partial conductivities at very low humidities as required by the current work.

Thus, in this paper we adopt an alternative methodology [20] for the determination of partial protonic, oxide-ion and electronic conductivities, by a defect chemistry process, that involves multiple measurements of total conductivity as a function of oxygen partial pressure. In addition, we conduct coulombic titration measurements and thermogravimetry aiming to provide experimental data for the calculation of the concentration of the electronic and protonic charge carriers, respectively. Therefore, the current work reports the first study of the electrochemical transport properties of $BaCe_{0.9}Y_{0.1}O_{3-\delta}$ (BCY10) in nominally dry reducing conditions, for p_{H2O} ~ 10^{-4} – 10^{-5} atm, in a relevant temperature range for potential protonic conduction (350 – 600 °C) to highlight its potential applicability to chemical synthesis.

4.2. Experimental

4.2.1. Electrochemical impedance spectroscopy measurements

Electrical measurements were performed by AC Electrochemical Impedance Spectroscopy (EIS) on BCY10 disk compacts obtained from uniaxial pressed commercial $BaCe_{0.9}Y_{0.1}O_{3-\delta}$ powder (TYK, Japan), sintered at 1450 °C for 6 h, with porous Pt electrodes deposited on both sides. Measurements were carried out using an Electrochemie-Autolab PGSTAT302N frequency response analyser in the frequency range 0.01 Hz – 1 MHz with signal amplitude of 50 mV. Measurements in single dry atmospheres (H_2, 10 % H_2-N_2 and N_2) were performed at 50 °C intervals in the direction of decreasing temperature, in the temperature range of 100 – 500 °C. In addition, analysis of the electrical behaviour as a function of hydrogen partial pressure (p_{H2}) were performed in the temperature range of 350 – 600 °C. Impedance spectra upon atmospheric changes were recorded with 1 h of stabilization time followed by a repeated measurement after 1 h to assess stability between each measurement. The impedance spectra were fitted using the software *ZView*© (Scribner Associates). Nominally dry atmospheres were controlled using a Varian gas moisture filter with a maximum total flowrate of 50 mL min^{-1} supplied by Bronkhorst Thermal Mass flow Controllers (EL Flow). Oxygen partial pressure values were collected from a YSZ p_{O2} sensor. Relative humidity data was collected using a JUMO humidity meter.

4.2.2. Coulometric titration measurements

Data on oxygen stoichiometry for the perovskite composition $BaCe_{0.9}Y_{0.1}O_{3-\delta}$ were obtained by the coulometric titration technique as a function of oxygen partial pressure (p_{O2}) in potentiostatic mode, as described elsewhere [21–23]. Variations in oxygen content were measured with respect to a reference point of atmospheric oxygen pressure ($p_{O2} \approx 0.21$ atm). The sample is positioned inside a non-permeable electrochemical cell composed by YSZ components acting as an electrochemical pump and a p_{O2} sensor. The oxygen partial pressure inside the cell was decreased by the application of different steps of voltage by an external *d.c.* source and the oxygen stoichiometry change after a generic step is determined by means of the integration of the current trough the pump between the starting and final steady state situations [21–23].

4.2.3. Thermogravimetric analysis

TGA measurements were performed by a NETZSCH STA 449 F3 thermal analyser, using dried Ar as a carrier gas and Alumina as the reference sample. Measurements were performed in nominally dry N_2 (p_{H2O} = ~ 10^{-5} atm) in steps of 50 °C on increasing and decreasing temperature in the range RT to 800 °C. Analysis of weight change was done at each step on decreasing temperature.

4.3. Results and discussion

The overall conducting behaviour of $BaCe_{0.9}Y_{0.1}O_{3-\delta}$ in nominally dry atmospheres was analysed by impedance spectroscopy between 100 – 500 °C in H_2, 10 % H_2-N_2 and N_2. It can be noted that the total conductivity follows the sequence $\sigma(H_2) > \sigma(10\ \%\ H_2\text{-}N_2) > \sigma(N_2)$ (Fig. 4.2a), albeit without considerable differences between each case. The current results of total conductivity measured in nominally dry H_2 are observed to be comparable to those of literature data for this material measured in humidified H_2 (Table 4.1). This similarity suggests elevated levels of hydration in all cases, as will be clarified in the later text.

Table 4.1 – Total conductivity of BCY10 in nominally dry H_2 obtained at 400 °C. Some values extracted from the literature for other studies in wet H_2 are also shown for comparison.

Conductivity (S cm^{-1})	**p_{H2O} (atm)**	**Reference**
3.59x10^{-3}	~10^{-4} (dry H_2)	This work
2.67x10^{-3}	~10^{-2} (wet H_2)	Coors *et al.*[7]
1.85x10^{-3}		Bonanos *et al.*[10]
1.96x10^{-3}		Ma *et al.*[8]
2.60x10^{-3}		Kreuer *et al.*[9]
8.48x10^{-4}		Slade *et al.*[11]

To investigate the impact of electronic carriers, the conductivity as a function of hydrogen partial pressure (p_{H2}) was also analysed in nominally dry conditions by impedance spectroscopy in the temperature range 350 – 600 °C (Fig. 4.2b). The results show a very low conductivity dependence on the hydrogen partial pressure, suggesting the contribution from electronic species to be minor.

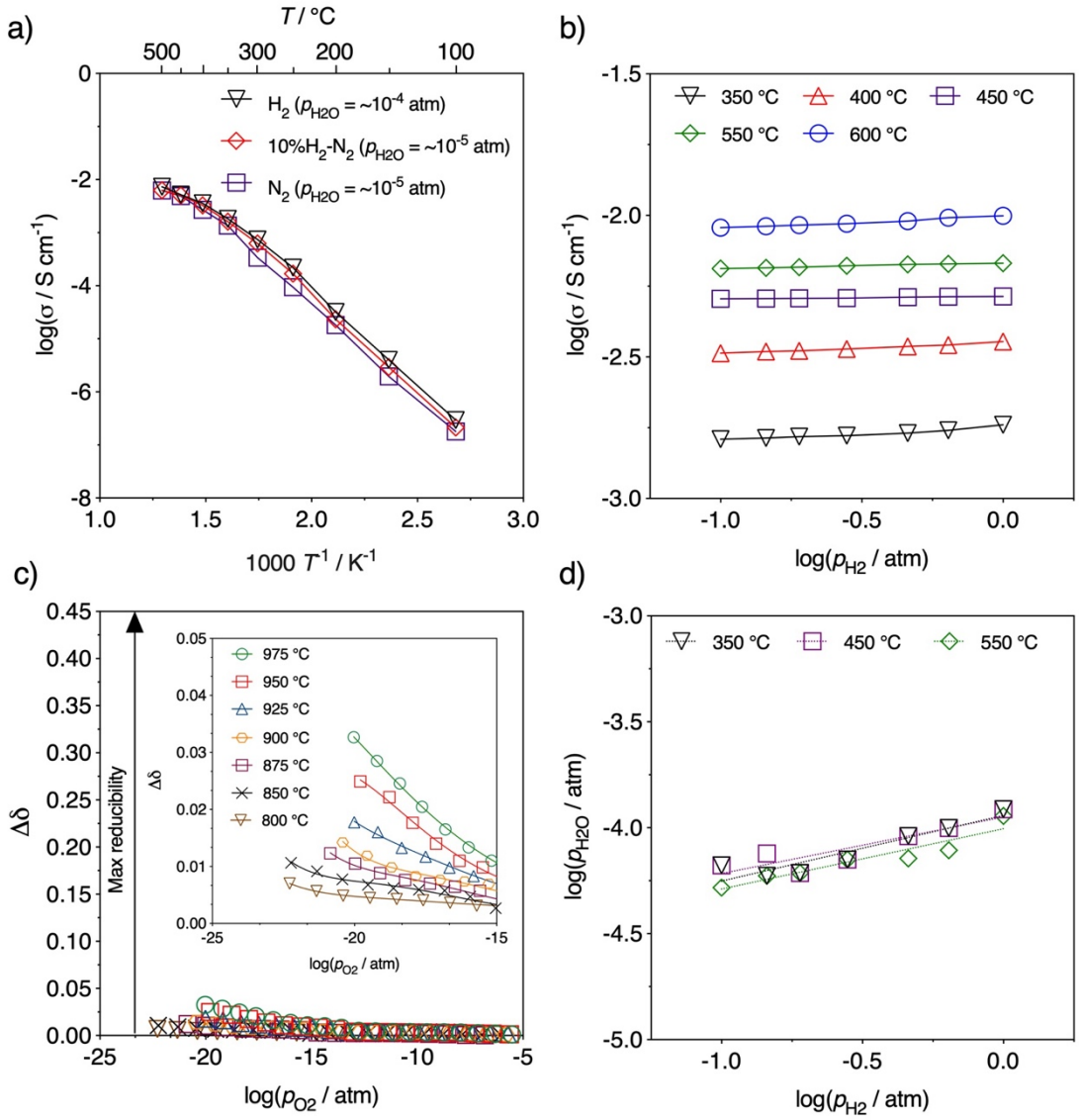

Fig. 4.2 – a) temperature-dependence of total conductivity of BCY10 obtained in the temperature range from 100 to 500 °C in nominally dry conditions for H_2, 10 % H_2-N_2 and N_2; b) BCY10 total conductivity (σ_T) vs. hydrogen partial pressure (p_{H2}) obtained in the temperature range from 350 to 600 °C in nominally dry conditions; c) dependence of oxygen non-stoichiometry on oxygen partial pressure determined from coulometric titration results (the inset shows a magnification for the observed differences in the oxygen non-stoichiometry between each temperature); d) dependence of p_{H2O} on p_{H2}.

To further elucidate the potential role of electronic contribution in $BaCe_{0.9}Y_{0.1}O_{3-\delta}$, coulometric titration measurements were performed at elevated temperatures. Fig. 4.2c depicts the effect of temperature and oxygen partial pressure on the oxygen non-stoichiometry change ($\Delta\delta$). A possible change in the oxygen non-stoichiometry in BCY10 at

high temperatures could be related with the reduction of Ce^{4+} to Ce^{3+} in reducing conditions according to:

$$2\mathrm{Ce}_{\mathrm{Ce}}^{\mathrm{x}} + \mathrm{O}_{\mathrm{O}}^{\mathrm{x}} \Leftrightarrow \mathrm{V}_{\mathrm{O}}^{\bullet\bullet} + 2\mathrm{Ce}_{\mathrm{Ce}}' + \frac{1}{2}\mathrm{O}_{2(\mathrm{g})} \quad (4.4)$$

with an equilibrium constant for reduction reaction described by:

$$K_{\mathrm{R}} \approx \frac{[\mathrm{V}_{\mathrm{O}}^{\bullet\bullet}][\mathrm{Ce}_{\mathrm{Ce}}']^2 p_{\mathrm{O2}}^{1/2}}{[\mathrm{O}_{\mathrm{O}}^{\mathrm{x}}][\mathrm{Ce}_{\mathrm{Ce}}^{\mathrm{x}}]^2} \quad (4.5)$$

The subsequent existence of mixed valence ascribed to cerium reduction would be expected to introduce small-polaron electronic conduction (*i.e.* a localized, mobile electron, $\mathrm{Ce}_{\mathrm{Ce}}'$), in addition to the oxide-ion and protonic conduction. In this respect, the results of coulometric titration show considerable variations of oxygen non-stoichiometry with oxygen partial pressure at higher temperature, while the importance of this feature rapidly diminishes as temperature decreases (Fig. 4.2c). This behaviour corresponds to the lower reducibility of cerium cations in the perovskite $BaCe_{0.9}Y_{0.1}O_{3-\delta}$ with decreasing temperature, as also reported for other doped-barium cerates, where very extreme reducing conditions and very high temperatures are required to produce appreciable alteration of the oxygen-vacancy and electronic concentrations [24,25]. Note these results contrast with those for fluorite-ceria-based materials that, conversely, show much high reducibility under reducing conditions [21,22].

From the results of oxygen-nonstoichiometry change, the corresponding equilibrium constant, K_R (Fig. 4.3) was extracted for the high temperature range (800 – 975 °C) where significant reduction occurs, following a methodology developed earlier [21,22]. A unique equation was then obtained for the temperature dependence of K_R:

$$K_{\mathrm{R}}(\mathrm{T}) = 2.54 \cdot 10^{21} \exp(-9.68 \cdot 10^4/\mathrm{T}) \ (\mathrm{atm}^{1/2}) \quad (4.6)$$

yielding a reduction enthalpy, ΔH_R = 804.99 kJ mol^{-1}. This value is significantly higher than those previously obtained for ceria-based materials [21,22,26–28], and is the factor responsible for the low reducibility of $BaCe_{0.9}Y_{0.1}O_{3-\delta}$ in such conditions of intermediate to low temperatures.

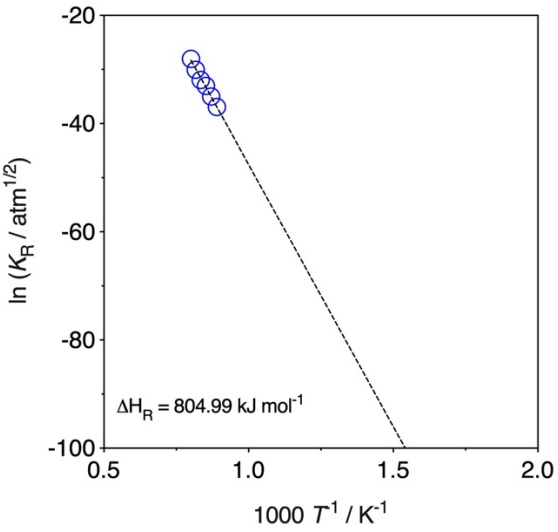

Fig. 4.3 – Values of K_R obtained from coulombic titration measurements as a function of temperature.

The effects of the partial components of conductivity on the total electrical behaviour were also analysed under different conditions of hydrogen partial pressure and temperature by means of the expected concentrations of the various defects according to the defect chemistry, provided by eqn (4.1) to (4.5), and the corresponding electroneutrality condition according to:

$$2[\mathrm{V_O^{\bullet\bullet}}] + [\mathrm{OH_O^{\bullet}}] \approx [\mathrm{Y'_{Ce}}] + [\mathrm{Ce'_{Ce}}] \tag{4.7}$$

Assuming that $[\mathrm{O_O^x}]$ and $[\mathrm{Ce_{Ce}^x}]$ are not considerably affected by p_{O2} and p_{H2O} at lower temperatures, eqn (4.3) and (4.5) can be rearranged to express the concentration of the protonic and electronic defects as a function of oxygen vacancy concentration, according to:

$$[\mathrm{OH_O^{\bullet}}] \approx \mathrm{A}[\mathrm{V_O^{\bullet\bullet}}]^{1/2}, \text{ with } \mathrm{A} = K'^{1/2}_{\mathrm{w}} p_{\mathrm{H2O}}^{1/2} \text{ and } K'_{\mathrm{w}} \approx K_{\mathrm{w}}[\mathrm{O_O^x}] \tag{4.8}$$

$$[\mathrm{Ce'_{Ce}}] \approx \mathrm{B}[\mathrm{V_O^{\bullet\bullet}}]^{-1/2}, \text{ with } \mathrm{B} = K'^{1/2}_{\mathrm{R}} \mathrm{p}_{\mathrm{O2}}^{-1/4} \text{ and } K'_{\mathrm{R}} = K_{\mathrm{R}}[\mathrm{O_O^x}][\mathrm{Ce_{Ce}^x}]^2 \tag{4.9}$$

Recombining eqn (7) to (9) we obtain the following polynomial equation

$$2x^3 + \mathrm{A}x^2 - [\mathrm{Y'_{Ce}}]x - \mathrm{B} = 0 \tag{4.10}$$

where $x = [\mathrm{V_O^{\bullet\bullet}}]^{1/2}$. The oxygen vacancy concentration can be determined by the numerical solution of eqn (4.10) for given pairs of p_{O2} and p_{H2O}, which allows the determination of

electronic- and protonic-defect concentrations by means of eqn (4.8) and (4.9). For this purpose, we used the equilibrium constant for hydration reaction at different temperatures determined by means of the standard reaction entropy (ΔS = -167.9 J (mol K)$^{-1}$) and enthalpy (ΔH = -163.3 KJ mol^{-1}) reported by *Kreuer* for $BaCe_{0.9}Y_{0.1}O_{3-\delta}$ [2] and the values of reduction-reaction constant obtained from the experimental results of coulometric titration (eqn (4.6)).

The defect-concentration profiles, represented in Fig. 4.4a, show a significant dominance of the ionic charge carriers over the electronic charge carriers in the studied temperature range. This is in good agreement with the low equilibrium constant for reduction (eqn (4.5) to (4.6)), leading to a very low electronic concentration under the studied conditions. Moreover, it is observed that the low temperature range, 350 – 400 °C, is dominated by protons, while the higher temperature range, 550 – 600 °C, is dominated by oxygen vacancies. The dominance of protonic defects at low temperatures is related with the very high equilibrium constant for water incorporation in $BaCe_{0.9}Y_{0.1}O_{3-\delta}$, (eqn (4.3)), that permits significant hydration even for p_{H2O} values as low as ~ 10^{-5} atm [29]. In contrast, the dominance of oxygen vacancies in the higher temperature region (550 – 600 °C) is related with the dehydration of the sample. Convergence of concentration of both protons and oxygen vacancies occurs at intermediate temperature, *i.e.* ~ 525 °C. Interestingly, the concentration of protonic charge carriers is always dominant at low temperatures, even for less reducing conditions (Fig. 4.3).

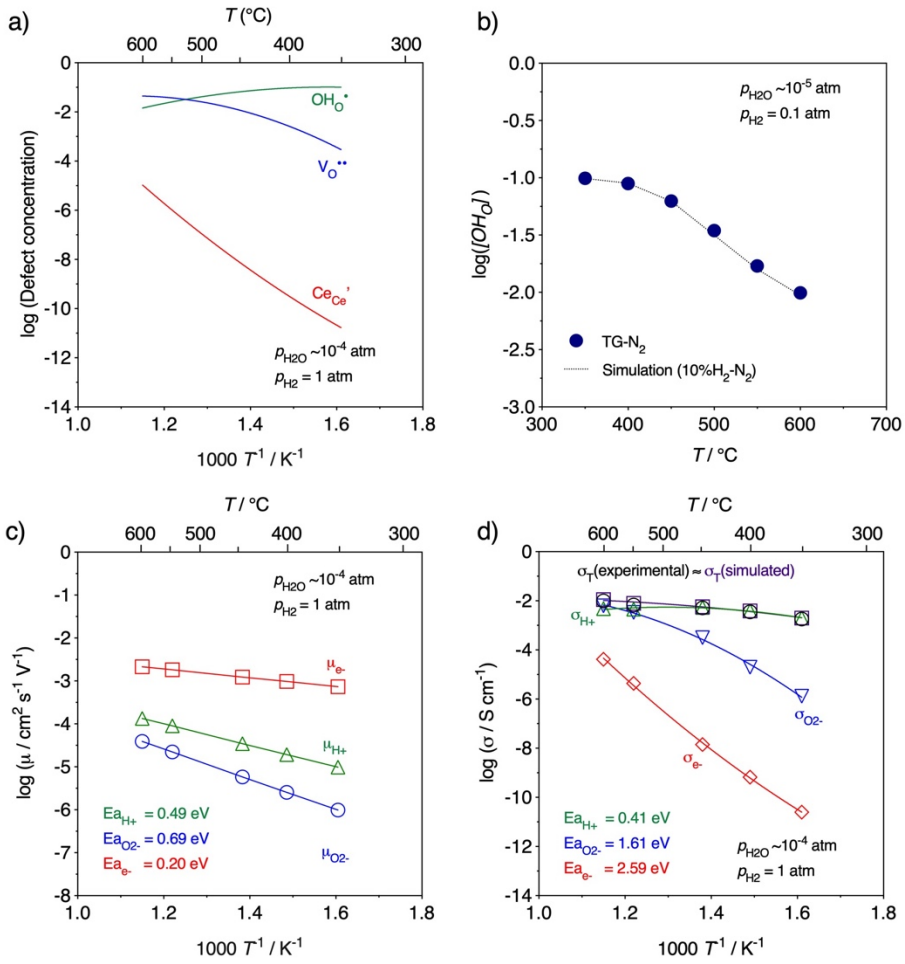

Fig. 4.4 – Temperature dependence of: a) defect concentration profiles; b) concentration protonic defects obtained from TG and from the simulation; c) mobility and activation energy associated to different charge carriers employed for fitting total conductivity results; d) total (experimental and calculated) and partial conductivities. Data obtained in the temperature range of 350-600 °C, in nominally dry conditions (p_{H2} ≈ 1 atm for a), c) and d) and p_{H2} ≈ 0.1 atm for b)).

Fig. 4.5 shows that the concentration of protonic defects effectively reaches the saturation limit at lower temperature for higher values of p_{H2}. This is followed by a practically imperceptible decrease as p_{H2} decreases, which is electrically balanced by the decrease of electronic concentration and the improvement of oxygen vacancy concentration. This behaviour is consistent with the experimental results of higher values of p_{H2O} as p_{H2} rises, shown in Fig. 4.2d, which also confirms the relevance of protonic species for p_{H2O} values as low as 10^{-5} – 10^{-4} atm. Furthermore, it explains why the total conductivity of BCY in current work remains comparable to that of previous literature studies (Table 4.2), despite analysis at much lower humidity. Fig. 4.4b compares the experimental hydration profile obtained by

thermogravimetry in nominally dry conditions and that calculated by the defect chemistry at $p_{H2O} \approx 6.64 \times 10^{-5}$ atm. using the values of ΔH and ΔS mentioned above and reported earlier [2]. The experimental profiles match those obtained by simulation, showing that hydration starts to increase on cooling below ~ 600 °C, where the higher value of hydration, in the studied temperature range, was found at ~ 350 °C.

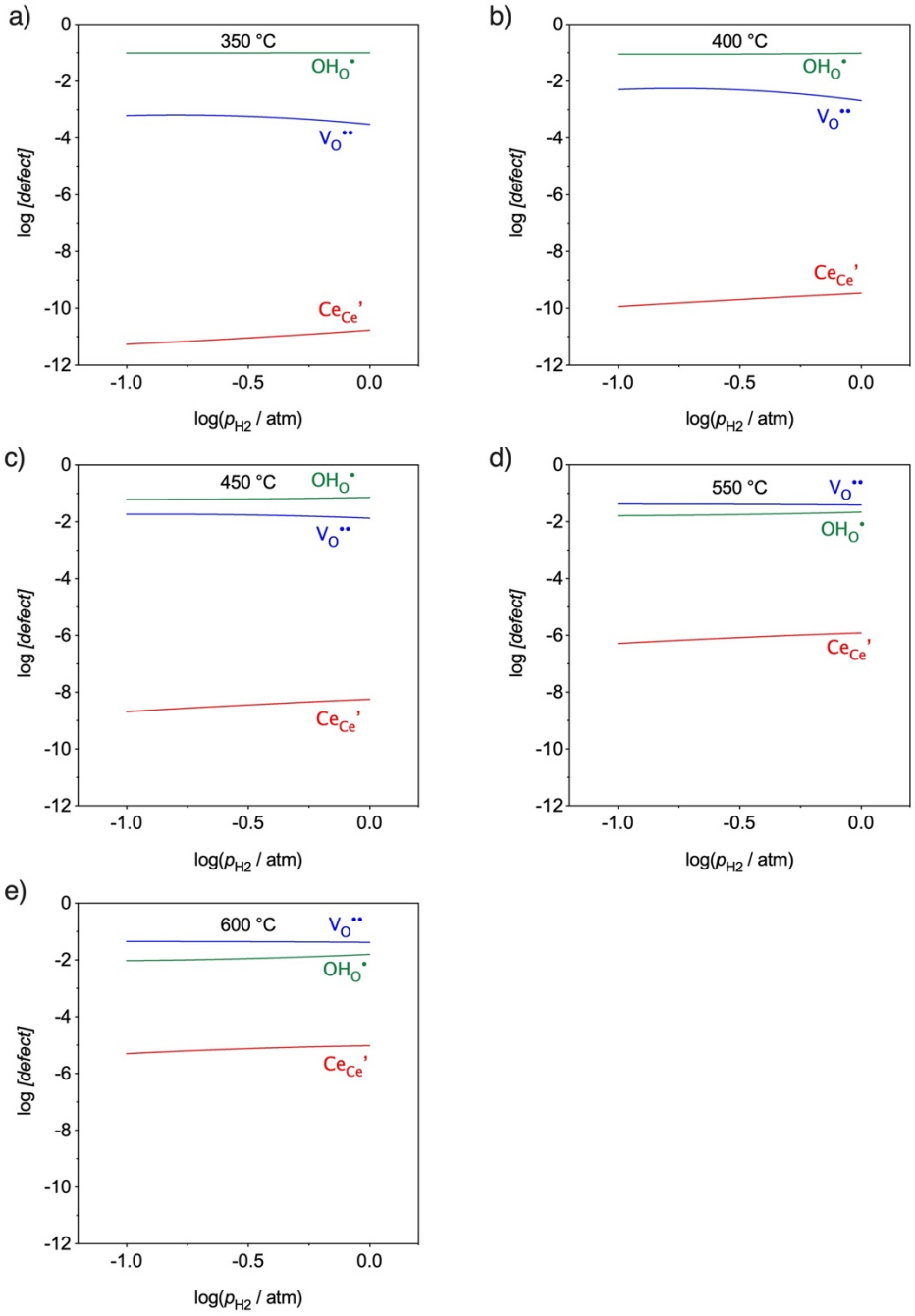

Fig. 4.5 – Defect concentration profiles as a function of hydrogen partial pressure.

The contribution of each species to the overall electrical conduction process is determined by combination of the defect concentration and the defect mobility, according to the following expression:

$$\sigma_{\mathrm{i}} = q_{\mathrm{i}}.\mu_{\mathrm{i}}.C_{\mathrm{i}} \qquad (4.11)$$

where q_{i}, C_{i} and μ_{i} represent the charge, the concentration and the mobility of the species i.

Results of total conductivity were fitted by the sum of contributions ascribed to different species by means of the defect profiles and using typical values of mobility and activation energy for the corresponding carriers, as shown in Fig. 4.4c, and are in close agreement with the available literature for barium-cerate materials [30] (Table 4.2). In the simulation procedure adopted in this work, the values for mobility were adjusted to fit the simulated total conductivity to the experimental values, following a procedure developed earlier [31]. As observed in Table 4.2, our mobility values for proton and oxide-ion diffusion agree well with those obtained by Kreuer *et al.* [30] for $BaCe_{0.9}Y_{0.1}O_{3-\delta}$. Note that the mobility values presented in Fig. 4.4c are the parameters that produce the fitting of the experimental results shown in Fig. 4.4d and Fig. 4.6, and, although being susceptible to a considerable uncertainty, they lie in the expected range of values for each species according to the literature.

Table 4.2 – Equilibrium constants for hydration and cerium reduction and mobility ratios between different charge carriers employed in the simulation of defect profiles and conductivities by means of the defect chemistry. Some values extracted from the literature for other perovskite systems are also shown for comparison.

Compound	K_w / **atm^{-1}**	K_R / **atm$^{1/2}$**	μ_{H+} / **cm^2 s^{-1} V^{-1}**	μ_{O2-} / **cm^2 s^{-1} V^{-1}**	μ_{e-} / **cm^2 s^{-1} V^{-1}**	μ_{H+}/μ_{O2-}	μ_{e-}/μ_{H+}	**Reference**
$BaCe_{0.9}Y_{0.1}O_{3-\delta}$	8024	~10^{-42}	1.94x10^{-5}	2.56x10^{-6}	9.73x10^{-4}	8	50	This work, 400 °C
$BaCe_{0.9}Y_{0.1}O_{3-\delta}$	8024	-	3.44x10^{-5}	1.98x10^{-6}	-	17	-	Kreuer *et al.* [30], 400 °C
$BaCe_{0.9}Y_{0.1}O_{3-\delta}$	10.01	~10^{-30}	1.34x10^{-4}	3,90x10^{-5}	2.14x10^{-3}	3	16	This work, 600 °C
$BaCe_{0.65}Zr_{0.2}Y_{0.15}O_{3-\delta}$	-	-	7.26x10^{-5}	1.25x10^{-5}	7.15x10^{-3}	6	98	Lim *et al.*[32], 700 °C
$SrCe_{0.95}Yb_{0.05}O_{3-\delta}$	-	-	-	-	-	20	100	Krug *et al.*[33], 600 °C
$SrCe_{0.95}Yb_{0.05}O_{3-\delta}$	-	-	5.40x10^{-6}	-	4.10x10^{-4}	-	76	Uchida *et al.*[34] , 600 °C
$BaCe_{0.9}Y_{0.1}O_{3-\delta}$	-	~10^{-17}	-	-	-	-	-	This work, 800 °C
$AB_{1-y}M_yO_{3-y/2\pm\delta}$	20	~10^{-17}	-	-	-	-	-	Bonanos *et al.*[20], 800 °C

According to the expected conductivity profiles (Fig. 4.4d and Fig. 4.6) by means of the equilibrium constants and mobilities, the protonic conductivity is orders of magnitude higher than the oxide ionic and electronic conductivities between 350 – 400 °C. Interestingly, protonic conductivity is maintained in the same order of magnitude in the whole hydrogen partial pressure range for each temperature (Fig. 4.6), even in less reducing conditions where the concentration of H_2 in the feed stream is lower, and the consequent p_{H2O} in the experimental setup is ~ 5 x 10^{-5} atm. Nonetheless, as temperature rises, proton conductivity denotes a change in the slope for $T \geq 450 - 500$ °C (Fig. 4.4d), where dehydration of the sample becomes significant and mixed conduction of both protons and oxygen ions is then relevant. This is related with the increased concentration of oxygen vacancies (Fig. 4.4a), which is in agreement with previous works from *Kreuer* [9,29] and *Coors* [7] for measurements in wet conditions.

On the other hand, under the strongly reducing conditions of the current work (p_{O2} ~ 10^{-44} – ~ 10^{-27} atm, in the range T = 350 – 600 °C), protonic charge carriers could also be formed by oxidative hydrogen uptake, according to:

$$\mathrm{H_{2(g)}} + 2\mathrm{O_O^x} \Leftrightarrow 2\mathrm{OH_O^\bullet} + 2\mathrm{Ce_{Ce}}' \qquad (4.12)$$

Nonetheless, this mechanism of proton uptake will probably have negligible influence to increase protonic conductivity as the low values of K_R (Fig. 4.3) at low temperature indicate a very low concentration of Ce_{Ce}', negating the possibility of significant proton uptake by cerium reduction. Moreover, according to eqn (4.12), the creation of a protonic species would be accompanied by the creation of an electronic carrier. Here, due to the expected higher mobility of electronic species (Table 4.2), this would be reflected in a predominance of the electronic conductivity (rather than the predominance of protonic conductivity). The low values of electronic conductivity found in this work, thus, suggest that this mechanism is not influencing the transport properties.

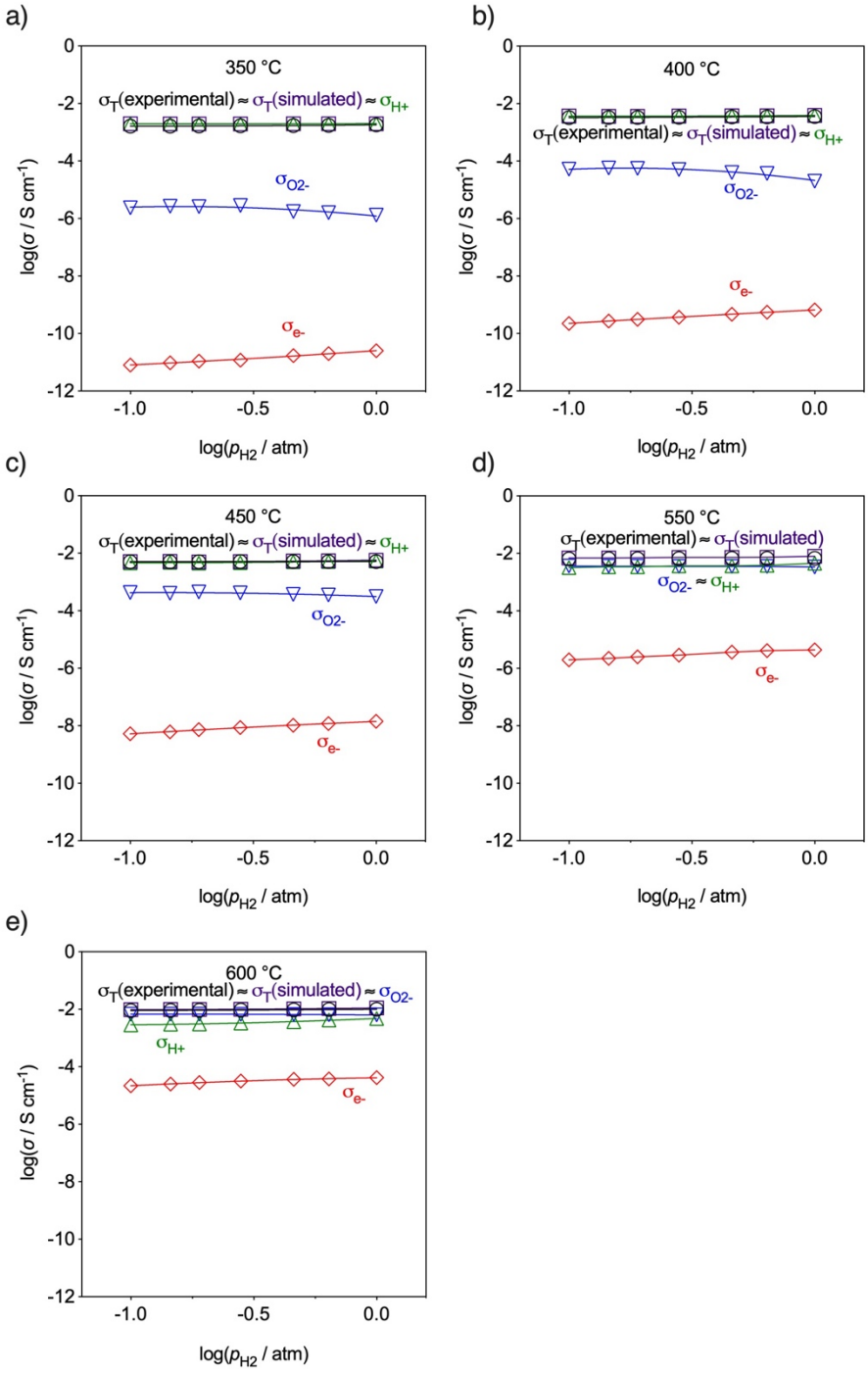

Fig. 4.6 – Partial conductivities as a function of hydrogen partial pressure.

Consequently, oxide-ion and protonic conductivities are of the same order of magnitude, for $T \approx 550$ °C (~ 10^{-3} S cm^{-1}). A characteristic activation energy for protonic conductivity Ea_{H+} ~ 0.41 eV [7] was calculated in the temperature range of 350 – 450 °C, where proton transport dominates with a linear behaviour in the *Arrhenius* representation and before any

discernible inflection associated to a mixed conducting regime. Conversely, the very high activation energy for oxide-ionic conductivity Ea_{O2-} ~ 1.61 eV in the lower temperature range is a consequence of the activation energy for the oxide-ion mobility (Fig. 4.4c) but also of the increased oxygen vacancy concentration with temperature (Fig. 4.4a). Furthermore, as expected from the very low equilibrium constant for cerium reduction in $BaCe_{0.9}Y_{0.1}O_{3-\delta}$ between 300 – 500 °C, the electronic conductivity is several orders of magnitude lower than that of the ionic contribution (H^+, O^{2-}). Instead, as a consequence of the very high reduction enthalpy, a very high activation energy for electronic conductivity Ea_{e-} ~ 2.59 eV, was obtained in the whole temperature range, which is in good agreement with previous reports on doped-barium cerates [24].

Conclusions

$BaCe_{0.9}Y_{0.1}O_{3-\delta}$ shows a predominantly protonic behaviour in low concentration of oxygen and humidity for low temperatures, *i.e.* < 400 °C, while still providing very attractive levels of conductivity, *e.g.* ~ 10^{-3} S cm^{-1}. Note, the scarcity of alternative proton-conducting ceramics, with such competitive protonic conductivity and negligible oxide-ion/electronic influence, have typically prevented the exploitation of electrochemical membrane reactors for chemical reactions in this low temperature range. This peculiar characteristic of $BaCe_{0.9}Y_{0.1}O_{3-\delta}$ of a very high equilibrium constant for hydration that allows competitive levels of proton conductivity to be obtained even in nominally dry gases is currently insufficiently highlighted in current literature, and yet is a highly desirable property for a wide range of chemical de-hydrogenation/ hydrogenation reactions. For these reasons, it is expected that $BaCe_{0.9}Y_{0.1}O_{3-\delta}$, and related doped barium cerates, can take a new role in the electrochemical promotion of chemical reactions in atmospheres of very low humidity, with significant impact on the future of proton-ceramic conductors.

References

1 S. H. Morejudo, R. Zanón, S. Escolástico, I. Yuste-Tirados, H. Malerød-Fjeld, P. K. Vestre, W. G. Coors, A. Martínez, T. Norby, J. M. Serra and C. Kjølseth, *Science,* 2016, **353**, 563–566.

2 K. D. Kreuer, *Annu. Rev. Mater. Res.*, 2003, **33**, 333–359.

3 L. Malavasi, C. A. J. Fisher and M. S. Islam, *Chem. Soc. Rev.*, 2010, **39**, 4370–4387.

4 E. Fabbri, A. D'Epifanio, E. Di Bartolomeo, S. Licoccia and E. Traversa, *Solid State Ionics*, 2008, **179**, 558–564.

5 D. J. L. Brett, A. Atkinson, N. P. Brandon and S. J. Skinner, *Chem. Soc. Rev.*, 2008, **37**, 1568–1578.

6 M. Liu, M. E. Lynch, K. Blinn, F. M. Alamgir and Y. Choi, *Mater. Today*, 2011, **14**, 534–546.

7 W. G. Coors and D. W. Readey, *J. Am. Ceram. Soc.*, 2004, **85**, 2637–2640.

8 G. Ma, T. Shimura and H. Iwahara, *Solid State Ionics*, 1999, **120**, 51–60.

9 K. D. Kreuer, T. Dippel, Y. M. Baikov and J. Maier, *Solid State Ionics*, 1996, **86**–**88**, 613–620.

10 N. Bonanos, B. Ellis, K. S. Knight and M. N. Mahmood, *Solid State Ionics*, 1989, **35**, 179–188.

11 R. C. T. Slade and N. Singh, *Solid State Ionics*, 1993, **61**, 111–114.

12 E. Fabbri, D. Pergolesi and E. Traversa, *Chem. Soc. Rev.*, 2010, **39**, 4355–4369.

13 Y. Li, P.-C. Su, L. M. Wong and S. Wang, *J. Power Sources*, 2014, **268**, 804–809.

14 J. Otomo, N. Noda and F. Kosaka, *ECS Trans.*, 2015, **68**, 2663–2670.

15 Z. Li, R. Liu, J. Wang, Z. Xu, Y. Xie and B. Wang, *Sci. Technol. Adv. Mater.*, 2007, **8**, 566–570.

16 G. Marnellos and M. Stoukides, *Science,* 1998, **282**, 98–100.

17 Y. Feng, J. Luo and K. T. Chuang, *J. Phys. Chem. C*, 2008, **112**, 9943–9949.

18 C. W. Bale, E. Bélisle, P. Chartrand, S. A. Decterov, G. Eriksson, A. E. Gheribi, K. Hack, I.-H. Jung, Y.-B. Kang, J. Melançon, A. D. Pelton, S. Petersen, C. Robelin, J. Sangster, P. Spencer and M.-A. Van Ende, *Calphad*, 2016, **54**, 35–53.

19 D. P. Sutija, T. Norby and P. Björnbom, *Solid State Ionics*, 1995, **77**, 167–174.

20 N. Bonanos and F. Willy Poulsen, *J. Mater. Chem.*, 1999, **9**, 431–434.

21 D. Pérez-Coll, D. Marrero-López, J. C. Ruiz-Morales, P. Núñez, J. C. C. Abrantes and J. R. Frade, *J. Power Sources*, 2007, **173**, 291–297.

22 J. C. C. Abrantes, D. Pérez-Coll, P. Núñez and J. R. Frade, *Electrochim. Acta*, 2003, **48**, 2761–2766.

23 D. Pérez-Coll, P. Núñez and J. R. Frade, in *Advances in Ceramics - Synthesis and Characterization, Processing and Specific Applications*, ed. C. Sikalidis, InTech, Rijeka, 2011.

24 N. Bonanos, *J. Phys. Chem. Solids*, 1993, **54**, 867–870.

25 W. Chen, A. Nijmeijer and L. Winnubst, *Solid State Ionics*, 2012, **229**, 54–58.

26 S. Wang, H. Inaba, H. Tagawa and T. Hashimoto, *J. Electrochem. Soc.*, 1997, **144**, 4076–4080.

27 T. Kobayashi, S. Wang, M. Dokiya, H. Tagawa and T. Hashimoto, *Solid State Ionics*, 1999, **126**, 349–357.

28 S. Wang, H. Inaba, H. Tagawa, M. Dokiya and T. Hashimoto, *Solid State Ionics*, 1998, **107**, 73–79.

29 K. D. Kreuer, *Solid State Ionics*, 1999, **125**, 285–302.

30 K. D. Kreuer, W. Münch, U. Traub and J. Maier, *Berichte der Bunsengesellschaft für Phys. Chemie*, 1998, **102**, 552–559.

31 A. L. Chinelatto, K. Boulahya, D. Pérez-Coll, U. Amador, C. Tabacaru, S. Nicholls, M. Hoelzel, D. C. Sinclair and G. C. Mather, *Dalt. Trans.*, 2015, **44**, 7643–7653.

32 D.-K. Lim, C.-J. Park, M.-B. Choi, C.-N. Park and S.-J. Song, *Int. J. Hydrogen Energy*, 2010, **35**, 10624–10629.

33 F. Krug, T. Schober and T. Springer, *Solid State Ionics*, 1995, **81**, 111–118.

34 H. Uchida, H. Yoshikawa, T. Esaka, S. Ohtsu and H. Iwahara, *Solid State Ionics*, 1989, **36**, 89–95.

5. Underscoring the transport properties of yttrium-doped barium cerate in nominally dry oxidising conditions

Abstract

The current work assesses the transport properties of $BaCe_{0.9}Y_{0.1}O_{3-d}$ (BCY10) in oxidising atmospheres as a function of water vapour partial pressure (p_{H2O} = ~ 10^{-7} – 0.1 atm) in the intermediate temperature range 350 – 600 °C. From these data, and the data of the previous chapter, **Chapter 4**, the transport numbers of this material in both reducing and oxidising conditions are compared. Contrary to that observed in reducing atmospheres, where feeding with nominally dry hydrogen-based atmospheres was sufficient to provide high levels of protonic conductivity, in oxidising conditions the material can only exhibit significant protonic conductivity by externally imposing more elevated p_{H2O} values ~ 10^{-5} – 10^{-4} atm. From this knowledge, we outline the limiting conditions of operation of BCY10 under low humidity values and, subsequently, outline its relevance to cell efficiency and membrane stability in the intermediate temperature range.

5.1. Introduction

Several perovskite-based materials show promising ionic conductivities at intermediate temperatures (400 – 600 °C) that have allowed them to find application in a range of ceramic membrane reactors [1–6]. Of the potential materials, the proton-conducting perovskites are particularly interesting, due to present higher ionic conductivities at intermediate temperatures in comparison to their oxide-ion-conducting counterparts. In this respect, barium cerate and barium zirconate-based perovskites are leading materials in this category that offer high levels of protonic conductivity. Due to this property, many examples of potential membrane applications can be found in the literature for the barium zirconate materials and for mixed compositions based on solid solutions between the barium zirconate and barium cerate end members [7–15]. Applications range from fuel cells [8] and electrolysers [13,14] to more specialised chemical reactors that can promote hydrogenation or de-hydrogenation reactions [7,10,15]. Nonetheless, significantly less attention has been given to prospective applications of the end member barium cerate, due to its poor stability in atmospheres containing carbon dioxide or moisture [16,17]. Some exceptions that can be found include ammonia synthesis [15,18,19], or the conversion of propane to propylene [20].

Despite this limitation, a major advantage for the use of cerate membranes is related to their higher equilibrium constant for water absorption in comparison to that of other proton-conducting oxides, that allows the cerate materials to exhibit one of the highest proton conductivities at low temperatures [17]. Moreover, a higher sinterability and improved grain growth of the cerate materials facilitate their processing, in comparison to the zirconate-based compositions, leading to simplified cell fabrication and better grain boundary conductivities [21–24]. It should be noted that these issues become increasingly critical when the material needs no operate at the intermediate temperature range, *e.g.* 350-600 °C, where the characteristic highly resistive grain boundaries of the zirconate-based electrolytes debilitate values of total conductivity [25].

Bearing this in mind, the use of a proton-conducting ceramic electrolyte that is capable of offering pure protonic conductivity and that is easy to densify in the referred targeted temperature range has significant interest. For the case of perovskite proton conductors,

the origin of proton conduction comes from the filing of oxygen vacancies ($V_O^{\bullet\bullet}$) that are generated as charge compensating defects by doping with a lower valence cation on the B-site, i.e. for the case of $BaCe_{1-y}Y_yO_{3-\delta}$ according to:

$$BaO + (1-y)CeO_2 + \left(\frac{y}{2}\right)Y_2O_3 \Longrightarrow Ba_{Ba}^{x} + (1-y)Ce_{Ce}^{x} + \\ +(y)\,Y_{Ce}' + \left(3-\frac{y}{2}\right)O_O^{x} + \left(\frac{y}{2}\right)V_O^{\bullet\bullet} \qquad (5.1)$$

Hydroxyl proton conducting species can then be formed by hydration of the oxygen vacancies with ambient water molecules

$$H_2O_{(g)} + V_O^{\bullet\bullet} + O_O^{x} \Leftrightarrow 2OH_O^{\bullet} \qquad (5.2)$$

where the equilibrium constant of eqn (5.2), K_w, is approximately given by:

$$K_w \approx \frac{[OH_O^{\bullet}]^2}{p_{H2O}[V_O^{\bullet\bullet}]} \qquad (5.3)$$

One of the best proton conductors is the cerate-based composition, yttrium-doped barium cerate, specifically $BaCe_{0.9}Y_{0.1}O_{3-\delta}$ (BCY10), that has been recently demonstrated to exhibit high protonic conductivity even in nominally dry conditions up to 450 – 500 °C (**Chapter 4**). In this chapter, the transport numbers of BCY10 were measured in nominally dry reducing conditions, obtained by use of hydrogen-containing atmospheres and professional gas driers that dry incoming gases to the level of $p_{H2O} \sim 10^{-7}$ atm. Despite this very strict drying step, the reported values of pure protonic conductivity up to 450 – 500 °C in such atmospheres (**Chapter 4**) were mostly related to the true presence of water vapour in the range $p_{H2O} \sim 10^{-5} – 10^{-4}$ atm generated by the equilibrium

$$H_{2(g)} + \frac{1}{2}O_{2(g)} \leftrightarrow H_2O_{(g)} \qquad (5.4)$$

with a mass action constant described by

$$K_w = \frac{p_{H2O}}{p_{H2}\cdot {p_{O2}}^{1/2}} \qquad (5.5)$$

The presence of this equilibrium in hydrogen-containing atmospheres, thus, provided sufficient hydration to BCY10 (by eqn (5.2)) to achieve pure protonic conductivity. In contrast, the same equilibrium cannot provide such high water vapour pressures in oxidising

conditions due to the lack of hydrogen that can be oxidised. As a consequence, the dominance of protonic conductivity of BCY10 in oxidising atmospheres in the intermediate temperature range may be deviated towards the requirement of higher, externally created, p_{H2O} levels, or alternatively, lower temperatures, potentially restraining the use of this material at higher oxygen partial pressures in nominally dry conditions. Another limitation of this material may be its characteristic p-type electronic conductivity in oxidising atmospheres that can exert a further important contribution on total conductivity. This contribution can be especially problematic in dry conditions, where the nominal absence of water can lead to an increase in the onset of electronic conductivity,

$$\frac{1}{2}O_{2(g)} + V_O^{\bullet\bullet} \leftrightarrow O_O^x + 2h^{\bullet} \quad (5.6)$$

with the following mass action constant

$$K_O \approx \frac{[h^{\bullet}]^2}{[V_O^{\bullet\bullet}].p_{O2}^{1/2}} \quad (5.7)$$

Due to these reasons, in this work, we aim to understand the operational limits of $BaCe_{0.9}Y_{0.1}O_{3-\delta}$ in more oxidising atmospheres at low humidity, by determining the transport numbers in N_2 and O_2 as a function of p_{H2O}. The transport numbers for this composition in oxidising atmospheres were firstly studied by Oishi *et al.* [26], where the authors applied a defect chemistry model to determine the transport numbers of $BaCe_{0.9}Y_{0.1}O_{3-\delta}$ and by means of total conductivity measurements a function of oxygen partial pressure (p_{O2}). Nonetheless, the work was only performed for temperatures higher than 500 °C and, more importantly, only in wet conditions (p_{H2O} values varying between 10^{-3} to 10^{-2} atm). Later, Grimaud *et al.* [27] extended the transport numbers of this composition as a function of water partial pressure (p_{H2O}), however, the measurements in that case were conducted only in air and for very high water vapour partial pressures (p_{H2O} > ~ 0.35 atm). More recently, Lim *et al.* [28] determined the concentration of charge carriers in $BaCe_{0.9}Y_{0.1}O_{3-\delta}$ by thermogravimetric analysis (TGA) under various humidity conditions (nominally dry, ~ 10^{-5} atm, and wet, ~ 10^{-3} atm) at a constant oxygen partial pressure of ~ 10^{-1} atm from room temperature to 1000 °C. Nevertheless, there was no further determination of specific mobilities or partial

conductivities, impeding a broader understanding of the transport numbers for this material and limiting the information to specific p_{O2} and p_{H2O} values.

Due to these limitations, the determination of the transport properties of the $BaCe_{0.9}Y_{0.1}O_{3-\delta}$ at temperatures below 600 °C and under very low humidity ($p_{H2O} \leq 10^{-4}$ atm) in oxidising conditions will be an important addition to the knowledge of the material's properties. From these data one can assess its applicability as an electrolyte membrane for fuel cell, electrolysers and other electrochemical-based applications. To facilitate this aim, comparison with our previous work in reducing conditions, **Chapter 4**, is performed to highlight important differences between reducing and oxidising atmospheres when operating in very low humidities and, thereby, to define suitable working limits and applications for this material.

5.2. Experimental

5.2.1. Sample preparation

Pellets of a commercial $BaCe_{0.9}Y_{0.1}O_{3-\delta}$ powder (TYK, Japan) with a relative density > 98 %, with ~ 1 mm thickness were obtained from uniaxial pressing and sintering at 1450 °C for 6 h, using sacrificial powder to prevent Ba-losses [29]. Pt electrodes were formed from application of a Pt-paste (Heraeus CL11-5349) on both sides of the pellets and by co-sintering at 900 °C for 20 min.

5.2.2. Electrochemical impedance measurements

Electrical measurements by AC Electrochemical Impedance Spectroscopy (EIS) were performed on the symmetric cells using an Electrochemie-Autolab PGSTAT302N frequency response analyser in the frequency range 1 MHz to 0.01 Hz with signal amplitude 50 mV. Measurements as a function of oxygen partial pressure (p_{O2}) were performed at 50 °C intervals in the direction of decreasing temperature, in the temperature range of 350 – 600 °C, between O_2 and N_2. Upon changing gas atmospheres, dwell times of 48 – 96 h were employed to ensure equilibrium conditions. The effectiveness of these waiting times was assessed by performing repeated impedance spectra under identical conditions after further dwell times of 1 to 1.5 h.

The impedance spectra were fitted using the software *ZView*© (Scribner Associates). Nominally dry atmospheres were controlled using a SGT super clean gas moisture filter (<0.1 ppm H_2O); while, humidification was controlled by mixing dried gases with wetted gases that had been bubbled through KBr-saturated H_2O. The gases were applied to the measurement jig with a maximum total flowrate of 50 mL min^{-1} supplied by Bronkhorst Thermal Mass flow Controllers (EL Flow). Oxygen sensor values were measured using a YSZ (Friatec) sensor inserted in the sample jig. Relative humidity was collected by using a temperature and humidity sensor for industrial applications (JUMO, 907023).

5.3. Methodology for the determination of partial conductivities

The methodology used in this work for the determination of the partial conductivities was developed by Frade [30], which combines eqn (5.3), (5.7) and the charge neutrality condition

$$[\mathrm{Y}'_{\mathrm{Ce}}] \approx 2[V_{\mathrm{O}}^{\bullet\bullet}] + [OH_{\mathrm{O}}^{\bullet}] \tag{5.8}$$

that can be derived into the following mathematical solutions:

$$[OH_{\mathrm{O}}^{\bullet}] \approx \frac{K_{\mathrm{w}}.p_{\mathrm{H2O}}}{4}\left[\left(1+\frac{8[\mathrm{Y}'_{\mathrm{Ce}}]}{K_{\mathrm{w}}.p_{\mathrm{H2O}}}\right)^{\frac{1}{2}}-1\right] \tag{5.9}$$

$$[V_{\mathrm{O}}^{\bullet\bullet}] \approx \frac{K_{\mathrm{w}}.p_{\mathrm{H2O}}}{16}\left[\left(1+\frac{8[\mathrm{Y}'_{\mathrm{Ce}}]}{K_{\mathrm{w}}.p_{\mathrm{H2O}}}\right)^{\frac{1}{2}}-1\right]^{2} \tag{5.10}$$

$$[h^{\bullet}] \approx \left(\frac{K_{\mathrm{O}}.K_{\mathrm{w}}}{16}\right)^{\frac{1}{2}}\left[\left(1+\frac{8[\mathrm{Y}'_{\mathrm{Ce}}]}{K_{\mathrm{w}}.p_{\mathrm{H2O}}}\right)^{\frac{1}{2}}-1\right].p_{\mathrm{H2O}}^{1/2}.p_{\mathrm{O2}}^{1/4} \tag{5.11}$$

The concentration of each charge carrier (eqn (5.9) – (5.11)) can then be inserted into the following equation for the partial conductivities

$$\sigma_{\mathrm{i}} = q_{\mathrm{i}}.\mu_{\mathrm{i}}.C_{\mathrm{i}} \tag{5.12}$$

where q_i, C_i and μ_i represent the charge, the concentration and the mobility of the species i. Consequently, assuming that the mobility is constant within the measured p_{O2} and p_{H2O} [31], the following expressions can be used to calculate the partial conductivities:

$$\sigma_{\mathrm{H}} = \sigma_{\mathrm{H}}^{0}.\left[\left(1+\frac{\alpha}{p_{\mathrm{H2O}}}\right)^{1/2}-1\right].\frac{p_{\mathrm{H2O}}}{(1+\alpha)^{1/2}-1} \tag{5.13}$$

$$\sigma_{\mathrm{o}} = \sigma_{\mathrm{o}}^{0}.\left[\left(1+\frac{\alpha}{p_{\mathrm{H2O}}}\right)^{1/2}-1\right]^{2}.\frac{p_{\mathrm{H2O}}}{\alpha} \tag{5.14}$$

$$\sigma_{\mathrm{h}} = \sigma_{\mathrm{h}}^{0}.\left[\left(1+\frac{\alpha}{p_{\mathrm{H2O}}}\right)^{1/2}-1\right].\frac{p_{\mathrm{H2O}}^{1/2}}{\alpha^{1/2}}p_{\mathrm{O2}}^{1/4} \tag{5.15}$$

where

$$\alpha = \frac{8[\mathrm{Y}'_{\mathrm{Ce}}]}{K_{\mathrm{w}}} \tag{5.16}$$

and σ_{H}^{0} is the proton conductivity at p_{H2O} = 1 atm, σ_{h}^{0}, the hole conductivity at p_{O2} = 1 atm and p_{H2O} = 0 atm; and σ_{o}^{0}, the oxide-ion conductivity when p_{H2O} = 0 atm. These constants take the form:

$$\sigma_{\mathrm{H}}^{0} = \left[(1+\alpha)^{1/2} - 1\right]\frac{K_{\mathrm{w}} q_{\mathrm{H}} \mu_{\mathrm{H}}}{4} \tag{5.17}$$

$$\sigma_{\mathrm{o}}^{0} = \frac{[\mathrm{Y_{Ce}'}]}{2} q_{\mathrm{o}} \mu_{\mathrm{o}} \tag{5.18}$$

$$\sigma_{\mathrm{h}}^{0} = K_{\mathrm{O}} \frac{[\mathrm{Y_{Ce}'}]}{2} q_{\mathrm{h}} \mu_{\mathrm{h}} \tag{5.19}$$

The partial conductivities of $BaCe_{0.9}Y_{0.1}O_{3-\delta}$ were determined from eqn (5.13) – (5.15), under the imposed conditions of p_{O2} and p_{H2O} on determining the constants α, σ_{o}^{0}, σ_{o}^{0}, and σ_{h}^{0}.

For any fixed value of p_{H2O}, the ionic conductivities (protonic and oxide-ion), including protonic and oxide-ion are effectively constant, and the electronic conductivity presents a ¼ power law dependence on the p_{O2}. Since

$$\sigma_{\mathrm{T}} = \sigma_{\mathrm{H}} + \sigma_{\mathrm{o}} + \sigma_{\mathrm{h}} \tag{5.20}$$

Therefore, the total conductivity may be expressed as a linear function:

$$\sigma_{\mathrm{tot}} = \mathrm{a} + \mathrm{b}.p_{\mathrm{O2}}^{1/4} \tag{5.21}$$

The intercept of eqn (5.21), $\mathrm{a} = \sigma_{\mathrm{H}} + \sigma_{\mathrm{o}}$, corresponds to

$$\mathrm{a} = \sigma_{\mathrm{H}}^{0}.\left[\left(1+\frac{\alpha}{p_{\mathrm{H2O}}}\right)^{1/2} - 1\right].\frac{p_{\mathrm{H2O}}}{(1+\alpha)^{1/2}-1} + \sigma_{\mathrm{o}}^{0}.\left[\left(1+\frac{\alpha}{p_{\mathrm{H2O}}}\right)^{1/2} - 1\right]^{2}.\frac{p_{\mathrm{H2O}}}{\alpha} \tag{5.22}$$

and the slope, b, is expressed as

$$\mathrm{b} = \sigma_{\mathrm{h}}^{0}.\left[\left(1+\frac{\alpha}{p_{\mathrm{H2O}}}\right)^{1/2} - 1\right].\frac{p_{\mathrm{H2O}}^{1/2}}{\alpha^{1/2}} \tag{5.23}$$

The slope of eqn (5.21) is dependent on p_{H2O}, according to eqn (5.23). The constants σ_{h}^{0} and α were determined from the combination of the slopes obtained at two different values of p_{H2O}. The value of α was determined by assuming $[\mathrm{Y_{Ce}'}]$ = 0.1 and using the values of K_{w} from Kreuer [32]. The value of α is then introduced in eqn (5.22), and the constants σ_{H}^{0} and σ_{o}^{0} can be calculated from the combination of the intercepts obtained at two different values of p_{H2O}.

5.4. Results and discussion

5.4.1. Partial conductivities and transport numbers in O_2 and N_2

Total conductivities of $BaCe_{0.9}Y_{0.1}O_{3-\delta}$ obtained in O_2 and N_2, wet and nominally dry gases measured in the temperature interval (350 – 600 °C) are represented in Fig. 5.1. From first inspection, total conductivity is, in general, higher in wet (p_{H2O} ~ 10^{-3} atm) conditions than in nominally dry conditions (p_{H2O} ~ 10^{-7} atm). This behaviour contrasts with that previously reported in nominally dry reducing atmospheres, where true water vapour partial pressures were measured to be in the range (p_{H2O} ~ 10^{-4} – 10^{-5} atm) (**Chapter 4**) due to the equilibrium for water formation (eqn (5.4)). This is perhaps not surprising, since the absence of hydrogen in oxidising conditions inhibits the equilibrium for water formation (eqn (5.4)) (**Chapter 4**), leading to a lower intrinsic water vapour partial pressure that can in turn decrease the protonic transport number.

We also observe the following differences in nominally dry oxidising atmospheres. In nominally dry N_2 (p_{H2O} ~ 10^{-7} atm) the total conductivity is lower in the whole measured temperature range in comparison to wet N_2 (p_{H2O} ~ 10^{-3} atm), as a result of dehydration of the sample according to the inverse of eqn (5.2). In contrast, in O_2, the total conductivity approaches that of wet O_2 at higher temperatures. In this respect, some p-type electronic conductivity (eqn (5.6)) is expected to be present in oxygen, even in this temperature range, especially for the nominally dry case [33,34]. This factor can explain the slightly higher activation energy registered in nominally dry O_2 of 0.49 eV, in comparison to that obtained in wet O_2 (0.37 eV) or in dry or wet N_2 (around 0.30 eV), where the latter three correspond to a higher contribution from protonic behaviour.

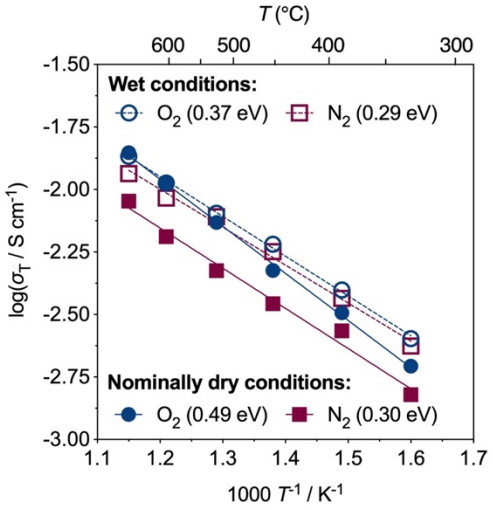

Fig. 5.1 – Total conductivity of $BaCe_{0.9}Y_{0.1}O_{3-\delta}$. Measurements performed in nominally dry (p_{H2O} = 10^{-7} atm) and wet (p_{H2O} = 10^{-3} atm) conditions.

For the determination of the transport properties of $BaCe_{0.9}Y_{0.1}O_{3-\delta}$, we selected conditions based on several criteria: i) we choose a temperature range where bulk conductivity is dominant to mitigate the contribution of the grain boundary conductivity (as its composition may differ from that of the bulk); ii) we select a p_{O2} range that would be relevant to cathodic environment of a solid oxide fuel cell, namely between N_2 and O_2.; iii) we select a p_{H2O} range including nominally dry conditions (10^{-7} atm) and moderate wet conditions (10^{-3} atm), where the latter condition is chosen to minimise potential depredations of the material with moisture that could lead to deviations in the determination of partial conductivities.

Fig. 5.2a and b depict the total conductivity of $BaCe_{0.9}Y_{0.1}O_{3-\delta}$ as a function of oxygen partial pressure, obtained in nominally dry and wet atmospheres, obtained between O_2 and N_2. Two main observations can be highlighted. Firstly, the inflexion towards high p_{O2} is more noticeable in nominally dry conditions, suggesting that the electronic conductivity is more pronounced in this case. Secondly, the total conductivity is higher in wet conditions at low temperatures, while, at high temperatures, total conductivity is higher in nominal dry conditions. Again, this behaviour possibly results from the expected increasing electronic contribution with sample dehydration (Inverse of eqn (5.2) and (5.6)). These observations are corroborated by the plots of total conductivity *vs.* $p_{O2}^{1/4}$ depicted in Fig. 5.2c and d, where

the presence of electron holes is more pronounced. The increasing slope with increasing temperature is expected due to the increased mobility of the predominant charge carriers.

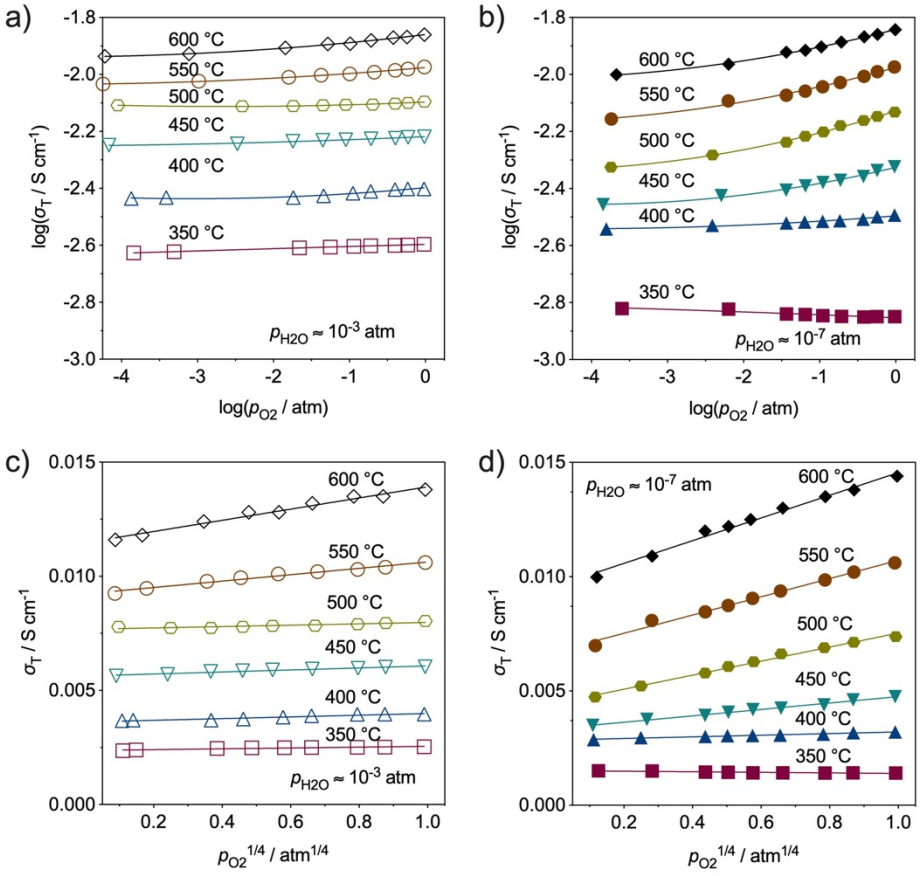

Fig. 5.2 – Total conductivity as a function of oxygen partial pressure (p_{O2}): a) and c) wet (p_{H2O} = 10^{-3} atm) and b) and d) nominally dry (p_{H2O} = 10^{-7} atm) conditions; alternative representation of the total conductivity according to eqn (5.21): b) and c).

The partial conductivities obtained in N_2 and O_2 in moderate wet conditions (p_{H2O} ~ 10^{-3} atm) are depicted in Fig. 5.3a and b. We can observe that the protonic conductivity is dominating in both cases, with activation energies (calculated between 350 and 500 °C) similar to that obtained for the protonic conduction (~ 0.4 – 0.5 eV) [3,4]. The activation energy for hole conductivity is observed to be higher in the case of O_2 atmosphere (1.77 eV) in comparison to that obtained in N_2 (1.29 eV), suggesting that the creation of holes by eqn (5.6) and (5.7) may become increasing unfavourable at high temperatures in less oxidising conditions.

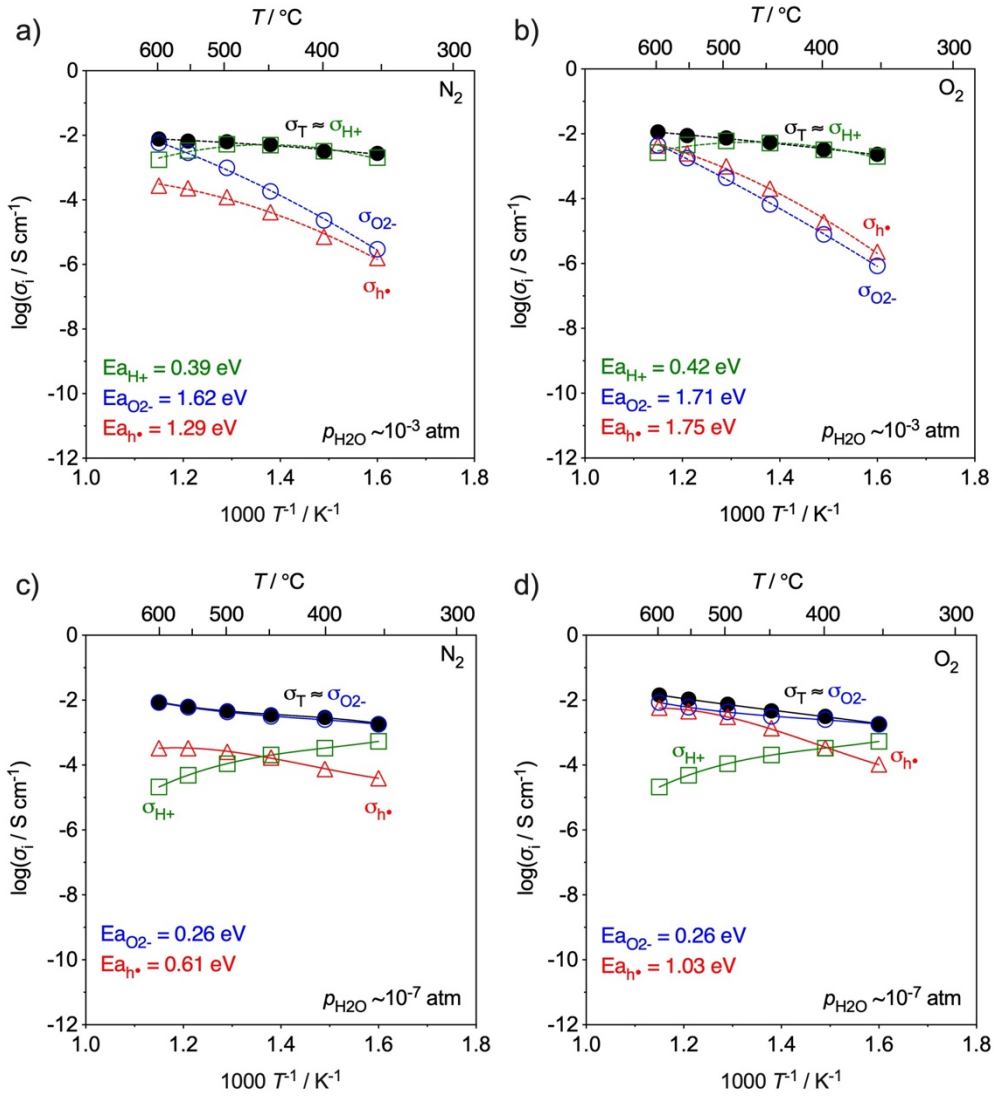

Fig. 5.3 – Partial conductivities obtained in wet and nominally conditions in a) and b) N_2, and c) and d) O_2. Activation energies calculated in the temperature range 350 and 500 °C

In nominally dry conditions (p_{H2O} ~ 10^{-7} atm), the oxide-ion conductivity predominates in both N_2 and O_2, as depicted in Fig. 5.3c and d. Furthermore, the protonic conductivity was found to decrease with increasing temperature, as a result of dehydration during heating. Finally, the activation energies obtained for hole conductivity were found to be significantly lower at p_{H2O} ~ 10^{-7} atm (0.61 – 1.03 eV, T = 350 – 500 °C) than those obtained for p_{H2O} ~ 10^{-3} atm (1.29 – 1.75 eV, T = 350 – 500 °C) due to the increasing role of oxide-ion conduction over the filling of oxygen vacancies and creation of electronic defects (eqn (5.6) and (5.7)), at higher temperature.

The corresponding transport numbers (t_i) were estimated as a function of the water partial pressure (Fig. 5.4), using the following equation:

$$t_i = \frac{\sigma_i}{\sigma_T} \tag{5.24}$$

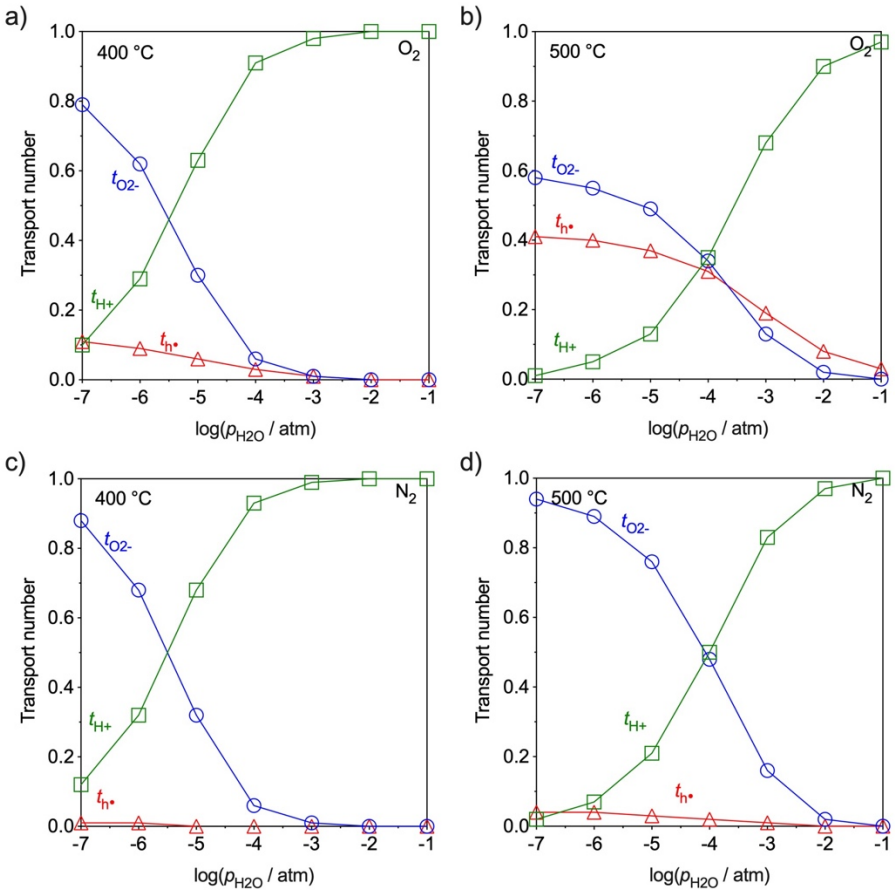

Fig. 5.4 – Transport numbers of BCY10 as a function of water partial pressure obtained for O_2: a) and b); and for N_2: c) and d).

From Fig. 5.4, we can clearly observe the impact of p_{H2O} in the protonic conductivity in oxidising atmospheres. This is especially noticeable in O_2, where the onset of electronic hole conduction is higher, showing an increase in the electronic transport number ($t_{h\bullet}$) up to 0.11 and 0.41, respectively, at 400 and 500 °C towards lower values of p_{H2O}. Conversely, in N_2, $t_{h\bullet}$ was found to be lower than 0.05 in the whole temperature range of study. Regarding the oxide-ion (t_{O2-}) and proton (t_{H+}) transport numbers, we can observe that t_{O2-} increases with decreasing p_{H2O}, whereas t_{H+} increases with increasing hydration. Notice, the dominance of the protonic transport number is only achievable for $p_{H2O} > 10^{-5}$ atm, at the

temperature of 400 °C (*i.e.*, t_{H+} > 0.8 – 0.9). In contrast, at the higher temperature of 500 °C, the protonic transport decreases and it is only possible to achieve dominant protonic conductivity when the p_{H2O} is increased by an order of magnitude (*i.e.*, > 10^{-4} atm).

The current observations highlight the limitations of operating in oxidising conditions at low humidity, where the p_{H2O} should be externally adjusted to values in the order of 10^{-4} – 10^{-5} atm, depending on the temperature, to ensure maximum protonic conductivity while continuing to keep low levels of gas humidification that could otherwise lead to $BaCe_{0.9}Y_{0.1}O_{3-\delta}$ degradation (**Chapter 4**). This level of humidity, required to achieve predominant proton conductivity, p_{H2O} = 10^{-4} – 10^{-5} atm, agrees very well with our previous chapter measured in hydrogen atmospheres in the same temperature range (**Chapter 4**). Nonetheless, it important to emphasise that this level of humidity is intrinsically formed in nominally dry hydrogen atmospheres by the equilibrium for water formation (eqn (5.4) (**Chapter 4**). In contrast, in the more oxidising conditions of the current work, this water vapour partial pressure must now be externally supplied. This factor will be discussed further in the later text.

5.4.2. A comparison between reducing and oxidising conditions

The transport properties of $BaCe_{0.9}Y_{0.1}O_{3-\delta}$ in oxidising conditions are now compared with those previously determined in reducing conditions (**Chapter 4**). Fig. 5.5 depicts the partial conductivities obtained in H_2, N_2 and O_2 for p_{H2O} ~ 10^{-4} atm. The first important observation is that total conductivity is essentially dominated by the protonic conductivity for $T \leq 450$ °C in all cases with this level of p_{H2O}, as previously discussed. This is perhaps not surprising as the formation of protonic species are mainly dependent on the uptake of water, according to eqn (5.2) and, thus, dependent on water vapour partial pressure. At the same time, the oxide-ion conductivity is shown to be lower than that of total conductivity by a factor of 2 – 4 in H_2 and 1 – 2 in N_2 and O_2, in the low temperature range ($T \leq 450$ °C). On the contrary, above this temperature, oxide-ion conductivity approaches that of the total conductivity, while the protonic conductivity decreases.

Regarding the electronic conductivity, it is shown to increase with increasing p_{O2}, i.e. following the sequence $H_2 < N_2 < O_2$. In **Chapter 4**, we have determined that the reducibility of Ce^{4+} to Ce^{3+} in the $BaCe_{0.9}Y_{0.1}O_{3-\delta}$ structure is almost negligible in the studied temperature range (350 – 600 °C), thus explaining the observed low electronic conductivity in H_2. In contrast, in oxidising atmospheres, the mechanism of electronic conduction is related instead to the formation of holes (eqn (5.6)), which become more prominent with increasing p_{O2}.

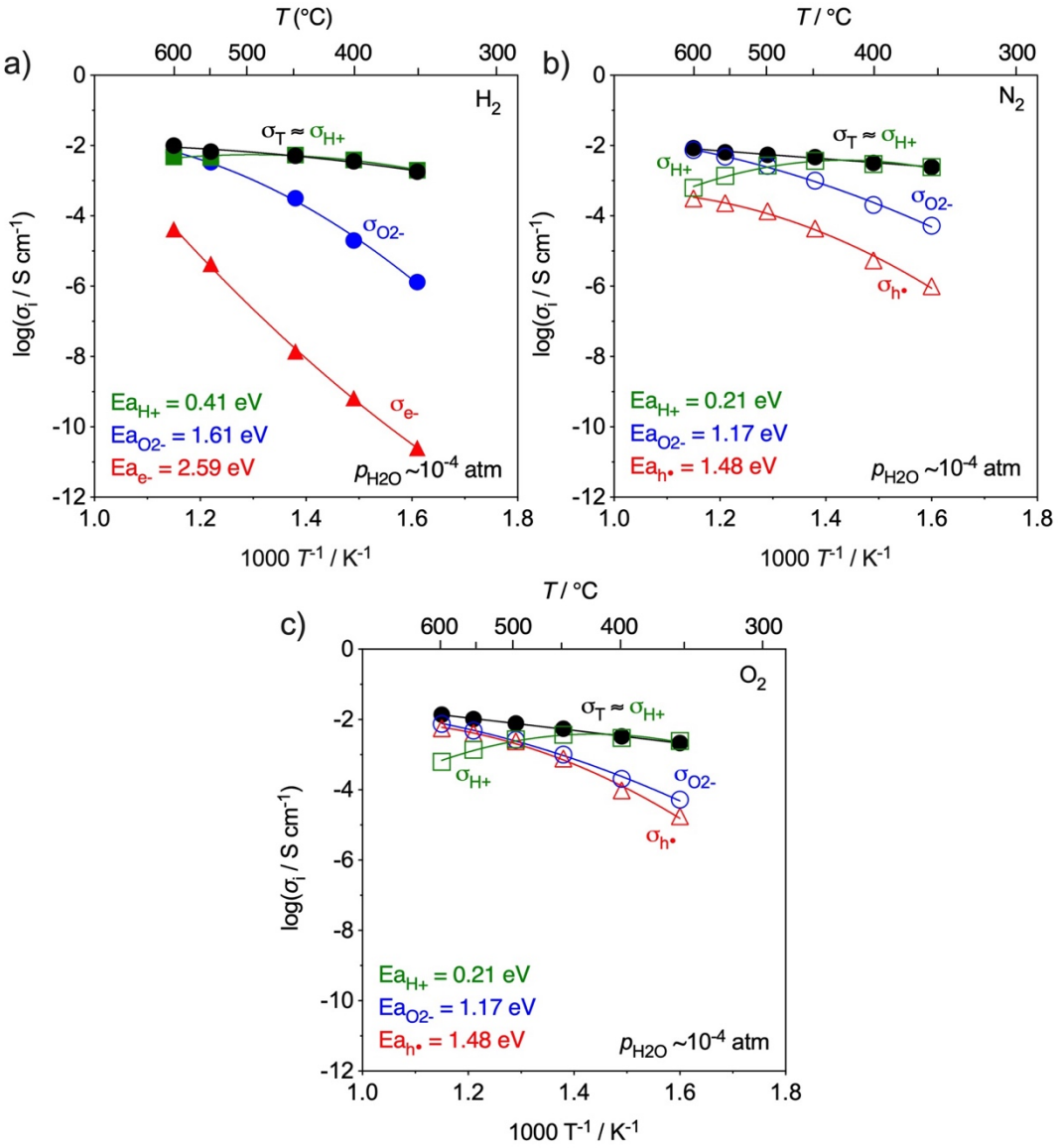

Fig. 5.5 – Partial conductivities obtained in nominally dry conditions: a) H_2 (**Chapter 4**), b) N_2 and c) O_2. Activation energies calculated in the temperature range 350 and 500 °C

Fig. 5.6 shows the transport numbers of $BaCe_{0.9}Y_{0.1}O_{3-\delta}$, calculated as a function of temperature in H_2, N_2 and O_2 for p_{H2O} ~ 10^{-4} atm. For low temperatures (350 – 450 °C), proton transference number is close to unity in pure H_2 (*i.e.* $t_{H+} > 0.95$) for values of p_{H2O} ~ 10^{-4} atm, and the corresponding transference numbers for oxygen-ion and electronic defects are negligible. However, towards oxidising conditions, we registered a decrease in the proton transference number in the same temperature range, followed by an increase in oxygen-ion transport number, which is associated to the elimination of protons by means of the creation of oxygen vacancies. In addition, in pure O_2, the electronic transference number is always higher than that of oxide-ion transference number, due to the concomitant dehydration and formation of holes. In contrast, at high temperatures (500 – 600 °C), the protonic transference number becomes less relevant, being total transport dominated by either the oxygen ion or holes.

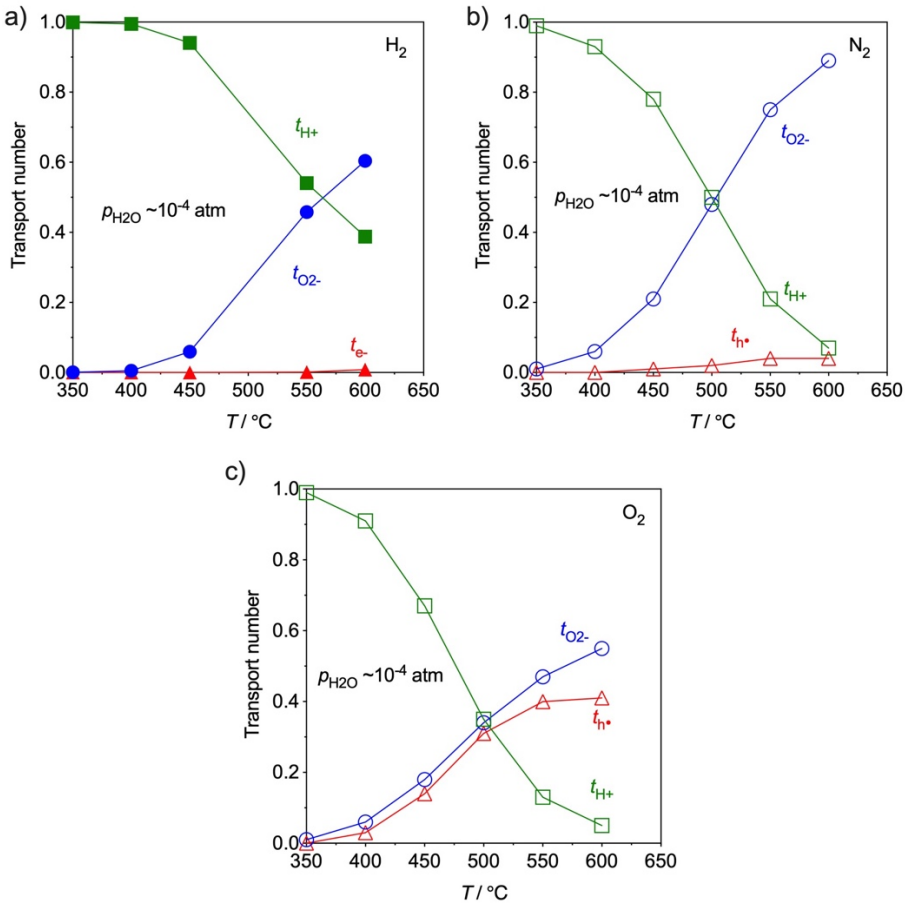

Fig. 5.6 – Transport numbers of BCY10 as a function of temperature obtained nominally dry conditions: a) H_2 (**Chapter 4**), b) N_2 and c) O_2.

5.4.3. Impact on potential applications

In order to discuss the effects of p_{H2O} on electrochemical cells using $BaCe_{0.9}Y_{0.1}O_{3-\delta}$ electrolytes, we now estimate the possible changes in the open circuit voltage (*OCV*) of an example cell that would result from the calculated transport properties. Therefore, we consider that the electrolyte is exposed to oxygen and/or water vapour partial pressure gradients, where the dependence of the *OCV* on the gradients of overall oxygen partial pressure (p_{O2}) and/or hydrogen partial pressure (p_{H2}) difference is given by [36]:

$$OCV_{\mathrm{co-ion}} = t_{\mathrm{O2-}} \frac{\mathrm{R}T}{4\mathrm{F}} \ln\left(\frac{p'_{\mathrm{O2}}}{p''_{\mathrm{O2}}}\right) - t_{\mathrm{H+}} \frac{\mathrm{R}T}{2\mathrm{F}} \ln\left(\frac{p'_{\mathrm{H2}}}{p''_{\mathrm{H2}}}\right) \tag{5.25}$$

which is expressed in terms of the averaged protonic and oxide-ionic transport numbers and considering non-polarisable electrodes. On considering the equilibrium between hydrogen, oxygen and water vapour $\left(\mathrm{H_2} + \frac{1}{2}\mathrm{O_2} \leftrightarrow \mathrm{H_2O}\right)$ from eqn (5.4), eqn (5.25) can be rearranged into:

$$OCV_{\mathrm{co-ion}} = t_{\mathrm{i}} \frac{\mathrm{R}T}{4\mathrm{F}} \ln\left(\frac{p'_{\mathrm{O2}}}{p''_{\mathrm{O2}}}\right) - t_{\mathrm{H+}} \frac{\mathrm{R}T}{2\mathrm{F}} \ln\left(\frac{p'_{\mathrm{H2O}}}{p''_{\mathrm{H2O}}}\right) \tag{5.26}$$

where $t_{\mathrm{i}} = t_{\mathrm{H+}} + t_{\mathrm{O2-}}$, and prime (') and double prime ('') indicate the cathode and anode sides of the electrolyte [36]. Fig. 5.7a depicts the predicted variation of the open circuit voltage for the mixed-conducting $BaCe_{0.9}Y_{0.1}O_{3-\delta}$ electrolyte as a function of p'_{H2O} in N_2 and O_2 atmospheres on the cathode side, with a reducing gas atmosphere present on the anode side. For the purpose of this example we consider the anode atmosphere to correspond to a H_2 atmosphere at a fixed p''_{H2O} ~ 10^{-4} atm, (data obtained from **Chapter 4**, where the transport numbers are averaged across the membrane. The results demonstrate that the variation of p_{H2O} at the cathode side strongly affects the open cell voltage, particularly at higher temperature.

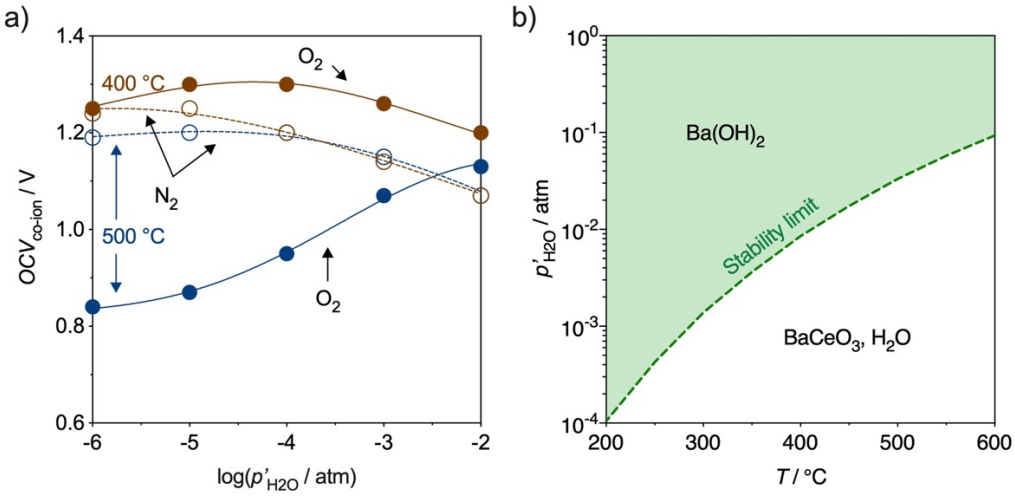

Fig. 5.7 – a) estimated open circuit voltage (*OCV*) obtained in N_2 and O_2 as a function of p_{H2O}, considering constant pure hydrogen flux on the anode side; b) stability limit of barium hydroxide formation resulting from the reactivity of $BaCe_{0.9}Y_{0.1}O_{3-\delta}$ and moisture (**Chapter 4**).

From Fig. 5.7a, we can predict that the use of oxygen as the cathodic atmosphere (typically used to promote a high open circuit potential) may fail with a BCY electrolyte due to electronic leakage. Furthermore, this effect will be aggravated at higher temperatures and for very low water vapour partial pressures. Experimental support for this theory may be found in the work of Lyagaeva *et al.* [37], where the authors noted that an electrochemical cell based on a Dy-doped $BaCeO_3$–$BaZrO_3$ proton-conducting electrolyte exhibited decreased *OCV* values with increasing temperature, due to an increasing average electronic transport number of the electrolyte. Conversely, at lower temperatures, Fig. 5.7a predicts that the *OCV* values will decrease upon excessive p_{H2O} values at the cathode under all atmospheres, due to an inversion of the p_{H2O} gradient across the cell in second term of eqn (5.26). As a result, the precise control of humidity can have an important impact on cell performance, where moderate cathode p_{H2O} values could be used as method to prevent the negative impacts of electronic leakage, especially in the oxygen atmosphere. Nonetheless, in a fuel cell application, the product water formed at the cathode must continue remain below the limit shown in Fig. 5.7b to maintain membrane stability; a criterion that may be difficult to achieve in practice due to requiring low conversions and large cathode gas flow rates.

Discussion, therefore, arrives to the most important results of this article that underscore that moderate water vapour pressures (p_{H2O} ~ 10^{-4} – 10^{-5} atm) are sufficient to permit BCY10

to be a predominant proton conductor in both reducing and oxidising atmospheres at sufficiently low temperatures ≤ 500 °C. Moreover, the level of conductivity measured in these conditions is high, *e.g.* ~ 10^{-2} S cm^{-1} (@ 400 °C). Predictions further highlight that a membrane operating in these conditions will present minimal electronic leakage.

These properties are highly exciting as there are many potential applications of BCY10 that have the requirements of very low humidity levels on both sides of the membrane and low temperatures of operation. The most well-known of these is that of ammonia electrochemical synthesis [15,18,19]. Many other processes concerning hydrogenation and de-hydrogenation reactions can also be considered (Table 5.1, Fig. 5.8). In all these scenarios, the presence of excessive amounts of water can be avoided, while both membrane stability (Fig. 5.7b), and its functionality as a predominantly proton conducting membrane can be maintained.

Table 5.1 – Examples of dehydrogenation/hydrogenation reactions [38] that can occur at very low humidity conditions.

Type	Reaction	ΔH^0_{298}/kJ mol^{-1}
Dehydrogenations	$2CH_4 \rightleftharpoons C_2H_4 + 2H_2$	202
	$6CH_4 \rightleftharpoons C_6H_6 + 9H_2$	89
	$C_3H_8 \rightleftharpoons C_3H_6 + H_2$	124.3
	$iC_4H_{10} \rightleftharpoons iC_4H_8 + H_2$	122
	$C_8H_{10} \rightleftharpoons C_8H_8 + H_2$	117.6
Hydrogenations	$C_{10}H_8 + 2H_2 \rightleftharpoons C_{10}H_{12}$	-134
	$C_6H_{10} + H_2 \rightleftharpoons C_6H_{12}$	-120
	$C_6H_6 + 3H_2 \rightleftharpoons C_6H_{12}$	-207
	$N_2 + 3H_2 \rightleftharpoons 2NH_3$	-109

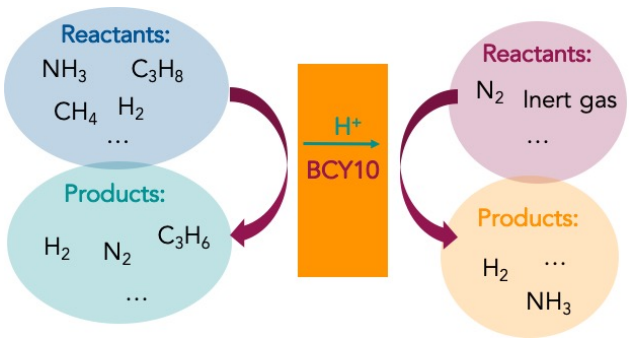

Fig. 5.8 – Potential applications of BCY10 membrane in nominally dry conditions (low oxygen and low water vapour contents).

Conclusions

The current results demonstrate that the transport properties of $BaCe_{0.9}Y_{0.1}O_{3-\delta}$ in nominally dry oxidising conditions differ significantly than in reducing conditions. While, it is possible to operate in the nominal absence of water in hydrogen-based atmospheres due to the equilibrium of water formation from hydrogen and oxygen, the same is not observed in the case of oxidising atmospheres. In the latter case, operation with nominally dry gases (p_{H2O} ~ 10^{-7} atm) is shown to lead to very low levels of hydration and to an increase in the onset of hole conductivity when increasing the oxygen partial pressure. On the other hand, very moderate water vapour pressures (p_{H2O} ~ 10^{-4} – 10^{-5} atm) are sufficient to permit BCY10 to be a predominant proton conductor in both reducing and oxidising atmospheres at sufficiently low temperatures ≤ 500 °C, with high values of conductivity. Such conditions open the possibility to use $BaCe_{0.9}Y_{0.1}O_{3-\delta}$ in hydrogenation and dehydrogenation reactions that benefit from very low humidity levels on both sides of the membrane and low temperatures of operation.

References

1 W. G. Coors and D. W. Readey, *J. Am. Ceram. Soc.*, 2004, **85**, 2637–2640.

2 G. Ma, T. Shimura and H. Iwahara, *Solid State Ionics*, 1999, **120**, 51–60.

3 K. D. Kreuer, T. Dippel, Y. M. Baikov and J. Maier, *Solid State Ionics*, 1996, **86**–**88**, 613–620.

4 N. Bonanos, B. Ellis, K. S. Knight and M. N. Mahmood, *Solid State Ionics*, 1989, **35**, 179–188.

5 R. C. T. Slade and N. Singh, *Solid State Ionics*, 1993, **61**, 111–114.

6 Da Han, X. Liu, F. Zeng, J. Qian, T. Wu and Z. Zhan, *Sci. Rep.*, 2012, **2**, 462.

7 S. H. Morejudo, R. Zanón, S. Escolástico, I. Yuste-Tirados, H. Malerød-Fjeld, P. K. Vestre, W. G. Coors, A. Martínez, T. Norby, J. M. Serra and C. Kjølseth, *Science*, 2016, **353**, 563–566.

8 S. Choi, C. J. Kucharczyk, Y. Liang, X. Zhang, I. Takeuchi, H.-I. Ji and S. M. Haile, *Nat. Energy*, 2018, **3**, 202–210.

9 Y. Kobayashi, N. Shimoda, Y. Kimura and S. Satokawa, *ECS Trans.*, 2017, **75**, 43–52.

10 M. Li, B. Hua and J.-L. Luo, *ACS Energy Lett.*, 2017, **2**, 1789–1796.

11 E. Ruiz-Trejo and J. T. S. Irvine, *Solid State Ionics*, 2012, **216**, 36–40.

12 E. Vasileiou, V. Kyriakou, I. Garagounis, A. Vourros and M. Stoukides, *Solid State Ionics*, 2015, **275**, 110–116.

13 L. Bi, S. Boulfrad and E. Traversa, *Chem. Soc. Rev.*, 2014, **43**, 8255–8270.

14 Y. Zheng, J. Wang, B. Yu, W. Zhang, J. Chen, J. Qiao and J. Zhang, *Chem. Soc. Rev.*, 2017, **46**, 1427–1463.

15 G. Marnellos and M. Stoukides, *Science*, 1998, **282**, 98–100.

16 H.-S. Kim, H. Bin Bae, W. Jung and S.-Y. Chung, *Nano Lett.*, 2018, **18**, 1110–1117.

17 K. D. Kreuer, *Annu. Rev. Mater. Res.*, 2003, **33**, 333–359.

18 J. Otomo, N. Noda and F. Kosaka, *ECS Trans.*, 2015, **68**, 2663–2670.

19 Z. Li, R. Liu, J. Wang, Z. Xu, Y. Xie and B. Wang, *Sci. Technol. Adv. Mater.*, 2007, **8**, 566–570.

20 Y. Feng, J. Luo and K. T. Chuang, *J. Phys. Chem. C*, 2008, **112**, 9943–9949.

21 E. Fabbri, L. Bi, D. Pergolesi and E. Traversa, *Adv. Mater.*, 2012, **24**, 195–208.

22 S. W. Tao and J. T. S. Irvine, *Adv. Mater.*, 2006, **18**, 1581–1584.

23 S. Tao and J. T. S. Irvine, *J. Solid State Chem.*, 2007, **180**, 3493–3503.

24 J. M. Polfus, M.-L. Fontaine, A. Thogersen, M. Riktor, T. Norby and R. Bredesen, *J. Mater. Chem. A*, 2016, **4**, 8105–8112.

25 C. Kjølseth, H. Fjeld, Ø. Prytz, P. I. Dahl, C. Estournès, R. Haugsrud and T. Norby, *Solid State Ionics*, 2010, **181**, 268–275.

26 M. Oishi, S. Akoshima, K. Yashiro, K. Sato, J. Mizusaki and T. Kawada, *Solid State Ionics*, 2008, **179**, 2240–2247.

27 A. Grimaud, J. M. Bassat, F. Mauvy, P. Simon, A. Canizares, B. Rousseau, M. Marrony and J. C. Grenier, *Solid State Ionics*, 2011, **191**, 24–31.

28 D.-K. Lim, H.-N. Im, S.-J. Song and H.-I. Yoo, *Sci. Rep.*, 2017, **7**, 486.

29 N. Nasani and D. P. Fagg, in *Combustion: Types of Reactions, Fundamental Processes and Advanced Technologies*, ed. J. M. Grier, Nova Publishers, 2014, pp. 245–267.

30 J. R. Frade, *Solid State Ionics*, 1995, **78**, 87–97.

31 H.-D. Baek, *Solid State Ionics*, 1998, **110**, 255–262.

32 K. D. Kreuer, *Annu. Rev. Mater. Res.*, 2003, **33**, 333–359.

33 G. Heras-Juaristi, D. Pérez-Coll and G. C. Mather, *J. Power Sources*, 2017, **364**, 52–60.

34 Á. Triviño-Peláez, D. Pérez-Coll and G. C. Mather, *Acta Mater.*, 2019, **167**, 12–22.

35 F. J. A. Loureiro, D. Pérez-Coll, V. C. D. Graça, S. M. Mikhalev, A. F. G. Ribeiro, A. Mendes and D. P. Fagg, *J. Mater. Chem. A*, 2019, **7**, 18135–18142.

36 D. Pérez-Coll, G. Heras-Juaristi, D. P. Fagg and G. C. Mather, *J. Power Sources*, 2014, **245**, 445–455.

37 J. Lyagaeva, N. Danilov, G. Vdovin, J. Bu, D. Medvedev, A. Demin and P. Tsiakaras, *J. Mater. Chem. A*, 2016, **4**, 15390–15399.

38 D. R. Stull, E. F. Westrum and G. C. Sinke, *The chemical thermodynamics of organic compounds*, J. Wiley, 1969.

6. Effect of humification on the grain boundary conductivity and space-charge effects in yttrium-doped barium cerate

Abstract

The highly resistive grain boundaries of proton-conducting ceramics are a major contributor to the impairment of total conductivity at low temperatures. Yttrium-doped barium cerate (BCY), was recognised, in **Chapters 4** and **5**, to exhibit pure proton conductivity in the nominal absence of water ($p_{H2O} \leq 10^{-4}$ atm) below 450 °C. Under these conditions, the well-known instability of this material against carbon dioxide and humidity can be minimised, potentially allowing its application even in hydrocarbon-based atmospheres. Nonetheless, the electrochemical transport properties of the grain boundaries of BCY are still not well understood at low temperatures. Therefore, we compare the specific grain boundary and space-charge properties of $BaCe_{0.9}Y_{0.1}O_{3-\delta}$ (BCY10) in both wet and low humidity atmospheres, under oxidising and reducing conditions, by means of impedance spectroscopy in the temperature range 100 – 300 °C. In H_2, we observe an increase the specific grain boundary conductivity in nominally dry conditions, while the bulk conductivity remains practically humidity independent. Conversely, in O_2, both bulk and specific grain boundary conductivities are shown to be higher in in wet conditions. Finally, a *Mott-Shottky* model is employed to calculate the potential barrier heights and thickness from the grain boundary core in oxidising atmospheres, highlighting that low levels of humidity $p_{H2O} \leq 10^{-4}$ atm are sufficient to maintain functional performance. This work thereby offers an advance to the knowledge of the transport properties of this family of materials at low temperatures, with special emphasis to conditions of low humidity, for potential future applications in proton-conducting electrolyte membranes.

6.1. Introduction

Solid Oxide Fuel Cells (SOFCs) allow for efficient conversion of chemical energy directly into electricity by oxidation of fuels such as H_2 or even hydrocarbons, with minimum pollution and silently. First-generation fuel cells were targeted to operate in the high-temperature range around 800 – 1000 °C. However, despite promising performances exhibited by these devices, research has continued to focus on lowering their operation temperature to the intermediate-temperature range (500 – 600 °C) to improve longevity and to make the overall SOFC technology more affordable. One main constituent that determines the minimum operating temperature is the choice of electrolyte [1,2]. Proton-conducting ceramics such as doped barium cerates and zirconates ($BaCeO_3$-$BaZrO_3$) show considerably higher conductivity at a lower temperature than the oxide-ion conductors [1,2], making these electrolytes attractive alternatives at under these conditions. Due to this property, recent works have highlighted the creation of fuel cell devices using these ceramic materials that are capable of achieving very high performances at intermediate temperatures (500 – 650 °C), *e.g.* ≥ 1 W cm^{-2} at 600 °C [3–5].

According to future technological advances in terms of optimisation of electrolyte thickness, microstructures and the performance of other cell components, further decreases in temperature can be suggested. In this case, the study of ceramic proton conductors at very low temperatures (*e.g.* below 400 °C) can be important to understand the limitations of these materials. In such conditions, the total conductivity is often dominated by the grain boundary processes, contrasting with those at higher temperatures that are typically dominated by the bulk [6–9]. In this respect, investigations made on the intrinsic grain boundary properties of proton-conducting ceramics have demonstrated the existence of a space-charge layer that governs the grain boundary resistance [6–9]. Resistive grain boundaries have been reported for a variety of different proton-conducting ceramic such as $BaCe_{1-x}Gd_xO_{3-\delta}$ [10], $BaZr_{1-x}Y_xO_{3-\delta}$ (BZY) [6–9] and Ca-doped $LaNbO_4$ [11].

One of the best ceramic proton-conductors at the lowest temperatures is that of doped barium cerate [1,2]. In particular, **Chapter 4** focused on the study of the electrical transport properties of the specific composition $BaCe_{0.9}Y_{0.1}O_{3-\delta}$ (BCY10) in nominally dry conditions in

the intermediate temperature range (350 – 600 °C), where this composition was shown to be able to retain proton conductivity to very low water vapour pressures (p_{H2O} > 10^{-4} – 10^{-5} atm). The work, thus, highlighted the extended applicability of these materials, not only as electrolytes for fuel cells but also for potential chemical synthesis electrochemical reactors, where low levels of water vapour are essential to avoid unwanted side reactions in possible hydrogenation and dehydrogenation reactions. Nonetheless, while the conductivity mechanism of the specific composition $BaCe_{0.9}Y_{0.1}O_{3-\delta}$ (BCY10) has been analysed in detail at intermediate temperatures (350 – 600 °C), limited information is available at lower temperatures, where grain boundary behaviour becomes more important.

Moreover, due to the poor stability of BCY10 in atmospheres containing significant levels of moisture and/or carbon dioxide, it is also very important to fully understand the factors that affect the chemical stability of this material [1]. In this respect, a recent work by Kim *et al.* [12] demonstrated that the presence of amorphous intergranular phases in $BaCeO_3$ polycrystalline materials can be very reactive to these acidic atmospheres and can be the main cause of the structural disintegration of this composition [12]. Such intergranular phases are also commonly responsible for the severe retardation of proton migration [12].

As highlighted in Fig. 6.1, the predicted limits for barium hydroxide, $Ba(OH)_2$, formation from barium cerate below 400 °C, highlight that chemical instability with water vapour can be avoided when p_{H2O} values are lower than ~ 10^{-4} – 10^{-3} atm. On the contrary, the stability restrictions predicted for barium carbonate formation, $BaCO_3$, require much more stringent p_{CO2} values (~ 10^{-9} – 10^{-8} atm, Fig. 6.1).

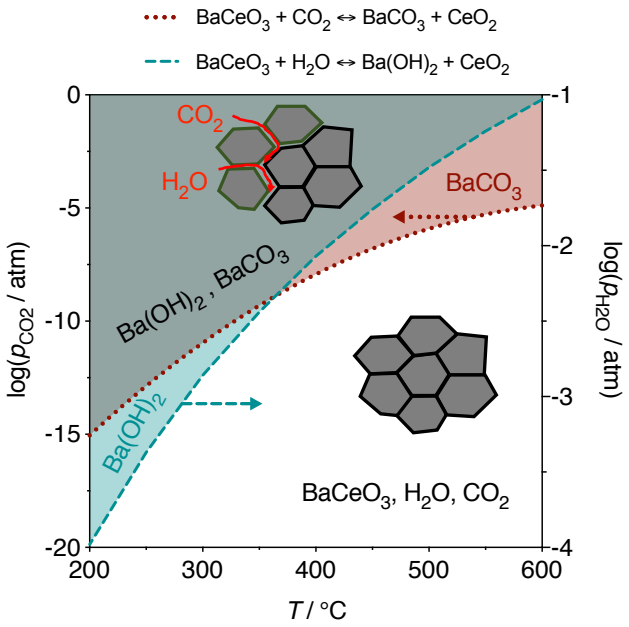

Fig. 6.1 – Stability diagram calculated from the thermodynamic equilibrium for the formation of barium carbonate in terms of carbon dioxide partial pressure (p_{CO2}) and for the formation of barium hydroxide in terms of water partial pressure (p_{H2O}) and temperature. Calculations performed using *FactSage* software [13]. The schematic inset in the figure illustrate the structural decomposition resultant from the interaction of H_2O and CO_2 with barium cerate.

Due to the substantial impact of these restrictions on both the conductivity and the chemical stability of BCY ceramics, the study of the grain boundary transport properties of this family of materials at very low humidity (*i.e.*, $\leq 10^{-4}$ atm) is, therefore, of critical interest for the optimisation of electrochemical cells using this composition at low temperatures.

In the present chapter we, therefore, aim to determine the influence of water vapour pressure (p_{H2O}) on the grain boundary electrochemical properties in both reducing and oxidising conditions of $BaCe_{0.9}Y_{0.1}O_{3-\delta}$ (BCY10). We performed measurements of conductivity in H_2 and O_2 in both wet ($p_{H2O} \sim 10^{-2}$ atm) and also in very low humidities ($p_{H2O} \leq 10^{-4}$ atm) that correspond to conditions of interest to potential chemical synthesis applications. The resultant bulk and specific grain boundary conductivities are discussed in detail in terms of their atmosphere dependency. We further employ a space-charge layer model to determine the intrinsic grain boundary properties of this important proton-conducting ceramic.

6.2. Experimental

6.2.1. Sample preparation and characterisation

Powder was synthesised using an acetate-H_2O_2 nitrate-free combustion method described elsewhere [14]. For this method, $Ba(CH_3COO)_2$ (Alfa Aesar), $Ce(CH_3COO)_3{\cdot}1.5H_2O$ (Alfa Aesar), $Y(CH_3COO)_3{\cdot}4H_2O$ (Alfa Aesar) and 30 wt% H_2O_2 (Sigma-Aldrich) were used as starting materials.

The calculated stoichiometric quantity of each acetate (fuel) precursor was dissolved in distilled water, and the mixed BCY-precursor salt was intimately dispersed using an ultrasonic bath. This process was followed by the addition of a calculated amount of H_2O_2 (oxidant) to attain a fuel to oxidant ratio of unity, according to the propellant chemistry [14]. After combustion, the BCY composition was calcined in ambient air at 1100 °C for 6 h, to obtain a pale-yellow powder.

Pellets were obtained from uniaxial pressing of the calcined BCY powder with 1 wt% of PVP (Polyvinylpolypyrrolidone, *Fluka*), followed by sintering at 1450 °C for 6 h. Pt electrodes were obtained from application of a Pt-paste (Heraeus CL11-5349) on both sides of the pellets with co-sintering at 900 °C for 20 min. Samples were examined for phase purity by X-ray diffraction (XRD) with a Shimadzu 7000 diffractometer (CuKα radiation, 40 kV and 40 mA) at room temperature. The x-ray diffraction patterns were obtained within the angular range $20 < 2\theta < 80°$, with scanning rate 2° per minute. *Rietveld* refinement was performed using Materials Analysis Using Diffraction (MAUD) software.

6.2.2. Electrochemical impedance measurements

Electrical measurements by AC Electrochemical Impedance Spectroscopy (EIS) were performed on the BCY electrolyte using an Electrochemie-Autolab PGSTAT302N frequency response analyser in the frequency range 0.01 Hz to 1 MHz with signal amplitude 50 mV. Measurements in single atmospheres (H_2 and O_2) were performed at 50 °C intervals in the direction of decreasing temperature, in the temperature range of 100 – 300 °C in wet ($p_{H2O} \sim 10^{-2}$ atm) and in low humidity atmospheres ($p_{H2O} \leq 10^{-4}$ atm) conditions.

Impedance spectra upon atmospheric changes were recorded with 1 to 1.5 h of stabilisation time between each measurement.

The impedance spectra were fitted using the software *ZView*© (Scribner Associates). Low humidity atmospheres were controlled using a professional SGT super clean gas moisture filter. This gas filter dries incoming gases to the level of p_{H2O} ~ 10^{-7} atm. Nonetheless, in hydrogen the true presence of water vapour was measured to be in the level of p_{H2O} ~ 10^{-4} atm due to the generation of water vapour by the equilibrium

$$\mathrm{H_{2(g)}} + \frac{1}{2}\mathrm{O_{2(g)}} \leftrightarrow \mathrm{H_2O_{(g)}} \qquad (6.1)$$

In contrast, the value of humidity in dried oxygen atmospheres was confirmed to be p_{H2O} ~10^{-7} atm due to the absence of hydrogen that can participate in the above equation.

For wetted gases, the humidification was controlled by bubbling gases through KBr-saturated H_2O at room temperature and the relative humidity was adjusted by mixing wet and dry gases to generate the p_{H2O} values ~ 10^{-4} and ~ 10^{-2} atm.

All gases were applied to the measurement jig with a maximum total flowrate of 50 mL min^{-1} supplied by Bronkhorst Thermal Mass flow Controllers (EL Flow). Oxygen sensor values were collected from a YSZ sensor. Relative humidity was collected from a JUMO humidity meter.

6.3. Results and discussion

6.3.1. Structural and microstructural characterisation

Fig. 6.2 shows the XRD pattern of $BaCe_{0.9}Y_{0.1}O_{3-\delta}$ (BCY10) obtained after calcination at 1100 °C. All the XRD peaks can be attributed to the pure perovskite yttrium-doped barium cerate, with no phase impurities observed. The phase was identified to exhibit orthorhombic symmetry at room temperature in air, according to the work of Takeuchi *et al.* [15] and Knight *et al.* [16], belonging to the space group n° 62 *Pmcn*. *Rietveld* refinement analysis was performed to retrieve structural (Table 6.1) and physical (Table 6.2) data. The obtained goodness of fit (X^2) was 2.56 %, denoting the accuracy of the simulation. The lattice parameters calculated for BCY10 are in agreement with previous works (Table 6.1).

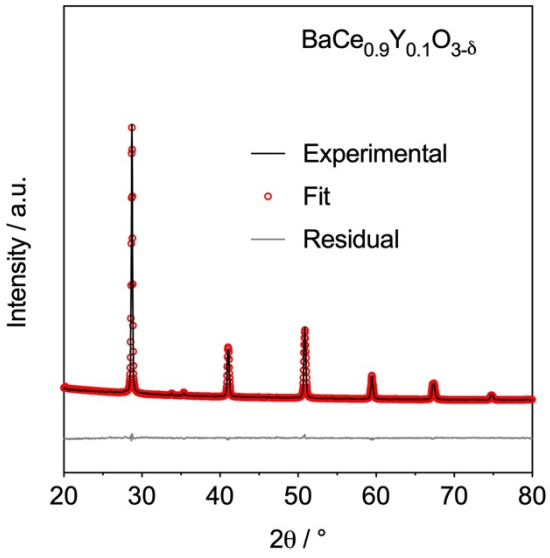

Fig. 6.2 – XRD patterns obtained for $BaCe_{0.9}Y_{0.1}O_{3-\delta}$ (BCY10) after calcination at 1100 °C for 6 h in air.

Table 6.1 – Structural parameters obtained for BCY10 from *Rietveld* refinement of the XRD data at room temperature. Literature data obtained for similar compositions under the same system is also shown for comparison.

Composition	Lattice parameter / Å			System	Volume / Å^3	R_{wp} / %	X^2	Ref.
	a	*b*	*c*					
BC	8.780(1)	6.237(1)	6.281(1)	*Pmcn*	-	7.2	-	[15]
BCY10	8.7679	6.2371	6.2132	*Pmcn*	339.78	8.0	2.56	This work
	8.774(1)	6.239(1)	6.204(1)	*Pmcn*	-	7.9	-	[15]

Fig. 6.3 illustrates the microstructure of the prepared sample, where we can observe a dense microstructure in agreement with the measured relative density of ~ 97 % (Table 6.2).

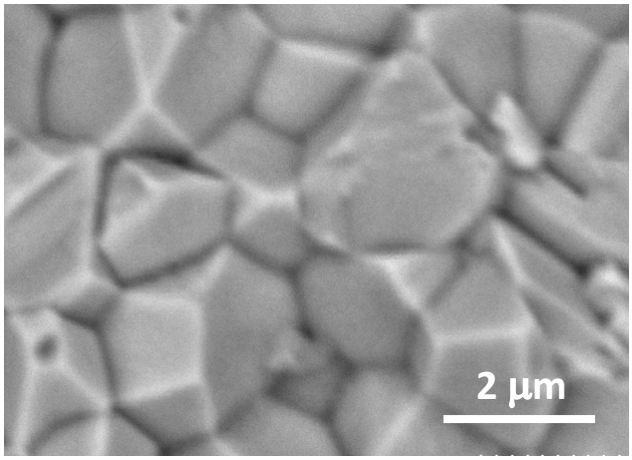

Fig. 6.3 – Cross-section microstructure of BCY10 sample synthesised by the nitrate free acetate–H_2O_2 combustion method, sintered at 1450 °C for 6 h.

Table 6.2 – Grain size and relative density of BCY10 compact synthesised by the nitrate free acetate–H_2O_2 combustion method and sintered at 1450 °C for 6 h.

Composition	**Theoretical density / g cm^{-3}**	**Relative density / %**	**Grain size / μm**
BCY10	6.2464	96.7	~1-3

6.3.2. The effect of water partial pressure in the bulk and specific grain boundary conductivities

Fig. 6.4 depicts an example of the impedance plots of BCY10 obtained in H_2 and O_2 at 100 °C for different water vapour partial pressures (p_{H2O} ~ 10^{-7}, ~ 10^{-4} and ~ 10^{-2} atm). We can observe that the spectra measured at 100 °C are composed of two separated semicircles corresponding to the high frequency bulk (C = ~ 10^{-11} F cm^{-2}) and the lower frequency grain boundary (C = ~ 10^{-8} F cm^{-2}) responses [14]. In addition, a small arc in some cases is also identified at low frequencies, which can be ascribed to the electrode processes (C ~ 10^{-6} F cm^{-2}) [14]. The bulk capacitance values were corrected for the strain capacitance arising from the equipment and connection cables and Pt wires, which was in the order of 10^{-11} F cm^{-2}. The impedance responses were fitted with two or three parallel *RQ* terms in series, each of them representing one of the mentioned processes. The effective capacitance was calculated by

$$C = R^{(1-\phi)/\phi} Q^{1/\phi} \tag{6.2}$$

where Q and ϕ are the usual parameters characterising the pseudo-capacitance.

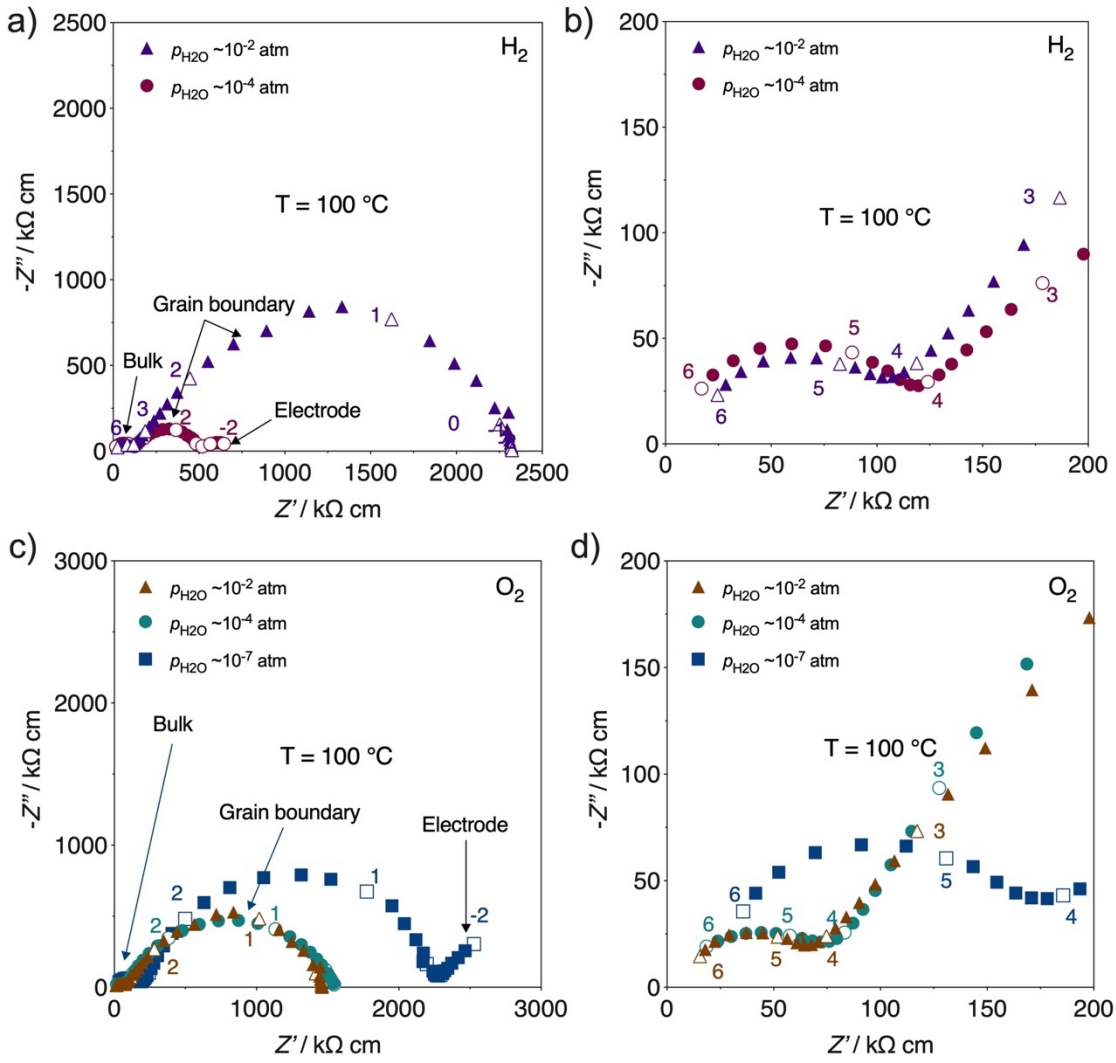

Fig. 6.4 – Examples of impedance spectra BCY10 in nominally dry (p_{H2O} ~10^{-4} atm) and wet (p_{H2O} ~10^{-2} atm) H_2, obtained at 100 °C. Numbers indicate the decades of the measuring frequencies.

Fig. 6.5 depicts the total, bulk and grain boundary and specific grain boundary conductivities of BCY10 in H_2 and in O_2, measured in wet (p_{H2O} ~ 10^{-2} atm) and in the low humidity atmospheres ($p_{H2O} \leq$ ~ 10^{-4} atm). We used the brick-layer model (BLM) to discriminate grain boundary *versus* bulk behaviour, which typically would require the knowledge of the grain boundary width ($\delta_{g.b.}$) as well as the grain diameter (D).

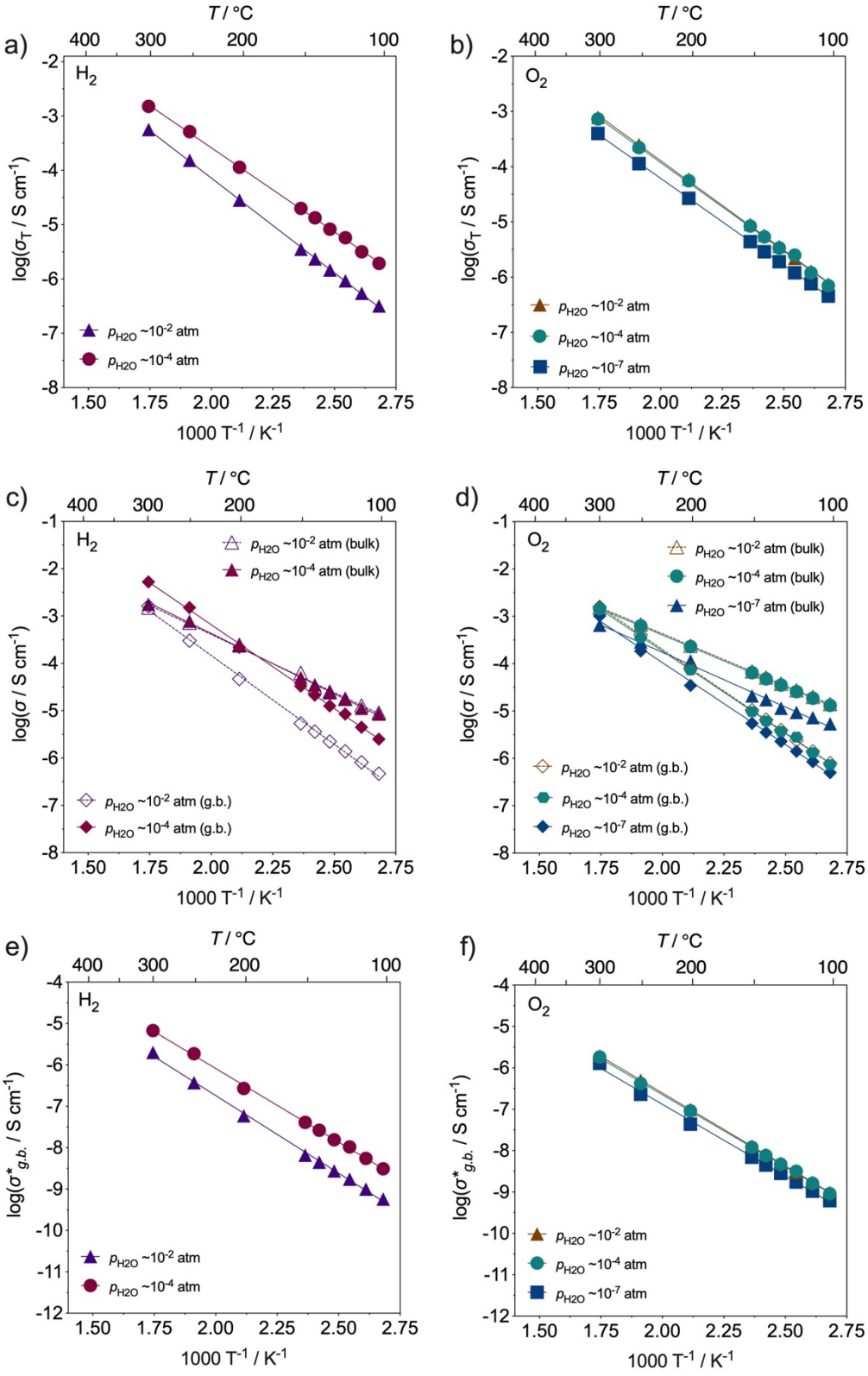

Fig. 6.5 – Temperature dependence of: a) and b) total; c) and d) bulk and grain boundary; e) and f) specific grain boundary ($\sigma^{*}_{g.b.}$) conductivities of BCY10, obtained in the temperature range 100 – 300 °C in H_2 (p_{H2O} ~ 10^{-2} and ~ 10^{-4} atm) and in O_2 (p_{H2O} ~ 10^{-2}, ~ 10^{-4} and ~ 10^{-7} atm).

The specific grain boundary conductivity ($\sigma^*_{\text{g.b.}}$) can be calculated from these terms by the following expression:

$$\sigma^*_{\text{g.b.}} = \frac{1}{R_{\text{g.b.}}} \cdot \frac{l}{A} \cdot \frac{\delta_{\text{g.b.}}}{D_{\text{grain}}} \quad (6.3)$$

In line with that commonly adopted in the literature [17,18], we assumed that the dielectric constant is similar for both bulk and grain boundary. In such a situation, $\sigma^*_{\text{g.b.}}$ can be calculated using the ratio of the bulk and grain boundary capacitances:

$$\sigma^*_{\text{g.b.}} = \frac{1}{R_{\text{g.b.}}} \cdot \frac{l}{A} \cdot \frac{C_{\text{bulk}}}{C_{\text{g.b.}}} \quad (6.4)$$

Fig. 6.5 shows that the total conductivity is dominated by the grain boundary response at low temperatures, < 300 °C, in all conditions, while at more elevated temperatures it is the bulk response that controls total conductivity. The total conductivity behaviour is shown to exhibit distinct atmosphere and p_{H2O} dependences. In H_2, the total conductivity is higher in nominally dry conditions (p_{H2O} ~ 10^{-4} atm), Fig. 6.5a, while in O_2, it is higher for values of $p_{H2O} \geq 10^{-4}$ atm (Fig. 6.5b). To explain these changes, the bulk and grain boundary conductivities will now be discussed separately.

Table 6.3 – Activation energy values obtained for the bulk, grain boundary and total conductivities.

Atmosphere		**Activation energy / eV**		
Gas	**p_{H2O} / atm**	**Bulk**	**Specific grain boundary**	**Total**
H_2	~ 10^{-2}	0.53	0.58	0.69
	~ 10^{-4}	0.53	0.60	0.63
O_2	~ 10^{-2}	0.45	0.60	0.64
	~ 10^{-4}	0.46	0.63	0.66
	~ 10^{-7}	0.47	0.62	0.64

The grain boundary responses show significantly higher activation energies (~ 0.6 eV) than those obtained for the bulk responses (~ 0.4 – 0.5 eV), as depicted in Table 6.3. The bulk conductivity in H_2 (Fig. 6.5c) is shown to be effectively independent of p_{H2O} in the tested humidity range. This is expected as BCY10 was shown to fully hydrate even in the measured low humidity conditions (p_{H2O} ~ 10^{-4} atm), due to its high equilibrium constant for water formation (**Chapter 4**). Therefore, it is expected that in the hydrogen atmosphere the

concentration of protonic charge carriers will be similar in for the bulk behaviour in both conditions of humidity:

$$H_2O + V_O^{\bullet\bullet} + O_O^x \Leftrightarrow 2OH_O^{\bullet} \quad (6.5)$$

Nevertheless, the specific grain boundary conductivity in H_2 (Fig. 6.5e) shows a pronounced negative dependence on p_{H2O}. This increase in the grain boundary conductivity of BCY10 in lower humidity is reflected by a related increase in total conductivity *e.g.* by a factor of ~ 3 at 200 °C shown in Fig. 6.5a in the drier condition. Such a behaviour in nominally dry reducing conditions could be associated to the presence of n-type electronic conductivity. Note the existence of n-type grain boundary conductivity has been previously observed in similar compositions in acceptor-doped CeO_2 [19] and $BaZr_{0.9}Y_{0.1}O_{3-\delta}$ [8], due to accumulation of electrons in the vicinity of a positively charged grain boundary core. On the other hand, while CeO_2 contains a reducible cation that could potentially lead to the formation of negatively charged electronic defects, the same is unlikely for the $BaZr_{0.9}Y_{0.1}O_{3-\delta}$ composition in the current conditions. An alternative hypothesis may, therefore, be necessary for the observation of this phenomenon in proton conductors. This explanation may come from the possibility to jointly produce electronic and protonic defects in the hydrogen atmosphere in these protonic materials, as given by the equation

$$H_2(g) + 2O_O^x \Leftrightarrow 2OH_O^{\bullet} + 2e' \quad (6.6)$$

In this respect, note that the mobility of electronic species is typically several orders of magnitude higher than that of protons at low temperatures [19–21], thus, potentially leading to the observed predominance of n-type grain boundary conduction. Although this situation is not observed for the bulk behaviour (**Chapter 4**), the exact composition of the grain boundary and, thus, the equilibrium constant of eqn (6.6) are unknown in the current case. It may also be likely that eqn (6.6) would be promoted in the vicinity of the grain boundary, due to the favourable accumulation of electrons in the neighbourhood of a positively charged grain boundary core.

Regarding the results in O_2, the bulk conductivity is shown to be higher for values of $p_{H2O} \geq 10^{-4}$ atm (Fig. 6.5d) and that effectively equal conductivities are obtained for the two humidity values p_{H2O} ~10^{-4} and ~10^{-2} atm. As noted in the experimental section, the

measured water vapour partial pressures in dry conditions in the O_2 atmosphere (p_{H2O} ~ 10^{-7} atm) are significantly lower than that obtained in the nominally dry hydrogen atmosphere (p_{H2O} ~ 10^{-4} atm), due to the effective absence of the water formation reaction (eqn (6.1)) in the former case. This much lower water vapour pressure does not provide conditions to maintain complete hydration of the BCY10 sample in the dry oxidising environment (**Chapter 5**), leading to the observed drop in bulk conductivity in comparison to that measured at higher levels of hydration, $p_{H2O} \geq 10^{-4}$ atm. Although this theory would explain the current results, the possibility of an increasing contribution of p-type electronic behaviour must also be taken into consideration in oxidising conditions, as previously reported [22]. The creation of p-type electronic carriers can be given by the following equation that results from the equilibrium between oxygen vacancies and holes:

$$\frac{1}{2}O_2 + V_O^{\bullet\bullet} \leftrightarrow O_O^x + 2h^{\bullet} \qquad (6.7)$$

Nonetheless, due to the competitive nature of equations 6.5 and 6.7, a higher grain boundary conductivity would be predicted in drier oxidising conditions [22] if the grain boundary were electronic in nature; a tendency that is contrary to that observed. In this respect, the previous study (**Chapter 5**) predicts that the concentration of electronic holes will be insufficient to dominate the total bulk transport at the low temperatures of the current work, and instead the bulk behaviour of BCY10 is likely to remain predominantly ionic [22]. Thus, although the exact composition of the grain boundary is uncertain, a comparable explanation based on dominant proton conduction can be suggested to support the similar observed p_{H2O} dependence of the specific grain boundary conductivity in oxidising conditions, depicted in Fig. 6.5f. To extend the assessment of the grain boundary behaviour of this material, further analysis of the grain boundary space-charge layer, is presented in the subsequent section.

6.3.3. The space-charge layer model

The grain boundary properties of polycrystalline materials are usually explained on the basis of space-charge effects [8,19,23]. Fig. 6.6 shows a schematic model of the grain boundary space-

charge layer, which is composed by a positively charged grain boundary core and two adjacent space-charge layers.

To assess the behaviour in the current materials, we considered a *Mott-Schottky* approximation [8] that assumes the acceptor dopant concentration $\left(c_{\mathrm{Y}}(\mathrm{x})\right)$, with an effective negative charge at the space charge layer, is frozen for temperatures lower than 1000 °C, with a similar distribution to that of the bulk $\left(c_{\mathrm{Y}}(\infty)\right)$. The relationship between the concentration profile of the species i at the space-charge layer with respect to the concentration in the bulk and the potential barrier height can be given by:

$$\frac{c_{\mathrm{i}}(\mathrm{x})}{c_{\mathrm{i}}(\infty)} = \exp\left[-\frac{z_{\mathrm{i}}\mathrm{e}}{\mathrm{k}T}.\Delta\varphi(0).\left(1-\frac{x}{\lambda^{*}}\right)\right] \qquad (6.8)$$

where the species i, with charge z_{i} has a concentration of $c_{\mathrm{i}}(\mathrm{x})$ and $c_{\mathrm{i}}(\infty)$ at position x in the space charge layer and in the interior of the bulk, respectively.

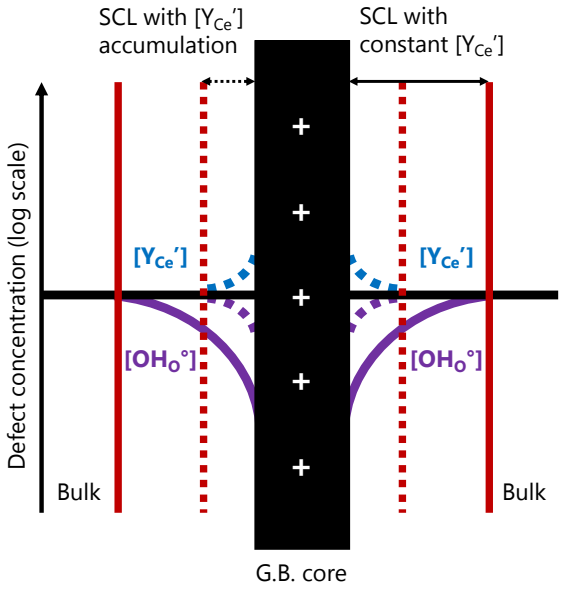

Fig. 6.6 – Schematic grain boundary core and both adjacent space-charge regions (adapted from [9]).

The *Schottky* barrier height ($\Delta\varphi(0)$) was determined by fitting the following equation:

$$\frac{\sigma_{\mathrm{bulk}}}{\sigma^{*}_{\mathrm{g.b.}}} = \frac{\exp\left(\frac{\mathrm{e}.z_{\mathrm{i}}.\Delta\varphi(0)}{\mathrm{k_B}.T}\right)}{2\frac{\mathrm{e}.z_{\mathrm{i}}.\Delta\varphi(0)}{\mathrm{k_B}.T}} \qquad (6.9)$$

The thickness of the space-charge layer is given by

$$\lambda^* = 2\lambda\sqrt{\frac{\mathrm{e}.\Delta\varphi(0)}{\mathrm{k_B}.T}} \tag{6.10}$$

where, λ is the *Debye* length

$$\lambda = \sqrt{\frac{\mathrm{k_B}.T.\varepsilon_\mathrm{r}.\varepsilon^0}{2\mathrm{e}^2 C_\mathrm{i}}} \tag{6.11}$$

where k_B is the Boltzmann constant, and C_i is the concentration of the species i. The following discussion excludes the behaviour in reducing conditions, as it was suggested in the previous section that both electronic and protonic charge carriers with different charges may exist in such conditions (eqn (6.6)). Such a situation prevents calculation of the space-charge properties in H_2 using eqn (6.9), without prior knowledge of the partial grain boundary conductivities in this atmosphere.

In contrast, in oxidising conditions, the previous chapter suggests that the conductivity is likely to be ionic in nature at these temperatures (**Chapter 5**). Thus, for values of $p_{H2O} \geq 10^{-4}$ atm, we may expect the dominance of protonic charge carriers, while for $p_{H2O} \sim 10^{-7}$ atm either protons or oxygen vacancies could be possible. We, therefore, calculate these values on assuming two potential scenarios: *i*) the dominance of protons; and *ii*) the dominance of oxide-ion vacancies, where the latter could become relevant in dry atmospheres.

Fig. 6.7a depicts the calculated *Schottky* barrier height as a function of temperature and humidification in O_2 by means of eqn (6.9), for these two potential species. In all cases, we obtained lower values for the *Schottky* barrier height in lower humidity conditions ($\Delta\varphi_{p_{\mathrm{H2O}}\sim 10^{-7}}(0)$) in comparison to that in wet ($\Delta\varphi_{p_{\mathrm{H2O}}\geq 10^{-4}}(0)$) (Table 6.4). Similar observations for lower $\Delta\varphi(0)$ values in dry conditions were also noted experimentally by Kjølseth *et al.* [8] for BZY10 in O_2 and theoretically by Bjørheim *et al.* [24]. The explanation given by Kjølseth *et al.* is based on changes in the core charge, where oxygen-ions at the grain boundary core are preferentially protonated while the oxygen vacancies in the bulk are preferentially consumed during hydration. This explanation would be in agreement with our results:

$$\mathrm{H_2O(g)} + \mathrm{V^{\bullet\bullet}_{O,bulk}} + 2\mathrm{O^x_{O,core}} \Leftrightarrow 2\mathrm{O^x_{O,bulk}} + 2\mathrm{OH^{\bullet}_{O,core}} \tag{6.12}$$

This equation describes such a scenario where the extent of positive charge carrier depletion in the adjacent zones of the grain boundary core, as depicted in Fig. 6.6, becomes aggravated in wet conditions due to *Coulombic* repulsion.

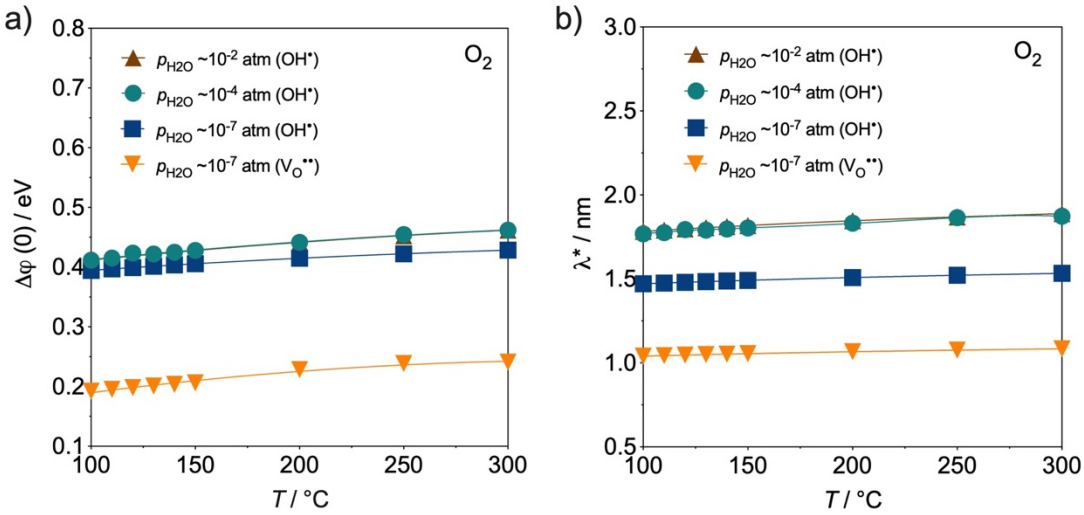

Fig. 6.7 – a) *Schottky* barrier height at the space-charge layer in O_2.; b) space-charge layer thickness. Calculations performed on the data obtained in O_2 ($p_{H2O,wet}$ ~10^{-2} and 10^{-4} atm, $p_{H2O,dry}$ ~10^{-7} atm).

The obtained values for the *Schottky* barrier height for BCY10 are comparable to similar compositions found in literature (Table 6.4).

Table 6.4 – *Schottky* barrier heights under wet and nominally dry O_2. Literature data for different proton-conducting ceramics is also shown for comparison. All values are based on conductivities obtained by eqn (6.9).

Composition	**Atmosphere**	$\Delta\varphi(0)$ **T = 200 °C**	**Ref.**
BCY10	Wet O_2 (p_{H2O} ~10^{-2} atm)	0.44 (OH•)	This work
	Dry O_2 (p_{H2O} ~10^{-4} atm)	0.44 (OH•)	
	Dry O_2 (p_{H2O} ~10^{-7} atm)	0.41 (OH•), 0.21 (V_O••)	
BC	Wet air	0.45 (226 °C) (OH•)	25
BC	Wet	0.40 (OH•)	26
BZY10	Wet O_2 (p_{H2O} ~10^{-2} atm)	0.51 (OH•)	8
	Dry O_2 (p_{H2O} ~10^{-5} atm)	0.22 (V_O••)	
	Wet O_2	0.47 (OH•)	27
BZY20	Wet O_2	0.41 (OH•)	10

Notwithstanding these changes between different p_{H2O} conditions (Fig. 6.7b), we have also determined a higher space-charge layer thickness, λ^*, in higher humidity conditions by means of eqn (6.10). For instance, at 200 °C, we estimated value of 1.83 and 1.85, respectively

for p_{H2O} ~ 10^{-4} and 10^{-2} atm; while, in dry conditions (p_{H2O} ~ 10^{-7} atm), we estimated values of 1.51 or 1.07 nm, respectively, considering dominance of protons or oxide-ion vacancies. This term can be directly related with the grain boundary thickness, given by:

$$\delta_{\mathrm{g.b.}} = 2\lambda^{*} + \delta_{\mathrm{g.b.,core}} \qquad (6.13)$$

thus, suggesting a lower grain boundary volume in drier conditions. Likewise, we also calculated the bulk-normalised concentration profiles by means of eqn (6.8), as depicted in Fig. 6.8, which shows the evolution of the concentration of defects along the grain boundary space-charge layer width at 200 and at 300 °C. The data highlights that the depletion of species is less severe in drier conditions and also at higher temperatures, in agreement with the space-charge barrier height and thickness values shown in Fig. 6.7. On the other hand, the greatest difference is only noted when assuming dominance of the double-positive charged oxide-ion vacancies in comparison to that of the single-positive charged hydroxyl group. An important feature is the very similar behaviour revealed between the two higher humidity values of p_{H2O} ~ 10^{-4} and 10^{-2} atm. that underscore that the nature of the space charge layer is effectively unchanged above p_{H2O} ~ 10^{-4}.

The benefit of operating at higher temperatures is apparent in Fig. 6.8 as, in all cases, the depletion of charge carriers in the grain boundary space-charge layers will be reduced as temperature increases.

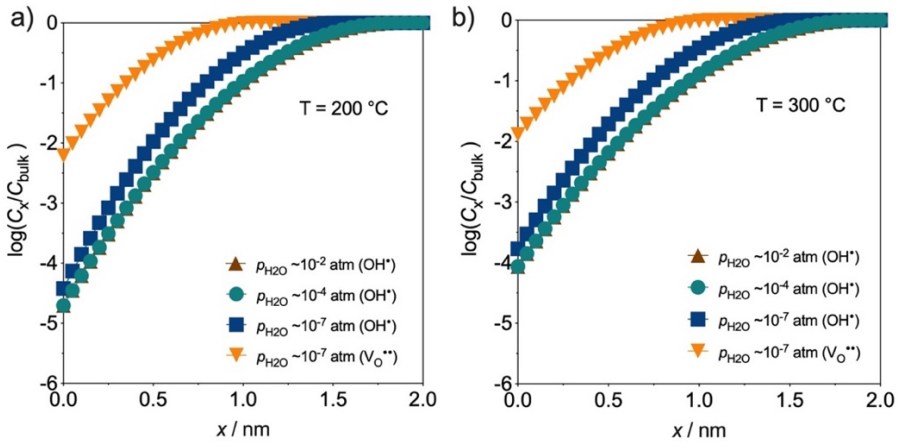

Fig. 6.8 – Bulk-normalised concentration profiles at the space-charge layer obtained at: a) 200 and b) 300 °C. Calculations performed on the data obtained in O_2 ($p_{H2O,wet}$ ~10^{-2} and 10^{-4} atm, $p_{H2O,dry}$ ~10^{-7} atm).

The results of the current chapter, therefore, highlight several important points. Firstly, the work underscores the difficulties that will be encountered on attempts to further reduce the operation temperature of BCY10. Below 300 °C, the grain boundary conductivity of this material is shown to become the dominating limitation to total conductivity, for all atmospheres. Moreover, in oxidising atmospheres, both the space-charge barrier height and thickness values become impaired with decreases in temperature. For these reasons, in order to be able to use this material at low temperatures one should concentrate efforts to optimise morphological variations to maximise grain sizes, or alternatively to engineer grain boundaries to improve the characteristics of the space charge layer, either by increases in the acceptor dopant concentration, as previously observed for the zirconate-based analogues [19], or by doping strategies that can provide a reduction in the positive charge of the space-charge core [28].

Secondly, important points are highlighted with respect to the minimum requirements of humidity. In oxidising atmospheres humidity levels $p_{H2O} \geq 10^{-4}$ atm are required to provide high bulk and specific grain boundary conductivities. In contrast, in hydrogen atmospheres, although the bulk conductivity remains unaffected by changes in humidity for the levels of p_{H2O} measured, the specific grain boundary conductivity is shown to become impaired as p_{H2O} increases.

Nonetheless, it is remarkable to denote that the relatively low humidity conditions of $p_{H2O} \sim 10^{-4}$ atm are sufficient to maintain high protonic conductivities for both the bulk and grain boundary contributions to total conductivity in BCY10 under all tested atmospheres at these temperatures. The ability of BCY10 to function under such low levels of humidity is highly interesting for potential applications, as these conditions have been previously suggested to be beneficial to avoid barium hydroxide formation and degradation of this material, according to thermodynamic predictions (**Chapter 4**).

Conclusions

The electrochemical behaviour of BCY10 is shown to be significantly dependent on the atmospheric conditions, namely on both the oxygen and water partial pressures. In reducing conditions (H_2), the bulk conductivity remains almost unaffected with respect to the p_{H2O} but denotes an increase of conductivity in the specific grain boundary response in nominally dry conditions that is suggested to be related to an increased effect of the n-type electronic conductivity over that of protonic conductivity.

In oxidising conditions, BCY10 is shown to have lower bulk and grain boundary conductivities in very dry conditions ($p_{H2O} \sim 10^{-7}$ atm), which can be related to the incomplete hydration of this composition under such conditions, in reference to that observed in the previous **Chapter 5**. Regarding the space-charge properties, it was found that the space-charge volume is lower in dry conditions and at higher temperatures, in agreement with literature data on similar protonic conducting perovskites, such as BZY10.

However, the most important conclusion of the current work is that by tailoring the water vapour partial pressure by using intermediate levels of $p_{H2O} \geq 10^{-4}$ atm, one can still use BCY10 as a pure proton conductor, where its bulk and grain boundary conductivities are maximised, while its stability against barium hydroxide formation can potentially still be maintained.

This work, thus, offers a new insight in the transport mechanism of the yttrium-doped barium cerates in conditions of low moisture and low temperature, while highlighting the challenges that remain to be overcome for them to become potential electrolyte membranes for chemical reactors operating in these conditions.

References

1 K. D. Kreuer, *Annu. Rev. Mater. Res.*, 2003, **33**, 333–359.

2 E. Fabbri, D. Pergolesi and E. Traversa, *Chem. Soc. Rev.*, 2010, **39**, 4355–4369.

3 S. Choi, C. J. Kucharczyk, Y. Liang, X. Zhang, I. Takeuchi, H.-I. Ji and S. M. Haile, *Nat. Energy*, 2018, **3**, 202–210.

4 H. An, H.-W. Lee, B.-K. Kim, J.-W. Son, K. J. Yoon, H. Kim, D. Shin, H.-I. Ji and J.-H. Lee, *Nat. Energy*, 2018, **3**, 870–875.

5 K. Bae, D. H. Kim, H. J. Choi, J.-W. Son and J. H. Shim, *Adv. Energy Mater.*, 2018, **8**, 1801315.

6 H. G. Bohn and T. Schober, *J. Am. Ceram. Soc.*, 2000, **72**, 768–772.

7 K. D. Kreuer, *Solid State Ionics*, 1999, **125**, 285–302.

8 C. Kjølseth, H. Fjeld, Ø. Prytz, P. I. Dahl, C. Estournès, R. Haugsrud and T. Norby, *Solid State Ionics*, 2010, **181**, 268–275.

9 S. Ricote, N. Bonanos, A. Manerbino, N. P. Sullivan and W. G. Coors, *J. Mater. Chem. A*, 2014, **2**, 16107–16115.

10 P. Babilo, T. Uda and S. M. Haile, *J. Mater. Res.*, 2007, **22**, 1322–1330.

11 R. Haugsrud and T. Norby, *Nat Mater*, 2006, **5**, 193–196.

12 H.-S. Kim, H. Bin Bae, W. Jung and S.-Y. Chung, *Nano Lett.*, 2018, **18**, 1110–1117.

13 C. W. Bale, E. Bélisle, P. Chartrand, S. A. Decterov, G. Eriksson, A. E. Gheribi, K. Hack, I.-H. Jung, Y.-B. Kang, J. Melançon, A. D. Pelton, S. Petersen, C. Robelin, J. Sangster, P. Spencer and M.-A. Van Ende, *Calphad*, 2016, **54**, 35–53.

14 N. Nasani, P. A. N. Dias, J. A. Saraiva and D. P. Fagg, *Int. J. Hydrogen Energy*, 2013, **38**, 8461–8470.

15 K. Takeuchi, C.-K. Loong, J. W. Richardson, J. Guan, S. E. Dorris and U. Balachandran, *Solid State Ionics*, 2000, **138**, 63–77.

16 K. S. Knight, M. Soar and N. Bonanos, *J. Mater. Chem.*, 1992, **2**, 709–712.

17 X. Guo and J. Maier, *J. Electrochem. Soc.*, 2001, **148**, E121–E126.

18 D. Pérez-Coll, P. Núñez and J. R. Frade, *J. Power Sources*, 2011, **196**, 8383–8390.

19 X. Guo, W. Sigle and J. Maier, *J. Am. Ceram. Soc.*, 2003, **86**, 77–87.

20 D. Perez-Coll, P. Nunez and J. R. Frade, in *Advances in Ceramics - Synthesis and Characterization, Processing and Specific Applications*, ed. C. Sikalidis, InTech, Rijeka, 2011, pp. 337–362.

21 D. Pérez-Coll, P. Núñez, J. R. Frade and J. C. C. Abrantes, *Electrochim. Acta*, 2003, **48**, 1551–1557.

22 M. Oishi, S. Akoshima, K. Yashiro, K. Sato, J. Mizusaki and T. Kawada, *Solid State Ionics*, 2009, **180**, 127–131.

23 M. Shirpour, B. Rahmati, W. Sigle, P. A. van Aken, R. Merkle and J. Maier, *J. Phys. Chem. C*, 2012, **116**, 2453–2461.

24 T. S. Bjørheim, M. Arrigoni, S. W. Saeed, E. Kotomin and J. Maier, *Chem. Mater.*, 2016, **28**, 1363–1368.

25 J. M. Polfus, M. Pishahang and R. Bredesen, *Phys. Chem. Chem. Phys.*, 2018, **20**, 16209–16215.

26 J.-H. Yang, B.-K. Kim and Y.-C. Kim, *J. Nanosci. Nanotechnol.*, 2015, **15**, 8584–8588.

27 S. B. C. Duval, P. Holtappels, U. F. Vogt, E. Pomjakushina, K. Conder, U. Stimming and T. Graule, *Solid State Ionics*, 2007, **178**, 1437–1441.

28 G. Heras-Juaristi, D. Pérez-Coll and G. C. Mather, *J. Power Sources*, 2016, **331**, 435–444.

7. Short-circuit analysis in *Ruddlesden-Popper*-based cathodes using yttrium-doped barium cerate symmetric cells

Abstract

The use of symmetric cells, where potential electrodes are deposited on both sides of an electrolyte substrate, is a common experimental method that permits the separation of the electrode performance from the overall cell behaviour. Unfortunately, the use of the promising electrolyte material, $BaCe_{0.9}Y_{0.1}O_{3-\delta}$ (BCY10), complicates the use of this experimental setup, due to possible internal short-circuiting of the electrolyte in oxidising conditions that can cause underestimation of measured polarisation resistances. Thus, the current work explores the influence of a parallel resistor in the equivalent circuit model in the high-order $La_4Ni_3O_{10-\delta}$ and $La_4Ni_3O_{10-\delta}$ – $BaCe_{0.9}Y_{0.1}O_{3-\delta}$ composite cathodes, deposited in both sides of a BCY10 proton-conducting electrolyte in the temperature range 350 – 550 °C. The results underscore that the cathode characteristics are highly dependent on the electronic leakage, especially at higher temperatures, and that suitable correction of data is imperative before discussion. Corrected values for polarisation resistance in wet O_2 reveal the composite cathode shows an improvement of total polarisation resistance by a factor of 1.5. The analysis on the oxygen reduction reaction mechanism allows to differentiate the rate-limiting processes between the electrodes, being the low-frequency term corresponding to surface processes, the dominant polarisation resistance and the most affected on formation of the composite.

7.1. Introduction

Decreasing the cathode polarisation resistance (R_p) is one of the main goals to leverage solid oxide fuel cells (SOFCs) into the energy conversion chain, especially for low temperatures of operation, where polarisation resistances resulting from the cathode can dominate the overall cell resistance [1,2]. Extensive research has been performed with respect to study different processing routes, electrical performances [3–6], and fundamental studies related to phase transitions, thermomechanical and transport properties, and oxygen reduction reaction (ORR) mechanisms, to improve the R_p of SOFC cathodes [3,6–9]. Mixed ionic electronic conductors (MIECs) have been extensively studied for this goal due to their high electronic/ionic conductivity [10], with some of the most common being the perovskite materials $La_{0.6}Sr_{0.4}Co_{0.2}Fe_{0.8}O_{3-\delta}$ (LSCF) [11–15] and $Ba_{0.5}Sr_{0.5}Co_{0.8}Fe_{0.2}O_{3-\delta}$ (BSCF) [16–18].

The use of proton-conducting electrolyte materials may benefit from the higher mobility of protons at lower temperatures, in comparison to that of oxide-ion conductors. Nonetheless, it is only very recently that researchers have attempted to design specific cathodes for the proton ceramic fuel cell (PCFC) application. In the limited number of works available, several distinct approaches have been adopted: *i)* mixed oxide-ion-electronic conductors, analogous to classical oxide-ion conducting solid oxide fuel cell (SOFC) cathodes [19,20]; *ii)* single phase mixed proton-electron proton-conducting oxides [21,22]; *iii)* composite electrodes of a proton-conducting oxide with a mixed oxide-ion and electron-conducting component [23]. Although it has been proposed that some proton conductivity in the electrode is required to lower the electrode polarization [24], it remains to be clarified which type of cathode concept (*i* – *iii*) is the most efficient and, thus, cathode design remains an important area of study.

Over the last years, a new material, the lanthanum nickelate, with general formula $[LaNiO_3]_n[LaO]$ (also known as $La_{n+1}Ni_nO_{3n+1}$), has emerged as a potential candidate to challenge the standard perovskite materials [25,26]. This family is part of the *Ruddlesden-Popper* series, where *n* represents the total number of consecutive trigonal, *R-3c*, $[LaNiO_3]$ layers that alternate with a rock-salt-type [LaO] block, stacked along the *c*-axis [25,26]. This

layered framework sustains even larger oxygen non-stoichiometry than the traditional perovskite structure, which makes the double-layered perovskites even more attractive to be used as SOFC cathodes, due to their higher oxide-ion conductivity, coupled with higher mechanical and thermal stabilities at elevated operating temperatures [25,26].

Particularly the high-order nickelates, such as the composition $La_4Ni_3O_{10-\delta}$ (n = 3), have shown increased conductivity with decreasing temperature, a feature that would potentially privilege this material to be used with proton-conducting devices to operate at intermediate temperatures, *e.g.*, below 500 – 600 °C. One good way to study the electrochemical performance these materials is to use a symmetrical cell configuration, where two identical electrodes are concentrically deposited in opposite sides of an electrolyte substrate [13,27–29].

In terms of the electrolyte, yttrium-doped barium cerates are among the best ionic conducting electrolytes to operate in low temperature conditions due to their ease of preparation, high total conductivities and high equilibrium constant for hydration[30]. The cerate-based composition, yttrium-doped barium cerate, $BaCe_{0.9}Y_{0.1}O_{3-\delta}$ (BCY10), has been recently demonstrated to exhibit high protonic conductivity even in conditions of low humidity (p_{H2O} ~10^{-4} atm), in both oxidising and reducing conditions, up to 400 °C (**Chapter 5**). Nonetheless, beyond these limits, this material starts to show significant p-type electronic conductivity when under oxidising conditions (**Chapter 5**).

The use of electrolyte substrates with significant electronic conductivity, caused by the formation of electrons or holes, can have a significant effect on the apparent electrode polarisation resistance [29,32,33]. Although this problem is partially solved in a functional SOFC, due to the much lower chemical potential of oxygen on the anode side, it is still a limitation that must be considered when using symmetrical cells [29,32,33]. This is due to the fact that in such a configuration the whole electrolyte is exposed to a single working gas atmosphere and, thus, the apparent electrode resistance may be dramatically affected [29,32,33].

Unfortunately, very few studies are available concerning the correction for this electronic short-circuit. The works that exist typically have approached this problem by the inclusion

of an external resistor in the equivalent circuit modelling that accounts for the electronic transference number, t_{eon}, of the electrolyte substrate [29,32,33]. Most of the available reports have been related to the correction for electronic leakage in the well-known ion-conducting $Ce_{1-x}Gd_xO_{2-\delta}$ (CGO) [29,32,33] electrolyte in reducing conditions. In contrast, minimal attention has been given to substrates based on proton conducting ceramics, *e.g.* as in the case of the Y-doped $BaZrO_3$ compositions [29], that may show significant p-type conductivity under oxidising conditions.

Thus, the current work explores the influence of a parallel resistor in the equivalent circuit model in the high-order $La_4Ni_3O_{10-\delta}$ and $La_4Ni_3O_{10-\delta}$ – $BaCe_{0.9}Y_{0.1}O_{3-\delta}$ composite cathodes, deposited in both sides of a $BaCe_{0.9}Y_{0.1}O_{3-\delta}$ (BCY10) proton-conducting electrolyte. The transport numbers of BCY10 in oxidising conditions have been determined in **Chapter 5**, where that study shows the existence of significant electronic conductivity at elevated p_{O2}, due to the formation of electronic holes with increasing temperature. Therefore, in the current chapter, we compare the electrode polarisation resistance of the $La_4Ni_3O_{10-\delta}$ in O_2 atmosphere in the temperature range 350 – 550 °C with and without electronic leakage correction.

7.2. Experimental

7.2.1. Powder preparation and characterisation

Powders of $La_4Ni_3O_{10-\delta}$ (LNO) were prepared using the citrate method, starting from Sigma-Aldrich chemicals of $La(NO_3)_3.6H_2O$, (98 %, Acros) and of $Ni(NO_3)_2.6H_2O$ (≥ 96 %, Sigma-Aldrich), which were dissolved in distilled water in stoichiometric proportions. After addition of citric acid ($C_6H_8O_7$, ≥ 99.5 %, Sigma-Aldrich) with metal:acid ratio 1:5, the solution was stirred vigorously for 30 minutes until a clear solution was obtained. Then, the solution was dried at 120 °C where it underwent-auto-combustion. The obtained powder was then calcined at 1075 °C for 6 h with a heating and cooling rate of 5 °C min^{-1} to obtain the respective *Ruddlesden-Popper* phase.

Samples were examined for phase purity by X-ray diffraction (XRD) with a Shimadzu 7000 diffractometer (CuKα radiation, 40 kV and 40 mA) at room temperature. The diffraction patterns were obtained within the angular range ($20 < 2\theta < 70°$) with scanning rate 2° per minute.

7.2.2. Symmetrical cell preparation and characterisation

LNO and LNO+BCY10 (40 vol% $BaCe_{0.9}Y_{0.1}O_{3-\delta}$ (BCY10, TYK Japan) particle suspensions were prepared in a ball-mill (PM200, Retsch, Haan, Germany) at 400 rpm for 2 h using 1 wt% of PVP (polyvinylpolypyrrolidone K30, 99.5 %, Fluka) and 6 mL of absolute ethanol, followed by ultrasonic bath (Ultrasons-H, JPSELECTA, Abrera, Spain) for 1 h, to break agglomerates and reduce the particle size distribution. Electrolyte disks of 1.5 mm thickness with a relative density > 95 % were obtained by uniaxially pressing BCY10 powder in an 18 mm mold at 200 MPa (1 min) and heated at 1400 °C for 6 h. The thin electrode films (~ 2 cm^2 of effective electroactive area) were deposited over the electrolyte support by spin-coating (spin coater model WS-650-23, Laurell Technologies Corporation, North Wales PA, USA) at 2000 rpm for 30 s. The symmetric cells of cathode-electrolyte assemblies were obtained by sintering in air at 1050 °C for 4 h, with heating and cooling rates of 1.5 °C min^{-1}.

Scanning electron microscopy (SEM, Hitachi Tabletop microscope TM4000Plus) was performed on cathode surface to assess their morphology and microstructure.

7.2.3. Electrochemical impedance spectroscopy measurements

Electrical measurements by AC Electrochemical Impedance Spectroscopy (EIS) were performed on the symmetric cells using an Electrochemie-Autolab PGSTAT302N frequency response analyser in the frequency range 0.01 Hz to 1 MHz with signal amplitude 50 mV. Measurements in single atmosphere (O_2) were performed at 50 °C intervals in the direction of decreasing temperature, in the temperature range of 350 – 550 °C in wet (p_{H2O} ~10^{-2} atm) conditions. Impedance spectra upon atmospheric changes were recorded after 1 h. Stabilisation was confirmed by a subsequent measurement after 1 h, coupled with a *Krammer-Kronings* Test.

The impedance spectra were fitted using the software *ZView*© (Scribner Associates). Nominally dry atmospheres were controlled using a Varian gas moisture filter; while, humidification was controlled by bubbling gases through a KBr-saturated H_2O at room temperature. The gases were applied to the measurement jig with a maximum total flowrate of 50 mL min^{-1} supplied by Bronkhorst Thermal Mass flow Controllers (EL Flow). Oxygen partial pressure (p_{O2}) values were collected from a YSZ sensor. Relative humidity values were collected from a JUMO humidity meter.

7.3. Results

7.3.1. Cathode composition and microstructure

The synthesised composite powder was analysed by X-ray diffraction (XRD) as depicted in Fig. 7.1. The powder consists of a single phase of $La_4Ni_3O_{10-\delta}$ (LNO, JCPDS 48-0124), yielding the expected *Ruddlesden-Popper* structure.

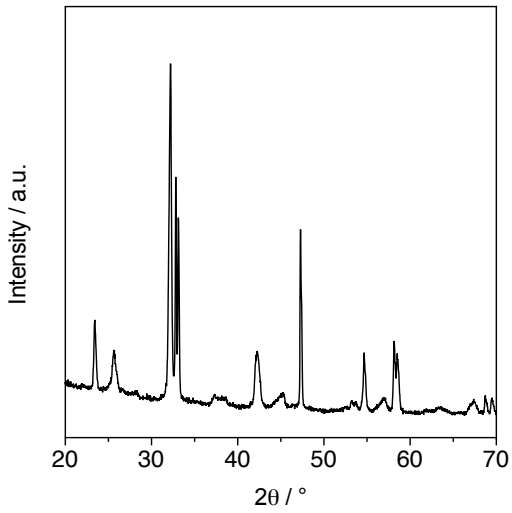

Fig. 7.1 – XRD pattern for the $La_4Ni_3O_{10-\delta}$ phase after calcination at 1050 °C for 4 h.

The typical microstructure of the sintered LNO and LNO-BCY10 cathode films are shown in Fig. 7.2. The electrode films show a fairly open microstructure and well percolated grains, which combined can facilitate gas-phase diffusion to the reaction sites [34]. Moreover, a uniform particle size distribution is observed, with particle size below ~ 1 – 2 μm. In addition, the EDS mapping shows a clear distinction between the LNO and the BCY10 phases as well as a homogenous distribution of the two phases.

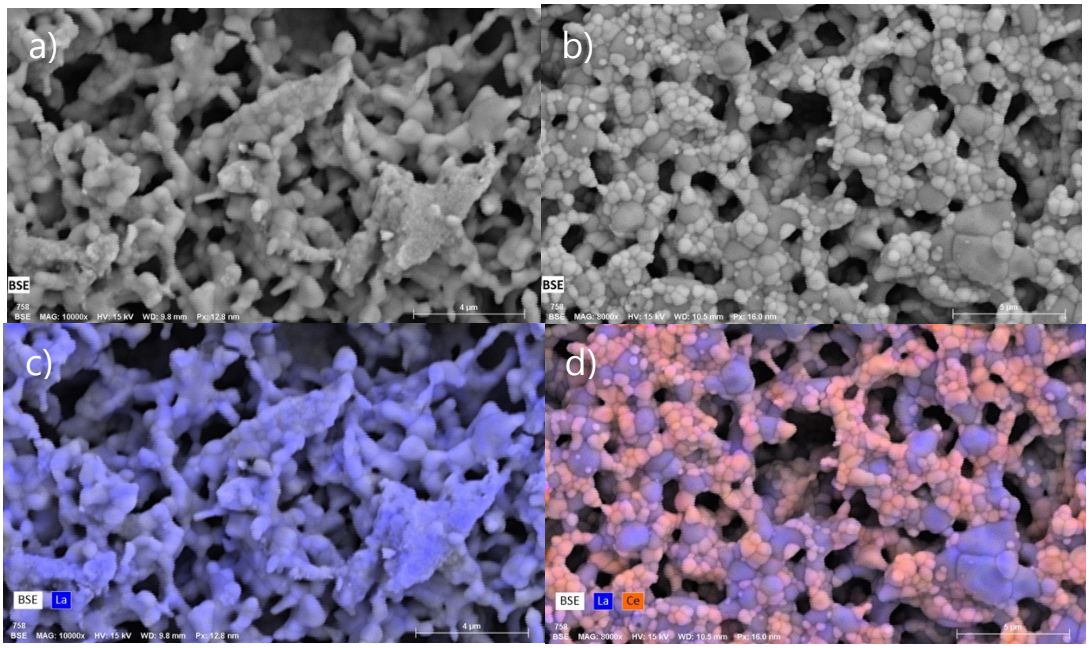

Fig. 7.2 – Top-view SEM microstructure of the a) LNO and b) LNO+BCY10 cathodes after sintering at 1050 °C for 4 h. EDS mapping performed in c) LNO and d) LNO+BCY10 cathodes.

7.3.2. Theoretical considerations on the electronic short-circuiting and chemical stability

The origin of electrical conduction in $BaCe_{0.9}Y_{0.1}O_{3-\delta}$ arises due to doping with a lower valence cation on the B-site, leading to the formation of charge compensating oxygen vacancies ($V_O^{\bullet\bullet}$), according to:

$$BaO + (1-y)CeO_2 + \left(\frac{y}{2}\right)Y_2O_3 \Longrightarrow Ba_{Ba}^{x} + (1-y)Ce_{Ce}^{x} + \\ +(y)\,Y_{Ce}' + \left(3-\frac{y}{2}\right)O_O^{x} + \left(\frac{y}{2}\right)V_O^{\bullet\bullet} \qquad (7.1)$$

Depending on the temperature and on the oxygen and water partial pressures (p_{O2}, p_{H2O}), these vacancies can be filled by water, promoting proton conductivity at lower temperatures:

$$H_2O_{(g)} + V_O^{\bullet\bullet} + O_O^{x} \Leftrightarrow 2OH_O^{\bullet} \qquad (7.2)$$

with the following mass action constant

$$K_{\mathrm{w}} \approx \frac{[\mathrm{OH}_{\mathrm{O}}^{\bullet}]^2}{p_{\mathrm{H2O}}[\mathrm{V}_{\mathrm{O}}^{\bullet\bullet}][\mathrm{O}_{\mathrm{O}}^{\mathrm{x}}]} \tag{7.3}$$

or by oxygen, promoting the characteristic p-type electronic conductivity in more oxidising atmospheres and with increasing temperature:

$$\frac{1}{2}\mathrm{O}_{2(\mathrm{g})} + \mathrm{V}_{\mathrm{O}}^{\bullet\bullet} \leftrightarrow \mathrm{O}_{\mathrm{O}}^{\mathrm{x}} + 2\mathrm{h}^{\bullet} \tag{7.4}$$

with the following mass action constant

$$K_{\mathrm{O}} \approx \frac{[h^{\bullet}]^2}{[V_{\mathrm{O}}^{\bullet\bullet}].p_{O2}^{1/2}} \tag{7.5}$$

Combining the fixed vacancy concentration ($[\mathrm{V}_{\mathrm{O}}^{\bullet\bullet}] \cong [\mathrm{Y}_{\mathrm{Ce}}^{\prime}]$) with the equilibrium constant (eqn (7.5)) yields

$$[\mathrm{h}^{\bullet}] \approx K_{\mathrm{O}}^{1/2}.[\mathrm{Y}_{\mathrm{Ce}}^{\prime}]^{1/2}.p_{\mathrm{O2}}^{1/4} \tag{7.6}$$

from which one obtains the well-known 1/4 power law for the dependence of electronic conductivity on oxygen partial pressure (p_{O2}). The total conductivity, σ_{T} (the sum of the ionic, σ_{ion}, and electronic, σ_{eon}, conductivities), thus exhibits an oxygen partial pressure dependence given as

$$\sigma_{\mathrm{T}} = \sigma_{\mathrm{ion}} + \sigma_{\mathrm{eon}} \tag{7.7}$$

The corresponding electronic transport number can, thus, be calculated by

$$t_{\mathrm{eon}} = \frac{\sigma_{\mathrm{eon}}}{\sigma_{\mathrm{T}}} \tag{7.8}$$

The electronic transport numbers for $BaCe_{0.9}Y_{0.1}O_{3-\delta}$ (BCY10) were calculated using the values of t_{eon} in O_2 obtained from **Chapter 5**. Fig. 7.3a depicts the electronic transport numbers related to the test conditions (p_{O2} = 1 atm and $p_{H2O} \sim 10^{-2}$ atm). From first inspection, we can observe that significant electronic transport may exist within the temperature range under study (T = 350 – 550 °C), which could subsequently influence the measured polarisation behaviour of the symmetrical cell arrangement.

Fig. 7.3b depicts the stability diagram of the $La_4Ni_3O_{10-\delta}$ phase that was calculated using the thermodynamic data reported elsewhere [35]. Typical decomposition of the double perovskite phase can be expected with increasing temperature and decreasing p_{O2}:

$$3La_4Ni_3O_{10(s)} \rightarrow 4La_3Ni_2O_{7(s)} + NiO_{(s)} + 0.5O_{2(g)} \quad (7.9)$$

Nonetheless, under the experimental conditions used in the current work (T = 350 – 550 °C), any typical phase decomposition yielding $La_3Ni_2O_{7-\delta}$ phase is not expected in O_2 atmosphere (Fig. 7.3b).

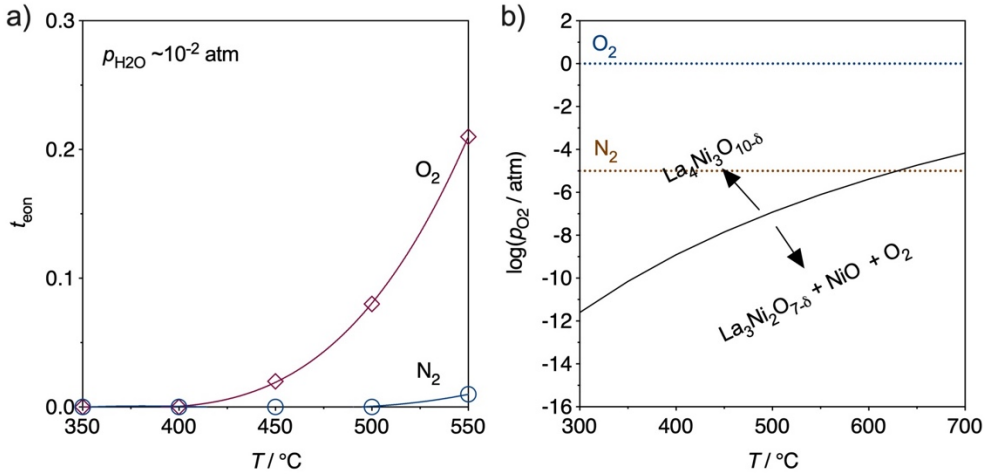

Fig. 7.3 – a) electronic transport number of BCY10 in wet and nominally dry O_2 obtained in **Chapter 5**; b) stability diagram of the $La_4Ni_3O_{10-\delta}$ (LNO) phase as a function of temperature (dashed lines indicate the oxygen partial pressure in typical atmospheres of O_2 and of N_2). Thermodynamic data reported elsewhere [35].

7.3.3. Equivalent Circuit Model (EQM) and Distribution Function of Relaxation Times (DFRT) analyses

Typical impedance spectra obtained at 500 °C in wet O_2 are depicted in Fig. 7.4a and b. In the case of a pure ion-conductor electrolyte, the total polarisation resistance (R_p) can be directly retrieved from subtracting the electrolyte resistance from total resistance [32]. However, in the case of a mixed ionic electronic conductor such as BCY10, R_p cannot be directly calculated due to the potential internal short circuit through BCY10. In our work,

the intercept of the impedance spectra with the real-axis at high frequency $\left(Z_{\mathrm{Q}} = 1/T(j\omega C)^{\phi} \to \infty\right)$ corresponds to the electrolyte electrical resistance (R_{ohm}), which corresponds to the sum, in parallel, of the ionic (R_{ion}) and electronic (R_{eon}) resistances, given by

$$\frac{1}{R_{\mathrm{ohm}}} = \frac{1}{R_{\mathrm{ion}}} + \frac{1}{R_{\mathrm{eon}}} \tag{7.10}$$

In contrast, the intercept at low frequency $\left(Z_{\mathrm{Q}} = 1/T(j\omega C)^{\phi} \to 0\right)$ corresponds to the total resistance (R_{T}) of the cell, given by

$$\frac{1}{R_{\mathrm{T}}} = \frac{1}{R_{\mathrm{ion}}+R_{\mathrm{p}}} + \frac{1}{R_{\mathrm{eon}}} \tag{7.11}$$

On this assumption, we can calculate the total polarisation resistance of the electrode by

$$R_{\mathrm{p}} = \frac{R_{\mathrm{T}}R_{\mathrm{eon}}}{R_{\mathrm{eon}}-R_{\mathrm{T}}} - R_{\mathrm{ion}} \tag{7.12}$$

where,

$$R_{\mathrm{eon}} = \frac{R_{\infty}}{t_{\mathrm{e}}} \tag{7.13}$$

Previous works on lanthanum nickelates-based cathodes report EQM models considering two or three processes to describe the oxygen reduction reaction mechanism occurring in the electrode [36–39]. Here, we considered the models represented in Fig. 7.4c and d, which consider the existence of three individual processes: $L_1[(R_{\mathrm{ion}}(R_{\mathrm{high}}Q_{\mathrm{high}})(FLW)(R_{\mathrm{low}}Q_{\mathrm{low}})]$ without short-circuiting correction; and $L_1[(R_{\mathrm{ion}}(R_{\mathrm{high}}Q_{\mathrm{high}})(FLW)(R_{\mathrm{low}}Q_{\mathrm{low}})||R_{\mathrm{eon}}]$ for the model with correction. In these circuits, L_1 corresponds to the inductance created by the equipment connection cables and platinum wires. R_{ion} is the electrolyte ionic resistance in series with 3 distinct electrode contributions consisting of resistances (R_{n}) in parallel with constant phase elements (Q_{n}), while R_{eon} is the electronic resistance from the electrolyte support, at it is in parallel with all resistances to account for the electronic leakage crossing the entire sample.

In the case of the *RQ* elements, the impedance can be defined by $Z_{\mathrm{Q}} = Q_{\mathrm{i}}^{-1}(\mathrm{i}\omega)^{-\phi}$, where ω is the angular frequency and Q_{i} and ϕ are the usual parameters characterising the pseudo-capacitance and the exponent of the angular frequency, respectively, and the

effective capacitance is given by $C = R^{(1-\phi)/\phi} Q^{1/\phi}$ [6,13,40,41]. However, the spectra were also fitted including an additional finite-length Warburg element (*FLW*), at intermediate frequencies, to represent the bulk diffusion, due to presence of the typical ~ 45 ° slope at intermediate frequencies [13,41]. The total anode polarisation resistance (R_p), characterising the anode electrochemical performance, was obtained from the sum of the overall electrode resistances (R_{high} + R_{mid} (*FLW*) + R_{low}) multiplied by the electrode surface area and divided by 2, to consider the symmetrical cell configuration [6,13,40,41]

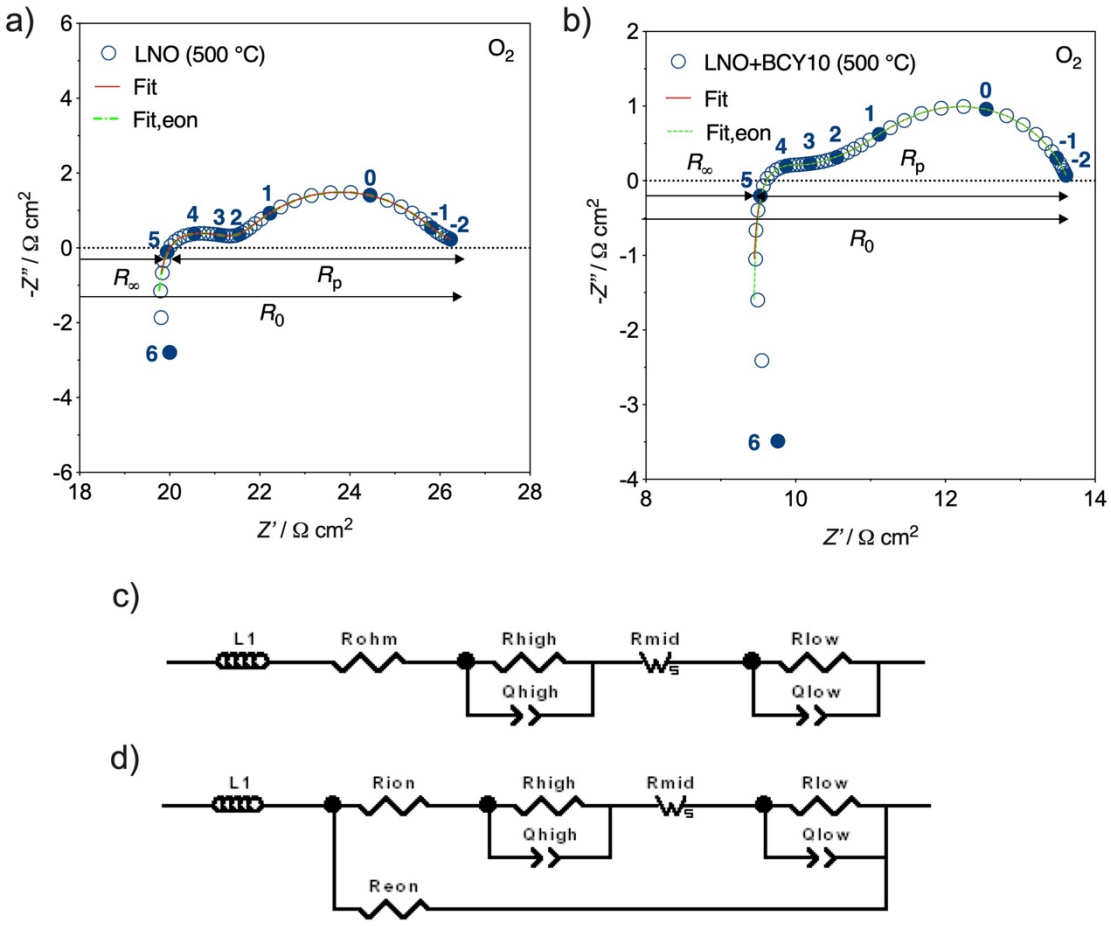

Fig. 7.4 – Impedance plots obtained for the a) LNO and b) LNO+BCY10 composite cathodes in wet O_2 at 500 °C; c) equivalent circuit used in this work to fit the impedance data without electronic pathway correction (*RQ*+*FLW*+*RQ*) and d) including a parallel resistor for the compensation of the electronic short-circuit (*RQ*+*FLW*+*RQ* ||R_{eon}).

Fig. 7.5a and b show examples of the so-called residuals plots of the fitting using both equivalent circuits to fit the impedance data from Fig. 7.4a and b. The plots represent the calculated residual differences between the real and the imaginary values of the data and the fitting versus log(*f*), which were calculated using the following expressions [42]:

$$\Delta_{\mathrm{real}}(\omega_{\mathrm{i}}) = \frac{Z_{\mathrm{data,real}}(\omega_{\mathrm{i}}) - Z_{\mathrm{fit,real}}(\omega_{\mathrm{i}})}{|Z_{\mathrm{data}}(\omega_{\mathrm{i}})|} \quad (7.14)$$

$$\Delta_{\mathrm{imag}}(\omega_{\mathrm{i}}) = \frac{Z_{\mathrm{data,imag}}(\omega_{\mathrm{i}}) - Z_{\mathrm{fit,imag}}(\omega_{\mathrm{i}})}{|Z_{\mathrm{data}}(\omega_{\mathrm{i}})|} \quad (7.15)$$

where $\omega = 2\pi f$. We can observe in the figures that a small error, *i.e.* < 0.5 %, was achieved by using both equivalent circuits in both fittings, which is indicative of the very good quality of the fitting [42]. This result is important to ensure the reliability of the relevant electrochemical parameters, extracted from the fittings and discussed in the next section.

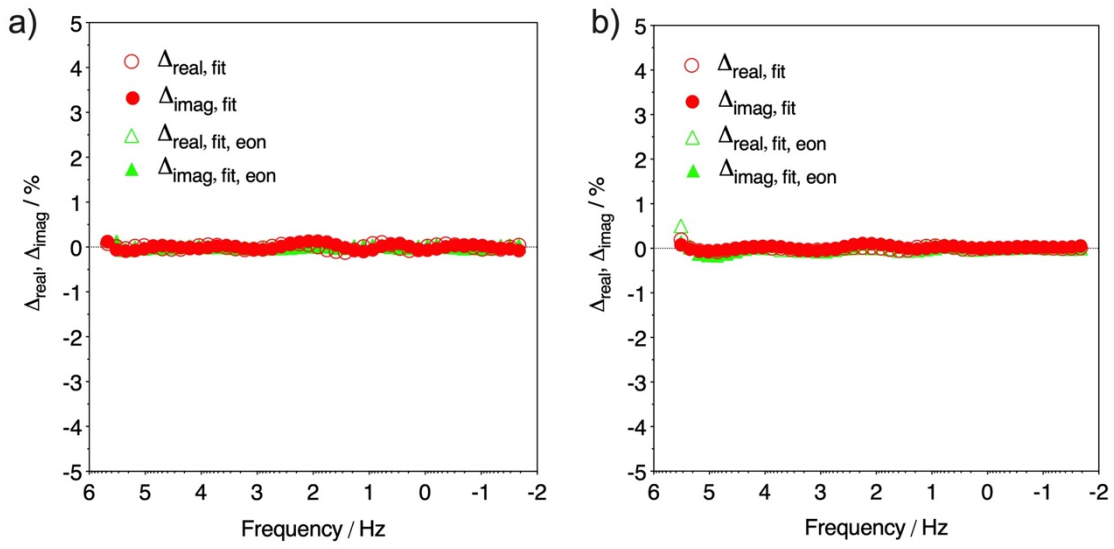

Fig. 7.5 – Residuals plots obtained for a) LNO and b) LNO+BCY10 composite cathodes in wet O_2 at 500 °C.

Fig. 7.6 depicts the Distribution Function of Relaxation Times (DFRT) analysis performed on the LNO and the LNO+BCY10 cathodes. This procedure was executed using the following expression [42,43]:

$$R_{\mathrm{i}}.G(\tau)_{\mathrm{RQ}} = \frac{R}{2\pi}.\frac{\sin((1-\phi)\pi)}{\cosh\left(n\ln\left(\frac{\tau}{\tau_0}\right)\right)-\cos((1-\phi)\pi)} \quad (7.16)$$

with: $\tau_0 = \omega_0^{-1} = \sqrt[\phi]{R_{\mathrm{i}}.Y_0}$.

Due to the limitation of this procedure to the *RQ* elements only, we have also adopted an alternative procedure to the *Finite Length Warburg* dispersion (*FLW*):

$$R_{\mathrm{i}}.G(\tau)_{\mathrm{FLW}} = \frac{R_{\mathrm{i}}}{\pi A}.\frac{\sin(\phi.\pi).\left(1-B^2\right)-2\cos(\phi.\pi).Y.\sin(2A.sin(\phi.\pi))}{1+2B.\cos(2A.sin(\phi.\pi))+B^2} \quad (7.17)$$

where $A = \left(\frac{\tau_0}{\tau}\right)^n$ and $B = \exp(-2\,cos(\phi.\pi))$.

The DFRT is then the sum of all separate contributions [42,43]:

$$R_{\mathrm{p}}.G(\tau) = \sum_i R_{\mathrm{i}}.G(\tau) \quad (7.18)$$

with $R_{\mathrm{p}} = \sum_i R_{\mathrm{i}}$. In addition, we have also utilised a *Fourier* transform to the impedance data using a Matlab programming code to the *Tikhonov* Regularization (TR) [42,43]. From Fig. 7.6, we can observe that the number of individual peaks obtained by the TR procedure has a relatively close match to those obtained by the exact representation of the DFRT, retrieved directly from the EQM analysis using eqn (16) – (18). This confirms the presence of the three distinguishable processes from the impedance data in Fig. 7.4a and b. Nonetheless, we can also denote small peaks in R_{mid} region, which are simply related to the elevated value of the parameter ϕ (close to 0.5) [43], in both samples (Fig. 7.6), and, thus, these features were not considered as individual polarisation processes.

The DFRTs calculated from eqn (16) – (18) denote a sharp peak at 10^{-3} – 10^{-2} s for both samples, which is related to the *FLW* element to characterise R_{mid}. In contrast, the broader peaks correspond to the R_{high} and R_{low} terms, with the time constants, respectively, at around 10^{-5} and 0.1 s. Another interesting aspect of this analysis is that the three individual polarisation processes have similar time constants for both samples, which increases our confidence in using the same EQM model for the interpretation of the oxygen reduction reaction mechanism of both cathodes.

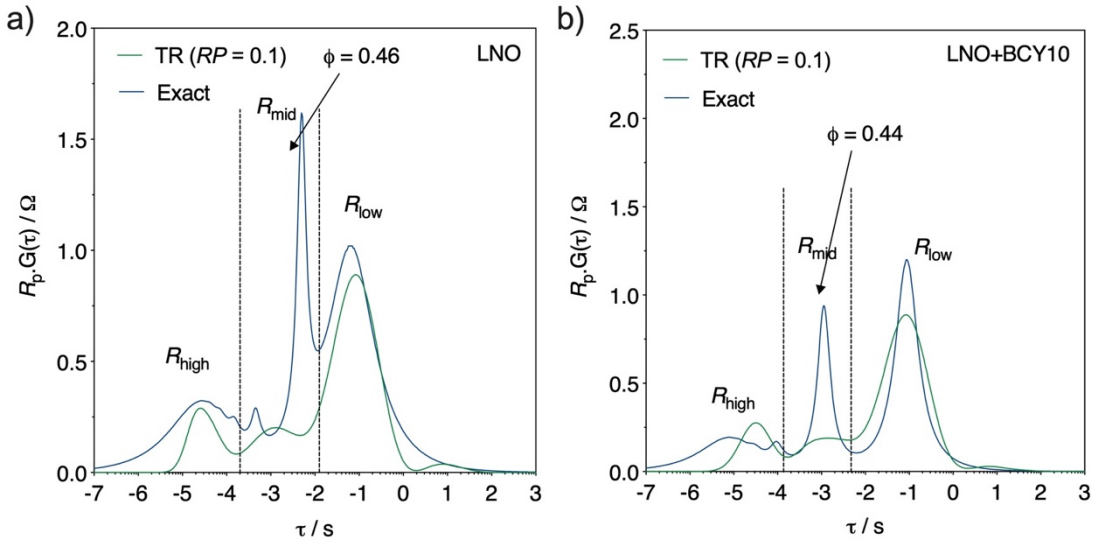

Fig. 7.6 – DFRT obtained from a EQM of a linear combination of (*RQ*) circuits and by using the *Tikhonov* Regularisation (TR) [42,43] at 500 °C.

The values obtained for the electronic short-circuiting resistance (R_{eon}) from the fitting of the offset resistance measured at high frequency (R_{ohm}) and eqn (7.13), are presented in Table 7.1 as a function of temperature. The results corroborate the previous discussion that the obtained R_{eon} values are noted to be vastly lower with increasing temperature, due to the increased electronic transference number (Fig. 7.3a). Moreover, we also noted that the value for R_{ohm} is lower in the case of the composite, a behaviour that has previously been ascribed to the increase of the TPB length with the BCY10 phase addition to the cathode structure.

Table 7.1 – Ionic and electronic resistances from the BCY10 electrolyte obtained from the fitting using the equivalent circuit from Fig. 7.4d.

Composition	**T / °C**	**Resistances / Ω cm²**	
		R_{ion}	R_{eon}
LNO	**350**	-	-
	400	-	-
	450	27.32	1338.50
	500	19.78	227.50
	550	16.08	60.48
LNO+BCY10	**350**	-	-
	400	-	-
	450	13.92	682.18
	500	10.06	115.68
	550	8.17	30.72

Subsequent adoption of the R_{eon} values from Table 7.1 and that of the ionic component (R_{ion}) from eqn (10) in the equivalent circuit from Fig. 7.4d allows fitting of the data and correction of the measured impedance measurements for electrolyte short-circuiting. Fig. 7.7 presents the comparison between the data of the polarisation resistances determined as a function of temperature for each sample, with and without correction using, respectively, the equivalent circuits from Fig. 7.4c and d. We can clearly observe that the largest deviation between corrected and uncorrected polarisation behaviour is noted at high temperature (550 °C), whereas only slight variations are shown below 450 °C.

Further discussion on the elementary steps governing the total polarisation resistance will be addressed in the following section.

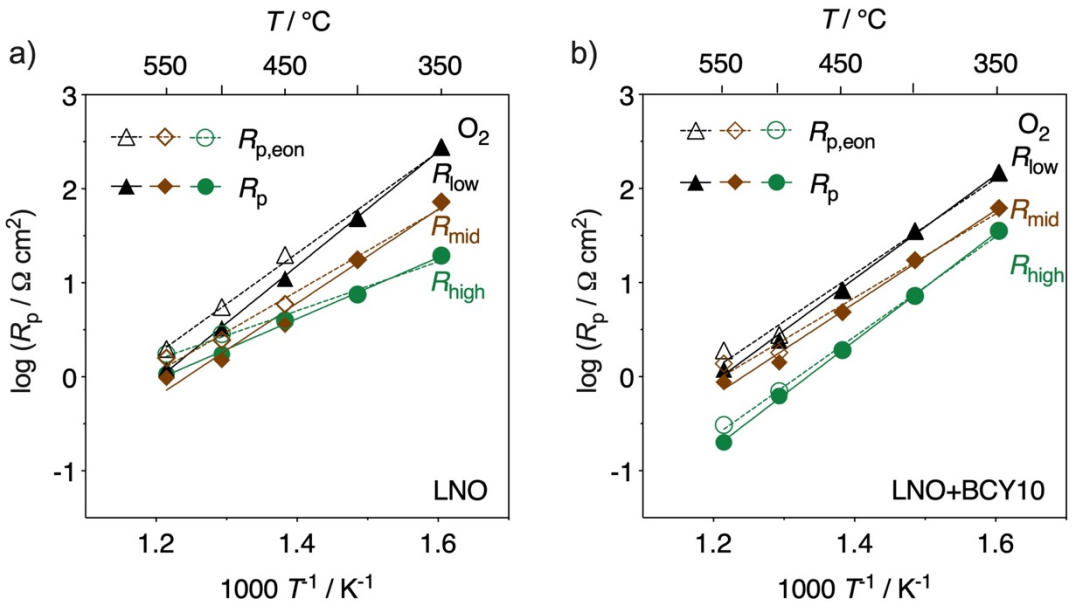

Fig. 7.7 – Temperature dependence of the polarisation resistances, R_{high}, R_{mid} and R_{low}, obtained for LNO (a) and LNO+BCY10 (b) cathodes, using the equivalent circuits from Fig. 7.4c and d (with, $R_{p,eon}$, and without, R_p, electronic pathway correction, respectively).

7.4. Discussion

Fig. 7.8 depicts the corrected polarisation resistances, $R_{p,eon}$, $R_{high,eon}$, $R_{mid,eon}$ and $R_{low,eon}$, as a function of temperature for the LNO and LNO+BCY10 cathodes in wet O_2 in the temperature range 350 – 550 °C. In terms of global behaviour, R_p was found to have an improvement by a factor of 1.5 by the addition of BCY10 phase. In addition, the activation energy (E_a) determined for this term (Table 7.2) was 0.95 eV for LNO and 1.03 eV for LNO+BCY10 composite cathodes, in agreement with previous reports on lanthanum nickelates [39,44].

The analysis will proceed with the interpretation of the elementary steps of the oxygen reduction reaction mechanism for both compositions that is schematically represented in Fig. 7.9. Regarding the high-frequency contribution, $R_{high,eon}$, it was found to have the smallest magnitude at lower temperatures for both samples (Fig. 7.7 and Fig. 7.8). However, a significant difference in the E_a calculated for this term was observed between the LNO (0.68 eV) and the composite (0.80 eV) cathodes (Table 7.2). The much higher E_a value obtained for the composite is most certainly a result of the increased TPB area due to the presence of the electrolyte phase within the cathode structure [6]. The capacitance value calculated for this term is in the order of ~ 10^{-6} F cm^{-2}, which can be related to a process occurring at the electrolyte/electrode interface [6,13,20,45]. Moreover, this is a typical value for the double-layer capacitance that is normally related to charge-transfer processes, as previously observed in other perovskite cathode materials [6,13,20,45].

The mid-frequency response, $R_{mid,eon}$, was found to have increased magnitude over that of $R_{high,eon}$ at lower temperatures for both compositions (Fig. 7.7 and Fig. 7.8). This term presents a very high capacitance value of ~ 1 F cm^{-2} at 350 °C, that can be considered typical of a chemical capacitance, C_{chem} [6,10,46]. However, at higher temperatures, this value decreases to ~ 0.01 F cm^{-2} at 550 °C. It is possible that this decrease in the C_{chem} with increasing temperature is due to an increase of the electroactive area of the TPB length that also leads to a decrease in resistance at higher temperatures [6,10,46]. Due to this feature, $R_{mid,eon}$ can be related to the diffusion processes occurring at the bulk of the electrode

[6,10,46]. The following equation represents the mechanism involved with an $O^{-}_{\text{reaction site}}$ ion at the reaction site that is incorporated in an oxygen vacancy [41,47]:

$$O^{-}_{\text{reaction site}} + e^{-} + V_O^{\bullet\bullet} \leftrightarrow O_O^{x} \tag{7.19}$$

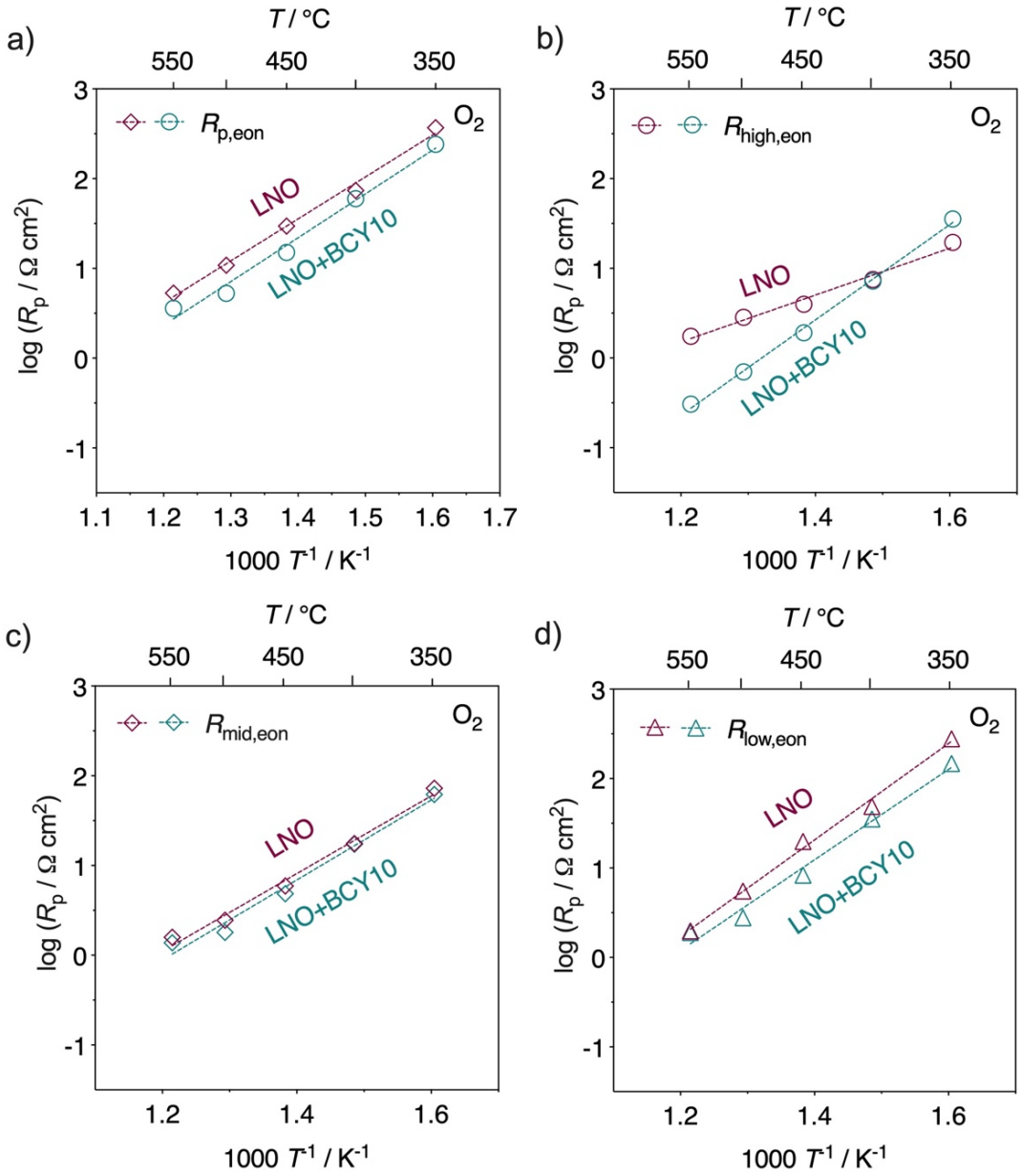

Fig. 7.8 – Temperature dependence of the corrected polarisation resistances, $R_{p,eon}$ (a), $R_{high,eon}$ (b), $R_{mid,eon}$ (c) and $R_{low,eon}$ (d), obtained using the equivalent circuit from Fig. 7.4d including the correction for the electronic leakage.

Despite these observations, Adler *et al.* [10] have determined that the individual steps taking place during the oxygen reduction reaction cannot be easily separated and do not

contribute additively to the total cell impedance. Thus, $R_{mid,eon}$ possibly includes the coexistence of different mechanisms. Such an analogy would correspond to previous literature that suggests the presence of non-charge transfer processes including solid-state diffusion and chemical exchange for this term, that will vary according to the temperature dependence of ambipolar conductivity in the electrode [10,14,46,48].

Furthermore, it is worth mentioning that only minor improvements to this term were obtained when adding the BCY10 phase, suggesting that the $R_{mid,eon}$ term is not significantly dependent on this component. In addition, the similarity of the E_a values registered in Table 7.2 for both samples (1.02 eV and 0.91 eV, respectively, for LNO and LNO+BCY10 cathodes) can also be a consequence from this effect.

Table 7.2 – Comparison of the activation energy values obtained in wet O_2 for both samples, using the equivalent circuit from Fig. 7.4d for the correction of the electronic leakage.

Composition	**Polarisation term**		**Activation energy / eV**
LNO	Total	$R_{p,eon}$	0.95
	High-frequency	$R_{high,eon}$	0.68
	Mid-frequency	$R_{mid,eon}$	1.02
	Low-frequency	$R_{low,eon}$	1.22
LNO+BCY10	Total	$R_{p,eon}$	1.03
	High-frequency	$R_{high,eon}$	0.80
	Mid-frequency	$R_{mid,eon}$	0.91
	Low-frequency	$R_{low,eon}$	0.87

Finally, regarding the low-frequency term, $R_{low,eon}$, which dominates the total polarisation resistance (Fig. 7.7 and Fig. 7.8), denotes an improvement of 1.4 by the addition of BCY10 phase, similar to that of the total polarisation resistance $R_{p,eon}$. This term is possibly associated to the processes occurring at the surface of the electrodes, as the capacitance values calculated for this term are in the range of ~ 10^{-2} – 10^{-1} F cm^{-2}, in agreement to that found previously [36]. The following equations illustrate the possible mechanism involved in this situation (Fig. 7.9) [41,47]:

$$O_2(g) \leftrightarrow 2O_{ad} \quad (7.20)$$

$$O_{ad} + e^- \leftrightarrow O_{ad}^- \quad (7.21)$$

$$O^-_{ad} \leftrightarrow O^-_{reaction\ site} \quad (7.22)$$

where O_{ad} and O^-_{ad} represent an adsorbed oxygen atom and a surface adsorbed ion, respectively. Moreover, the differences in the activation energies also found for this term are (1.22 eV and 0.87 eV, respectively, for LNO and LNO+BCY10 cathodes, in Table 7.2) are a possible indication of an improvement of the catalytic activity in the case of the composite, due to the lower E_a value registered for this composition.

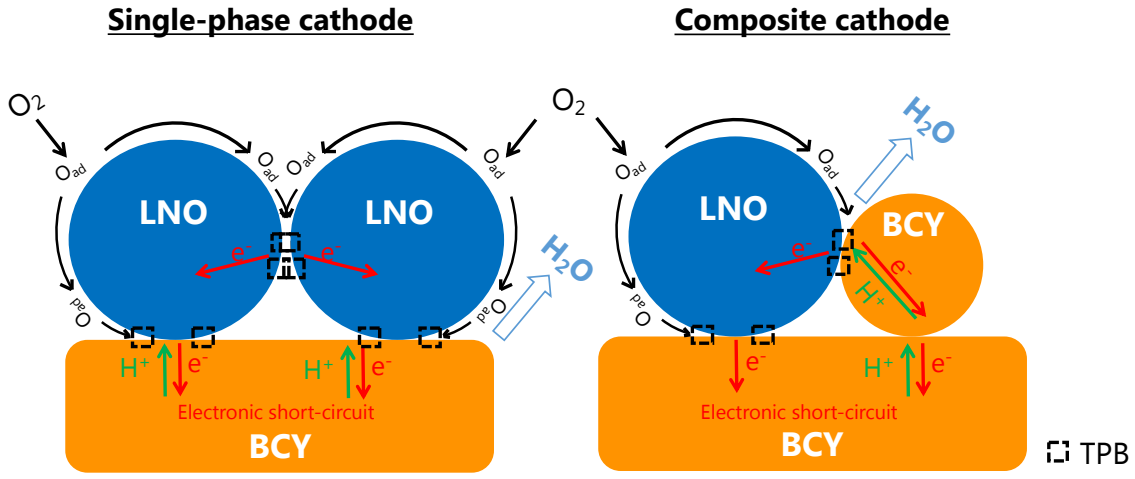

Fig. 7.9 – Schematic representation of the oxygen reduction reaction mechanism in LNO and LNO+BCY10 cathodes using BCY10 electrolytes.

Conclusions

We demonstrate that the role of the electronic conductivity in BCY10 has a significant impact on the electronic leakage and that this factor can lead to significant changes in the electrochemical performance of the cathode. It is, thus, highly important to correct data for electrolyte shorting in the symmetrical cell arrangement to be able to generate a database of information on cathode performance that is free of this limitation.

To date, this process has not been widely adopted in the literature and this situation currently prevents the quantitative comparison of electrocatalytic properties of potential cathodes as a function of temperature. Hence, we expect the current work to provide a rational basis for researchers to adopt this method to generate quantitative databases for future accurate identification and optimisation of potential cathode materials for proton ceramic fuel cells.

The use of a Distribution Function of Relaxation Times (DFRT) analysis in combination with Equivalent Circuit Modelling (EQM) allowed for a better understanding of the number of elementary steps for the Oxygen Reduction Reaction (ORR) mechanism. The ORR mechanism of both LNO and LNO+BCY10 composite cathodes revealed that the rate-limiting processes are those of charge-transfer, diffusion and surface adsorption. The high-frequency term, possible associated to charge-transfer, was found to be highly affected by the addition of BCY10 phase, denoting changes in activation energy as result of the increase of the TPB length. The mid-frequency term, possible related to diffusion processes, is shown to be the least affected term by the addition of BCY10 phase. However, larger improvements have been shown to the low frequency response, which also was found to dominate the total polarisation resistance.

References

1 N. Mahato, A. Banerjee, A. Gupta, S. Omar and K. Balani, *Prog. Mater. Sci.*, 2015, **72**, 141–337.

2 Z. Yang, M. Guo, N. Wang, C. Ma, J. Wang and M. Han, *Int. J. Hydrogen Energy*, 2017, **42**, 24948–24959.

3 J. D. Castro-Robles, N. Soltani and J. Á. Chávez-Carvayar, *Mater. Chem. Phys.*, 2019, **225**, 50–54.

4 X. Chen, J. Lin, L. Sun, T. Liu, J. Wu, Z. Sheng and Y. Wang, *Electrochim. Acta*, 2019, **298**, 112–120.

5 X. Chen, W. Ni, X. Du, Z. Sun, T. Zhu, Q. Zhong and M. Han, *J. Mater. Sci. Technol.*, 2019, **35**, 695–701.

6 F. J. A. Loureiro, D. A. Macedo, R. M. Nascimento, M. R. Cesário, J. P. F. Grilo, A. A. Yaremchenko and D. P. Fagg, *J. Eur. Ceram. Soc.*, 2019, **39**, 1846-1853.

7 V. A. Sadykov, E. Y. Pikalova, Z. S. Vinokurov, A. N. Shmakov, N. F. Eremeev, E. M. Sadovskaya, J. G. Lyagaeva, D. A. Medvedev and V. D. Belyaev, *Solid State Ionics*, 2019, **333**, 30–37.

8 C. Wang, H. Soga, T. Okiba, E. Niwa and T. Hashimoto, *Mater. Res. Bull.*, 2019, **111**, 61–69.

9 A. Subardi, K.-Y. Liao and Y.-P. Fu, *J. Eur. Ceram. Soc.*, 2019, **39**, 30–40.

10 S. B. Adler, J. A. Lane and B. C. H. Steele, *J. Electrochem. Soc.*, 1996, **143**, 3554–3564.

11 D. Marinha, L. Dessemond and E. Djurado, *J. Power Sources*, 2012, **197**, 80–87.

12 F. S. Baumann, J. Fleig, H.-U. Habermeier and J. Maier, *Solid State Ionics*, 2006, **177**, 1071–1081.

13 F. J. A. Loureiro, T. Yang, D. G. Stroppa and D. P. Fagg, *J. Mater. Chem. A*, 2015, **3**, 12636–12641.

14 V. C. Kournoutis, F. Tietz and S. Bebelis, *Fuel Cells*, 2009, **9**, 852–860.

15 E. P. Murray, M. J. Sever and S. A. Barnett, *Solid State Ionics*, 2002, **148**, 27–34.

16 Z. Shao and S. M. Haile, *Nature*, 2004, **431**, 170–173.

17 P. Ranran, W. Yan, Y. Lizhai and M. Zongqiang, *Solid State Ionics*, 2006, **177**, 389–393.

18 A. Giuliano, M. P. Carpanese, D. Clematis, M. Boaro, A. Pappacena, F. Deganello, L. F. Liotta and A. Barbucci, *J. Electrochem. Soc.*, 2017, **164**, F3114–F3122.

19 A. Grimaud, F. Mauvy, J. M. Bassat, S. Fourcade, L. Rocheron, M. Marrony and J. C. Grenier, *J. Electrochem. Soc.*, 2012, **159**, B683–B694.

20 J. Dailly, S. Fourcade, A. Largeteau, F. Mauvy, J. C. Grenier and M. Marrony, *Electrochim. Acta*, 2010, **55**, 5847–5853.

21 E. Fabbri, I. Markus, L. Bi, D. Pergolesi and E. Traversa, *Solid State Ionics*, 2011, **202**, 30–35.

22 R. Mukundan, P. K. Davies and W. L. Worrell, *J. Electrochem. Soc.*, 2001, **148**, A82–A86.

23 L. Yang, C. Zuo, S. Wang, Z. Cheng and M. Liu, *Adv. Mater.*, 2008, **20**, 3280–3283.

24 P. Batocchi, F. Mauvy, S. Fourcade and M. Parco, *Electrochim. Acta*, 2014, **145**, 1–10.

25 Q. Meng, W. Wang, X. Weng, Y. Liu, H. Wang and Z. Wu, *J. Phys. Chem. C*, 2016, **120**, 3259–3266.

26 R. J. Woolley and S. J. Skinner, *Solid State Ionics*, 2014, **255**, 1–5.

27 A. R. O. Sousa, A. J. M. Araujo, G. S. Souza, J. P. F. Grilo, F. J. A. Loureiro, D. P. Fagg and D. A. Macedo, *Mater. Lett.*, 2017, **191**, 141–144.

28 G. Amow, I. J. Davidson and S. J. Skinner, *Solid State Ionics*, 2006, **177**, 1205–1210.

29 D. Poetzsch, R. Merkle and J. Maier, *J. Power Sources*, 2013, **242**, 784–789.

30 M. Oishi, S. Akoshima, K. Yashiro, K. Sato, J. Mizusaki and T. Kawada, *Solid State*

Ionics, 2009, **180**, 127–131.

31 F. J. A. Loureiro, D. Pérez-Coll, V. C. D. Graça, S. M. Mikhalev, A. F. G. Ribeiro, A. Mendes and D. P. Fagg, *J. Mater. Chem. A*, 2019, **7**, 18135–18142.

32 M. Liu and H. Hu, *J. Electrochem. Soc.*, 1996, **143**, L109–L112.

33 H. Hu and M. Liu, *J. Electrochem. Soc.*, 1997, **144**, 3561–3567.

34 W. G. Wang and M. Mogensen, *Solid State Ionics*, 2005, **176**, 457–462.

35 D. O. Bannikov and V. A. Cherepanov, *J. Solid State Chem.*, 2006, **179**, 2721–2727.

36 S. M. Babiniec, S. Ricote and N. P. Sullivan, *J. Electrochem. Soc.* , 2014, **161**, F717–F723.

37 C. Solís, L. Navarrete and J. M. Serra, *J. Power Sources*, 2013, **240**, 691–697.

38 N. Hildenbrand, P. Nammensma, D. H. A. Blank, H. J. M. Bouwmeester and B. A. Boukamp, *J. Power Sources*, 2013, **238**, 442–453.

39 R. Sayers, M. Rieu, P. Lenormand, F. Ansart, J. A. Kilner and S. J. Skinner, *Solid State Ionics*, 2011, **192**, 531–534.

40 J. R. D. Santos, F. J. A. Loureiro, J. P. F. Grilo, V. D. Silva, T. A. Simões, D. P. Fagg and D. A. Macedo, *Electrochim. Acta*, 2018, **285**, 214–220.

41 E. B. G. A. Fulgêncio, F. J. A. Loureiro, K. P. V Melo, R. M. Silva, D. P. Fagg, L. F. A. Campos and D. A. Macedo, *J. Alloys Compd.*, 2019, **788**, 148–154.

42 B. A. Boukamp and A. Rolle, *Solid State Ionics*, 2017, **302**, 12–18.

43 B. A. Boukamp and A. Rolle, *Solid State Ionics*, 2018, **314**, 103–111.

44 F. Mauvy, C. Lalanne, J.-M. Bassat, J.-C. Grenier, H. Zhao, L. Huo and P. Stevens, *J. Electrochem. Soc.*, 2006, **153**, A1547–A1553.

45 S. Ricote, N. Bonanos, F. Lenrick and R. Wallenberg, *J. Power Sources*, 2012, **218**, 313–319.

46 S. B. Adler, *Chem. Rev.*, 2004, **104**, 4791–4844.

47 S. Wang, T. Chen and S. Chen, *J. Electrochem. Soc.*, 2004, **151**, A1461–A1467.

48 Y.-M. Kim, S.-I. Pyun, J.-S. Kim and G.-J. Lee, *J. Electrochem. Soc.*, 2007, **154**, B802–B809.

8. Characterisation of yttrium-doped barium cerate in electrolyser and fuel cell/ion pump modes

Abstract

The effect of polarisation on the electrochemical characteristics of a BCY10-based single-cell is evaluated. Distribution function of Relaxation Times (DFRT) analysis is employed to model the impedance spectra under open circuit voltage (*OCV*) and under applied potential difference revealing the existence of multiple electrode processes. Nonetheless, due to the similarity of time constants, these were grouped in two main processes attributed to charge-transfer and diffusion. Transport numbers are dramatically affected under applied difference of potential due to the significant changes in the local level of water vapour partial pressure (p_{H2O}). In fuel cell/ion pump mode, hydration occurs, leading to an increase in the local levels of p_{H2O}, exceeding the limits of stability of BCY10. In contrast, in electrolyser mode, p_{H2O} decreases leading to an excessive decrease in protonic conductivity.

8.1. Introduction

Power generation by Solid Oxide Fuel Cells (SOFCs) and high-temperature electrolysis via Solid Oxide Electrolyser Cells (SOECs) are both promising devices for either energy conversion or for production of synthetic fuels (*e.g.*, H_2, CO, syngas, …), respectively [1–3]. The reasons behind the attractiveness of these technologies are due to their high efficiency, low pollution and multi-fuel compatibility. Proton-conducting ceramics, including doped barium zirconates and cerates, have attracted the attention of fuel cell researchers as next-generation electrolytes for ceramic Solid Oxide Cells (SOCs), working at lower temperature. These protonic analogues are called Proton Ceramic Fuel Cells, PCFCs, or Proton Ceramic Electrolyser Cells, PCECs, respectively [3,4]. These devices can operate in a variety of modes, including electrolyser, fuel cell and ion pump modes [5,6], as exemplified in Fig. 8.1.

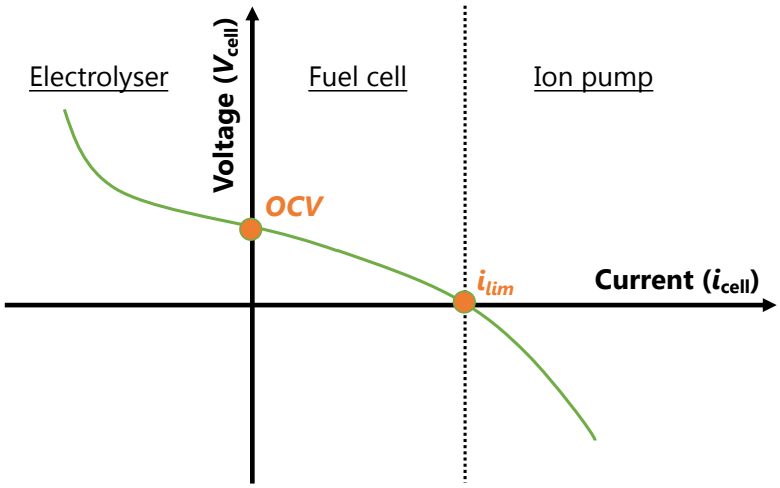

Fig. 8.1 – Operating modes of solid oxide cells (SOCs) [5,6].

At open circuit voltage (*OCV*) conditions, (i_{cell} = 0), the membrane reactor is operated potentiometrically as a sensor without any net current through the electrolyte. The concentration of reactants can be monitored via the *OCV*, based on *Nernst*'s law. When the working voltage is lower than the *OCV*, the cell works in the fuel cell mode, and can generate electricity and heat, with the consumption of fuels. However, if the current exceeds a certain limiting value $i_{lim} > 0$, the cell voltage becomes inverted. In this ion pump mode, charged species are driven through the solid electrolyte at the expense of external electric energy input to the system. On the other hand, when the working potential is higher than the *OCV*,

the cell can work reversely in the electrolyser mode, splitting oxidised gaseous products, such as H_2O into H_2 and O_2, with the consumption of electricity [5,6].

Among the most well recognised electrolytes, Yttrium-doped barium cerate is considered one of the best compositions to operate at intermediate temperatures, with the specific composition $BaCe_{0.9}Y_{0.1}O_{3-\delta}$ (BCY10) able to permit pure protonic conductivity at temperatures as low as 400 °C, in very low humidites (p_{H2O} ~ 10^{-4} atm) (**Chapters 4, 5**). Nonetheless, such analyses were conducted on symmetrical cells made of Pt||BCY10||Pt by *a.c.* impedance spectroscopy in the absence of applied *d.c.* bias and in unique gas atmospheres, thus, the electrochemical behaviour of this material in is yet not well understood under real SOC conditions, *i.e.*, under applied *d.c.* polarisation in atmosphere gradients.

Several studies reported the analysis of BCY-based single-cells cells under applied difference of potential [7–12]. For instance, Jyng *et al.* [9] reported a methodology to determine the transport properties of $BaCe_{0.85}Y_{0.15}O_{3-\delta}$ (BCY15) under fuel cell operation in a H_2/air atmosphere gradient using embedded Pt electrodes inserted in separated regions along the electrolyte thickness (~ 40 μm). These electrodes allowed to measure the difference of potential between each position and the cathode and anode sides, allowing to correlate the observed voltage differences to the changes in oxygen and hydrogen chemical potentials. In this way, the authors managed to investigate ionic and electronic transport properties through the BCY electrolyte. The authors found that the central region of the electrolyte is predominantly ionic in nature, blocking electronic leakage through the entire electrolyte.

In another example, Suksamai & Metcalfe [10] studied the conductivities of 10 % and 25 % Y-doped $BaCeO_3$ (BCY10 and BCY25) under fuel cell conditions, *i.e.*, 5 % hydrogen in argon at the anode with air at the cathode, using a dual-chamber SOFC reactor. The performance of BCY-based SOFCs with Pt electrodes were measured over a temperature range of 500 – 800 °C. The authors observed that BCY10 exhibits predominant proton conductivity up to 700 °C, while BCY25 exhibits mixed conduction at temperatures above 550 °C.

Stuart *et al.* [12] also reported on $BaCe_{0.9}Y_{0.1}O_{3-\delta}$ (BCY10) as electrolyte for proton conducting SOCs. Despite their performance being somewhat poor, in comparison with the oxide ion

conducting SOECs, BCY10 has been confirmed as a suitable electrolyte material for a reversible proton conducting SOC. Large losses were observed, however, at lower temperatures in electrolysis mode and attributed to the slow progression of reactions at the electrodes.

Although, these previous works have tested BCY-based electrochemical single-cells in the various operation modes, the current interest is to assess the ability of this material to function in very low humidity conditions at low temperatures, where both stability and protonic conductivity have been shown to be maintained (**Chapters 4** and **5**). Hence, in this chapter, we aim to assess the *j-V* characteristics of a single-cell made of BCY10 electrolyte in all modes of operation at 400 °C under nominally dry gases.

For this purpose, we used standard electrode materials, such as Ni-BCY10 cermet as anode [2,13] and Pt as cathode. The reason for using of this Ni-BCY10 cermet configuration is related to the high electronic conductivity of the nickel phase, as well as its good electrocatalytic activity, and low cost [2,13].

8.2. Experimental

8.2.1. Sample preparation

The anode powder of 40 vol% Ni (Alfa Aesar) – 60 vol% BCY10 (TYK, Japan) was prepared by ball milling (Retsch PM200) for 2 h, 250 rpm using ethanol as liquid medium. Then, the suspension was dried overnight, and the resultant powder was pressed uniaxially in a stainless-steel die of 2.5 cm diameter and, finally, pre-sintered at 950 °C for 2 h with heating and cooling rates of 3 °C min^{-1} to attain sufficient mechanical rigidity.

Then, the stable electrolyte suspension was prepared using the BCY10 electrolyte powder in 26 wt% concentration, dispersed in pure ethanol; and 1 wt% polyvinylpyrrolidone (PVP) was used as a thickener. The suspension was ball milled at 400 rpm for 2 h, followed by 1 h ultrasonication. The suspension was then deposited on the pre-sintered anode using the spin-coating technique (*Laurell*, automated spin coater, model WS-650-23). Subsequently, the half cells (anode/electrolyte) were pre-co-sintered at 1100 °C for 3 h, using heating and cooling rates of 1.5 °C min^{-1} in ambient air to obtain a pre-electrolyte layer. The final electrolyte film was achieved by spin-coating further layers of the same BCY10 suspension and sintering at 1400 °C for 5 h, using heating and cooling rates of 1.5 °C min^{-1} after an initial drying step at 350 °C for 2 h to burn the organics. The thickness of electrolyte film was controlled by the number of spin-coated layers. For the electrochemical tests, Pt paste (brush-painted and fired at 900 °C for 20 min) was used as cathode.

8.2.2. Electrochemical impedance measurements

The electrochemical performance of the anode supported single-cell was evaluated using a home-built fuel cell testing station. The button-shaped single-cell was sealed with *Thermiculite*® sheets according to the scheme in Fig. 8.2. The H_2-electrode was fed with nominally dry H_2 (p_{H2O} ~ 10^{-4} atm) and the N_2-electrode was fed with dry N_2 (p_{H2O} ~ 10^{-7} atm) at a constant flow rate of 50 mL min^{-1} using mass flow controllers (Agilent). Platinum paste was employed on the N_2-electrode to function as both electrode and as a current collector; Pt wires were used as leads to carry the electrochemical measurements.

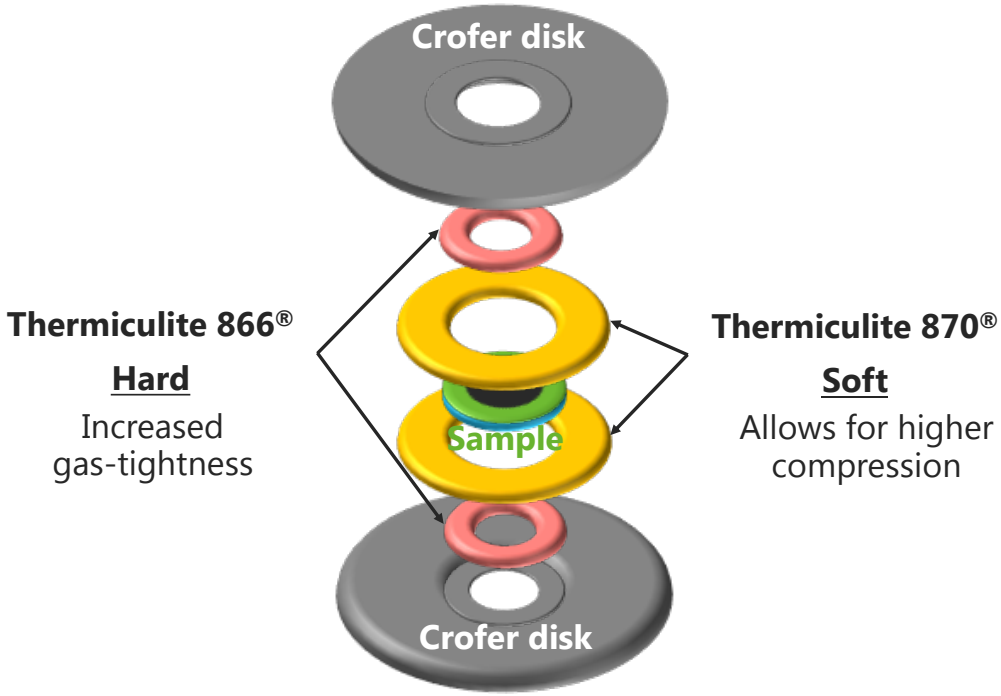

Fig. 8.2 – Schematic representation of the sealing with *Thermiculite*® sheets.

Nominally dry atmospheres were controlled using a SGT super clean gas moisture filter (<0.1 ppm H_2O); while, humidification was controlled by bubbling gases trough a KBr-saturated H_2O at 35 °C. The gases were applied to the measurement jig with a maximum total flowrate of 50 mL min^{-1} supplied by *Bronkhorst* Thermal Mass flow Controllers (EL Flow). Oxygen sensor values were collected from a YSZ sensor. Relative humidity was collected from a JUMO humidity meter.

The electrochemical studies of the single cell were performed at 400 °C using Electrochemie-Autolab PGSTAT302N Potentiostat/Galvanostat controlled through the *Nova* program. The electrochemical impedance spectra (EIS) were recorded under open circuit potential conditions (*OCV*) and under applied polarisation in all modes of operation, in the frequency range of 1 kHz – 0.01 Hz with a signal amplitude of 10 mV. The current density-voltage (*j-V*) characteristics of the single cell were appraised once the *OCV* was stabilised. The impedance spectra were fitted using *DRTtools* software [14].

8.3. Results and discussion

8.3.1. Microstructure and chemical composition

The configuration of the prepared Ni-BCY10||BCY10||Pt cell is shown in Fig. 8.3a along with representative cross-section microstructure obtained by SEM after analysis in the reactor (Fig. 8.3b, c and d). As intended, a fully dense electrolyte can be observed in Fig. 8.3b, showing a thickness of ~ 20 µm with good adhesion with the anode support. A porous Pt layer, ~ 1 – 2 µm thick, is also presented on the reverse side of the BCY10 electrolyte, showing good adhesion over the electrolyte (Fig. 8.3b).

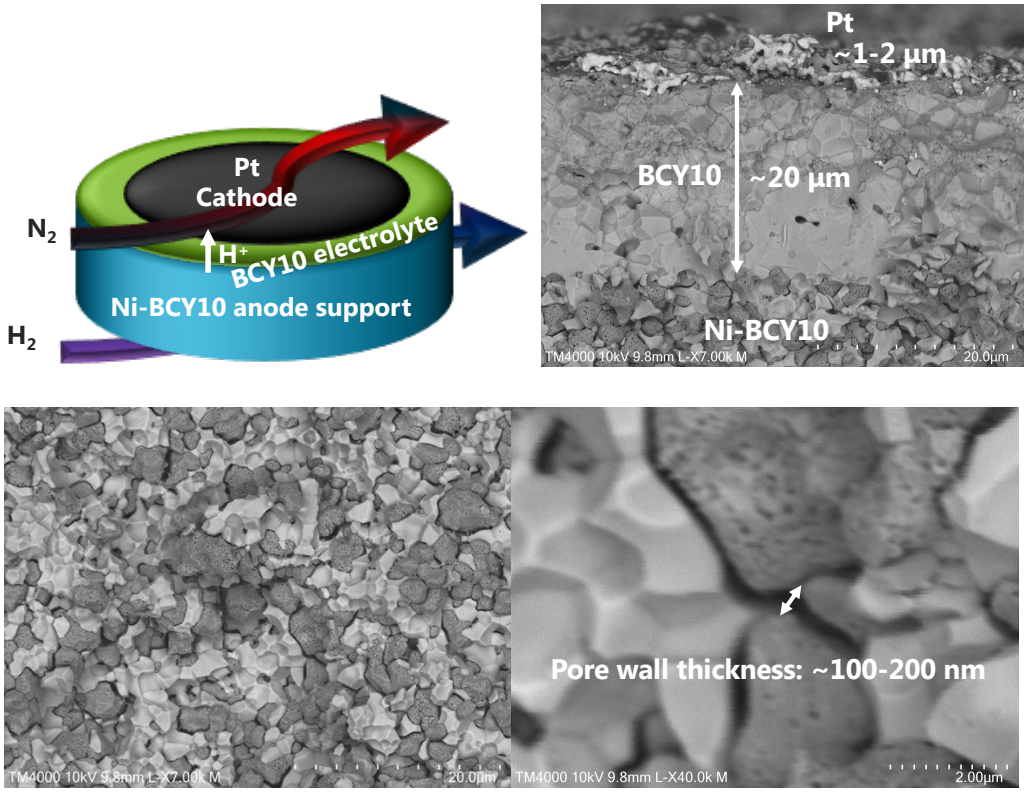

Fig. 8.3 – Cross-section microstructure of the Ni-BCY10||BCY10||Pt single-cell.

Regarding the Ni-BCY10 support, we can observe a homogeneous distribution of both Ni and BCY10 phases, which is also confirmed from the EDS mapping (Fig. 8.4). Moreover, the pore-wall thickness also confirms the effectiveness of the NiO reduction process (400 °C overnight) to metallic Ni, generating porosity without the need of any additional porogen [15].

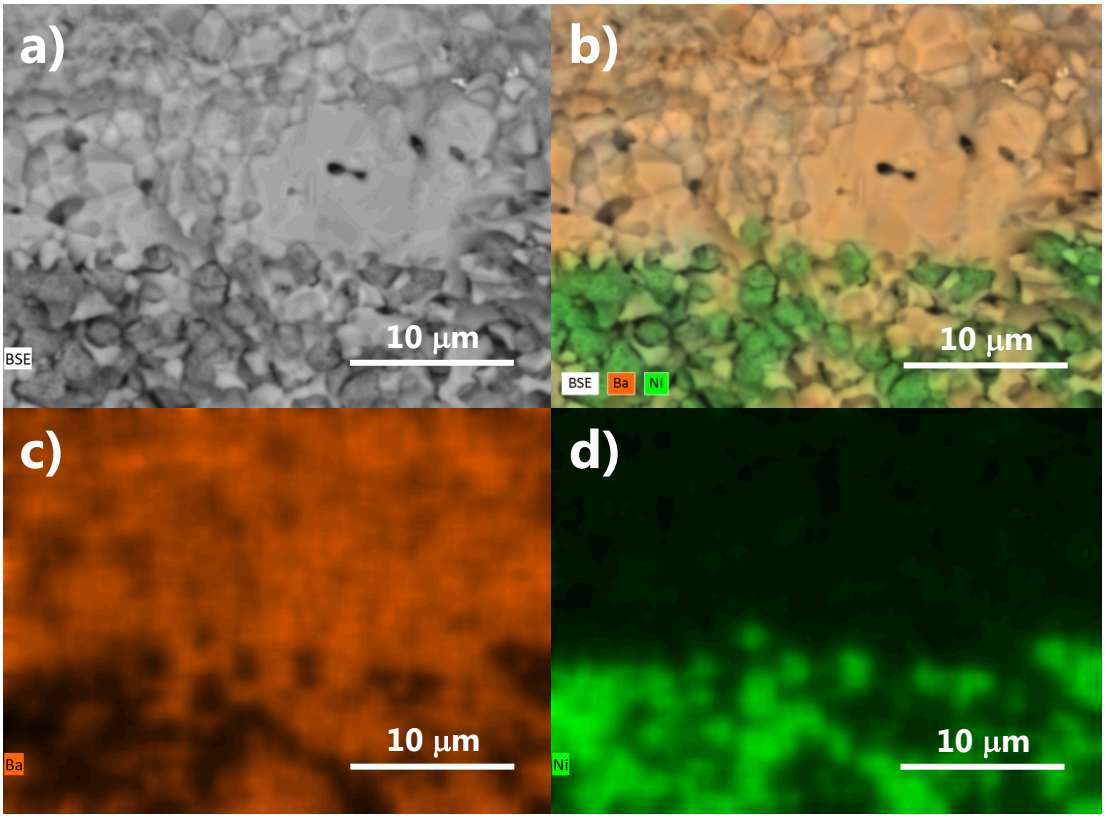

Fig. 8.4 – Cross-section of Ni-BCY10||BCY10||Pt single-cell: a) BSE image; b), c) and d) EDS mapping.

8.3.2. Electrochemical characterisation at *OCV*

To analyse the electrochemical performance of the Ni-BCY10||BCY10||Pt single-cell, we measured the polarisation resistances at *OCV* conditions by electrochemical impedance spectroscopy (EIS), as shown in Fig. 8.5a. In the EIS Nyquist plot, the high-frequency intersection on the real axis represents ohmic resistance from the electrolyte (R_{ohm}), while the semicircle diameter arises from polarisation processes at the electrodes (R_p). An inductance (L) can also be found at it is related to *e.g.*, connecting wires and measurement devices.

The spectrum was analysed by the aid of the DFRT from Fig. 8.5b. From the plot, we can observe that modelling with typical equivalent circuit modelling would result in a very complicated analysis, due to the relatively high number of peaks found in the DFRT. Therefore, in this work, the analysis of the impedance data was performed only by DFRT. The utilization of this analysis is especially justified when the rate-determining steps of the

electrochemical process have very similar relaxation times [16–18]. Despite the large number of processes identified from the plot in Fig. 8.5b, some of them share similar time constants, and, thus, we were able to group them into two main processes: *i*) the high-frequency electrode polarisation responses, with capacitance values in the range 10^{-4} – 10^{-3} F cm^{-2} (Table 8.1), which can be ascribed to the charge-transfer processes on the surface of the electrodes [19,20]; *ii*) the low-frequency responses, which presented capacitance values that are in the range 10^{-2} – 0.1 F cm^{-2} (Table 8.1), being possible related to gas-phase diffusion processes on the porous electrodes [2,21]. The estimated capacitance values for each peak in DFRT were calculated based on the following equation:

$$C_i = \frac{\tau_{0,i}}{R_i.W} \quad (8.1)$$

where R_i is the resistivity of each process, which can be directly retrieved by the integration of the area under the $R.G(\tau)$ *vs.* $\ln(\tau)$ curve of the DFRT, and W (= 0.5) is the width of the peak at half height, using the gaussian function in the *DRTtools* software [14].

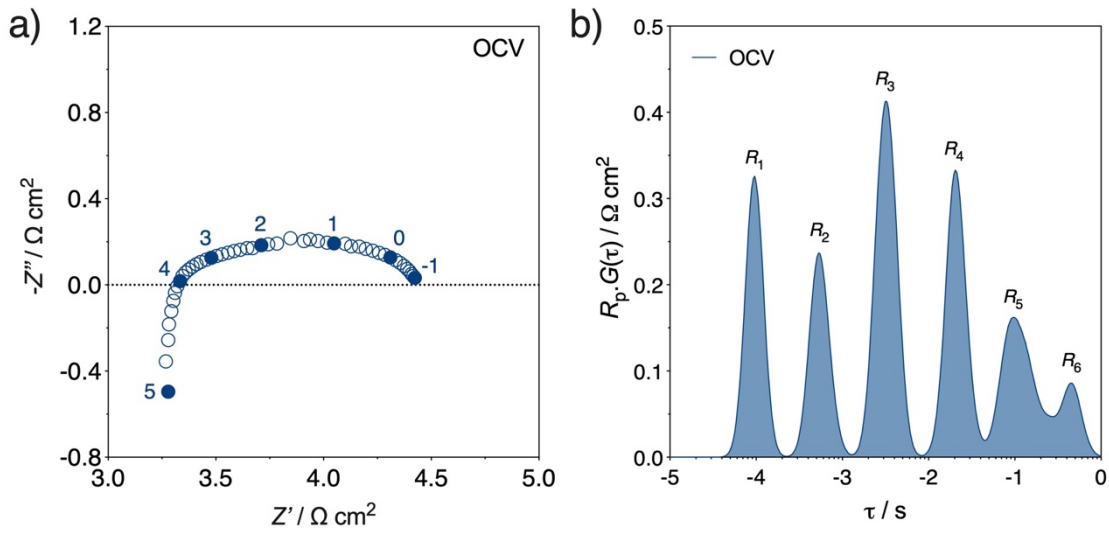

Fig. 8.5 – a) Impedance spectra obtained for the Ni-BCY10||BCY10||Pt single-cell under *OCV* conditions at 400 °C with flowing 50 mL min^{-1} H_2 on the anode side and 50 mL min^{-1} N_2 on the cathode side; b) DFRT obtained from using the *Tikhonov* Regularisation (TR) [17,18] at 500 °C (with a regularisation parameter = 10^{-5}).

Interestingly, Fig. 8.5a clearly shows that R_{ohm} dominates the overall resistance of the tested cell, suggesting that R_p is sufficiently suppressed even using a simple electronic conductor – platinum – as N_2-electrode. However, there remains room for further improvements by

potentially changing this electrode with a mixed ionic electronic conducting electrode to obtain increased performance [4]. In addition, further minimisation of the electrolyte thickness can also lead to even lower ohmic resistance of the electrolyte impedance. As typical for complete cell measurements, the current results do not allow the deconvolution between H_2-electrode and N_2-electrode contributions due to the probability of very similar relaxation frequencies in both cases [22].

Table 8.1 – Parameters obtained from the DFRT analysis on impedance spectra from the Ni-BCY10||BCY10||Pt single-cell at 400 °C at *OCV* conditions.

Process	τ_0 / s	C / F cm^{-2}	R_i / Ω cm^2
R_1	9.64 x 10^{-5}	2.78 x 10^{-3}	0.20
R_2	5.51 x 10^{-4}	8.84 x 10^{-3}	0.36
R_3	3.15 x 10^{-3}	6.04 x 10^{-2}	0.29
R_4	2.04 x 10^{-2}	0.51	0.22
R_5	9.51 x 10^{-2}	3.31	0.16
R_6	0.44	43.21	5.76 x 10^{-2}
R_p	-	-	1.29

Table 8.2 presents a literature comparison of the polarisation resistances of other similar reported single-cells under *OCV* conditions at 400 °C. It is important to comment that the majority of reports present studied using O_2 instead of N_2, which greatly improves the performance the single-cell. In any case, the behaviour reported here competes well with that of high performance SOFCs based on protonic conductors. As we can see from the provided table, the Ni-BCY10||BCY10||Pt single-cell demonstrated equivalent electrochemical characteristics than those from other cells from the literature.

Table 8.2 – Comparison of polarisation resistances obtained for Ni-BCY10||BCY10||Pt single-cell at *OCV* conditions and at 400 °C with single-cells based on similar compositions from literature.

Reference	Composition	Electrolyte thickness / μm	Polarisation resistance / Ω cm^2			Atmosphere	
@ *OCV*	Single cell (anode|electrolyte|cathode)		R_{ohm}	R_p	R_{Total}	Anode	Cathode
This work	Ni-BCY10|BCY10|Pt	~20	3.32	1.29	4.61	Dry H_2	Dry N_2
[4]	Ni-BZCYYb|BZCYYb|PBSCF	~15	~6	~0.6	~6.6	Wet H_2	Dry air
[23]	Ni- $BaCe_{0.5}Zr_{0.3}Y_{0.2}O_{3-\delta}$ |$BaCe_{0.5}Zr_{0.3}Y_{0.2}O_{3-\delta}$|$Ca_3Co_4O_{9-\delta}$	~25	~4.35	~28.36	~32.71	Wet H_2	Static air
[24]	Ni-$BaZr_{0.85}Y_{0.15}O_{3-\delta}$| $BaCe_{0.4}Zr_{0.4}Y_{0.2}O_{3-\delta}$| $Pr_2NiO_{4+\delta}$	~5	~1.58	~140.78	~142.36	Wet H2	Dry air

8.3.3. Electrochemical characterisation under polarisation

Fig. 8.6a and b depict the current density–voltage (*j-V*) graph obtained at 400 °C by feeding nominally dry H_2 on the Ni-BCY10 electrode and nominally dry N_2 on the Pt electrode, in various modes of operation. A very low *OCV* of ~ 0.09 V was experimentally obtained under these conditions. Although electronic leakage through the electrolyte would be one explanation for a drop in measured *OCV*, previous works, **Chapters 4** and **5**, show that this possibility is unlikely for BCY10 under the current conditions, as its transport properties are predicted to be predominantly protonic. In this respect, several previous studies made by Bondalti on similar electrochemical cells, which also used N_2 instead of O_2 as oxidant, have reported comparably low *OCV* (*e.g.* ~ 0.2 V) values without any noted leakage. In these works, such low *OCV* values have been attributed to a lower oxygen partial pressure gradient between both sides of the membrane. Nonetheless, in the current work the *OCV* values is still below than what was expected, as a possible result of insufficient sealing. Such leak is likely in the current experiment due to the very high diffusion coefficient of hydrogen, an effect that is also compounded by the lack of oxygen of the cathode side that can buffer such leaks by water formation. The *Thermiculite*® sheets, thus, may not be the best option to provide adequate sealing for the current experimental conditions.

Fig. 8.6a and b show the *j-V* characteristics obtained in both fuel cell/ion pump and electrolyser modes, respectively. From the first inspection, we can observe that a maximum current density of ~ 300 mA cm^{-2} was obtained at -1 V in fuel cell/ion pump mode, while a lower value of maximum current density of ~ 200 mA cm^{-2} was obtained at +1 V in electrolyser mode.

The short-term stability analysis of the measured MEA is depicted in Fig. 8.6c and d. From the figures, we can observe that the current density is quite stable at low and high values of applied voltage, whereas some turbulence in current density are observed under short polarisation times for intermediate values of applied potential in both modes of operation.

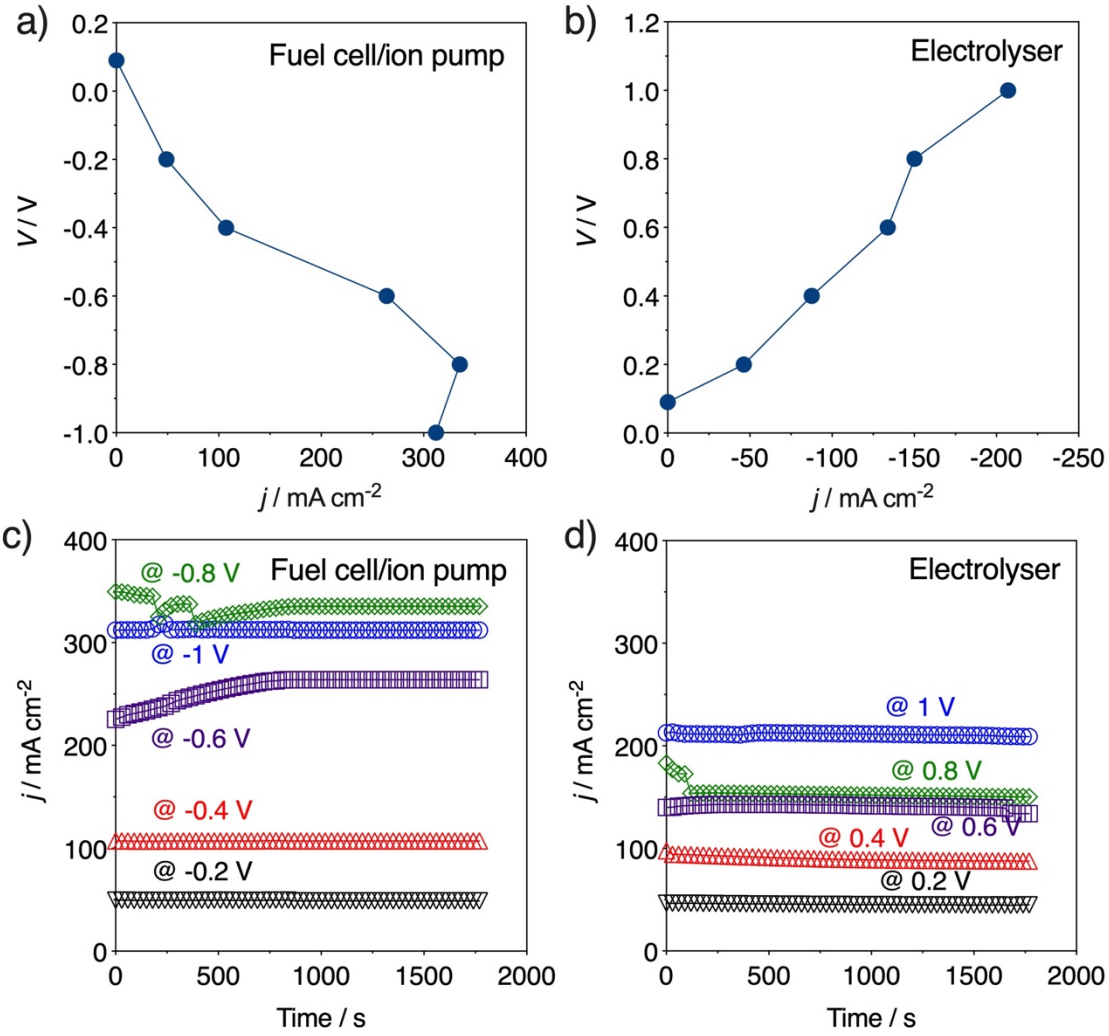

Fig. 8.6 – a) comparison of *j-V* characteristics of a Ni-BCY10||BCY10||Pt MEA in H_2 and N_2; b) short-term current density stability.

Fig. 8.7a and b depict the impedance spectra at *OCV* and under applied voltage (±1 V) in both fuel cell/ion pump and electrolyser modes, respectively. Interestingly, from the DFRT analyses, we can observe that, in both cases, the low frequency terms disappear on polarisation, which may indicate that diffusion processes become less important with increasing polarisation (within the measured range). An additional R_0 term at high frequency arises in fuel cell/ion pump mode, although more study is required to identify the nature of this process.

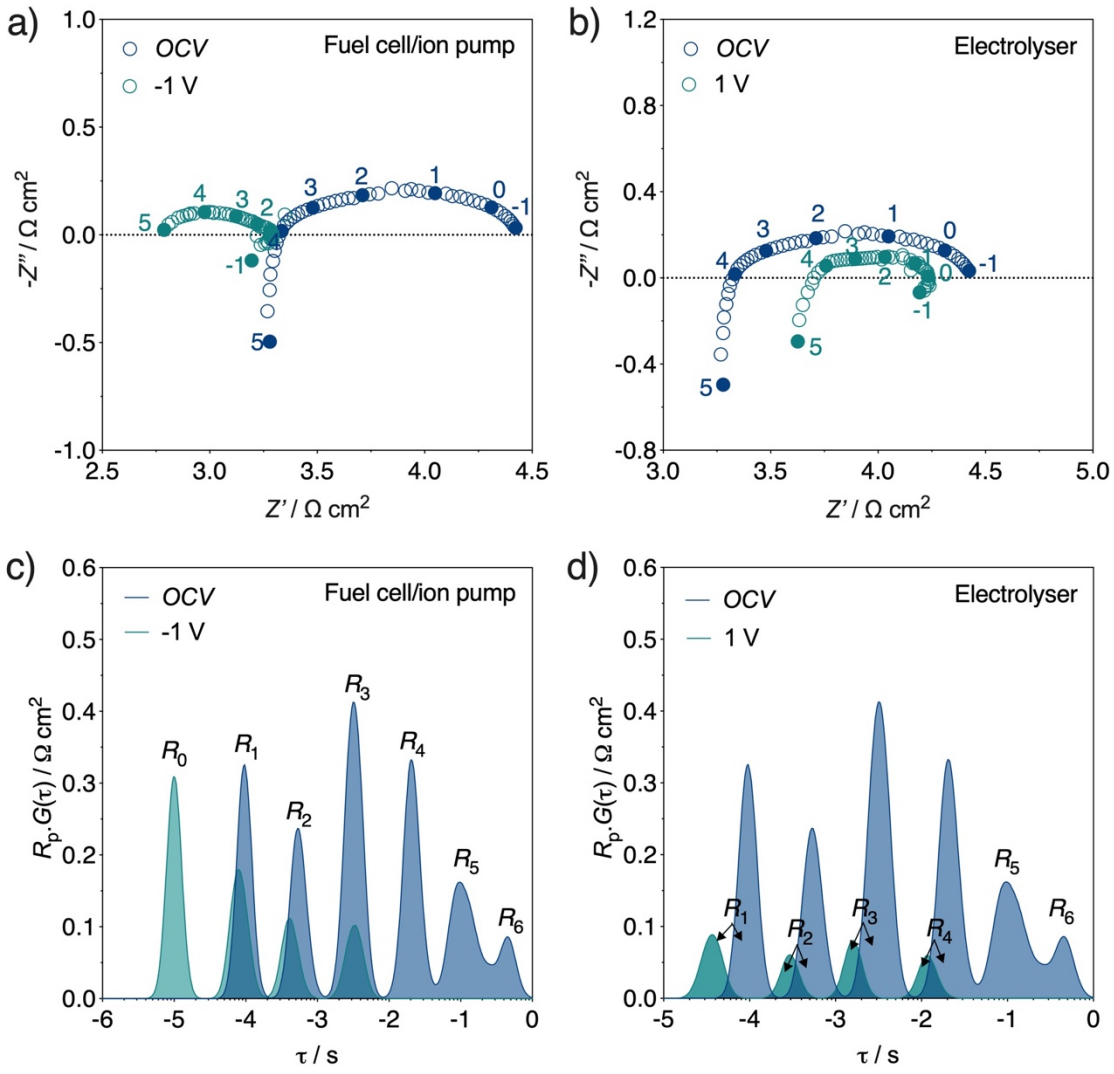

Fig. 8.7 – Impedance spectra obtained for the Ni-BCY10||BCY10||Pt cell in a) fuel cell/ion pump (-1 V) and b) electrolyser (+1 V) modes at 400 °C, with flowing 50 mL min^{-1} H_2 on the anode side and 50 mL min^{-1} N_2 on the cathode side. DFRT obtained using the *Tikhonov* Regularisation (TR) [17,18] (with a regularisation parameter = 10^{-5}), in c) fuel cell/ion pump and d) electrolyser modes.

Fig. 8.8 summarises these partial contributions to the total resistance of the cell (R_{total}) as a function of polarisation under the different modes of operation. In this case, we can understand that the total resistance of the cell (R_{total}) is dominated by the electrolyte resistance (R_{ohm}), in agreement with that observed at *OCV* conditions (Fig. 8.5a). This is an important observation as it shows that the electrodes are providing high operational performance under these conditions, with the overall cell limitations instead resulting from the electrolyte. In all methods of operation, we can observe that electrode polarisation resistances typically become lower under larger applied potentials. This feature is commonly

observed in SOC when alterations in the local chemical potential of the mobile ionic species at the electrode/electrolyte interface, induced by the applied potential, are not efficiently replenished from the gas phase due to the presence of limiting surface exchange. In such a case a chemical potential difference (and hence, a driving force for proton diffusion) is maintained across the electrodes that serves to benefit electrode kinetics [25,26]. At the highest applied potential in the fuel cell/ion pump mode, this tendency is shown to be inverted with the electrode polarisation resistance measured at -1 V being greater than that at -0.8 V. This inversion can be possibly considered to be due to cell degradation. In this respect, note in Fig. 8.8 both the electrode and the electrode resistance show this feature. One possibility is that such extensive polarisation in the fuel cell/ion pumping regime may locally oxidise the Ni-cermet anode, leading to both a depleted electrode performance and lower effective electrolyte area due to impaired current collection [27]. Another possibility is given by the work of Park *et al.* [28] who related performance degradations to decomposition of the electrolyte due to barium loss under high local water vapour partial pressures, which are generated upon fuel cell operation. In that work, such degradations were shown to be irreversible, highlighting that maximum limits in applied potential must be adopted in this polarisation mode.

Another interesting feature is the variation in the ohmic resistance with polarisation. In the electrolyser mode, R_{ohm} is shown to be relatively constant with applied potential. In contrast, in the fuel cell/ion pump modes, significant decreases in R_{ohm} are generally noted with increasing applied potential. In this respect, previous literature has shown that the internal chemical potential gradients generated across BCY electrolytes, due to the presence of external atmosphere gradients, do not vary linearly across the electrolyte thickness. Instead, non-negligible electronic contributions to total conductivity, typically, can be induced in the electrolyte layers adjacent to the electrodes [28,29]. Such an effect would reduce the functional thickness of the electrolyte that corresponds to purely ionic behaviour, resulting in an apparent reduction in the resistance of this component, as observed. The literature also shows that this distribution of internal chemical potential gradients is a complex function of applied polarisation[29] and electrode thickness [28], with thin electrolytes, as in the current case, being highly susceptible to the local nature of the cathode atmosphere. Further work must,

therefore, be performed to understand this phenomenon, for example as a function of different external gas atmospheres.

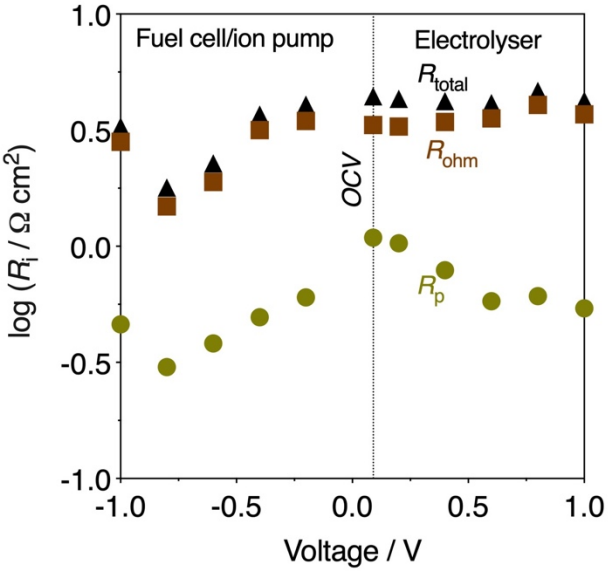

Fig. 8.8 – Polarisation resistances as a function of applied polarisation.

We now conclude by addressing a few comments related to the impact of the above findings in the utilisation of electrochemical reactors based on BCY10 electrolytes for the production of chemicals. Firstly, the performance of this preliminary electrochemical cell is shown to be high, producing attractive maximum current densities in all modes of operation. Not only does this support interest in this type of device for potential future applications for both hydrogenation and dehydrogenation reactions, but it also demonstrates the adoption of successful cell preparation techniques. Furthermore, the electrode polarisation resistances measured in the current atmospheres are shown to not be limiting factor to the cell performance, shifting focus on to that of the electrolyte performance. Improvements are, however, needed in replacement of the *Thermiculite*® sheets for alternative sealing methods of higher efficiency. Further work is also necessary to understand the local chemical potential gradients generated across BCY electrolytes upon operation and their impact on electrolyte performance.

Conclusions

Preliminary assessment of the BCY10 electrolyte under applied polarisation in very low humidity conditions (low oxygen and water vapour contents) under both fuel cell/ion pump and electrolyser modes demonstrate distinct features regarding the electrolyte behaviour. While the ohmic resistance decreases significantly under fuel cell/ion pump mode, they remain effectively constant in the electrolyser mode.

The DFRT analysis is revealed to be a suitable alternative to the traditional equivalent circuit modelling for the analysis of a complete single-cell reactor, being able to calculate the polarisation resistance values as well as to extract capacitance and time constant values for each individual process. Despite the precision of the DFRT method, the interpretation was based on assuming two major processes that correspond to charge-transfer and to diffusion, due to the similar capacitance values of most individual processes. The diffusion response was found to disappear under large applied potentials, for both fuel cell/ion pump and electrolyser modes, while distinct improvements were also noted in all the remaining polarisation resistance responses.

The results here demonstrated must be considered as preliminary and future work is still required to better understand the behaviour of BCY10 under applied polarisation, namely by extended study in various temperature and atmosphere conditions, to provide a deeper understanding of operational limits, cell stability, electrolyte performance and electrode behaviour.

References

1 L. Wang, M. Chen, R. Küngas, T.-E. Lin, S. Diethelm, F. Maréchal and J. Van herle, *Renew. Sustain. Energy Rev.*, 2019, **110**, 174–187.

2 K. Zhao, X. Hou, M. G. Norton and S. Ha, *J. Power Sources*, 2019, 226732.

3 S. W. Tao and J. T. S. Irvine, *Adv. Mater.*, 2006, **18**, 1581–1584.

4 S. Choi, C. J. Kucharczyk, Y. Liang, X. Zhang, I. Takeuchi, H.-I. Ji and S. M. Haile, *Nat. Energy*, 2018, **3**, 202–210.

5 S. Gunduz, D. Dogu, D. J. Deka, K. E. Meyer, A. Fuller, A. C. Co and U. S. Ozkan, *Catal. Today*, 2019, **323**, 3–13.

6 K. Sundmacher, L. K. Rihko-Struckmann and V. Galvita, *Catal. Today*, 2005, **104**, 185–199.

7 G. Chen, X. Zhang, Y. Luo, Y. He, H. Liu, S. Geng, K. Yu and Y. Dong, *Int. J. Hydrogen Energy*, Accepted.

8 Y. Itagaki, Y. Yamamoto, H. Aono and H. Yahiro, *J. Ceram. Soc. Japan*, 2017, **125**, 528–532.

9 M. G. Jung, Y. J. Kim, Y.-G. Jung and H.-T. Lim, *Int. J. Hydrogen Energy*, 2014, **39**, 16576–16584.

10 W. Suksamai and I. S. Metcalfe, *Solid State Ionics*, 2007, **178**, 627–634.

11 Y. Okuyama, S. Kawano, G. Sakai, N. Matsunaga and Y. Mizutani, *ECS Trans.*, 2017, **78**, 1953–1961.

12 P. A. Stuart, T. Unno, J. A. Kilner and S. J. Skinner, *Solid State Ionics*, 2008, **179**, 1120–1124.

13 T. Takeguchi, Y. Kani, T. Yano, R. Kikuchi, K. Eguchi, K. Tsujimoto, Y. Uchida, A. Ueno, K. Omoshiki and M. Aizawa, *J. Power Sources*, 2002, **112**, 588–595.

14 T. H. Wan, M. Saccoccio, C. Chen and F. Ciucci, *Electrochim. Acta*, 2015, **184**, 483–499.

15 N. Nasani, D. Ramasamy, A. D. Brandão, A. A. Yaremchenko and D. P. Fagg, *Int. J. Hydrogen Energy*, 2014, **39**, 21231–21241.

16 F. Ciucci and C. Chen, *Electrochim. Acta*, 2015, **167**, 439–454.

17 B. A. Boukamp and A. Rolle, *Solid State Ionics*, 2018, **314**, 103–111.

18 B. A. Boukamp and A. Rolle, *Solid State Ionics*, 2017, **302**, 12–18.

19 R. Sayers, M. Rieu, P. Lenormand, F. Ansart, J. A. Kilner and S. J. Skinner, *Solid State Ionics*, 2011, **192**, 531–534.

20 S. P. Jiang and S. P. S. Badwal, *Solid State Ionics*, 1999, **123**, 209–224.

21 B. Philippeau, F. Mauvy, C. Mazataud, S. Fourcade and J.-C. Grenier, *Solid State Ionics*, 2013, **249**–**250**, 17–25.

22 D. Pérez-Coll and A. Aguadero, *Fuel Cells*, 2011, **11**, 91–101.

23 E. Pikalova, A. Kolchugin, M. Koroleva, G. Vdovin, A. Farlenkov and D. Medvedev, *J. Power Sources*, 2019, **438**, 226996.

24 N. Nasani, D. Ramasamy, S. Mikhalev, A. V Kovalevsky and D. P. Fagg, *J. Power Sources*, 2015, **278**, 582–589.

25 A. M. Svensson, S. Sunde and K. Nisancioglu, *Solid State Ionics*, 1996, **86**–**88**, 1211–1216.

26 D. Pérez-Coll, A. Aguadero, M. J. Escudero and L. Daza, *J. Power Sources*, 2009, **192**, 2–13.

27 T. Kawasaki, J. Matsuda, Y. Tachikawa, S. M. Lyth, Y. Shiratori, S. Taniguchi and K. Sasaki, *Int. J. Hydrogen Energy*, 2019, **44**, 9386–9399.

28 M. Y. Park, M. G. Jung, S. Y. Bae and H.-T. Lim, *Electrochim. Acta*, 2016, **204**, 183–191.

29 M. Y. Park, K. D. Seo, J.-Y. Park and H.-T. Lim, *J. Alloys Compd.*, 2018, **735**, 2341–2347.

Conclusions and future work

The current thesis accomplishes important results that have both scientific and technological impact to the fields of fuel cells and chemical reactors that use proton ceramic membranes.

$BaCe_{0.9}Y_{0.1}O_{3-\delta}$ (BCY10) is shown to offer predominantly protonic bulk behaviour in nominally dry H_2 atmospheres (p_{H2O} ~ 10^{-5} – 10^{-4} atm) at low temperatures, *i.e.* < 400 °C, while still providing very attractive levels of conductivity, *e.g.* ~ 10^{-3} S cm^{-1} @ 400 °C. This behaviour is a result of its very high equilibrium constant for water absorption that allows BCY10 to fully hydrate under very low humidities (p_{H2O} ~ 10^{-5} – 10^{-4} atm), supressing both oxide-ion and n-type bulk conductivities. These features were not well known until now for this composition, and yet could be of significant interest for its application in the electrochemical promotion of a wide range of chemical de-hydrogenation/hydrogenation reactions. This is particularly relevant because the scarcity of alternative proton-conducting ceramics, with such competitive protonic conductivity and negligible oxide-ion/electronic influence, have typically prevented the exploitation of electrochemical membrane reactors for chemical reactions in this low temperature range.

Contrary to that observed in reducing atmospheres, where feeding with nominally dry hydrogen-based atmospheres was sufficient to provide high levels of bulk protonic conductivity, in oxidising conditions the material can only exhibit the same behaviour by externally imposing p_{H2O} values $\geq$ 10^{-5} – 10^{-4} atm. In these conditions, minor p-type electronic bulk conductivity is noted to become significant for temperatures > 350 °C, especially in dry O_2.

The grain boundary conductivity of BCY10 was also analysed, by comparing the specific grain boundary conductivity in both wet and dry conditions in reducing and oxidising atmospheres. In reducing atmospheres (H_2), the specific grain boundary denotes an increase of conductivity in nominally dry conditions over that in wet conditions (p_{H2O} ~ 10^{-2} atm), which is most likely related to an increased effect of the n-type electronic by the accumulation of electrons in the space-charge layers adjacent to a positively charge grain

boundary core. In contrast, in oxidising conditions, BCY10 is shown to have lower specific grain boundary conductivity in nominally dry conditions (p_{H2O} ~ 10^{-7} atm), due to dehydration. Nonetheless, by externally imposing a very mild water vapour partial pressure of ~ 10^{-4} atm, the conductivity is found to be equivalent to that obtained in typical very wet conditions (p_{H2O} ~ 10^{-2} atm). The analysis on the grain boundary was further complemented by employing a *Mott-Shottky* model to analyse the differences occurring in the space-charge properties by changing the p_{H2O} in O_2. The results reveal that BCY10 exhibits a decreased depletion of charge carrier species in the space-charge layers in very low humidity conditions (p_{H2O} ~ 10^{-7} atm), but that similar performance is offered in both moderate and highly wet conditions (p_{H2O} ~ 10^{-4} and ~ 10^{-2} atm, respectively). The similar grain boundary transport properties between these two conditions of humidity suggest that the grain boundary of BCY10 is predominantly protonic under moderate wet conditions, with the special advantage that such low humidity values (p_{H2O} ~ 10^{-4} atm) can potentially offer increased stability against barium hydroxide formation, allowing its safe use at these low temperatures.

The role of the minor p-type electronic conductivity in BCY10 is exemplified by studying $La_4Ni_3O_{10-\delta}$ and $La_4Ni_3O_{10-\delta}$+BCY10 composite cathodes in symmetric cells made of BCY10 substrate, where possible electronic leakage in oxidising conditions can lead to a decrease in the apparent polarisation resistance. The work demonstrates that the use of an equivalent circuit modelling including the electronic resistance is necessary to accurately determine the true polarisation resistance of the cathodes in such arrangement. Moreover, the oxygen reduction reaction (ORR) mechanism of both cathodes was studied by the use of a combination of Distribution Function of Relaxation Times (DFRT) analysis and Equivalent Circuit Modelling (EQM). The ORR mechanism of both LNO and LNO+BCY10 composite cathodes reveal that the rate-limiting processes are those of charge-transfer, diffusion and surface adsorption. In particular, the mid-frequency term related to diffusion processes is shown to be the most affected polarisation response by the addition of BCY10 phase, denoting an improvement with increasing temperature.

The work also successfully produced a single-cell based on Ni-BCY cermet anode, BCY electrolyte and Pt cathode, with a state of the art anode supported geometry with BCY

electrolyte film thickness of 20 μm. Preliminary assessment of this cell under applied polarisation in very low humidity conditions (low oxygen and water vapour contents) under both fuel cell/ion pump and electrolyser modes demonstrates distinct features regarding the electrolyte behaviour. While the ohmic resistance is relatively constant in electrolysis mode, it is shown to decrease dramatically under fuel cell/ion pump mode, due to a possible increase in electronic conductivity in regions of the electrolyte that are adjacent to the electrodes. In addition, the DFRT analysis is revealed to be a suitable alternative to the traditional equivalent circuit modelling for single-cell testing, being able to calculate the polarisation resistance values as well as to extract capacitance and time constant values for similar electrode processes.

Overall, the current thesis presents a comprehensive analysis on the electrochemical behaviour of BCY10 in both wet and nominally dry/low humidity conditions. All studies were mostly conducted in a low temperature range (*i.e.*, below 600 °C) where there is currently not much information available in literature, but where this temperature range offers special relevance to the research goals of Bondalti. Special emphasis was given to the capability of this material to operate in low humidity conditions where its stability in atmospheres containing acidic compounds (H_2O, CO_2, …) can still be maintained while still providing appreciable levels of protonic conductivity. It is expected that the methodologies and conclusion here reported will, therefore, be of a great addition to Bondalti's research division, and that it will help further developments regarding the optimisation and understanding the electrochemical membrane reactors that are currently under study by the company. Importantly, this research also opens the way to explore new proton conductor compounds like BCY10 and valuable characteristics in new technological fields that require low humidities and low temperatures of operation.

Further work can also be suggested, mainly related to the study of electrochemically assisted chemical reactions, and to the optimisation of the microstructure and single-cell fabrication:

- Increase the low temperature conductivity and stability of BCY10 by decreasing the grain boundary volume. This can potentially be done by testing different

processing routes and sintering cycles, or by the use of sintering additives such as Ni or Zn. Such methods may also lead to increases in the specific grain boundary conductivity and to the subsequent modification of the space-charge characteristics;

- Further study of the electrochemical behaviour of BCY10 in a single-cell upon introducing changes in temperature and atmosphere compositions. This work will allow to retrieve important parameters such as activation energies at OCV and under applied polarisation as well as providing a deeper understanding of the noted variations in electrolyte ohmic resistance under cell operation;
- Assessing the variation of oxygen and water vapour pressures by thermodynamic models in order to establish limits of operation under applied polarisation;
- Performing chemical reactions using BCY10-based membranes in the nominal absence of water such as the ammonia electrochemical synthesis;
- Fabrication of larger single-cells by adopting scale-up methods such as the tape-casting that is expected to significantly increase both current and electrocatalytic area, facilitating monitoring of gaseous products by techniques such as gas chromatography.